Chitin and chitosan nanomaterials for efficient removal of heavy metals from waste water.

by

Alicia Botes

Thesis presented in partial fulfilment of the requirements for the degree of Doctor of Science in the Faculty of Science at Stellenbosch University

Supervisor: Prof. Suprakas Sinha-Ray, Prof. Albert Van Reenen, Dr. Marietjie Lutz

December 2019

Acknowledgments

I thank God for all the strength He gave me to stay positive and keep on going. I also want to thank my friends and colleagues for all their advice and help during my studies. Thank you for making this experience a fun and memorable one.

I give thanks to my supervisers and study leaders, Prof Albert Van Reenen, Prof Suprakas Sinha-Ray and Dr Marietjie Lutz, for granting me so many oppurtunities to grow and giving me their valued support and advise, and helping my research receive the funding it required. I appreciate all your help. It has been an honor working with you and learning from you. Many thanks to my supporting parents for their constant sacrifice in order to give me every oppurtunity. And last but not least my dear husband for constantly giving me energy and strength when I needed it.

I would also like to thank the following people, for their support and contributions to my project:

1. The Olefins research group.
2. Chemistry and polymer science department.
3. Madeleine Frazenburg and Elrika Harmzen (Geology Department).
4. Divann Robertson
5. Technical Assistants and Financial Staff at the Polymer Science Devision.
6. Bursary funded by the National Research Foundation.
7. Roediger Agencies (TGA analysis and tensile testing)
8. Charney Anderson (ICP analysis)
9. Lize Engelbrecht at CAF (Central Analytical Facility)
10. Vincent Ojijo and colleagues at CSIR (Council of Scientific and Industrial Research)
11. Dewald Botes

Declaration

"I, the undersigned, hereby declare that the work contained in this thesis is my own original work unless indicated otherwise."

Signature: .....

A. Botes

Date: .....

Abstract

Heavy metal contamination is a serious problem that is responsible for water pollution that can cause serious health issues to animals and humans. The problem is being addressed by various researchers through the attempt to manufacture low-cost adsorbents that are friendly to the environment and non-toxic. Several adsorbents show good adsorption capabilities for various type of heavy metal ions. One of these is chitosan, that has been investigated for the removal of lead, chromium, cadmium and mercury amongst other heavy metals. Some modifications have been implemented for chitosan to create a better surface area to improve the affinity for the above mentioned and other metal ions. In this study, chitosan has been modified into various new forms in an attempt to utilise the adsorption sites of this natural polymer effectively. Chitin nanowhiskers, which are (like chitosan) a derivative obtained from chitin, was investigated for the first time, to the best of our knowledge, for the removal of various type of heavy metal cations, while being subjected to varying pH conditions. The removal of hexavalent chromium, nickel, zinc, lead and copper were investigated during this study. Unlike other studies about low-cost adsorbents featuring chitosan that are grafted or crosslinked, which affects the bio-friendly characteristics of the chitosan (CTS) polymer, this project focuses using polymers that are bio-friendly and easy to manufacture. Characterisation of all five biosorbents in this study was done by using DSC, ATR-FTIR, TEM, SEM, TGA and confocal fluorescence microscopy. Some effects were seen in relation to the thermal stability of the biosorbents after the heavy metal ions were adsorbed. A horizontal electrospinning technique was used to synthesise nanofibers containing chitosan, chitosan nanoparticles and chitin nanowhiskers with poly(ethylene-co-vinyl alcohol) as a scaffold, respectively. A chitosan sponge was synthesised using poly(ethylene-co-vinyl alcohol) as a matrix and the mechanical strength of this material was tested using a tensile tester. A zetasizer was used to determine the surface charge and behaviour of the chitin-derived material in an aqueous solution with pH varying from 3 to 11. Inductively coupled plasma spectroscopy (ICP-AES) was used to analyse the aqueous solution after each sorption process and to determine the amount of heavy metal ions present in the solution after specific time intervals. The effect of pH, initial sorbate (heavy metal ions) concentration and the contact time were investigated for each of the biosorbents. The initial sorbate concentration were investigated at 2, 5, 10, 20 and where required 50 and 100 $mg.L^{-1}$ (ppm). The effect of pH was investigated at pH 2, 5 and 11. Samples were taken at time intervals of 10, 30, 60, 80, 100 and 120 minutes. The sorption process was investigated for longer than 2 hours

but saturation occurred after 2 hours mainly because of the small amount of biosorbents used during the sorption process, which were 0.002 g.mL^{-1}. Chitosan nanofibers (CTS-NF) showed the highest adsorption capacity for all heavy metal ions, followed by chitosan nanoparticles with poly(ethylene-co-vinyl alcohol) nanofibers (CTS-NP/EVOH NF), with the exception of Cr(VI). Langmuir and Freundlich isotherms were used along with Pseudo-First- and Second-Order kinetic models to establish the mechanism of interaction between the metal ion and the biosorbent as well as the adsorption capacity and constants required to understand the behaviour of each biosorbent during the sorption processes. The Langmuir isotherm was favoured by all the biosorbents indicating monolayer adsorption. The theoretical and experimental adsorption capacities corresponded well using Langmuir. The Pseudo-Second-Order kinetic model was favoured for all biosorbents indicating that the sorption process followed a chemisorption mechanism. The theoretical and experimental adsorption capacities also corresponded well using Pseudo-Second-Order kinetic model. Desorption studies were also done, using ethylenediaminetetraacetic acid (EDTA), for each biosorbents at varying initial sorbate concentrations to establish the reusability of the biosorbents. The biosorbents, with the exception of CTS-NF and CTS powder, proved to be economic and reusable after 3 to 5 times. A decrease in adsorption capacity was after the first to 3rd cycle of re-use for CTS and CTS-NF.

Uitreksel

Swaarmetaalkontaminasie is 'n ernstige probleem wat water-en omgewingsbesoedeling veroorsaak en dodelike gesondheidsprobleme by mense en diere kan veroorsaak. Die probleem is deur verskeie navorsers aangepak om 'n oplossing wat goedkoop en maklik bekombaar is, te vind. Die materiale moet nie net goedkoop en maklik vervaardigbaar wees nie, maar ook nie skadelik vir die omgewing en mense wees nie. Chitosaan is een van die polimere wat ondersoek is vir adsorpsie as gevolg van die natuurlike polimeer se goeie eienskappe. Daar is al in die verlede modifikasies gedoen aan chitosaan om die oppervlakarea beter te maak, maar daar is gevind dat meeste van die modifikasies kan die goeie kwaliteite van die polimeer onderdruk sowel as die vervaardiging daarvan meer laat kos. In die studie is chitosaan gebruik en in 'n meer natuurlike manier gemodifiseerd. Daar is ook na chitien nanovesels, wat net soos chitosaan afstam van chitin, gekyk. Chitien nanokristalle is tot dusvêr nog nie ondersoek vir die verwydering van swaarmetale nie. Die verwydering van sink, koper, chromium, nikkel en lood is bestudeer. Vyf materiale was gebruik vir die studie oor die verwydering van die swaarmetale, waarvan 3 nuut was. Die materiale se chemiese en fisiese eienskappe is met DSK, VTR-FTIR, TEM, SEM, TGA en 'n Konfokale fluoresensie mikroskoop analise ondersoek. Daar was 'n negatiewe effek op die termiese stabiliteit na die materiale swaarmetale opgeneem het. 'n Horisontale elektrospintegniek is gebruik om die nanovesels te vervaardig, wat uit alleenlik chitosaan bestaan het en dan chitosaan nanopartikels en chitien nanokristalle wat albei poli(etileen-ko-vinielalkohol) as ondersteuning materiaal bevat. 'n Chitosaan spons is vervaardig met 'n poli(etileen-ko-vinielalkohol) matriks en die meganiese sterkte was gemeet met 'n tensiel instrument. 'n Zetasiser is gebruik om die lading van die oppervlakte te meet van die chitien-gebaseerde materiale, met 'n pH wat varrieer van pH 3 to 11. Induktiefgekoppelde plasma spektroskopie is gebruik om die hoeveelheid swaarmetaalione wat opgeneem is te analiseer vir elk van die polimeer materiaal. Die pH was van pH 2 tot 5 en dan na 11 gevarieer. Monsters was by tyd intervalle van 10, 30, 60, 80, 100 en 120 minute geneem, waarna die materiale versadig was. 'n Hoeveelheid van 0.002 mg.L^{-1} van die adsorberende materiale is gebruik. Chitosaan nanovesels (CTS-NF) het die hoogste hoeveelheid verwydering vir elke swaarmetaal gewys, gevolg deur chitosan-nanopartikels/poli(etileen-ko-vinielalkohol) nanovesels (CTS-NP/EVOH NF), met die uitsondering van Cr(VI). Langmuir en Freundlich isoterme is gebruik vir die analiese van die manier waarop die swaarmetale interaksies met die materiale het. Pseudo-Eerste-Orde en Pseudo-Tweede-Orde kinetiese modelle is ook gebruik om die meganisme van adsorpsie te verstaan. Die Langmuir

isoterm en die Pseudo-Tweede-Orde kinetiese model het die beste by al die materiale se eksperimentele data gekorreleer. Desorpsies is gedoen op die materiale om te sien of hulle herwinbaar en stabiel is na verskeie gebruike. Chitosaan en CTS-NF het minder stabiliteit gewys na 1-3 hergebruike waar die ander materiale nog na 5 keer gebruik kon word.

Contents

List of Figures

List of Tables

Abbreviations

CTS Chitosan

chnw Chitin Nanowhiskers

TFA Trifluoro-acetic acid

EVOH Poly(ethylene-co-vinyl alcohol)

NaTPP Sodium Tripolyphosphate

DSC Differential scanning calorimetry

ATR-FTIR Attenuated total reflectance-fourier transform infrared spectrometry

TGA Thermogravimetric analysis

wt% Weight percentage

TEM Transmission electron microscopy

SEM Scanning electron microscopy

CTS-NP Chitosan nanoparticles

IR Infrared

DCM Dichloromethane

q_e Adsorption capacity

ICP-AES Inductively coupled plasma spectroscopy-atomic emission spectrometry

rpm Rotations per minute

FITC Fluorescein isothiocyanate

NF Nanofibers

T Temperature in degrees celsius (°C)

MCL Maximum contaminant levels

WAC Water absorption capacity

EN Electronegativity

HSAB Hard-soft-acid-base

R^2 Correlation coefficient

EDTA Ethylenediaminetetraacetic acid

Chapter 1

Introduction and objectives

1.1 Introduction

Heavy metal contamination is a serious problem in countries around the world. Because of the increasing scarcity of water, scientists are looking for ways to make water re-usable and, where possible, safe for drinking. Heavy metals such as chromium, lead, copper, zinc, iron and nickel are dangerous when leached into the environment [1–3]. Heavy metals are highly soluble in water and can, therefore, be absorbed by plants and other living organisms [4,5]. These hazardous chemicals cannot be broken down naturally by a person's metabolism or by the environment which results in a concentrated presence of pollutants that accumulate over time. Over-exposure to heavy metals depending on the type of heavy metal can cause mild to serious damage and health defects. Heavy metals predominantly result from industrial wastewater that is not treated correctly. Mining industries, metal plating and other manufacturing companies produce wastewater containing heavy metals on a large scale [6]. There are other sources of heavy metal contamination such as illegal landfills, fertilizer and even more natural occurring contaminations that occur via the degradation of water pipes. Metals such as zinc, nickel, lead, copper, and chromium are most often found in wastewater.

Zinc poisoning causes headaches, diarrhoea and nausea, but in higher dosages, it can interfere with the uptake of trace metals important to the metabolism of the body, such as copper and iron. This can lead to deficiencies in the human body and damage to the mechanisms of the body. The World Health Organisation (WHO) has placed a limit on the concentration of zinc in safe drinking water that should not exceed 3 $mg.L^{-1}$ [7].

The maximum contaminant level (MCL) standards for nickel are reported to be 0.20 $mg.L^{-1}$ by Barakat et al. [8] which differs from the reported concentration limit given by the WHO of 0.02 $mg.L^{-1}$ [9]. Ni(II) acts as a human carcinogen, and if Ni(II) is accumulated in the body, it can cause symptoms such as dermatitis, nausea, chronic asthma and coughing. Nickel contamination is caused by electroplating, mining of nickel, the aircraft industry, the pigmentation and ceramic industries [10].

Copper has a reported MCL standard of 0.25 mg.L^{-1}, and if this concentration is exceeded in water, it can cause liver damage, Wilson's disease and insomnia. In many studies, Cu(II) appear to compete well for active sites in the presence of other heavy metals. Lead is extremely toxic to humans, and small children are extremely susceptible to lead in small quantities. It can damage a foetus's brain and cause renal failure as well as problems with the circulatory and nervous system of the human body. Lead, and copper contamination mainly come from electrical industries and paints. Hexavalent chromium is used in staining amongst other applications and is considered a very corrosive toxin if ingested.
Cr(VI) is a carcinogen, that can attack the respiratory system and gastrointestinal tract. It has an MCL of 0.05 mg.L^{-1} [8]. Chromium can only effectively be adsorbed in the anionic form. Reduction of chromium can occur in the presence of an electron donating active site [11]. Cr(III) is not as soluble in water compared to hexavalent chromium (Cr(VI)) making Cr(III) less dangerous [12–15]. Hexavalent chromium is dissolves more easily in water and contributes more to the problem of heavy metal contamination of water sources and the well being of all living organisms that are dependant on these water sources.

Processes for the removal of heavy metals and other pollutants, other than adsorption processes, are biological treatment, membrane processes, advanced oxidative processes and chemical and electrochemical techniques [16]. Adsorption has become more well known for being an uncomplicated equilibrium separation technique. This technique has grown popular because it is such an effective and economical process. There has been researching on many types of adsorbents such as zeolites, clays, silica beads, agricultural waste and activated carbon, of which the latter is the most popular [17]. The important factor that needs to be considered for the selection of an adsorbent is the price [18]. The adsorbent in question needs to be cost-effective and abundantly available. The other important factor is that it should be easily processible, safe and non-toxic and stable in various pH conditions within the water. The synthesis of activated carbon is very expensive, and so is the desorption procedure that, most often leads to the deterioration of the adsorbent.

Natural polymers, such as chitin and chitin derivatives such as chitosan (CTS), gained interest over the years because they are naturally abundant and cheap. They have positive physical and chemical characteristics. These biopolymers have functional groups such as hydroxyl, amino and acetamido groups that allows reactivity and can aid in selectivity [19]. In previous studies that focused on utilising polysaccharides for the removal of heavy metals, the effect of chemical and physical modifications of CTS was investigated. CTS has poor stability in a highly acidic solution due to increased solubility.

In current and previous literature studies, it has been found that crosslinking can enhance

the stability of CTS in an acidic medium. However, as the degree of crosslinking increases, the amorphous regions are increased. The crosslinking lowers the mobility of the polymer chains, and thus the polymer becomes more rigid. This can lower the interaction between the binding sites and the metal ions. As the degree of crosslinking increases, the diffusion of heavy metal ions is hindered and the adsorption capacity is reduced. Crosslinking agents that are most commonly used for the crosslinking of polysaccharides, glutaraldehyde (GLA) and epichlorohydrin (EPI), are toxic and carcinogenic as well as considered neurotoxins in the case of GLA. Tripolyphosphate, sodium trimetaphosphate and citric acid that are non-toxic were investigated as alternatives crosslinking agents, but the adsorption capacities obtained for this material were not as high as seen for the polymers that used GLA or EPI as crosslinking agents [20, 21].

Grafting additional polymers onto the polysaccharide could add functional groups to the material. Grafting can enhance the surface polarity, hydrophilicity and selectivity of the polymer. The disadvantage of this method is the lack of reproducibility, hindering this method to be used on a larger scale for industrial application. The surface morphology of grafted and crosslinked polysaccharides are not homogenous and therefore vary in physical and chemical properties that can greatly affect the adsorption capacity. CTS beads produced by Varma et al., [22], shows how these beads cannot withstand low pH but after crosslinking shows more stability in the same conditions. However, they also reported a reduction of adsorption capacity from 250 to 100 $mg.g^{-1}$ for Cd^{2+} after crosslinking. As mentioned, this is attributed to the hindered diffusion of metal ions caused by the reduced flexibility of the polymer, but also the lowered availability of adsorption sites available on the polymer surface due to the crosslinking interaction that occupies some of the active sites during the chemical reaction [22, 23]. This negatively affects the chelation mechanism of the ions with the amino groups.

Another option for the modification of polysaccharides such as CTS and chitin is immobilization of the polymer using an additional polymer (matrix) forming a composite or blend. This additional polymer needs to include some criteria for selection. It requires to be mechanically stable (strong) and contribute to the physical and chemical properties of the material; an example would be poly(ethylene-co-vinyl alcohol) (EVOH) which is biocompatible, hydrophilic, thermally stable and chemically resistant [24, 25]. The cost should remain low for the entire process. This additional polymer matrix should have good surface area and porosity. The advantage of this modification method is that the crystallinity and therefore mobility of the polysaccharide is not affected by the additional polymer. The adsorption capacity remains unaffected, as well as the kinetics of sorption and the diffusion behaviour for the metal ions. Physical modification of a polysaccharide could help improve the surface area and mechanical stability during adsorption. Modifying CTS and chitin nanowhiskers (chnw) into a nanofiber morphology exposes more

surface adsorption sites and allows for pores to exists increasing the available sites and interaction between the adsorbent and metal ions [26].

Some disadvantages of using polysaccharides like chitin and CTS as an adsorbent exist. The derivatives of chitin generally have a low affinity to metal ions and tend to have a small surface area [27]. The surface area of CTS flakes or powders was determined using a Brunauer Emmet Teller (BET) instrument, and was found to be 2-30 $m^2.g^{-1}$ [19]. It has been noticed in general that as the particle size increases, the time it takes to reach an equilibrium increases while the surface area decreases. The source of chitin, crab and shrimp shells and others, vary from one batch to the next and therefore it is challenging to keep consistency in terms of molecular weight and N-acetylation. This can influence the crystallinity and number of active sites available (amino groups and hydroxyl groups). As mentioned, polysaccharides tend to perform below average in acidic conditions due to protonation that occur on the polymer chain which incur electrostatic repulsion for metal cations.

There are a few significant mechanisms of adsorption that can take place simultaneously during adsorption of heavy metal ions while using these natural polymers. Ion exchange, complexation and electrostatic attractions are the main mechanisms of adsorption of heavy metal ions. Acid-base interaction and hydrogen bond formation, as well as physical adsorption and hydrophobic interactions, can also occur during adsorption [22,28,29] The main contributing parameters that control the mechanism of adsorption are the pH of the solution, the initial concentration of the sorbate (heavy metal ions), the chemical structure of the adsorbent and the presence of ligands. Other lesser contributing factors are temperature during adsorption, agitation and ionisation of heavy metal salts in solution as well as the presence of contaminants. CTS and chitin are dependent on the pH of the solution for effective adsorption and selectivity.

The interaction with specific metal ions (anionic or cationic) can, therefore, shift between chelation or ion exchange. As seen for hexavalent chromium, the speciation of the metal ion is important and can influence the mechanism of adsorption from complexation to electrostatic interaction, in varying pH conditions [11]. Weak acid-base interaction leads to hydrogen bond formation while stronger acid-base interactions can lead to chemical complexation. The adsorbent may also have an interaction with itself during the agitation and applied temperature and pH changes. This behaviour can affect the adsorption capacity and the way the adsorbent acts in aqueous solutions. The ionic radius and molecular weight of the heavy metal ion also affect the mechanism. The surface area, porosity and particle size of the adsorbents also influence the mechanism type. Isotherms such as Langmuir and Freundlich Isotherms are often used to describe the behaviour of adsorbents in aqueous solutions and can help understand the mechanism of adsorption

for specific heavy metals under specific conditions and is more thoroughly discussed in Chapter 2, Section 2.6 [30].

It is interesting to find that studies concerning chitosan nanofibers (CTS-NF), without additional modifications or polymers, are rarely discussed for adsorption studies in literature [31,32]. The softness and brittleness of CTS-NF are considered the reason that few studies for adsorption capacity are available. It has been found that CTS-NF can be considered strong enough to remain stable and hold mechanical integrity during adsorption even under continuous water flow [33]. If the electrospinning parameters are monitored carefully, it is not difficult to obtain stable nanofibers with small diameters [34]. Horzum et al. [33] and Park et al. [35] (using 1,1,1,3,3,3-hexafluoroisopropanol as solvent) are some of the limited number of studies that reported the use of CTS-NF without any additional polymer. Adding polymers for the electrospinning process of CTS can decrease the surface area as well as cause counterproductive effects to the beneficial qualities of CTS in the environment, possibly lowering biodegradability and increasing toxicity.

Another form of chitin which, to the best of our knowledge, have been neglected for investigation of the removal of heavy metals are chitin nanowhiskers (chnw). The nanofibers we created in our lab consist of a blend of chnw and EVOH (chnw/EVOH NF). Chnw are synthesized through HCl-hydrolysis of chitin, removing the amorphous regions of chitin, as described in Section 3.2 [36]. This gives more crystalline and rigid structures with nanoscale diameters and enhanced surface area [37,38]. Chnw has similar beneficial qualities as CTS, being non-toxic, environmentally friendly, easily obtainable and cost-effective. These chitin derivatives (CTS and chnw) have antimicrobial and antioxidative qualities that can also contribute to applications in water treatment [39]. Added to chnw/EVOH NF, two additional novel sorbent materials have been synthesised and investigated for this study namely, chitosan/EVOH sponges and chitosan-nanoparticles/EVOH nanofibers.

1.2 Objectives

The first objective for this study was the preparation and characterization of CTS-and chnw-based biosorbents using EVOH as an additional polymer where relevant as is discussed in Chapter 3.

The second objective was to investigate the effect that pH, contact time and initial sorbate concentration have on the 5 biosorbents for heavy metals ions, Zn(II), Pb(II), Cu(II), Cr(VI) and Ni(II).

The third objective was to obtain experimental adsorption capacities at equilibrium for each biosorbent at time intervals of 10, 30, 60, 80, 100 and 120 minutes using solutions with varying pH of 2, 5 and 11. This data is to be obtained using inductively coupled plasma (ICP) spectroscopy.

The final objective was to use an isotherm to calculate and compare maximum adsorption capacities and theoretical adsorption capacities at equilibrium of each of the biosorbents for all heavy metals. The results will then be compared to other low-cost adsorbents available in the literature as well as each other.

1.3 Methodology

1. Synthesis and characterization of chnw
2. Incorporation of chnw into EVOH and electrospinning
3. Preparation of CTS and EVOH sponge
4. Preparation of CTS-NP
5. Incorporation of CTS-NP into EVOH and electrospinning to form CTS-NP/EVOH NF
6. Electrospinning of CTS-NF
7. Analysis of thermal, mechanical and morphological properties of the biosorbents
8. Analysis of the adsorption capacity of each biosorbent for a range of heavy metals
9. Comparison of biosorbents and investigation into the mechanism of sorption process.

1.4 Outline of chapters

1. Introduction: A outline of the current studies available on chitin and chitosan as well as the problems of heavy metal contamination that need to be addressed. This chapter also contains a brief summarisation of the objectives and methodology of this research project.
2. Background: This chapter shines light on current chitosan-hybrid materials that have been studied and gives an overview of the various materials that are available for the use of heavy metal adsorption and discusses some advantages as well as disadvantages and some research gaps.

3. Experimental: This is an in-depth decription of the experimental work that was perfomed in the laboratory for this research project. This includes the protocols of the preparation and characterisation of all chitin-and chitosan-based materials that were prepared for the adsorption analyses.

4. Results and discussion: Characterization of biosorbents: This chapter discusses the results obtained on the characterisation of the materials that were prepared.

5. Results and discussion: Adsorption of heavy metal ions: The chapter evaluates the chitin- and chitosan-based materials as sorbents for various heavy metals from aqueous solutions. The sorption capcity were investigated and the effect that various parameters have on the sorption efficiency were investigated and discussed.

6. Results and discussion: Isotherms and Kinetic Models: The experimental and theoretical mechanisms of interaction between the various heavy metals and the different sorbents are discussed in this chapter. Two well-known isotherms are employed for the experimetal data. Two popular kinetic models are also used to evaluate the types of driving force that contributes to adsorption.

7. General conclusions and recommendations: The main findings are summarised and future work that may contribute to the work already reported are mentioned in this chapter.

8. References and appendices are located at the end of Chapter 7.

Chapter 2

Background

2.1 Chitin

Chitin [IUPAC name: (1,4)-N-acetyl-D-glucos-2-amine] with an empirical formula of $(C_8H_{13}NO_5)_n$ is a naturally abundant polysaccharide and easily obtainable, second only in abundance to cellulose [40]. Chitin is popularly sourced from discarded crab and shrimp shells and can be considered very cost-effective for research purposes. This discarded waste is obtained from canning industries at sites in Oregon, Washington, Virginia, Japan and by fishing fleets in the Antarctic. Countries such as India, Japan, Poland, Norway and Australia began producing chitin and chitosan commercially because of the useful carotenoids such as astaxanthin that serves as a food additive in aquaculture e.g. salmon [41, 42]. Chitin has been found effective for the regulation of photosynthesis for maize and soybeans. It can also act as a component in anti-cancer drugs, and in other biomedical applications such as dental restoration, drug delivery systems and structural constituent in synthetic organs [26]. Chitin also found uses in composite reinforcement due to its good mechanical properties.

Three types of polymorphic forms of chitin exist known as α-, β- and γ-chitin. The crystal structure of each varies due to the varying polarities of the adjacent chains in successive sheets and the layering or packing of these same sheets [41]. Chitin is highly basic, unlike most other natural polysaccharides. The natural abundant polymorphic form is α-chitin with an antiparallel configuration. The α-chitin has a highly ordered crystalline structure and strong hydrogen bonding between its chains due to the anti-parallel arrangements. This is what mainly affects the rigidity and insolubility of chitin. The β-chitin has a parallel configuration while the γ-chitin has a random configuration varying between anti-parallel and parallel. The arrangements for α-, β- and γ-chitin can be seen in Figure 2.1.

Chitin has lower reactivity than chitin-derivatives, for examples CTS, because of the more ordered hydrogen bonding occurring between the chains as can be seen in Figure

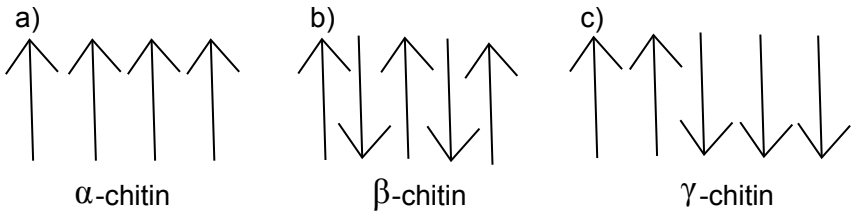

Figure 2.1: The types of arrangements of chitin polymer chains, a) alpha, b) beta, and c) gamma.

2.2. Chitin is not soluble in water especially in ambient conditions due to the rigid structure caused by hydrogen bonding between the polymer chains. Poor swelling behaviour and processing characteristics are also displayed and are also accredited to the strong hydrogen bonds within the chemical structure of chitin. Chemical modification of chitin has been found to improve the solubility in general organic solvents as seen in studies done by Kurita et al. [43] and Inoue et al. [44].

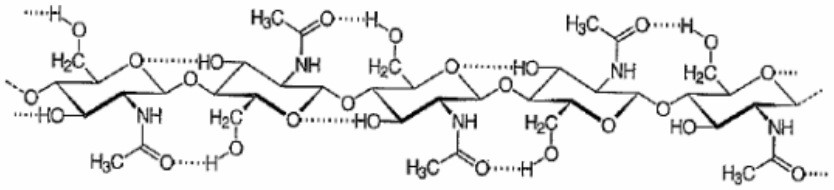

Figure 2.2: The chemical structure of chitin.

Chitin is a mucopolysaccharide and contains more nitrogen than cellulose. This natural polymer is a suitable candidate for chemical modification due to the amide moieties and hydroxyl groups [19] present on chitin. This allow reations such as hydrolysis, oxidation, grafting and enzymatic degradation. These reactive groups present on the 2-,3- and 6-positions on the glucose unit can engage directly in esterification or etherification substitution reactions. The fundamental units of chitin are bound by glycosidic bonds. Chitin also adds many positive attributes to research applications, such as being friendly to the environment, biocompatible and renewable [41]. Immunogenicity and toxicity are very low though nitrogen is present on the polymer [45]. Chitin and chitin derivatives have been used for studies concerning tissue engineering or the growing of cells for living organisms, without inducing a humoral or cell-mediated immune response [46–48]. Crini et al. [19] studied the application of polysaccharide-based materials as adsorbents in wastewater treatment of heavy metal contaminated wastewater. The high nitrogen content present on chitin contributes greatly to the interest of the use of chitin-derived polymers in the application for heavy metal removal.

2.1.1 Chitin nanowhiskers

Chitin nanowhiskers (chnw) can be extracted from chitin using a variety of techniques such as acid hydrolysis [49–54], (2,2,6,6-Tetramethylpiperidin-1-yl)oxyl (TEMPO)-mediated oxidation [55–57], ultrasonication [58], mechanical treatment [59–61] and gelation [62].

The highly crystalline structure of chnw results in high strength and modulus. The size of chnw also cause it to be almost completely free of defects. Chitin nanowhiskers are easy to chemically modify, light-weight, and possess a high surface area and good aspect ratio [41,60]. Due to the source of chitin that is naturally abundant and environmentally friendly, the synthesis of chnw contributes to recycling of discarded crab shells and other shell-fish waste that would have otherwise been challenging to dispose of [63–65].

Acid hydrolysis helps to remove the amorphous regions in the chitin by breaking the glucose bonds. This method is popular for the synthesis of chnw. After acid hydrolysis, the suspension is centrifuged, placed in dialysis tubes and dialyzed for 7 to 10 days until it has reached a pH close to 7 (neutral) [49]. The stable colloidal chnw suspension has amino groups that can be protonated in solutions with low pH, yielding a positively charged suspension. This protonation helps to stabilize the watery colloidal dispersions of chnw due to the repulsive forces between the crystallites [36]. The final dried product (chnw), using a freeze-drying technique, can be seen in Figure 2.3.

The various sources and methods for how chnw can be extracted are presented in Table 2.1. The aspect ratio indicated in the table for each source of chitin descirbes the relationship between the width and the height of the polymer. The aspect ratio indicates the shape of the chitin. Chitin with a high aspect ratio from one source has a long and narrow shape, whereas wider and shorter chitin from a different source will show a lower aspect ratio. The table shows how the structural characteristics of chnw differ when extracted from different chitin sources. The length and diameter of chnw are very important for water treatment applications as a higher aspect ratio and smaller diameters will result in better interaction with EVOH during the synthesis of nanofibers (via electrospinning), while it can also contribute to the adsorption capacity of the polymer [36, 41].

Table 2.1: List of chitin nanowhisker sources

Nr	Chitin Sources	Extraction Method	Structural parameters of nanowhiskers			Ref.
			Length (nm)	Diameter (nm)	Aspect Ratio	
1	Crab shells	Hydrochloric acid hydrolysis	50-300	6-8	15	[50]
2	Crab shells	Hydrochloric acid hydrolysis	100-600	-	16	[41]
3	Crab shells	Hydrochloric acid hydrolysis	100-650	-	10±5	[54]
4	Crab shells	Hydrochloric acid hydrolysis	200-500	-	15-20	[66]
5	Chitin powder from crab shells	Hydrochloric acid hydrolysis	255±56	-	8	[67]
6	Crab shells	TEMPO-mediated oxidation and subsequent ultrasonic treatment	340	8	-	[56]
7	Chitin powder from crab shells	Partial deacetylation with NaOH by fibril surface cationization and subsequent disintegration	250±140	6.2±1.1	-	[57]
8	Chitin powder from crab shells	Gelation with 1-allyl-3-methylimidazolium bromide followed by regeneration with methanol	Several hundred	20-60		[62]
9	Shrimp shells	Hydrochloric acid hydrolysis	150-800	5-70		[68]
10	Shrimp shells	Hydrochloric acid hydrolysis	231-969	12-65	18	[46]
11	Shrimp shells	Hydrochloric acid hydrolysis	180-820	8-74	10	[51]
12	Shrimp shells	Hydrochloric acid hydrolysis	110-975	8-73	7.5	[56]
13	Squid pen	Hydrochloric acid hydrolysis	50-300	10	15	[51]
14	Squid pen	TEMPO-mediated oxidation	Few microns	3-4		[56]
15	Riftia Tubes	Hydrochloric acid hydrolysis	500-10000	18	120	[52]

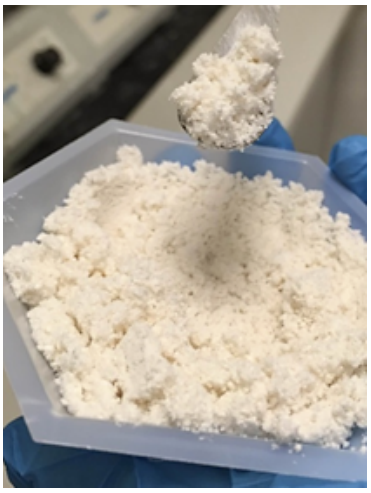

Figure 2.3: The physical appearance of chnw after the freeze drying step.

2.1.2 Chitosan

Chitosan (CTS) [IUPAC name:(1→4)-2-amino-2-deoxy-β-D-glucan] has been reported in several papers for the removal of heavy metals from aqueous solutions [26,39,65,69–72]. It is a polycationic, non-toxic, biodegradable, low cost (approximately USD \$1.3 kg^{-1}) and is prepared from chitin which is naturally abundant [11, 27]. The molecular structure of CTS compared to chitin is shown in Figure 2.4. CTS is synthesized by the N-deacetylation of chitin. The extent of deacetylation of CTS controls the amount of amine and hydroxyl groups available for adsorption. The surface area of CTS powder has been established to be approximately 10 $m^2.g^{-1}$ using Brunauer-Emmet-Teller (BET) surface area measurements [73]. Typically, a lower surface area means a lower adsorption capacity due to the longer diffusional pathways constricting interaction between the sorbent and sorbate [58]. Even so, CTS has shown good adsorption for various heavy metals in literature studies at optimal conditions due to the negatively charged backbone. CTS possesses amine and hydroxyl groups that participate in adsorption and can also allow for uncomplicated chemical modification [74]. Various chemical and physical modifications of CTS powder were investigated to improve the surface area such as forming membranes [8], spherical beads [40], crosslinked CTS networks, coating CTS onto polymers with better surface area, the formation of porous CTS sponges using freeze drying [75] and synthesizing CTS nanofibers (CTS-NF) [76, 77]. Other properties and applications of CTS and chitin have been reviewed by Khateeb et al. [78]

The preparation of CTS-NF is a simple method to improve the surface area of of materials prepared from this polymer. This increases the available adsorption sites and enhances the mobility of the polymer. A CTS-NF mat consist of pores that can allow metal ions of various size to pass through and interact with more available sorption sites. It has been found that CTS-NF are slightly more amorphous than CTS powder due to the electrospinning process that forces the polymer to collect on a base-collector directly from a

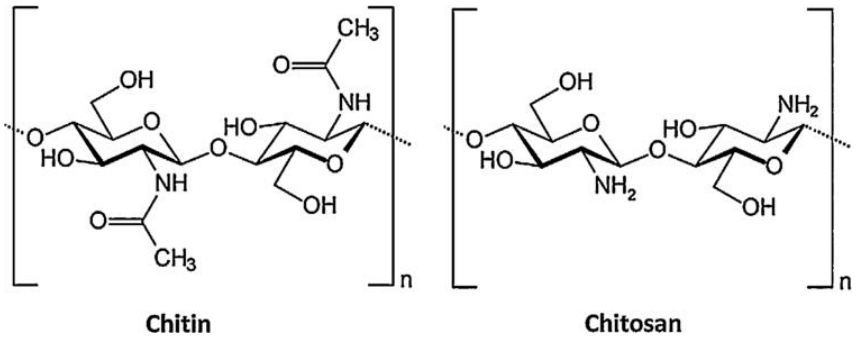

Figure 2.4: The molecular structure of chitin and CTS.

solution, not giving enough time for crystal realignment [33]. This allows the active sites on the nanofibers to be more readily available compared to CTS powder. The mechanical and thermal properties of CTS have been investigated by Devarayan et al. [79], and Ohkawa et al [65].

Trifluoracetic acid (TFA) has been established as the most commonly used solvent for the electrospinning of CTS-NF. TFA is able to form salts with the amino groups of CTS. There are of course problems with using TFA as a solvent when the application is meant for water treatment. There are steps that can be taken to ensure that all the solvent has been removed from the nanofibers before use in such applications, such as washing with an alkaline solution or acetone and drying. If dichloromethane (DCM) is added to the electrospinning solution the solvent becomes more volatile and the chitosan is more spinnable, forming a gel-like substance due to acylation that occurs in the presence of chloride and a strong acid. The solvent type affects the viscosity along with the concentration of the chitosan in the solution. The viscosity affects the fibre morphology significantly.

CTS-NP are defined as such if the particle sizes are between 1 and 1000 nm. CTS-NP are synthesised via 4 popular methods, namely the emulsion-, ionic gelation-, reverse micellar-, and self-assembling-method[58, 80, 81]. In this study, CTS-NP was prepared via the ionic gelation method using sodium-tripolyphosphate (NaTPP) to create an ionic reaction that can promote gelation. TPP is a multivalent crosslinking agent that is non-toxic. CTS-NP was synthesised for the application in drug delivery systems or enzyme immobilization [34, 65]. These small particles have a very good surface area that can contribute to the good interaction between the particle and the metal ion due to the availability of shorter diffusional pathways [71]. These enhanced properties, along with the other beneficial properties associated with CTS, promises to show good interaction with heavy metal ions if utilised correctly for water treatment purposes.

2.2 Poly(ethylene-*co*-vinyl alcohol)

EVOH is a promising copolymer for the synthesis of composites and nanofibers. It has been substantially used in an array of applications including antimicrobial packaging, wound healing treatment and tissue engineering [82]. EVOH is an amphoteric polymer which means that it consists of randomly distributed hydrophobic ethylene and hydrophilic vinyl alcohol segments. This is produced by a hydrolysis reaction of ethylene-co-vinyl acetate polymer (EVA). As shown in Figure 2.5, the acetoxy groups become transformed to a secondary alcohol [25].

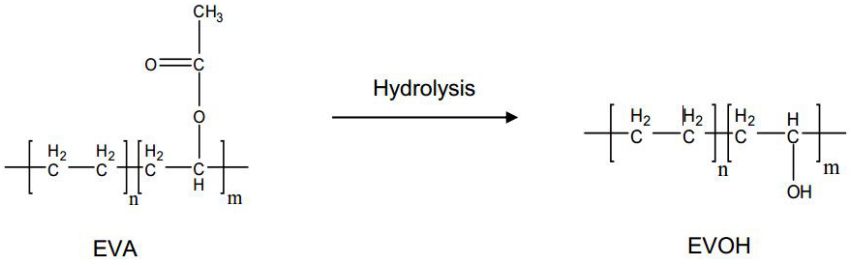

Figure 2.5: The conversion of EVOH from EVA

EVOH can be easily electrospun into nanofibers [83]. Although EVOH is not as highly biodegradable as poly(vinyl alcohol) because of the ethylene component, it has many other positive attributes like biocompatibility, biological and chemical resistance and EVOH can easily be sterilized [84,85]. One of the most commendable properties of EVOH is the specific interaction it can have with chemical species due to its hydroxyl group which allows surface functionalization. The hydroxyl groups present on EVOH can also form hydrogen bonds with other polymers that possess hydroxyl functional groups. The possibility of modifying EVOH makes this polymer compatible in blends and with fillers or for other uses such as water treatment.

EVOH is used in two general types, each utilized for a specific applications. The first type is normally used for adhesives where the EVOH has an ethylene content of 82-90 mol%. The ethylene content is what determines the properties of EVOH. The other type of EVOH contains 60-75 mol% vinyl alcohol. This second type of EVOH is commonly used in barrier materials for packaging, where the vinyl alcohol component contributes greatly to the impressive barrier properties of EVOH [86]. Strong intra- and intermolecular-hydrogen bonding that exists between the hydroxyl groups can form a barrier for oxygen as well as other gases or organic solvents. The higher ethylene content of the first type causes the polymer to have some resistance to moisture and good mechanical and thermal properties. EVOH hydrophilicity varies according to the ethylene content which means

that is wettable in aqueous solutions [24].

2.3 Sorption studies

Metal hydroxide formation and precipitation is the main concern during adsorption studies under alkaline conditions and is important to understand the behaviour of each heavy metal ion in the aqueous environment and be aware that the heavy metals can exist in highly alkaline media [87]. In alkaline solutions Cr(III) can be oxidised to Cr(VI), which is the most toxic form of chromium. Ni(II) and Cu(II) can exist in the presence of excess ammonia at a pH 13, which is also a reason why investigation of adsorption capacity at higher pH is required to establish the possibility of leaching of heavy metals from highly alkaline media into the environment. The results obtained for the investigation of the effect of pH on the speciation of different types of each heavy metals are presented in Section 4.6.

Ni(II) and Cu(II) forms hydroxides at pH 11 in the presence of ammonia. Both metal ions can dissolve in excess ammonia (pH 13). It is possible to dilute Ni(II) and Cu(II) ions in water to pH 11 without the subsequent formation of a precipitate. The formation of hydroxides in the presence of ammonia is presented in Reactions 2.1 and 2.2 for Ni(II) and Cu(II). The dissolution that occurs in the presence of excess ammonia is shown in Reactions 2.3 and 2.4 for Ni(II) and Cu(II). Pb(II) forms a basic salt at pH 13 in the presence of excess ammonia as seen in Reaction 2.5.

$$Ni^{2+} + 2\,NH_{3(aq)} + 2\,H_2O_{(l)} \rightleftharpoons Ni(OH)_{2(s)} + 2\,NH^{4+}{}_{(aq)} \tag{2.1}$$

$$Cu^{2+} + 2\,NH_{3(aq)} + 2\,H_2O_{(l)} \rightleftharpoons Cu(OH)_{2(s)} + 2\,NH^{4+}{}_{(aq)} \tag{2.2}$$

$$Ni(OH)_{2(s)} + 6\,NH_{3(aq)} \rightleftharpoons [Ni(NH_3)_6]^{2+}{}_{(aq)} + 2\,OH^{-}{}_{(aq)} \tag{2.3}$$

$$Cu(OH)_{2(s)} + 4\,NH_{3(aq)} \rightleftharpoons [Cu(NH_3)_4]^{2+}{}_{(s)} + 2\,OH^{-}{}_{(aq)} \tag{2.4}$$

$$Pb^{2+}{}_{(aq)} + 2\,NH_{3(aq)} + 3\,H_2O_{(l)} + 2\,NO_3{}^{-}{}_{(aq)} \rightleftharpoons Pb_2O(NO_3)_{2(s)} + H_2O_{(l)} + 2\,NH^{4+}{}_{(aq)} \tag{2.5}$$

$$CrO_4{}^{2-}{}_{(aq)} + 2\,H^{+}{}_{(aq)} \rightleftharpoons Cr_2O_7{}^{2-}{}_{(aq)} + H_2O_{(l)} \tag{2.6}$$

$$HCrO_4{}^{-}{}_{(aq)} + 7\,H^{+}{}_{(aq)} + 3\,e^{-} \rightleftharpoons Cr^{3+} + 4\,H_2O_{(l)}\ E = 1.20V \tag{2.7}$$

$$NH_3 + H_2O \rightleftharpoons NH^{4+} + OH^{-} \tag{2.8}$$

$$Zn(OH)_2 + NH_{3(excess)} \rightleftharpoons Zn(NH_3)_4{}^{2+} + 2\,OH^- \tag{2.9}$$

The hexavalent chromium ions does not exist in $[Cr(H_2O)_6]^{6+}$ form within an aqueous medium but rather as the oxyanions, $Cr_2O_7{}^{2-}$ or predominantly as $HCrO_4{}^-$ (in an acidic solution) and $CrO_4{}^{2-}$ (in a solution closer to neutral), as shown in Reaction 2.6 [88]. Cr(VI) have a high redox potential (E°) of 1.33 and 1.38 V [11]. Both chromate and dichromate are considered strong oxidising agents especially in the presence of good electron donors. In this study, the hydroxyl and amine groups on CTS can act as electron donors. During the physiochemical interaction between the Cr(VI) and the adsorbent, reduction of the hexavalent chromium can occur, forming Cr(III) as shown in Reaction 2.7.

The positive charge of Cr(III) and the negative charge present on the surface of the adsorbent can be involved in coulombic interactions. It is expected that the negatively charged surface of the adsorbent acts as a Lewis base and can transfer electrons to the Cr(III) centres that act as Lewis acid sites. Cr(III) ions can interact with three adjacent hydroxyl functional groups on the surface of the adsorbent, resulting in the formation of surface oxide species.

The dissolution of ammonia in aqueous media is shown in Reaction 2.8, leading to the formation of ammonium and hydroxide ions. It is possible that $Zn(OH)_2$ in the presence of excess ammonia, forms $Zn(NH_3)_4{}^{2+}$ as shown in the Reaction 2.9 allowing zinc to become soluble under high pH conditions.

2.4 Adsorption and Absorption

Absorption is a term most often confused with the word adsorption. Both these terms involve the transfer of a particle from liquid to solid phase, but the process for this physical transfer differs greatly. Figure 2.6 is used to explain the differences between these two terms more clearly.

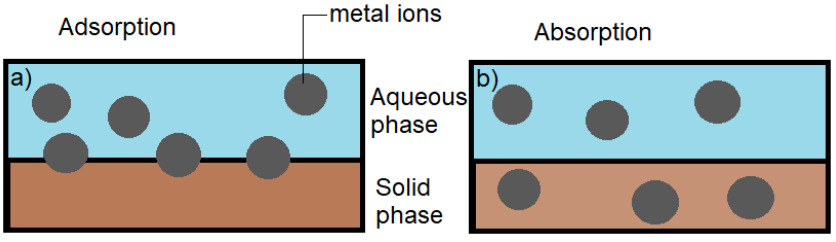

Figure 2.6: Difference between a) adsorption and b) absorption.

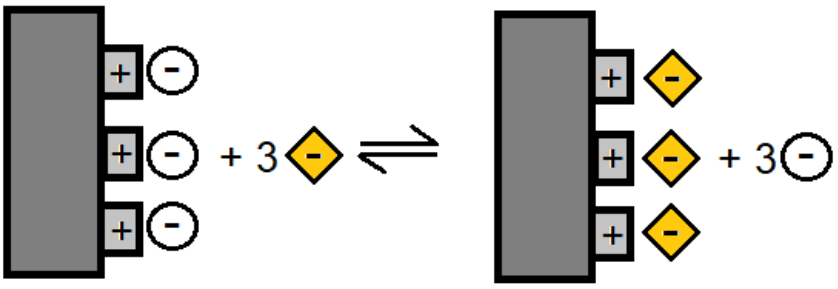

Figure 2.7: The principle of the ion exchange process

Metal ions (sorbate) are able to accumulate on a surface during adsorption. This surface usually consists of adsorption sites that are comprised of functional groups. In many cases, these can be charged and may have significant steric properties. Absorption, however, occurs through migration of the metal ions into the internal regions of solid phase material. Absorption will mainly be seen when the material has a porous structure that will allow encapsulation of the heavy metal ions. Sorption is used to combine these two terms since both these processes can be observed during metal ion removal by the sorbent materials.

Two sorption types exist. Physisorption is mainly based on Van Der Waals forces, dipole forces, dipole-dipole forces, dispersion forces, and induction forces [89]. Chemisorption describes the interaction between the sorbate and the sorbent via chemical bond formation. These interactive forces are much stronger compared to physisorption.

2.5 Ion Exchange

The charged sorption sites found internally and on the outer surface of the material can interact with the metal ions. Ion exchange is not exactly part of the sorption process since there is an interchange of ions required while the electroneutrality of the solution must be maintained [89]. Figure 2.7 shows the principle of the ion exchange process.

Fixed protonated functional groups are found on the chitin-based materials and the exchange occur with protons dissociating from the functional groups of the sorbent material and these are replaced by metal ions [90]. This was expected to be the process that occurred during the removal of some heavy metals [89, 91]. A large reduction in pH was observed as a result of the increase in proton concentration following the ion exchange that took place during the adsorption process of Cr(VI) for example. Ion exchangers, such as the functional groups present on the polymer materials used as biosorbents in this study, are good at interaction with metal ions. The pKa for the functional groups that will most likely be the main sorption sites on the chitosan-based sorbent materials, are considered

as mildly basic with a pKa of 6-8. The hydroxyl groups found on all biosorbents used in this study are considered as weak acids with a pKa of 9-10.

These surface hydroxyl groups are cation exchangers and will be more likely to interact with cations, in a protonated environment. The amine groups and amide moieties found on CTS-based sorbent materials and chitin nanowhisker-based sorbent materials respectively are anion exchangers that will be better for removing anions, as long as the functional groups remain in a protonated environment.

Ion exchange can be described, using well known isotherms and kinetic models, like Langmuir and Freundlich isotherms and First-Order and Second-Order kinetic models, as a phyisco-chemical process [92]. Ion exchange is usually placed under the same category as the sorption process, whereas previously mentioned the process is classified as a physisorption and chemisorption process. Ion exchange is however more correctly classified using columbic forces as a proper description of the process. Electrostatic forces are a driving force for ion exchange. In general, an ion exchange process is favoured by biosorbents for ions that have high charge, large size, and are poorly solvated in water [90].

2.6 Adsorption isotherms

Isotherms are used to determine the theoretical maximum adsorption capacity of an adsorption system. It is also a valuable method to obtain information about the mechanism of adsorption for the different types of adsorbents and heavy metal ions. There are quite a number of isotherms available for the investigation of the sorption system of various types of adsorbent-adsorbate scenarios. There are however only a few that describe solid-liquid phase adsorption, namely Tempkin, Sips, Redlich-Peterson, Freundlich and Langmuir isotherms [93, 94]. Tempkin contains a factor that specifically takes the adsorbent and adsorbate interaction into account during adsorption. This derivation assumes that the binding sites all have the same energies distributed uniformly across the surface of the adsorbent [95,96]. The Sips isotherm is a combination of Freundlich and Langmuir isotherm models. It is derived for the purposes of studying heterogeneous systems. This isotherm is a three parameter equation making it more troublesome to determine the isotherm parameters and constants. The use of a trial and error optimisation of the correlation coefficient is required. It is most commonly suited to experimental data that consist of a molecule occupying two adsorption sites.

The Redlich-Peterson isotherm model is also a hybrid isotherm that features Langmuir and Freundlich isotherms. It also includes three parameters due to this hybridisation.

Due to the optimisation of the correlation coefficient, during the determination of parameters and constants, the isotherm can give high R^2 values and can superficially indicate a good fit which is often misleading. The most commonly used and most popular models are the Langmuir and Freundlich isotherm models since these models are more inclusive in the range of heavy metal ions and types of adsorbents used in solid-liquid phase adsorption [97–99]. The mathematical simplicity of these isotherms is also appealing to many researchers as well as the accuracy due to less independent parameters used during the determination of the maximum adsorption. It is however important that the study should cover a large range of initial sorbate concentrations in order to minimise errors and increase reproducibility [94].

2.6.1 Langmuir isotherm

Irving Langmuir was awarded the Nobel Prize in 1932 for developing the isotherm that attempts to describe the surface chemistry during adsorption [100]. It is necessary to correlate equilibrium data for the adsorbent and metal ions in order to understand the efficiency of each adsorbent. The Langmuir isotherm is the most popularly used isotherm for adsorption because it tends to fit well with a wide range of experimental results, even at low sorbate concentrations. It has been found that the isotherm follows Henry's law at low concentrations, where C_e (concentration at equilibirum) is equal to 0 at low sorbate concentrations, see the expression presented in Equation 2.10, where q_e (adsorption capacity obtained at equilibrium) is made the subject [101]. This isotherm assumes that adsorption of heavy metals occurs via monolayer adsorption on a homogenous surface where no interaction occurs between attached ions and ions dispersed in the solution. In this system, it is assumed that the adsorbent has uniform adsorption sites of equal energy, dispersed evenly across the surface.

All sites, therefore, possess the same amount of affinity for each heavy metal ion. The main assumption for the Langmuir Isotherm model is that no interaction occurs between the sorbate species and that once a metal ion occupies a sorption site, no further sorption takes place. A theoretical saturation value is reached indicating the formation of a monolayer and no further sorption is then possible. Deviations that tend to occur for this isotherm are indications of pH effects and the types of surface complexes that are formed between the ions and active sites (adsorption sites) on the adsorbent, as well as the availability and amount of active sites [11]. The Langmuir isotherm equation can be used to find a linearized relationship between the number of heavy metal ions adsorbed and the concentration at equilibrium as shown in Equation 2.10.

$$\frac{1}{q_e} = \frac{1}{a_m b}\frac{1}{C_e} + \frac{1}{a_m} \tag{2.10}$$

$$q_e = \frac{(C_i - C_e)V}{W} \tag{2.11}$$

The Langmuir constant a_m represents the maximum adsorption capacity ($mg.g^{-1}$) while b is correlated to the energy required for adsorption of heavy metal ions and can, therefore, indicate the affinity of the metals for the adsorption sites of the adsorbent. The experimental value of q_e, using the data obtained through ICP analysis of the metal content, was calculated using Equation 2.11 and compared later with the theoretical q_e calculated with the linearised equation that corresponded to the best fit to the experimental data. There are four types of Langmuir linearisation and plots. If b increases, the affinity for the adsorption sites increases. These Langmuir constants, a_m ($mg.g^{-1}$) and b ($L.mg^{-1}$), can be determined from the intercept and slope respectively, using the equation for Type 1 with the linearized plot of $\frac{1}{q_e}$ and $\frac{1}{C_e}$. The linearized equation for each Type are shown below in Table 2.2 [42]. C_e and q_e are the concentration at equilibrium ($mg.L^{-1}$) and the amount of heavy metal ion adsorbed at equilibrium ($mg.g^{-1}$).

Table 2.2: Type of linear form for Langmuir isotherm.

Type	Linear equation	plot
1	$\frac{1}{q_e} = \frac{1}{a_m b}\frac{1}{C_e} + \frac{1}{a_m}$	$\frac{1}{q_e}$ vs $\frac{1}{C_e}$
2	$\frac{C_e}{q_e} = \frac{1}{a_m b} + \frac{1}{a_m}C_e$	$\frac{C_e}{q_e}$ vs C_e
3	$q_e = a_m - \frac{1}{b}\frac{q_e}{C_e}$	q_e vs $\frac{q_e}{C_e}$
4	$\frac{q_e}{C_e} = a_m b - b q_e$	$\frac{q_e}{C_e}$ vs q_e

If the theoretical adsorption capacity correlates well with the experimental adsorption capacity, and the correlation coefficient (R^2) is close to 1, then the isotherm indicates a good fit with the experimental data. There are three other types of plots to determine the parameters of the Langmuir isotherm. Type 1 and 2 indicated the best fit for the biosorbents in this study and was used for the plotting and calculations of all values (parameters and constants) for each adsorption process to establish the mechanism of adsorption as well as the theoretical maximum adsorption capacity and adsorption capacity at equilibrium ($q_{e(theo)}$).

The feasibility of Langmuir isotherms are expressed by the dimensionless separation factor, R_L. R_L indicates favourable adsorption in a single metal ion system if $0<R_L<1$ [102]. The separation factor can be calculated using the Equation 2.12 presented below.

$$R_L = \frac{1}{1 + bC_i} \tag{2.12}$$

2.6.2 Freundlich isotherm

Herbert Freundlich developed the Freundlich isotherm in earlier days which are still used as an alternate to the Langmuir isotherm today. The Freundlich isotherm better describes data obtained at lower concentrations. The Freundlich isotherm is older than the Langmuir isotherms and is an empirical equation that is used to describe non-ideal adsorption processes particularly where the surface of the adsorbent is not homogeneous, and sorption may most likely occur in a multilayer fashion due to the irregularly distributed adsorption sites. This isotherm therefore assumes that the adsorbent possesses a heterogeneous surface. This isotherm also suggests that as the concentration of sorbate increases, the adsorption capacity increases. The linearized equation of the Freundlich isotherm is presented below in Equation 2.13.

$$log\ q_e = log\ K_F + \frac{1}{n} log\ C_e \tag{2.13}$$

The linear plot of log q_e vs log C_e has an intercept, log K_F and a slope, $\frac{1}{n}$. The constants K_F and n are Freundlich dimensionless constants that indicate an affinity for the binding site of the sorbate and the degree of heterogeneity of the adsorbent, respectively. If the slope, $\frac{1}{n}$ is close to 1 it indicates that the adsorbent contains more homogeneously spread adsorption sites on the surface. Sorption is considered favourable if $1<n<3$ [103]. If K_F is high, it means that the adsorption becomes more effective.

The Freundlich isotherm has been considered to possess some limitations since it does not seem to correlate accurately at low sorbate concentrations and lacks a rudimentary thermodynamic basis that cannot be reduced to Henry's law in less concentrated solutions.

2.7 Kinetic models

It is important to understand the rate-controlling step for each adsorbent and metal ion adsorption experiment to understand the strengths and flaws of each material. The kinetics of adsorption of heavy metal ions from an aqueous solution onto an adsorbent can be described using two type of rate laws, pseudo-first-order and pseudo-second-order [101]. In general, if the metal ions removal process occurs via ion exchange, the process should be expected to be fast. This is not always the case as reported by other research groups

[91, 104]. Better correlation between the kinetic models and experimental data can be seen if the rate of metal ion removal is fast. If the concentration of the sorbate is high, the step during the removal of the metal ions that will affect the rate of sorption will be the diffusion of the ions through the sorbent material. There are, however, a number of experimental parameters that can influence the sorption kinetics. The nature of the sorbent material and the counter ions, the level of agitation, the concentration of ions, the solution chemistry of the metal complex and the physical properties, such as size of the metal ions and porosity of sorbent material (surface area) can all have an effect on the kinetics of the removal process [89].

2.7.1 Pseudo-first-order kinetic model

The pseudo-first-order equation proposed by Lagergren have an expression as presented in Equation 2.14. This equation can be integrated to the expression seen in Equation 2.15. A general trend seen for the pseudo-first-order rate law is that it is directly dependant on the initial concentration of the sorbate (heavy metal concentration) [105]. The first-order rate constant k_1 is a combination of k_a and k_d, which is the adsorption and desorption rate constants respectively. After plotting k_1 vs C_i (initial sorbate concentration) the linear plot can be used to determine k_a and k_d from the slope and intercept [73, 87]. The adsorption and desorption rate constants assist in determining the metal ion uptake through the sorbent with respect to time at a constant concentration. The equilibrium constant can then be determined using Equation 2.16. The expression $k_1(q_e\text{-}q_t)$ does not consider the number of active sites that are available on the adsorbent. Also, the ln q_e is convertible as a parameter and does not always correlated to the intercept of a plot of $\ln(q_e\text{-}q_t)$ vs t, which makes it possible that the experimental values might differ from the theoretical values [101].

$$\frac{dq_e}{dt} = k_1(q_e - q_t) \tag{2.14}$$

$$q_t = q_e(1 - e^{-k_1 t}) \tag{2.15}$$

$$K = \frac{k_a}{k_d} \tag{2.16}$$

$$-k_1 = \frac{x}{2.303} \tag{2.17}$$

The first-order rate constant, k_1, can be determined, using Equation 2.17. The x is equal to the value obtained from the slope of the graphs from the pseudo-first-order plot of $\ln(q_e\text{-}q_t)$ vs t, using the expression in Equation 2.18. The q_t is the adsorption capacity at a certain contact time (minutes). As seen in Equation 2.18, the slope of this linear plot is equal to $-\frac{k}{2.303}$ and the intercept is ln q_e. The theoretical adsorption capacity can thereby also be determined by this linear plot and equation mentioned above [73].

$$ln\ (q_e - q_t) = ln\ q_e - \frac{k_1}{2.303}t \tag{2.18}$$

The pseudo-first-order rate law is most often used for adsorption in a liquid/solid adsorption system that is reversible [6]. In many cases it has been found that pseudo-first-order-rate law does not fit well with the entire range of contact times used for an adsorption study, it is generally more applicable for the initial stage of adsorption. Poor fit also tends to occur if the initial concentration of sorbate is very low during adsorption studies. It has been found that if the state of equilibrium is reached in a short contact time, it can lead to a good correlation between the theoretical and experimental data and higher R^2 value. A good correlation value does not, however, ensure that the experimental and theoretical equilibrium adsorption capacity will fit well, as found in literature studies [106].

2.7.2 Pseudo-second-order kinetic Model

The chemisorption kinetic rate can be expressed using a pseudo-second-order rate equation as seen in Equation 2.19. A trend that has been seen in literature studies, indicates that the adsorption transforms to the pseudo-second-order rate law as the initial concentration of sorbate decreases. The second-order rate constant, k_2, can be determined using the linearized expression seen in Equation 2.20, where x is the slope value. There is more than one type of linear plot available for the pseudo-second order rate expression as seen in Table 2.3. The k_2 can be determined from the plot using the Equation 2.21. The first type, which is more popular and often found as a better fit for most literature studies using low-cost adsorbents, are the linear plot of $\frac{t}{q}$ vs t, where the slope is $\frac{1}{k_2(q_e)^2}$ while the intercept is $\frac{1}{q_e}$. The adsorption rate is proportional to the square of the difference between the amount of sorbate adsorbed at equilibrium and sorbate adsorbed at a certain time. The amount of sorbate adsorbed after a specific time is q, and the time is t. Type 2 is plotted as $\frac{1}{q}$ vs $\frac{1}{t}$, while type 3 has a plot expressed by $\frac{1}{t}$ vs $\frac{1}{q}$. Type 4 is plotted as $\frac{q}{t}$ vs q [106]. In some cases, the Type 2 Second-order-rate expression also showed good correlation while the most imperfect correlation was seen from the expression plotted using Type 4.

$$\frac{dq_t}{dt} = k_2(q_e - q_t)^2 \tag{2.19}$$

$$\frac{t}{q} = \frac{1}{k_2(q_e)^2} + \frac{1}{q_e}t \tag{2.20}$$

$$k_2 = \frac{1}{x(q_e)^2} \tag{2.21}$$

Table 2.3: Type of linear form for the Pseudo-Second-Order Kinetic model.

Type	plot
1	$\frac{t}{q}$ vs t
2	$\frac{1}{q}$ vs $\frac{1}{t}$
3	$\frac{1}{t}$ vs $\frac{1}{q}$
4	$\frac{q}{t}$ vs q

The pseudo-second-order rate law is based on the concentration of the metal ion present initially in the solution as well as the affinity of the adsorbent for these ions. If experimental data correlates well to the theoretical results of the pseudo-second-order rate law, the adsorption may follow a chemisorption mechanism, and electron exchange occur forming covalent forces between the metal ion and the adsorbent.

2.8 Desorption studies

The ability for an adsorbent to be regenerated and re-used is important to increase the cost-effectiveness of this polymer. The recovery of valuable metals, such as Au, is also possible if an adsorbent can desorb. Factors that indicate good regeneration of an adsorbent are the fact that the morphology and stability of the adsorbent are not diminished and that the solution should have high concentrations of metal ions present after desorption. The adsorbent should not have reduced adsorption capacity and maintain reproducibility over several desorption and adsorption cycles. The mechanism of adsorption is important to determine the type of desorption process that will be required. The cation interacts with the amine groups and the reaction involves the lone pair on the nitrogen being transferred from the N centre to the electron deficient metal centre to form a dative covalemt metal-N bond. Tihs is why acidic solution closer to pH 2 or 3 can cause metal desorption [21]. HCl and NaOH are often used to mediate desorption. Ethylenediaminetetraacetic acid (EDTA) is also used for desorption because it is such a strong chelating agent and suitable for adsorbents that dissolve in acidic solutions. These desorption agents manage to interfere with the metal ion reaction on the surface of the adsorbent. The percentage of desorption was calculated for each of the adsorbents, as seen in Equation 2.22, where

C_a and C_d are the concentration after adsorption and concentration after desorption respectively. This also gives an indication of the sorbent's affinity for the heavy metal ions, according to how long it takes to release from the adsorbent and the reusability of the material.

$$\%Desorbed = \frac{C_d}{C_a}(100) \tag{2.22}$$

2.9 Electrospinning

The parameters that influence the diameter and morphology of nanofibers the most during electrospinning are viscosity and conductivity. Other parameters are distance from needle tip to the base collector, humidity and temperature, as well as the flow rate. The formation of a stable Taylor cone on the tip of a needle is an indication that good electrospinning is possible [107] as shown in Figure 2.8. When an electrospinning solution forms a stable Taylor cone it suggests that the viscosity and conductivity of the solution, as well as the distance from tip to collector base, flow rate and voltage that is introduced into the system are acceptable for electrospinning and that the formation of nanofibers can be expected. If the viscosity of an electrospinning solution is too low, electrospraying may occur causing a beaded morphology. When the viscosity of the electrospinning solution is too high, the fibre diameter may increase. Low conductivity of the electrospinning solution and poor flow rate (that is too slow or too fast) can also cause electrospraying [34].

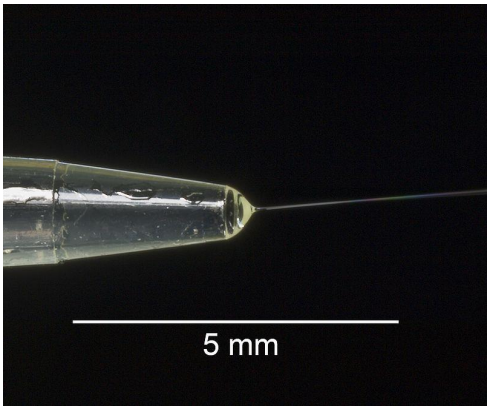

Figure 2.8: The formation of a stable Taylor cone. [107]

2.9.1 Process and setup

A high electric field is applied to a solution within a needle in a controlled environment. The applied voltage determines the degree of electrostatic charge that will induce the ejection of the polymer-jet solution from the needle to an oppositely charged base-collector.

The grounded collecting plate can be stationary or rotating. A rotating collecting plate allows the fibres that are electrospun to be more aligned and uniform [108]. Uniaxially orientated nanofibers can be fabricated by electrospinning onto a rotating cylinder collector. Fibre alignment can improve the mechanical properties of a nanocomposite even further than randomly orientated fibres. Both the needle of the syringe acts as an electrode causing deformation in the droplet that forms at the tip of the needle at the end of the set-up. This droplet formation is known as a Taylor cone. The solvent evaporates during the process of electrospinning, yielding a dry fiber mat collected after the electrospinning procedure. This process is illustrated in Figure 2.9.

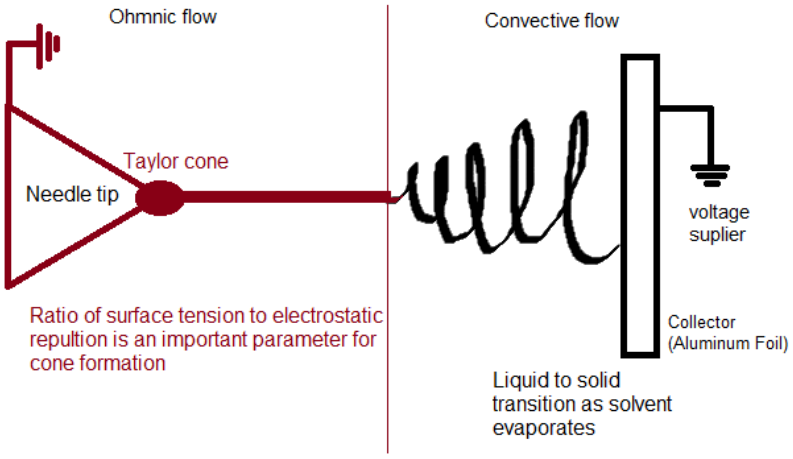

Figure 2.9: The electrospinning procedure [109].

Other types of electrospinning procedures exist, such as ball electrospinning that allows fibres to be electrospun from multiple points due to the formation of multiple Taylor cones caused by a rotating roller within the electrospinning solution as shown in Figure 2.10. Instead of a needle a small glass ball, called a ball spinneret, is placed in the solution and rotated while an electrical field is applied. The fibres are spun upwards which helps prevent polymer solution from dripping onto the fibre mat that is collected on the collector plate.

Multi-needle electrospinning techniques, such as co-axial electrospinning, have also been investigated where more than one needle is used in the electrospinning system and more than one type of electrospinning solution is produced by each needle nozzle. A large working environment is required for multi-needle electrospinning so that the strong interferences between adjacent solution jets can be avoided.

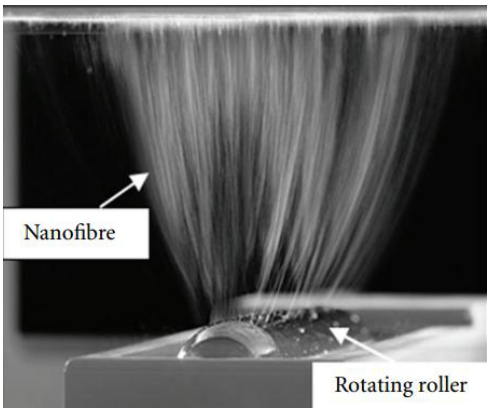

Figure 2.10: The procedure of ball spinning. [109]

The conventional setup (horizontal or vertical) is used widely in hundreds of labs all over the world. In this study only, the conventional horizontal setup was used. There are important parameters to consider when conducting an electrospinning procedure as discussed in Section 2.9.2.

2.9.2 Parameter effects

Electrospinning has many factors that can influence the diameter and morphology of fibres [109]. The variables and parameters are summarized in Table 2.4. The most important parameters are conductivity, viscosity, distance from the needle to base collector and flow rate. Intrinsic properties of the electrospinning solution such as the polymer type, chain conformation, viscosity, elasticity, polarity and electrical conductivity, are all important contributions to the properties of the nanofibers. The surface tension of the solvent also influences the way that the solution will electrospun. Minimization of the surface tension of the solvent causes one or more spherical droplets to form from the electrospinning solution jet. The electrostatic repulsion between the charges on the jet surface tends to increase the surface area of the droplet. This is favourable for the formation of a thin electrospinning jet rather than electrospraying. Good viscoelastic forces within the polymer solution prevent rapid changes in the shape of the fibre and afford more support for the formation of smooth fibre morphology [109]. The conditions within the lab also contribute to the product of the electrospinning process. The last two factors that can impact the morphology and diameter of the fibre-mat are humidity and temperature [110].

Table 2.4: Parameter that affect electrospinning.

	Solution Properties		**Processing Properties**
1	Concentration and Viscosity	1	Applied voltage
2	Molecular Weight and Architecture	2	Flow rate
3	Conductivity	3	Tip to collector distance
		4	Atmospheric Temperature and Humidity

Chapter 3

Experimental

3.1 Materials

Medium molecular weight chitosan (CTS) (deacetylation 85%) and chitin (sourced from shrimp shells) were obtained from Sigma Aldrich. Trifluoroacetic acid (TFA), dichloromethane (DCM) and 37% Hydrochloric acid (HCl) were procured from MINEMA as were analytical grade $Zn(NO_3)_2{\cdot}6H_2O$, $Ni(SO_4){\cdot}7H_2O$, $K_2Cr_2O_7$, $Pb(NO_4)_2$ and $Cu(NO_3)_2{\cdot}3H_2O$. Poly (ethylene-co-vinyl alcohol) (EVOH) (32 wt% ethylene content) was provided by Sigma Aldrich along with isopropanol. SnakeSkinTM dialysis tubing (10K MWCO, 22 mm) was provided by Thermo Fischer Scientific. Potassium nitrate (KNO_3)(98-100%) was obtained from Barrs Industrial Enterprises. Ethylenediaminetetraacetic acid (EDTA) was obtained from Sigma Aldrich. Fluorescein isothiocyanate (FITC) was provided by Sigma Aldrich. Glacial acetic acid (100%) was provided by Merck.

3.2 Preparation of chitin nanowhiskers

Chitin nanowhiskers (chnw) were prepared by acid hydrolysis of chitin [36]. Chitin flakes (3g) were hydrolyzed in HCl (3M, 90 mL) at 100 ℃. The hydrolysis took place under reflux and was terminated after 4 hours by the addition of cold deionized water (90 mL). The hydrolysis step was then followed by centrifugation. The solution was decanted into centrifuge tubes and the initial (yellow) supernatant was discarded after which the substrate was washed with more deionized water and centrifuged again. These steps were repeated until the supernatant became milky (turbid) indicating the presence of chnw. The turbid suspension was retained and dialyzed against deionized water using snakeskin dialysis tubes (20 to 25 ℃) until a neutral pH was obtained (typically after 2 weeks). The chnw suspension was then frozen with liquid nitrogen and freeze-dryed to obtain white cotton-like chnw.

3.3 Labeling of chitin nanowhiskers, chitosan and chitosan nanoparticles

Freeze dried chnw (250 mg) was added to a round bottom flask containing NaOH (0.1 M, 25 mL). FITC (10 mg) was added to the solution. The flask was closed immediately using a stopper and covered with aluminium foil. It was stirred in darkness for three days. After this the contents of the flask was decanted into centrifuge tubes, centrifuged twice and washed with distilled water while the solid material was collected and centrifuged again. Centrifugation was repeated until the suspension was clear. The chnw that was collected after washing was then dialyzed in distilled water for approximately a week until a neutral pH has been reached. The same procedure was used for the labeling of chitosan nanoparticles and chitosan powder.

3.4 Preparation of chitin nanowhiskers/poly(ethylene-co-vinyl alcohol) composite nanofibers

Chitin nanowhiskers (3 wt% w/v) in a mixture of isopropanol/water (70/30% v/v) was sonicated for 60 minutes at room temperature (25 ℃). EVOH (5 wt% w/v) was then dissolved in a similar isopropanol/water mixture at 90 ℃ (2 hours). The chnw solution was added to the EVOH solution and mixed for 5 minutes. The electrospinning procedure was as follows:

An IR lamp was used to maintain the temperature of the solution in the syringe above 30 ℃ (Figure 3.1). This was necessary to prevent clogging in the needle and allow for better control over the flow rate. The flow rate was held constant at 10 μL.min^{-1} with an applied voltage of +10 and -5 kV. The humidity varied between 20 - 40% but was controlled using the IR lamp and closed environment. The nanofibers were collected on a non-rotating collector base that was placed 15 cm from the tip of the needle. The resulting chnw/EVOH composite nanofibers are shown in Figure 3.2. It is important to note that the same amount of chnw and EVOH was used for all chnw/EVOH composite nanofiber synthesis. The wt% was calculated with regards to the mass solution.

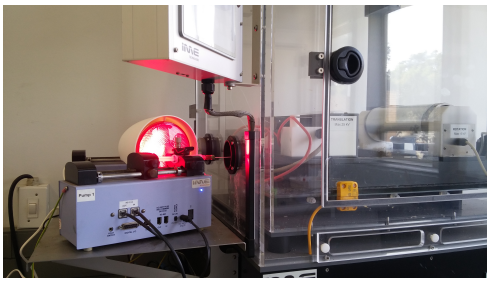

Figure 3.1: Electrospinning setup with IR-lamp

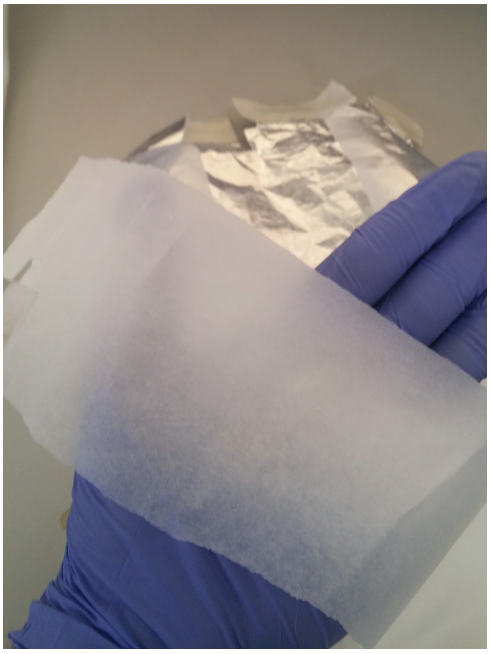

Figure 3.2: Electrospun chnw/EVOH nanofibers

3.5 Preparation of chitosan nanofibers

CTS (7 wt% w/v) was dissolved in a mixture of TFA and DCM (70/30%v/v) for 4 hours at 70 ℃. This yielded a viscous (yellow) chitosan solution. The horizontal electrospinning technique was used for the synthesis of nanofiber-based biosorbents. The electrospinning procedure was as follows:
An IR lamp was once again utilized to maintain constant temperature and humidity conditions. The flow rate was maintained at 4 μL.min^{-1} with an applied voltage of +10 kV and -15 kV at 15 cm from the tip of the needle to non-rotating collector base covered with aluminum foil.

All of the CTS-NF instantly dissolved once it was introduced into a aqueous solution. This dissolution was ascribed to TFA that was trapped within the CTS-NF. No amount of drying could remove the solvent from the nanofibers without harming the morphology of the nanofibers itself. The CTS-NF were treated with a 25% ammonia solution (carefully added dropwise) to neutralize the strong acid. The CTS-NF were then washed in

ultrapure water to remove the remaining TFA and ammonia without dissolving, and dried at 30 ℃. This treatment appeared to improve the stability of the CTS-NF in aqueous solutions.

3.6 Preparation of a chitosan/poly(ethylene-co-vinyl alcohol) sponge

The EVOH (5 wt% w/v) was dissolved in a mixture of Isopropanol/distilled water (70/30% v/v) at 90 ℃ for 2 hours. CTS was dissolved (2% v/v) in an aqueous solution of acetic acid at 25 ℃ for 2 hours. The EVOH solution was cooled down to 40 ℃ and added to the CTS solution. The blend was then stirred together for 30 minutes. The solution was taken up into an open-edged syringe as seen in Figure 3.3 and extruded onto a petri-dish after being allowed to cool down. A viscous gel was formed during solvent evaporation after 3 days (Figure 3.4). The extruded polymer blend was washed with acetone and then allowed to dry further until all solvent was evaporated leaving behind a flexible tube-like sponge as shown in Figure 3.5. The shape of the CTS/EVOH can be adapted to the specifically required shape depending on where it is applied in the environment, by simply using a different mold or choosing a syringe with a different diameter. Experimentation with the loading percentage of chitosan into the sponge indicated that the amount of chitosan should be present in large amounts within the sponge to yield optimal adsorption capacity. There is, however, a limit to the amount of CTS that can be successfully incorporated without causing heavy agglomeration and negative effects on the mechanical attributes of the sponge. As seen in the Figure 3.3, different loads of CTS (1 and 2.5% w/v) was used, with regards to the mass solution. The CTS/EVOH sponge containing CTS (2.5 wt% w/v) was chosen as the best option to use for adsorption studies.

Figure 3.3: The initial stage of a CTS/EVOH sponge preparation after blending

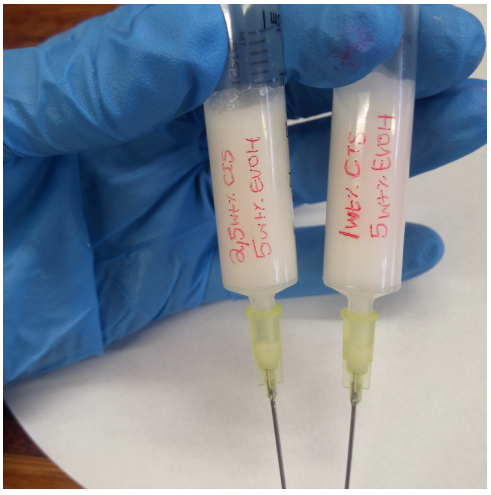

Figure 3.4: Final stage before extrusion during synthesis of a CTS/EVOH sponge

3.7 Preparation of chitosan nanoparticles

Chitosan nanoparticles (CTS-NP) were prepared via an ionic gelation method [111]. CTS powder (0.5 g) was added to a 100 mL 2% (v/v) aqueous acetic acid and dissolved under vigorous stirring. Sodium tripolyphosphate (NaTPP) (0.25 wt% w/v) was dissolved in 100 mL water and added to CTS to form an opalescent mixture. This mixture was then decanted into centrifuge tubes and centrifuged 4 times. The supernatant was discarded and the pellet remaining after cenrifugation was washed with distilled water each time before centrifugation. The resulting product was then dispersed in 100 mL distilled water (Figure 3.6). The dispersion was then frozen using liquid nitrogen and freeze-dried for 24 hours [34, 74, 112].

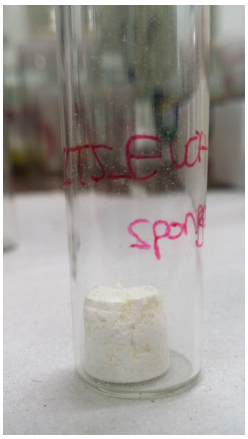

Figure 3.5: CTS/EVOH sponge

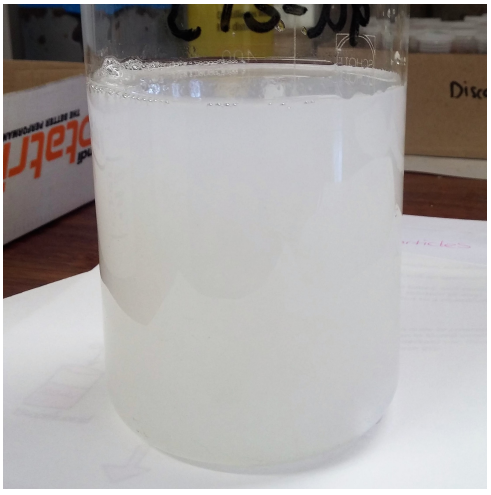

Figure 3.6: Dispersion of CTS-NP

3.8 Preparation of chitosan nanoparticles/poly(ethylene-co-vinyl alcohol) composite nanofibers

EVOH (5wt% w/v) was dissolved in 70/30% v/v Isopropanol/distilled water at 90 ℃ for 2 hours. CTS-NP (2.5 wt% w/v) were added to the solution and stirred for 30 minutes at 60 ℃. The mixture was taken up via a syringe and then electrospun at a total charge of 15 kV and collected onto a positively charged collector base, covered with aluminum foil, 15 cm away from the tip of the needle. An IR lamp was present during electrospinning to ensure the solution within the syringe retains consistent viscosity during the entire electrospinning process. The fibers on the collector plate were dried and the resultant fiber mat was peeled from the aluminum foil and used for further analysis.

3.9 Methods of characterization

3.9.1 Transmission electron microscopy

Transmission electron microscopy was used to obtain images of chitin nanowhiskers. A dilute droplet of redispersed chitin nanowhiskers was placed on a carbon-coated TEM grid and was negatively stained with urinal acetate. An LEO 912 EM TEM instrument was used to obtain images of varying magnification.

3.9.2 Attenuated total reflectance-FTIR spectroscopy

One hundred scans were done for each sample and repeated 3 times. All biosorbents were investigated using ATR-FTIR. The analysis was done at room temperature using a ThermoFisher Nicolet iS10 spectrometer in ATR mode with a resolution of 4 cm^{-1}.

3.9.3 Thermogravimetric analysis

The thermal stability of the biosorbents were analyzed by using a Q500 TGA7 instrument (Perkin Elmer, USA). The TGA analyses were done under a nitrogen atmosphere. The samples were heated up over a temperature range of 25 - 900 ℃ at a rate of 20 ℃.min^{-1}.

3.9.4 Scanning electron microscopy

A MERLIN scanning electron microscope at the Central Analytical Facility (CAF) of Stellenbosch University was used to analyze the morphology of the electrospun fibers mats and other biosorbents. Gold coated samples were mounted on a stub using double-sided carbon tape. Images were obtained in low and high magnifications (X100 and X1000 respectively). Beam conditions during surface analysis were 7 KV and approximately 1.5 nA, with a working distance of 13 mm and a spot size of 150.

3.9.5 Differential scanning calorimetry

Crystallization and melting temperature of the biosorbents were recorded using a Q100 (TA instruments) DSC instrument combined with an indium standard. The procedure consisted of three cycles and a heating/cooling rate of 10 ℃.min^{-1}. The temperature range was set for -40 to 220 ℃ and the sample was kept isothermal for 5 min at each set temperature. The sample was initially heated up to 220 ℃ and kept isothermal for 5 minutes. It was then cooled down to -40 ℃. The sample was then reheated to the same

set temperatures mentioned above to obtain the melting and crystallisation point.

3.9.6 Tensile testing

The thickness for each CTS/EVOH sponge tube was measured before analysis. At least five specimens were tested for the CTS/EVOH sponge, after being submerged in water and after being dried respectively. The analysis was done using an LRX (LLOYD instruments) tensile tester. The test speed was 50 mm.min^{-1} and the initial force was 1 N. The sample dimensions were: gauge length 15,62 mm, width 2,95 mm, thickness 2,40 mm.

3.9.7 Confocal microscopy

FITC was used as green fluorescence dye. The color green appears around 510 nm on the emission spectrum and that is what the confocal microscope was set to detect. Chitin nanowhiskers were dispersed in 1M NaOH and sonicated for 5 min and then covered with foil. FITC and 1M NaOH were mixed in a polytop and transferred to the chnw solution which was once again covered with foil and left to stand for 72 hours. The solution was centrifuged 4 times, after decanting the supernatant and washing before each repetition with distilled water while keeping the solid substrate. Image acquisition was performed on a Carl Zeiss Laser Scanning Microscope (LSM) 780.

The setup for the experiment was as follows:

1. Laser: 488 nm (set at 4.5% laser power)
2. Beam splitters (used to direct light to the sample):
    - MBS: 488
    - MBS InVis: Plate
3. FW1: None LSM
4. Master gain: 800
5. Filter (used to detect emitted fluorescence) 490-578
6. Z-stack was performed with an increment of 1.500 μm
7. Objective used: alpha Plan-Apochromat 100 x
8. The Images were acquired with a pixel dwell time of 3.15 μs.
9. Zoom: 1.0
10. Pin hole: 77 μm

3.9.8 ICP-AES

After adsorption, the biosorbents were removed from solution using a filter paper (for CTS powder) or sterilized spatula (for other biosorbents). The filtrate was then digested in ultrapure water, with an internal standard and 65% nitric acid added so that the samples are acidified to 2% final acid concentration. The adsorption efficiency was tested using inductively coupled plasma (ICP-AES) spectroscopy. Particulates are left to settle out prior to analysis. The results obtained is therefore a dissolved fraction of the sample. These prepared samples are introduced into the instrument via autosampler by peristaltic pump. The sample passes through the nebuliser which produces a fine aerosol. The large droplets are removed by a spray chamber and small droplets then pass through to the plasma. The solvent is evaporated and the residual sample atomised and ionised. The ions excite in the plasma and emit characteristic light which is measured by the Echelle optical design and Charge Injection device (CID) solid-state detector to provide elemental analysis. The Instrument is controlled, and data processed, by iTEVA software. The Thermo iCAP 6000 is used for analysis for samples ranging from high mid ppb to high ppm levels. Unknown samples are analysed against NIST traceable standards and independent quality control solutions. Calibration acceptance criteria of R^2>0.9995 is used. The instrument conditions are listed below in Table 3.1. The detection wavelengths and limits are tabulated in Table 3.2 and 3.3 for some heavy metals.

Table 3.1: Thermo iCAP 6000 series Instrument conditions.

RF Power (W)	1350
Carrier gas (L.min^{-1}) (Argon)	0.65
Aux gas (L.min^{-1}) (Argon)	1.0
Nebuliser	2 mL.min^{-1} Micro mist
Internal Standard used	1 ppm Yttrium

Table 3.2: Wavelengths (nm) for known elements

Element	**Wavelength (nm)**
Cr	283.5
Fe	239.5
Ni	221.6
Pb	220.3

3.9.9 Zeta potential measurements

A 0.01 M KNO_3 stock solution was prepared along with a 0.01 M NaOH and 0.01 M HCl stock solution (for pH manipulation). Samples containing 10 mL KNO_3 solution was

Table 3.3: Reporting detection limit ($mg.L^{-1}$) for known elements

Element	Reporting Detection Limit $mg.L^{-1}$
Cr	0.01
Fe	0.01
Ni	0.01
Pb	0.05

adjusted to the preferred pH of 3, 5, 7, 9 and 11. 100 μL of CTS powder paste (made up with a small amount of deionized water) was then added to the solutions immersed for two days. The zeta potential measurements were taken at the University of Cape Town (UCT) using a Zetasizer. An attempt to measure zeta potential for the nanofibers failed due to the coagulation (folding) that occurs spontaneously, leading to sedimentation errors during measurements.

3.9.10 Water absorption capacity

Water absorption was specifically measured for the CTS/EVOH sponge. The CTS/EVOH sponge was dried for 2 days at 30 ℃. The WAC was calculated by subtracting the difference of the weight (mg) of the dry CTS/EVOH sponge with the weight (mg) of the CTS/EVOH after it has been left in a neutral aqueous solution for a 120 minutes.

The amount of swelling was used to indicate how effective the WAC of the sponge is. This information is crytical in order to understand the behaviour of the sponge in aqueous solutions during the adsorption of heavy metals.

3.10 Adsorption studies

Heavy metal adsorption studies were conducted as batch experiments, for each biosorbent with metal cations, Pb(II), Cu(II), Zn(II), Ni(II) and Cr(VI), obtained from heavy metal salts described in Section 3.1. It was assumed that shaking allowed the entire surface area of the biosorbent to come into contact with the heavy metal ions. A stock solution of 1000 $mg.L^{-1}$ was prepared in ultrapure water. The stock solution was then diluted to the standard solution with initial concentration for each heavy metal ion of 2, 5, 10 and 20 $mg.L^{-1}$ for analysis using ICP. For some biosorbents, where the saturation value was slightly less clear, initial sorbate concentrations of 50 and 100 $mg.L^{-1}$ was also investigated. Since pH is such an important factor in heavy metal removal, the sorption studies for each biosorbent was done over a wide range of pH conditions, pH 2, 5 and 11, for each sorbate solution. The wide pH range is important to determine the behavior of each

modified biosorbents under all types of conditions. In order to compare the sorbent materials, the comparison must be done at the same initial concentration of heavy metal ions since the kinetics for pollutant adsorption is dependant on the starting concentration of the sorbate. The same types of experimental procedure must be executed every time and contaminants and other ions, as well as the pH, should be the same. If these conditions change during a sorption study, the results can be significantly changed.

3.11 Speciation of heavy metals

The speciation of the heavy metal ions that are used in this study will be discussed further in the results. It is important to understand the behaviour of the heavy metals in a aqueous solution in varying pH. The behaviour of each heavy metal in varying pH solutions can determine how it will interact with the biosorbent. Understanding the speciation of each metal ion can aid in the prediction of which type of solution may potentially show favourable adsorption excluding the influence of the biosorbent. If the heavy metal ion tend to percipitate in higher pH solutions and form salts then that will inhibit interaction between the biosorbent and the heavy metal and lower the amount of adsorption. This percipitation can lead to inaccurate results and false conclusions. It is therefore crucial that each stock solution is checked for any percipitation before the dilutions are made and adsorption experiments are continued. The pH of each heavy metal solution, that were used for adsorption studies, were adjusted using ammonia (basic) and HCl (acidic) solutions. The effects of excess ammonia on the solubility of the metal salts was determined. Results are shown in Section 4.6.

Chapter 4

Results and discussion: Characterization of biosorbents

4.1 Chnw/EVOH composite nanofibers

4.1.1 Transmission electron microscopy

Transmission electron microscopy was used to analyse the diameter and length of chitin nanowhiskers (chnw). The fibre length of the chnw was between 150 - 250 nm with an average fibre diameter of 15 nm. Some single nanowhiskers could be seen in Figure 4.1 as well as some aggregation but with no apparent defects or flaws [109]. The aggregation is due to the high specific area and hydrogen bonding that occurs among the chitin nanowhiskers [107]. Observations with the naked eye showed that chitin nanowhiskers that were redispersed in distilled water began to settle at the bottom of the polytop whereas chnw that have not undergone the freeze-dried process showed better dispersion within a solvent. However, to prepare the correct concentration of chnw for electrospinning blend with EVOH, it is necessary to add the freeze-drying step. The freeze-drying step does, however, lead to some aggregation due to H-bonding. It is important to add an ultra-sonication step during the preparation of solutions containing chnw to disperse chnw more evenly.

4.1.2 FTIR analyses

The compatibility of EVOH with chnw are mainly based on the absorption spectra of the hydroxyl groups present in both polymers. The FTIR spectrum illustrated in Figure 4.2 (e) presents the characteristic absorption peaks of chnw from approximately 1750 to 1600 cm^{-1} that belong to the amide moieties and carbonyl group [113]. The peak at 1580 cm^{-1} belongs to N-H stretching of the amide bond while the two peaks at 1652 cm and 1662 cm^{-1} were allocated to the C=O stretching vibrations that belong to the amide groups present on the chitin structure. The broad peak seen at 3600 to 3000 cm^{-1} are

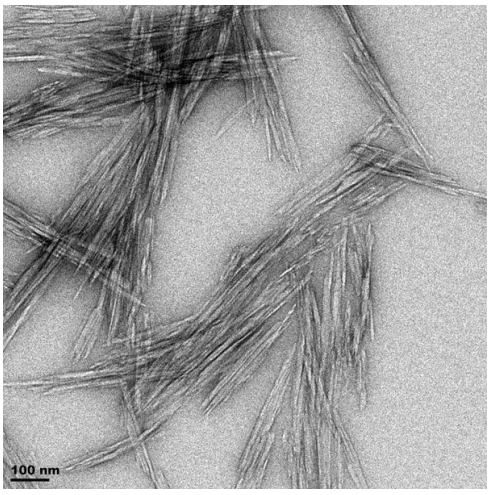

Figure 4.1: TEM image of chnw.

attributed to the combined vibrations of N-H and O-H groups. The N-H secondary amine stretch can be seen at 3250 cm^{-1} and the NH-CO group at 3100 cm^{-1}. Concentration cannot be accurately determined using ATR-FTIR, the intensity of the characteristic peaks for specific functional groups belonging to chnw or EVOH respectively show that there has been an increase in chnw or EVOH content within the nanofiber as seen in Figure 4.2 [107]. The successful incorporation of the chnw within the nanofiber can thus be established by using FTIR and the compatibility of the EVOH and chnw is also confirmed.

The infrared spectra for EVOH (Figure 4.2 (a)) show the absorption band of the hydroxyl group at 3050 cm^{-1} to 3550 cm^{-1} [25, 71, 114]. The peak corresponding to the CH-stretching vibration within the EVOH can be seen at 2920 cm^{-1} [85]. These peaks at 2920 cm^{-1} overlap with the C-H stretching of chnw and it is important to note that the intensity of the EVOH peaks are much stronger than that of the chnw. The peak at 1420 cm^{-1} can be attributed to saturated CH-groups from the ethylene component of EVOH.

The important active sites, on the chnw/EVOH nanofibers, that may participate in adsorption are detected using FTIR for samples after adsorption of heavy metal ions occurred. Adsorption of heavy metals onto chnw/EVOH nanofibers can be observed using FTIR. A small, almost insignificant reduction in the adsorbance can be seen for the functional groups that belong to chnw in Figure 4.3.
The baseline was corrected and the two spectra of chnw/EVOH composite NF before and after adsorption was normalized to scale. In Figure 4.3, the FTIR spectra of Cu(II) adsorbed to chnw/EVOH nanofibers, and a native chnw/EVOH nanofibers spectrum can be seen respectively. Figure 4.3 shows the entire spectra selecting the highest peak for normalization, however, the overall appearance may be misleading and to compare the specific peak of each spectrum it is necessary to focus on each section of the spectra individually. It does appear that the changes are insignificant to the peak intensities of

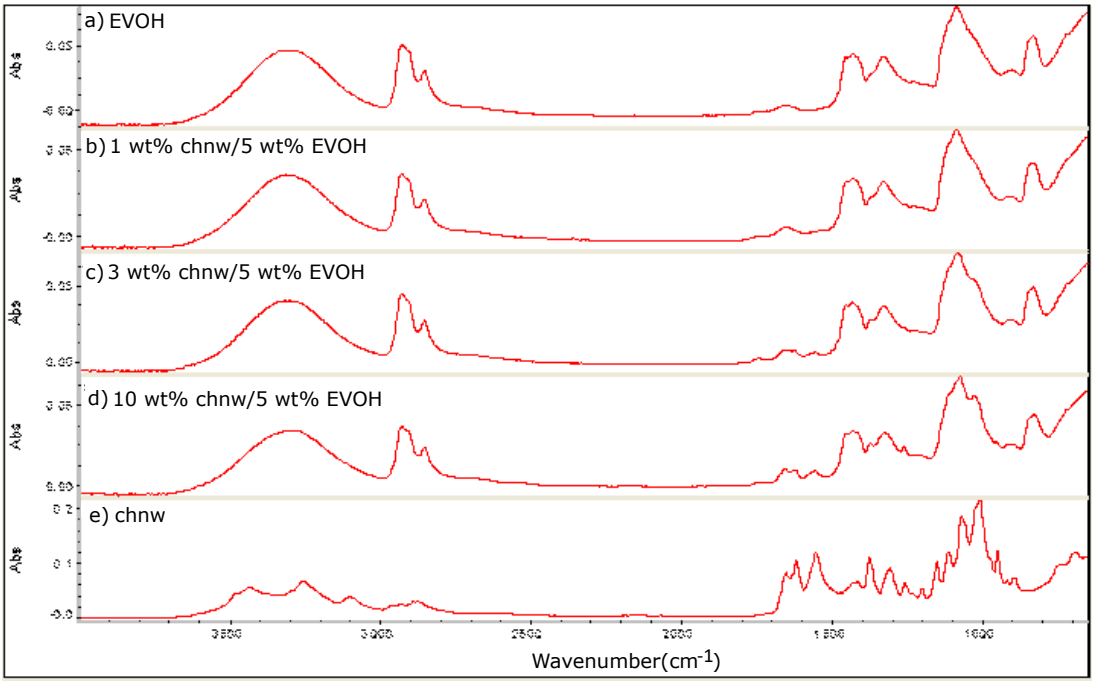

Figure 4.2: FTIR spectra of chnw, EVOH and blends of chnw and EVOH.

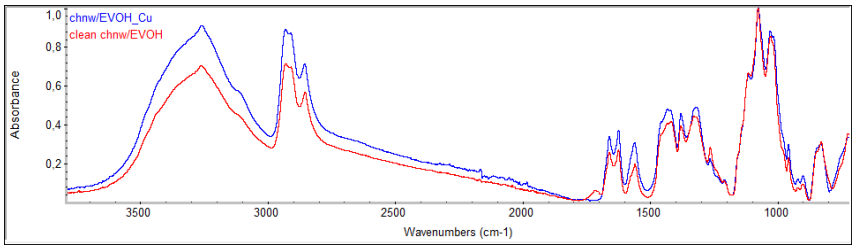

Figure 4.3: Influence of Cu(II) on the FTIR spectra of chnw/EVOH nanofibers.

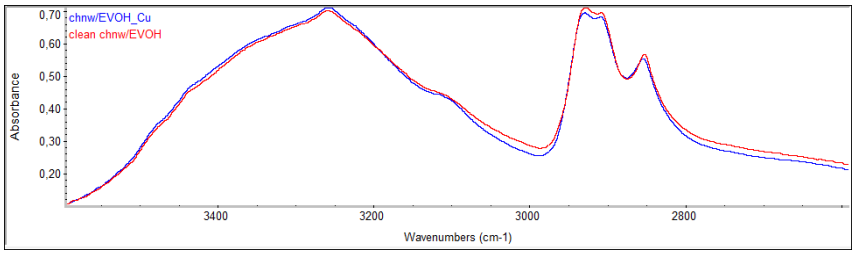

Figure 4.4: Influence of Cu(II) on the peak in the region 3400 to 2800 cm^{-1} of chnw/EVOH composite nanofibers.

chnw/EVOH after Cu(II) has been adsorbed as seen in Figure 4.4. There should also be a shift in peak positions on coordination to the metal, especially peaks for the amide functionality, which are not clearly visible. Figure 4.5 shows the effect of Cu(II) on section of the IR spectrum referred to as the fingerprint (lower wavenumber section). The apparent absence of the peak in the region 1750 to 1700 cm^{-1} that corresponds with the carbonyl group and amide moieties belonging to the chnw which indicate that some interaction with Cu(II) took place [40, 41]. This is the only observable difference that appear between the two spectra.

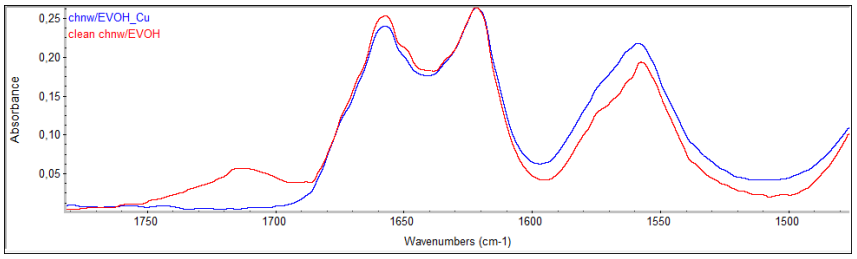

Figure 4.5: Influence of Cu(II) on the in the region 1750 to 1500 cm^{-1} of chnw/EVOH composite nanofibers.

Adsorption studies have been done for EVOH, without the presence of chnw, to establish if the functional groups on the EVOH are participating in any sorption activity with the heavy metal ions. Small changes in the concentration of heavy metal ions were seen after adsorption with EVOH, as shown in Appendix B.1. The small changes were seen in Figure 4.6 and 4.7 for EVOH after Zn(II) adsorption are shown that some interaction may occur between available hydroxyl sites. The interaction between heavy metal ions and pristine EVOH may be limited possibly due to the hydrophobic nature of EVOH. The heavy metal ions appeared to favour interaction with oxygenated functional groups as well as nitrogen-rich functional groups that all acted as electron donors during the adsorption process [115]. As seen in Figure 4.8 and 4.9, chnw/EVOH nanofibers showed good overall behaviour as a sorbent material.

Figure 4.8 showed the same aparent "loss of peak" than what was seen for Cu(II) adsorption, as a shift in the peak in the region of 1750 cm^{-1} to 1700 cm^{-1} occured due to complexation of the metals with the sorption sites on the surface of the chnw/EVOH composite nanofibers. This helps to indicate that interaction between the chnw and the heavy metal ion does occur. A more clear decrease in peak intensity around 3000 cm^{-1} is seen for the adsorption of Cr(VI). These changes are visible after each heavy metal adsorption and the full spectra along with additional FTIR spectra for each chnw/EVOH composite nanofiber sample after adsorption with Pb(II), Ni(II) and Zn(II) are shown in Appendix B.

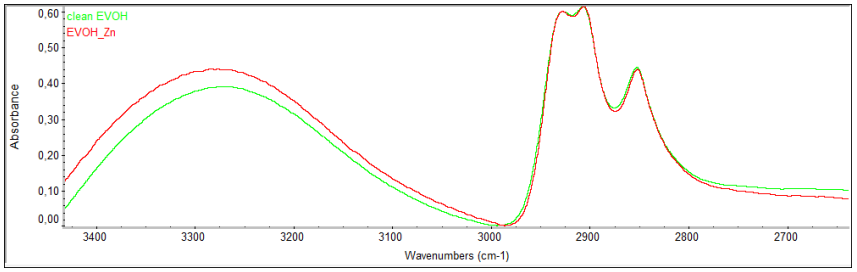

Figure 4.6: Influence of Zn(II) on the hydroxyl peaks at 3300 cm^{-1} of EVOH.

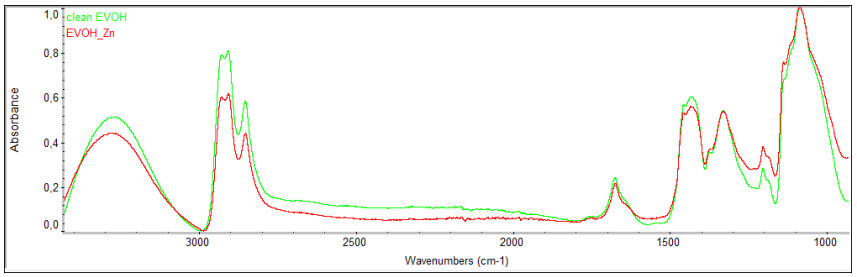

Figure 4.7: Full FTIR spectra of EVOH before and after Zn(II) adsorption.

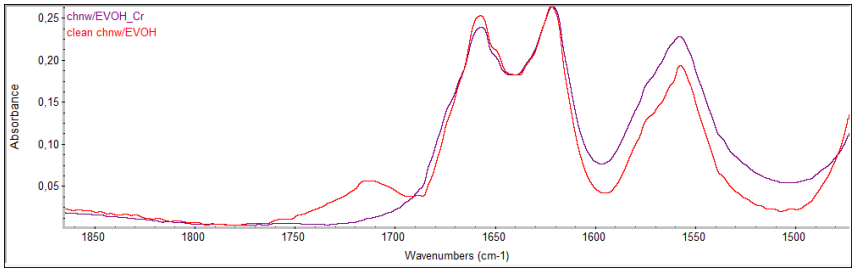

Figure 4.8: Influence of Cr(VI) in the region 1750 to 1500 cm^{-1} of chnw/EVOH composite nanofibers.

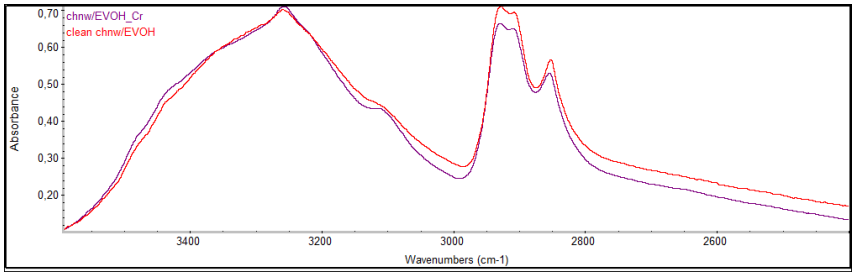

Figure 4.9: Influence of Cr(VI) in the region 3500 to 2600 cm^{-1} of chnw/EVOH composite nanofibers.

The FTIR spectra in Figure 4.10 shows the effect of initial sorbate concentration on the adsorption efficiency of the chnw/EVOH nanofibers for Ni(II) specifically. The effect of the initial sorbate concentration on the spectrum of the chnw/EVOH composite nanofibers is visible for all the heavy metals as shown in Appendix B. As the initial concentration increases for the Ni(II), the normalized spectrum appear to shift up of chnw/EVOH nanofibers but as the initial Ni(II) concentration is increased further it shift down. This trend is seen most commonly for chnw/EVOH composite nanofibers where the effect of initial sorbate concentration is concerned. The increase in initial sorbate concentration increases the interaction between the adsorption sites and the heavy metal (Ni(II)) but as the concentration is increased further the competition between the heavy metal ions and the available adsorption sites increases lowering the interaction. This effect seems to correlate well with the results seen in Section 5.3. It has been found that the optimal initial sorbate concentration differs for each biosorbent and correlates with the availability of high energy adsorption sites and other factors such as the surface area [116].

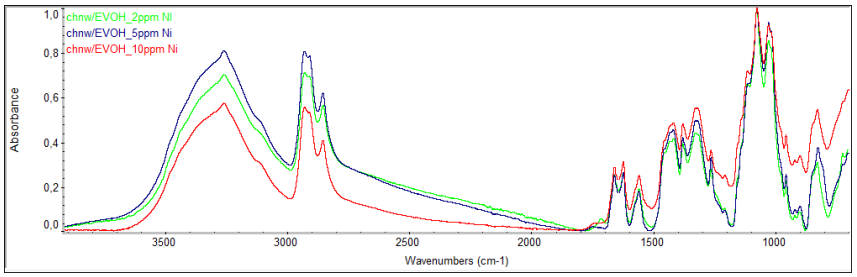

Figure 4.10: FTIR spectra of chnw/EVOH composite nanofibers with initial sorbate concentration of Ni(II).

4.1.3 SEM analyses

The higher the chnw content, the more viscous the electrospinning solution and unacceptable nanofiber diameter and surface morphology resulted. The ideal concentration of chnw for electrospinning was determined by manufacturing various fiber mats containing different amount of chnw. The fibermats that showed the best electrospun fiber mats, as well as the most uniform and on a nano-scale fibers were used. The most ideal fibermat contained 3 wt% (w/v) chnw. Illustrated by the example shown in Figure 4.11, a chnw/EVOH composite nanofibre mat maintained largely stable fibrous structure under the pH conditions used in this study and did not dissolve during adsorption at pH < 5. Zn(II) with a concentration of 1000 mg.L^{-1} can be detected using SEM. The adsorbed zinc was visible on the chnw/EVOH composite nanofibers due to some precipitation and salt formation that might have occurred due to the high concentration of zinc and also drying during SEM preparation. The heavy metal appeared to adsorb onto the surface of the nanofibres and expected to migrate further inside the porous network created by the nanofibres. Figure 4.12 a) and b) presents the morphology of the fibres after exposure to pH 11 and 2. The fibre-morphology of the chnw/EVOH composite nanofibers is still visible and appear to be stable under all conditions during the adsorption processes of this study.

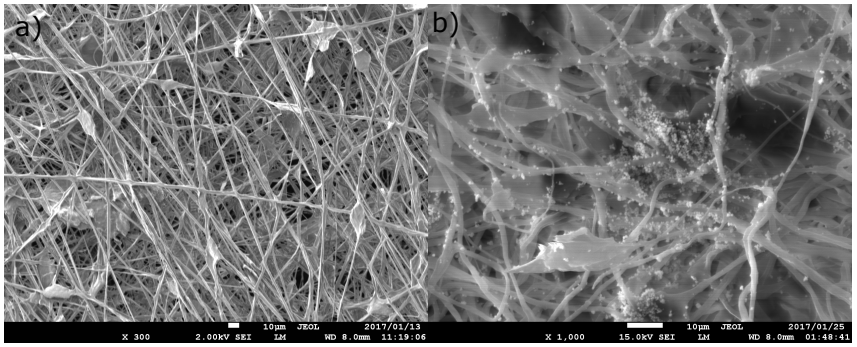

Figure 4.11: SEM images of chnw/EVOH composite nanofibers a) before adsorption and b) after, at pH 5 for 1000ppm Zn(II)

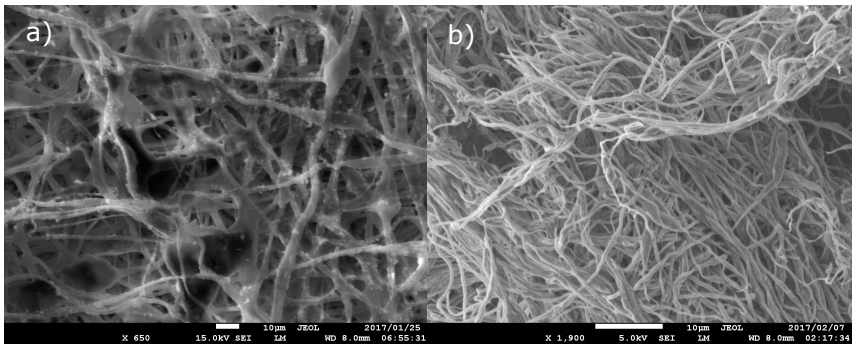

Figure 4.12: SEM images of chnw/EVOH composite nanofibers after adsorption a) at pH 11 and b) and pH 2.

4.1.4 Confocal fluorescence microscopy analyses

The distribution of chnw was investigated within the EVOH matrix using confocal fluorescence microscopy. The electrospinning method was compared to the more conventional method of solvent casting to produce films. As can be seen in Figure 4.13, the solvent casting method yields a composite that is not uniform, and the chnw tended to agglomerate within the matrix much more readily compared to the dispersion seen after the electrospinning process. The distribution of FITC-labelled chnw in the nanofibers after the electrospinning method is shown in Figure 4.14. Chnw is uniformly dispersed throughout the nanofiber, at the concentration of 3 wt%. A chnw concentration lower than this causes beading during electrospinning due to a spraying effect caused by the low viscosity of the electrospinning solution. A concentration higher that 3 wt% chnw cause an increase in fibre diameter because of increased viscosity of the electrospinning solution, and defects in the fibre due to the agglomeration of chnw within the matrix. Changing the concentration of EVOH appeared to also have an effect on the morphology and diameter of the fibers. Increasing the content of EVOH also has an effect on the viscosity. If the viscosity is to high, the fibers will become larger in diameter. If the viscosity decreases, taylor cone formation becomes more challenging leading to electrospraying that forms beading in between fibers or sometime no fiber formation and beading overall.

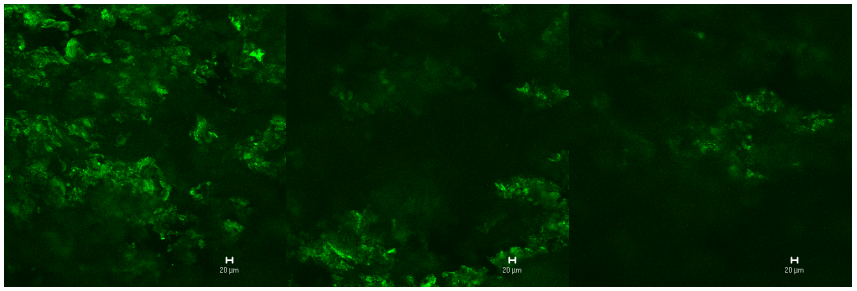

Figure 4.13: Confocal fluorescence microscopy 3D image slices of chnw in EVOH after solvent casting.

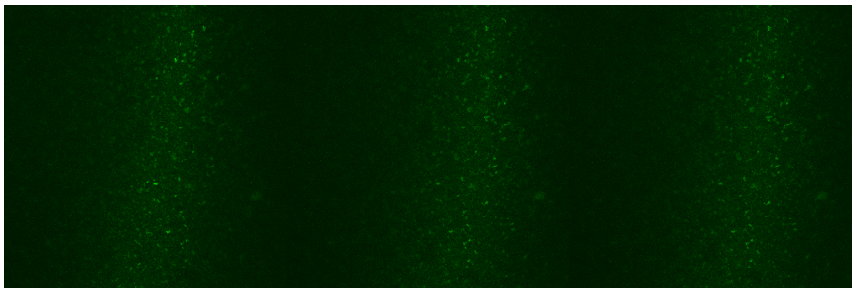

Figure 4.14: Confocal fluorescence microscopy 3D image slices of chnw dispersed in EVOH matrix within the electrospun nanofiber.

4.1.5 TGA

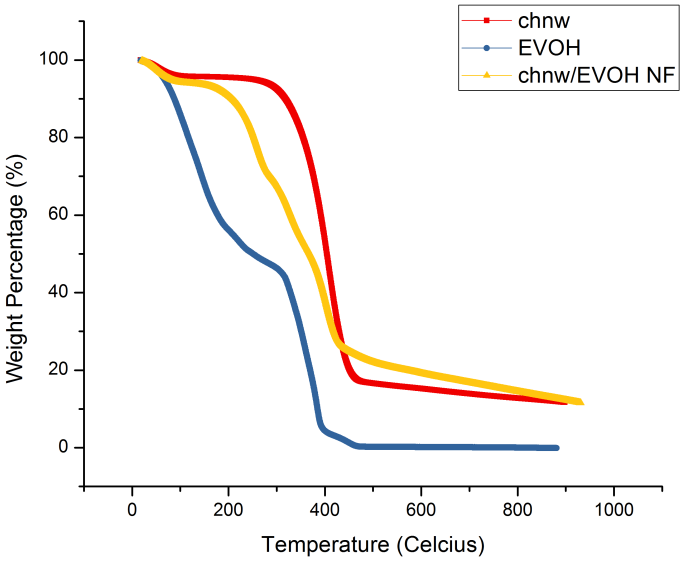

Figure 4.15: TGA curve of chnw, EVOH and chnw/EVOH composite nanofiber (NF).

Figure 4.15 presents the TGA curve for chnw, EVOH, and chnw/EVOH composite nanofibers. An immediate drop in the initial slope belonging to the chnw could be due to the weight loss attributed to the evaporation of residual solvent. This loss of weight continues up to approximately 100 ℃ and then stabilises for a while. An increase in weight loss then continues with a decline in rate of weightloss at 400 ℃ and becomes more gradual at approximately 480 ℃ [107]. No initial moisture loss can be observed for EVOH. The small or lack of an initial moisture loss for EVOH indicates that EVOH does not absorb moisture as well as chnw. The first significant weight loss peak for EVOH can be seen at a temperature range of 100 ℃ with a further weight loss that continues at 200 and 380 ℃. This loss in mass is attributed to the loss of the major component of the copolymer that is the vinyl alcohol component [117]. The second part of the curve that follows directly after this previously mentioned weight loss is caused by the ethylene component at approximately 410 ℃. Polyethylene acts as a thermal stabiliser in EVOH [117]. After

the weight loss of the ethylene part, the total weight loss is reached at 500 ℃.

A small initial weight loss for chnw/EVOH composite nanofibers appears immediately and is also caused by a loss of excess solvent and then stabilises after reaching approximately 100 ℃. Further weight loss commences at 200 ℃ up to approximately 440 ℃ [107]. The weight loss then follows a more gradual slope up to 900 ℃. Total weight loss for chnw and chnw/EVOH composite nanofibers is not reached at 900 ℃. The blend of chnw and EVOH indicated good compatibility between the two polymers, where the loss of excess solvent as well as loss of any retained moisture that may have occured after 100 ℃ is similar to that of chnw while the overall thermal properties are a blend between EVOH and chnw.

4.1.6 DSC analyses

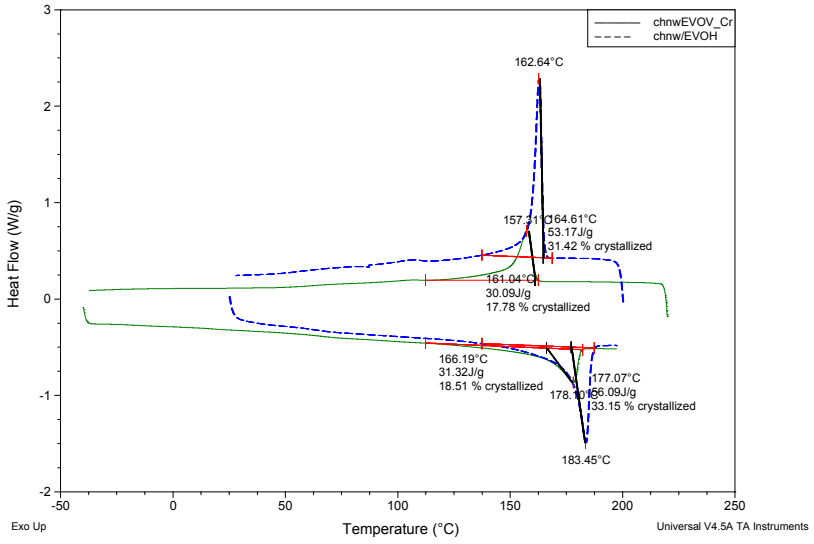

Figure 4.16: DSC curves of chnw/EVOH composite nanofibers before and after adsorption of Cr(VI)

Figure 4.16 presents the DSC curves of chnw/EVOH composite nanofibers before and after sorption of Cr(VI). Large shifts in the melting and crystallisation peak of the partially crystalline material are observed. The shifting to lower temperature indicates that there is a decrease in the crystallinity of the material after sorption occurred. Major reduction in peak intensities, as well as a broadening of the peaks, can be seen, indicating a loss in the crystalline structure. Adsorption of the metal ion has a negative effect on the thermal properties of the polymer and can confirm that adsorption of the heavy metal took place and that there is interaction with the functional groups of chnw/EVOH composite

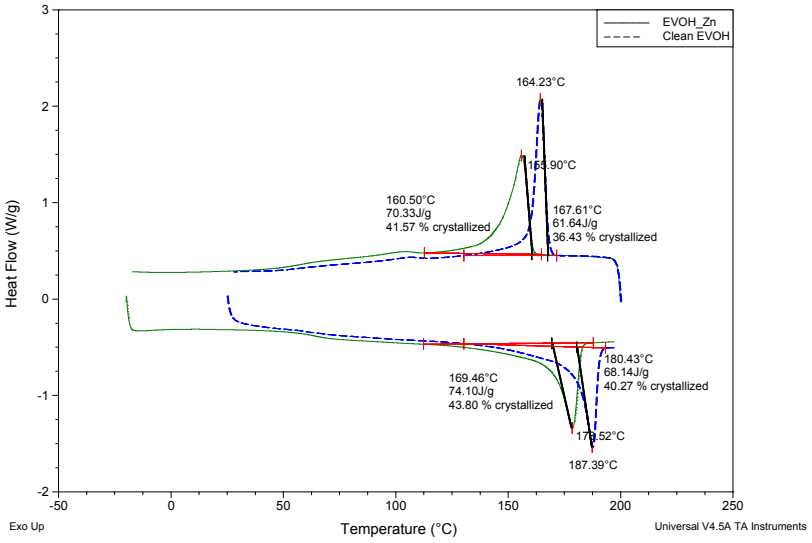

Figure 4.17: DSC curves of EVOH before and after adsorption of Zn(II).

nanofibers.

Figure 4.17 shows DSC curves of EVOH before and after adsorption in the presence of Zn(II). These result help to confirm that EVOH does have some sorption capability to a certain extent, especially when not bonded with chnw, as shown in Appendix B.1. The overall results indicate that heavy metal ions have an effect on the thermal properties of the sorbent even when present in small quantities.

4.2 CTS powder

4.2.1 FTIR spectroscopy analyses

CTS powder has characteristic peaks at 1550 - 1650 cm^{-1} that is attributed to the amino groups on the polymer chain. The peak that was present for chitin at 1550 cm^{-1} disappeared, thus indicating deacytelation largely occurred during the preparation of CTS. Amide I (C=O) at 1655 cm^{-1}, amide II, which is a combination of C-N-H stretching and N-H bending, at 1560 cm^{-1}, and C-N stretching at 1166 cm^{-1} are identified in Figure 4.18 of the full spectra of the CTS powder before and after adsorption of Cu(II) [38]. The hydroxyl stretching and amine stretching peaks is a broad peak that can be seen at 3450 cm^{-1} and 3264 cm^{-1} to 3105 cm^{-1} (N-H stretching) respectively. The broad peaks of the stretching of these functional groups indicate the presence of hydrogen bonding between the chains. The peaks belonging to C-H stretching is seen at 2900 cm^{-1}. Changes between the two sepctra become more clearly visible after closer inspection in Figure 4.19

for adsorption of Cu(II). A slight reduction in the peak intensity in the region 3000 to 2800 cm^{-1} is seen after Cu(II) was adsorbed to CTS. This region is ascribed to the amine and hydroxyl broad peaks. This changes may however be too small to be considered significant. There is some indication that adsorption has an effect on the peaks of the FTIR sepctrum of CTS. More DSC curves can be viewed for other heavy metals removal in Appendix B.

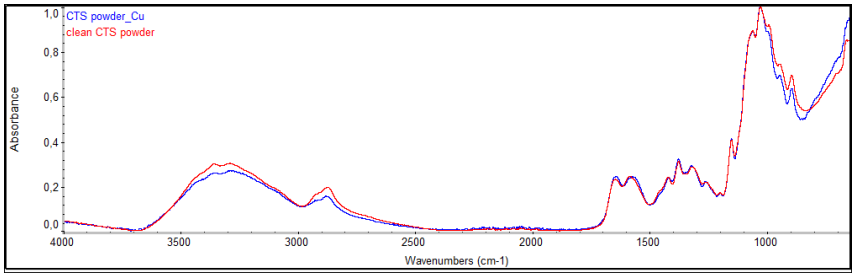

Figure 4.18: Full spectra of the effect of Cu(II) adsorption on CTS powder.

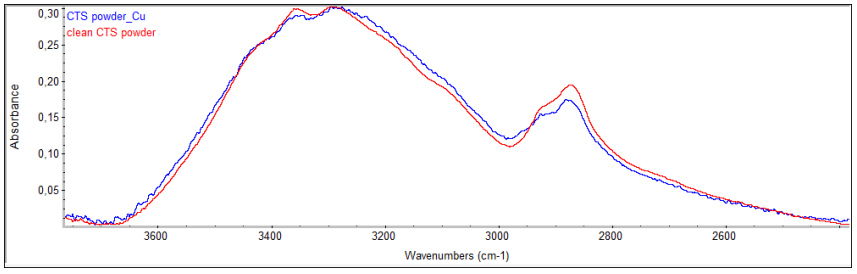

Figure 4.19: FTIR of CTS powder before and after Cu(II) adsorption in the region 3500 to 2600 cm^{-1}.

Ni(II) show some more visible changes to the spectra of CTS powder. The shape, as well as the peak intensity, are effected. The changes in shape may indicate a change in crystallinity. This change in crystallinity is later also seen by using DSC **??**. Figure 4.20 shows the significant changes around 3300 cm^{-1} and 2900 cm^{-1}. The 2900 cm^{-1} belongs to -C-H aldehydic bonds on the CTS. The amine and hydroxyl groups are located in this region. This is a good indidcation that interaction could have occured mainly around these functional groups for CTS.

The initial sorbate concentration affects the adsorption capacity of a sorbent as investigated in Chapter 5. When the sorbate concentration is not high enough for effective interaction with the CTS powder, it can affect the adsorption effectiveness. Hindered interaction can also be caused by poor suspension of ions present in the solution at low sorbate concentration. The differences between the spectra shown in Figure 4.21 initially for Cu(II) concentrations of 2 to 5 ppm are rather insignificant but compared to the spectrum that belongs to 10 ppm Cu(II), it is possible to see how the initial sorbate

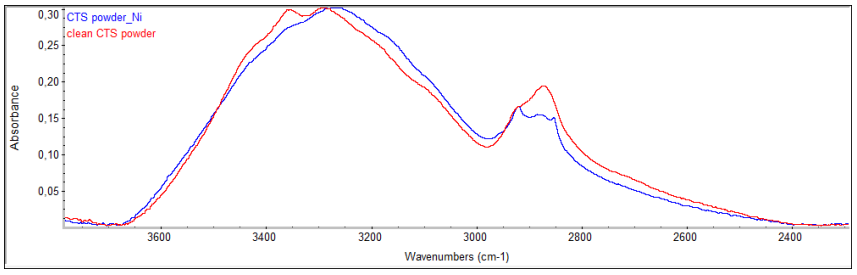

Figure 4.20: FTIR of CTS powder before and after Ni(II) adsorption in the region 3500 to 2600 cm^{-1}.

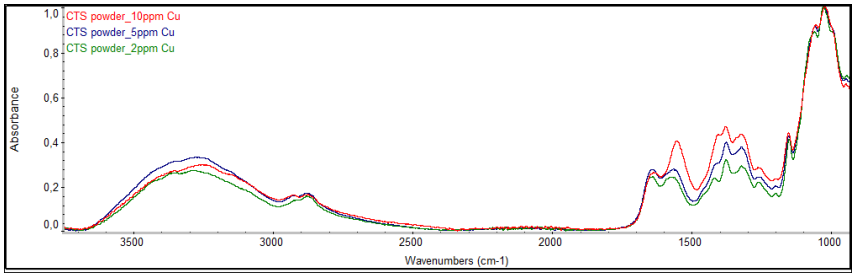

Figure 4.21: Full FTIR spectra of CTS powder with different sorbate concentrations of Cu(II).

concentration effects the adsorption effeiciency of the sorbent, CTS. The higher peak intensity at around 600 cm^{-1} for 10 ppm Cu(II) shows that the adsorption did not occur perhaps as effectively as it could have compared to the lower concentration of Cu(II) in solution.

4.2.2 SEM

The SEM images of the surface of CTS powder is presented in Figure 4.22. These granules are large and irregular as seen in Figure 4.22 a). CTS powder has low surface area due to the irregular size and surface of the granules. CTS powder is however still capable of relatively good adsorption despite the large particle size. The effect that a poor surface morphology has on the adsorption effectiveness becomes more obvious after longer exposure times in the solution. At longer exposure (contact) times, retention of heavy metal ions seems to become a problem for CTS powder. Figure 4.22b) shows the CTS powder after adsorption at pH 5 for 1000 ppm Zn(II). The white substances seen on the CTS powder particles are the heavy metal, zinc, adsorbed to the surface. The irregular surface of the CTS powder can be seen more clearly in this image.

The adsorption occurs on the surface of the CTS powder granules and as the pH conditions change the particles aggregate causing the reduction in available adsorption sites. As the contact time is increased some of these metal ions are weakly bonded to the surface and causes desorption. The effect of pH and contact time will be discussed in more detail in

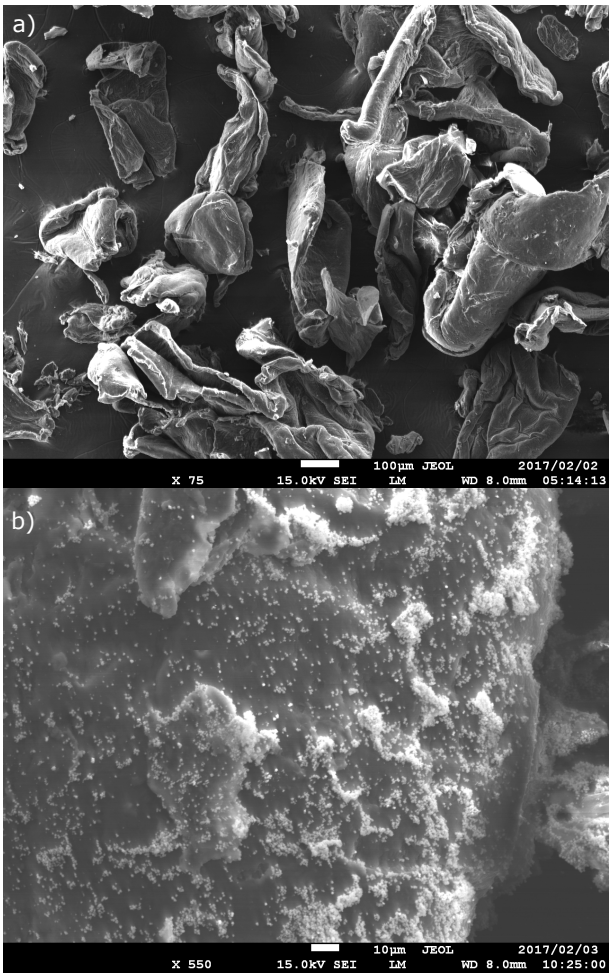

Figure 4.22: SEM image of CTS powder a) before adsorption and b), at pH 5 for 1000ppm Zn(II).

Chapter 5. The effective adsorption capacity of CTS is more dependent on the conditions of the solution and can be easily reduced in capacity because of the unfavourable surface area. Competitive ions such as protons in acidic solution and sulfates and nitrates in alkaline solutions can have a larger effect on the adsorption capacity due to the limited adsorption sites available [28, 114].

4.2.3 Thermo-gravimetric analysis

The TGA plot of CTS before metal adsorption in Figure 4.23 shows an initial peak that is correlated to the loss of solvent. This initial solvent-loss peak is from 0 to 100 ℃ after which stabilisation occurs. A drastic loss in weight follows at 300 ℃. This is attributed to thermal degradation of CTS powder. After 400 ℃ is reached, the slope of degradation then levels out to a more gradual loss after 50% of the weight of CTS powder have been lost. Complete loss of weight is not obtained after 900 ℃. The same behaviour under these thermal conditions was seen for CTS-NF (Section 4.3).

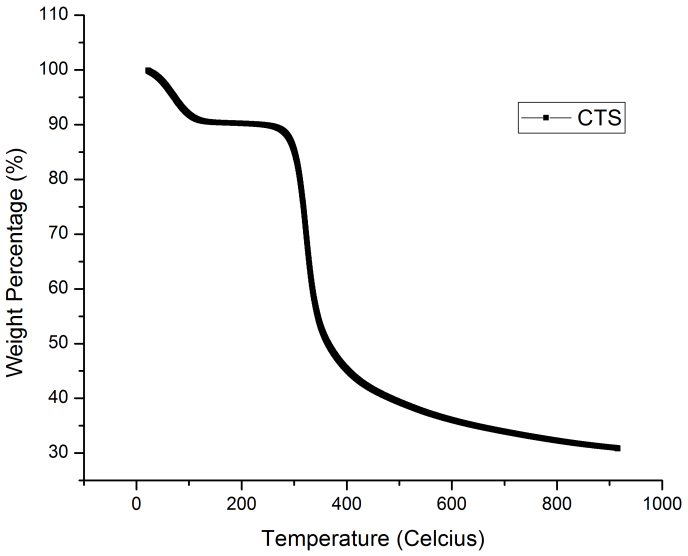

Figure 4.23: TGA thermogram of CTS powder.

4.2.4 DSC

Figure 4.24 presents the DSC thermograms of CTS powder before and after adsorption of Zn(II). Slight shifts in the peaks of the partially crystalline polymer can be seen as well as a slight decrease in the peak intensity. The changes give some indication just like chnw/EVOH NF that adsorption of the metal ion could affect the thermal properties (crystallinity and melting temperature) of the polymer. Similar results could be seen for the DSC thermograms of CTS-NF (Section 4.3).

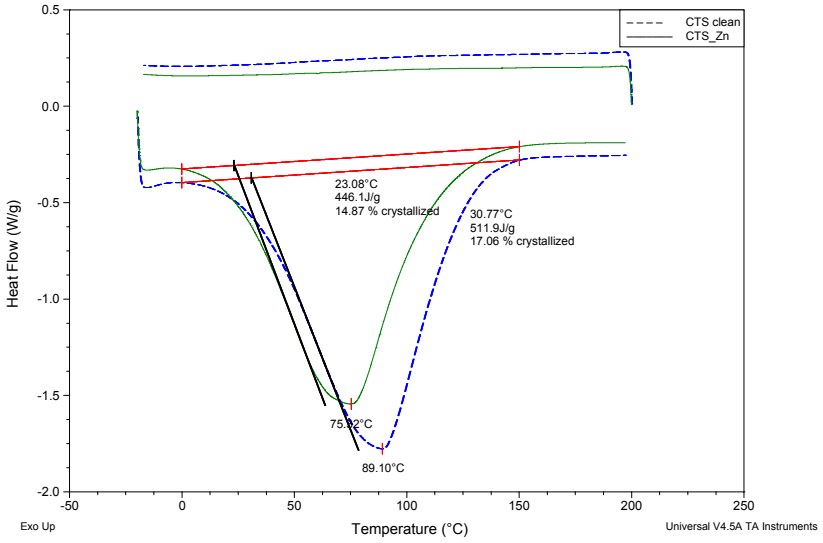

Figure 4.24: DSC thermogram of CTS powder before and after Zn(II) removal.

4.2.5 Zeta potential

A zeta potential curve at various pH values is shown in Figure 4.25. It can be seen that as the pH increases the charge on the surface of chitosan increases. Changes in the protonation of the functional groups on CTS causes the polymer to become more negatively charged in solutions with higher pH and less negatively charged as the pH decrease. Ion exchange then becomes possible between the biosorbent and the sorbate because of the increased affinity on the surface of the biosorbent, caused by the differences in charge.

4.3 CTS nanofibers

4.3.1 FTIR spectroscopy

The FTIR spectra presented below were investigated to observe whether the presence of heavy metal on the CTS-NF can be seen through changes in the peak intensities. The same peaks seen for CTS powder are relevant to the FTIR spectrum of CTS-NF. The secondary amine stretch (N-H) is visible at 3450 cm^{-1} as well as the broad peak is seen for the 3600 - 2800 cm^{-1}, indicating strong intermolecular hydrogen bonding between the polymer chains. The amide I and II functionalities are also presented by peaks at a similar position as found for CTS powder around 1665 and 1550 cm^{-1}. In Figure 4.26, the effect of the initial Ni(II) concentration shows an effect on the peaks of the CTS-NF. The effect of initial concentration of Ni(II) becomes more significant as the sorbate concentration increases, the lowering in the peak intensity indicate that more interaction with the CTS-

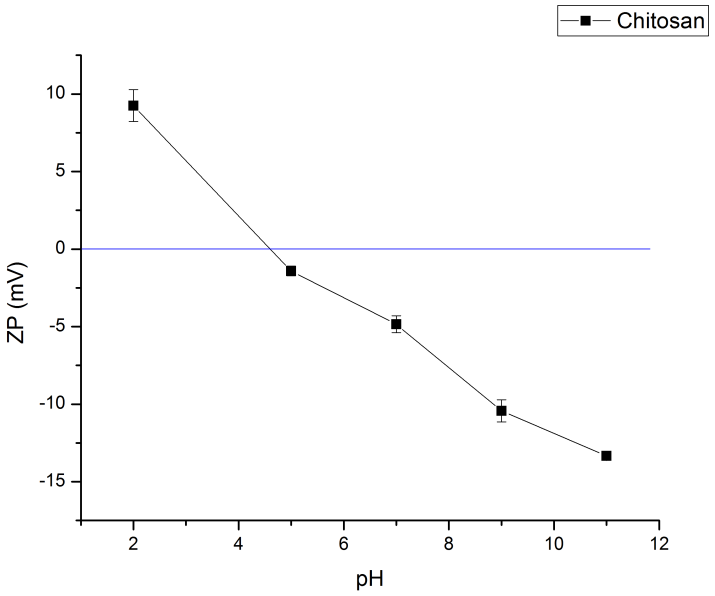

Figure 4.25: Zeta potential measurements of CTS.

NF occurred at higher Ni(II) concentration.In this case, the better interaction occurred between 10 mg.L^{-1} of Ni(II) and CTS-NF. The decrease in peak intensity as the Ni(II) concentration increases can show that CTS-NF has a good availability of sorption sites.

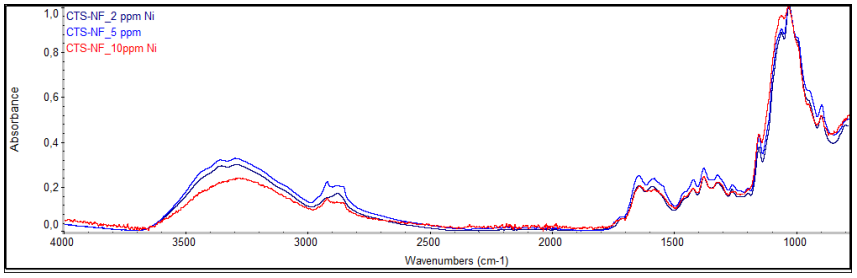

Figure 4.26: Full FTIR spectra of CTS-NF with initial sorbate concentration of Ni(II).

In Figure 4.27 the normalized spectra for CTS-NF with Cu(II) is compared to native CTS-NF, showing significant indications of an interaction between the copper ions and CTS-NF. On closer inspection, a clear reduction of the peak intensities occurred with the presence of Cu(II), for the amine groups at 1640 and 1586 cm^{-1} and the peaks belonging to -C-N at 1375 and 1419 cm^{-1} as seen in Figure 4.28. Changes in the shape and shifting of peaks can be seen at 1700 cm^{-1} which is approximately where the carbonyl bands of the amide functionalities are found. These shifts show dissociation of the protons of the oxygen-based functional groups. Figure 4.29 also shows a fairly large reduction in the peak belonging to the amine and hydroxyl groups at 3000 and 2800 cm^{-1}. The change in these peaks are all signs that the oxygen of the hydroxyl groups as well as the nitrogen of the amine groups may be implicated in the adsorption process and that there is a change

in the environment of the nitrogen donor sites that are involved after adsorption. Please note that all other heavy metal FTIR spectra are shown in Appendix B.

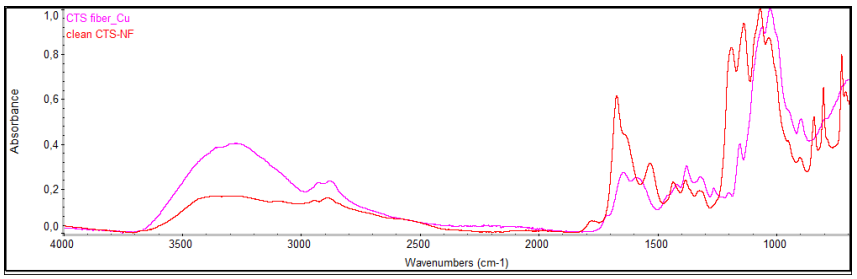

Figure 4.27: Full spectra of the effect of Cu(II) adsorption on CTS-NF.

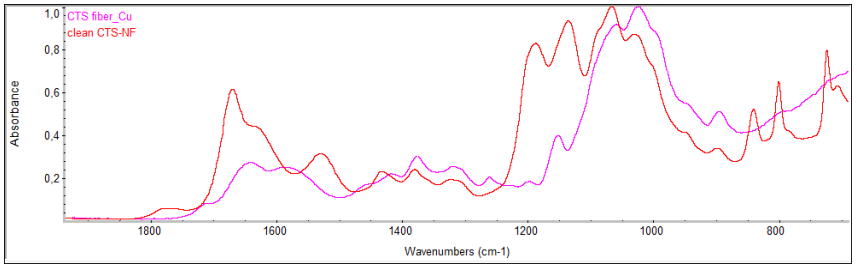

Figure 4.28: The influence of Cu(II) on the FTIR spectrum of CTS-NF in the region 1800 to 800 cm^{-1}.

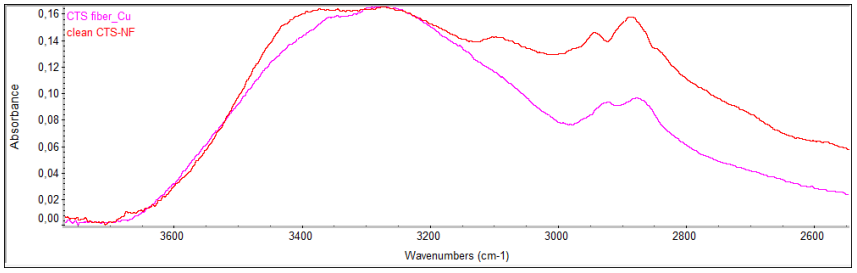

Figure 4.29: The influence of Cu(II) on the FTIR spectrum of CTS-NF in the region 3600 to 2600 cm^{-1}.

4.3.2 SEM

The SEM images in Figure 4.30 shows the CTS-NF morphology before and after exposure to the heavy metal ions in the aqueous solution at pH 5. Looking closely at Figure 4.30 a), it is possible to see the fibres are compressed after removal and drying, but still available for repeated adsorption at pH 5.

Figure 4.30 b), shows the layer of sorbate covering the chitosan fiber mat after removal from a 1000 ppm Zn(II) solution with a pH of 5. The highly acidic and highly alkaline solution conditions do affect the CTS-NF respectively as seen in Figure 4.31 a) and b). CTS-NF that were exposed to solutions of pH 2 especially is not ideal for re-use, because of congealing and agglomeration that occur after removal from the solution. It was necessary to use a fresh nanofiber for each new experiment. CTS-NF shows more stability in acidic solutions than CTS powder since CTS-NF does not fully dissolve after prolonged 2 hours. It may be possible that strong intra-molecular bonding that may occur between the nanofibers can delay the dissolution of CTS-NF in highly acidic solutions.

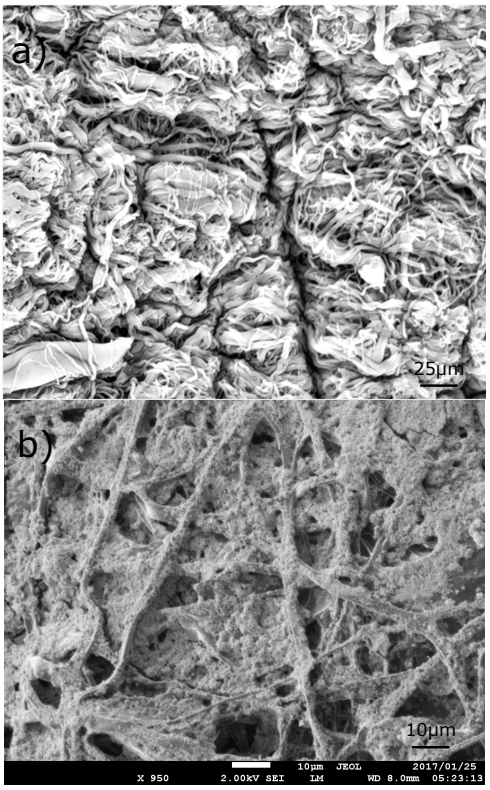

Figure 4.30: SEM images of CTS-NF a) after repeated exposure to water and b) after heavy metal adsorption, at pH 5 for 1000 ppm Zn(II).

4.4 CTS/EVOH sponge

4.4.1 FTIR spectroscopy

In Section 3.6, two sponges were made with varying CTS content and the sponge with the best porous surface and mechanically stable structure was chosen for further use in adsorption experiments, where the CTS load within the sponge was 2.5wt%. The FTIR spectra for the CTS/EVOH sponge show a broad peak at 3400 - 3200 cm^{-1} correlated to

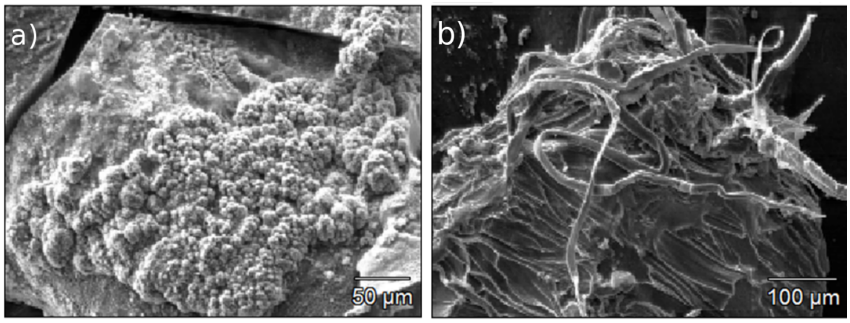

Figure 4.31: The effect of pH on the morphology of CTS-NF in a solution of a) pH 2 and b) pH 11.

the hydroxyl for the functional OH-groups from the CTS polymer chain overlapping with the peak correlating to the hydroxyl groups of EVOH. C-O stretching can also be seen at 100-1300 cm^{-1} for CTS. Figure 4.32 shows the full spectra of CTS/EVOH sponge before and after Zn(II) adsorption. The changes in the peak intensity of CTS/EVOH that occur with the presence of Zn(II) are clearly visible after normalization has been done and the baseline has been corrected. All spectra concerning the influence of heavy metals on the CTS/EVOH sponge will be shown in Appendix B.

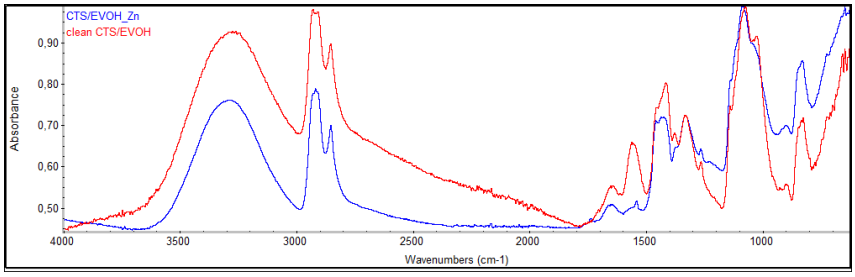

Figure 4.32: The influence of Zn(II) on the FTIR spectrum of CTS/EVOH sponge.

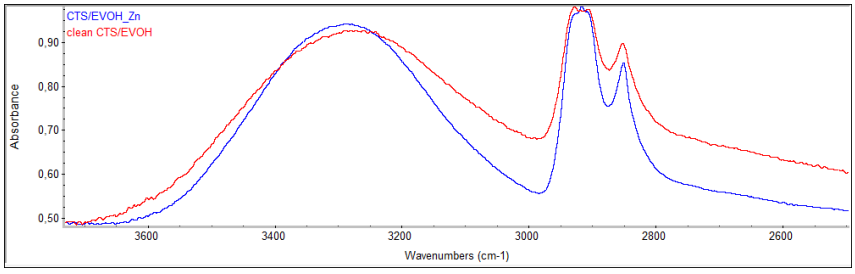

Figure 4.33: The influence of Zn(II) on the FTIR spectrum of CTS/EVOH

As seen in Figure 4.33, the hydroxyl and amine peak intensities at 3400 - 3200 cm^{-1} and 3000 - 2800 cm^{-1} are reduced indicating possible interaction with Zn(II). Figure 4.34 show how the presence of Zn(II) also changed the peaks belonging to the amide peaks,

showing a reduction in peak intensity at around 1600 cm^{-1}.

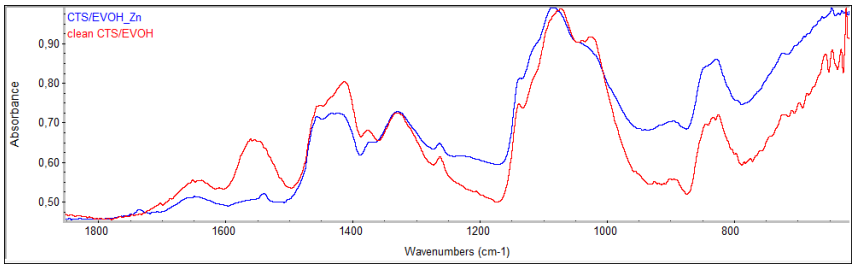

Figure 4.34: The influence of Zn(II) on the FTIR spectrum of CTS/EVOH

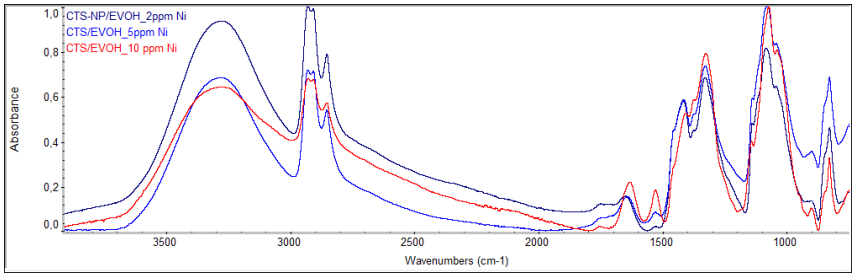

Figure 4.35: FTIR spectra of CTS/EVOH with initial sorbate concentration of Ni(II).

In Figure 4.35 shows the reduction of the peaks for amine and hydroxyl groups on the surface of the sponge as well as the effect that the initial Ni(II) concentration has on the adsorption effectiveness pf CTS/EVOH sponges. An increase in Ni(II) concentration caused a decrease in the peak intensity of the broad band CTS/EVOH at approximately 3000 cm^{-1}. As seen for 2 $mg.L^{-1}$ (ppm) Ni(II) on the spectra the low concentration show that less interaction occurs between the CTS/EVOH sponge and the nickel ion than was seen for the concentration of 5 $mg.L^{-1}$ Ni(II) and higher. The optimal initial concentration of the heavy metal ions for good adsorption appears to be 10 $mg.L^{-1}$.

4.4.2 SEM

The SEM images of the CTS/EVOH sponge is presented in Figure 4.36. All three images show various sides of the sponge indicating the porous distribution throughout the composite material. The pore sizes were determined from SEM micrographs using the SEM diameter analyses program. Pore size varied from 43.9 nm – 130 nm. The pore size varies due to phase separation that occurs during solvent evaporation. These pores provide entry into the material and access to the CTS adsorption sites that are also present within the CTS/EVOH sponge. As mentioned before the CTS/EVOH with 2.5 wt% chitosan content was used for the rest of the adsorption and characterisation studies due to the

optimal chitosan amount relative to EVOH that gives a good amount of pores and wettability as well as the relatively good dispersion of CTS within and around the material.

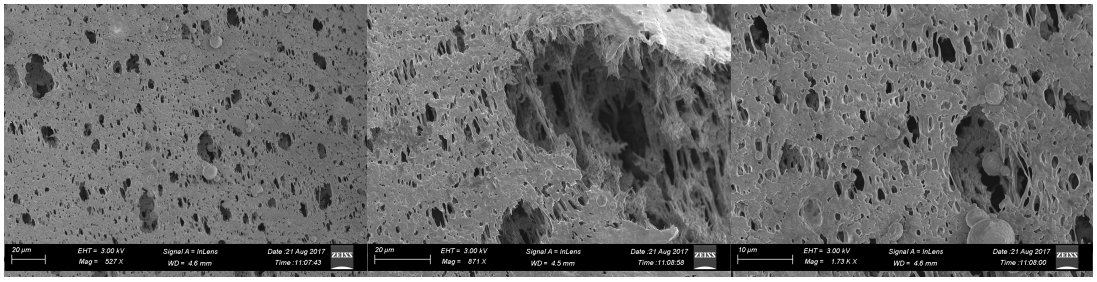

Figure 4.36: SEM images of CTS/EVOH sponge.

4.4.3 Confocal Fluorescence microscopy

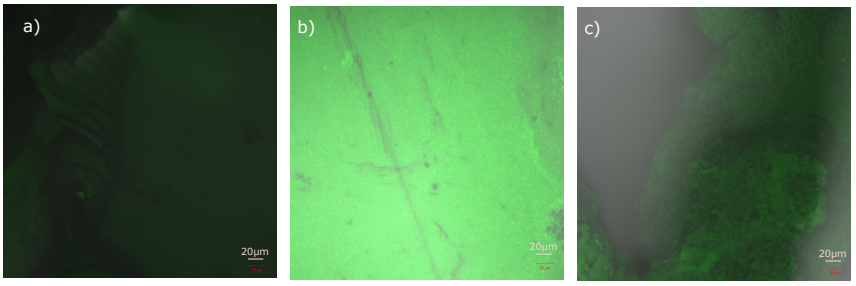

Figure 4.37: Confocal fluorescence microscopy image of a) the surface, b) the centre and c) the sides of the CTS/EVOH sponge.

Figure 4.37 shows the distribution of CTS within the EVOH matrix of the sponge. The fluorescence is visibly stronger in the middle section of the sponge. The surface and the side view of the sponge segment also shows the presence of CTS. The uniform presence of CTS within the centre of the sponge segment is interesting to observe and is caused by the phase separation that occurs between the EVOH and CTS after the solvent begins to evaporate and the material starts to cool down. This was seen for every CTS/EVOH sponge sample. This morphology will affect the way the heavy metal ions interact with the sponge. CTS is present on the outside of the sponge, but the low fluorescence indicates that the sorption sites of CTS are limited on the surface and more abundant in the centre. The pores found on the surface of the sponge varies in size, and it is therefore expected that the heavy metal ions will saturate the sorption sites on the surface of the sponge and limit the access to the pores and the CTS sorption sites available within the sponge. Smaller ions may be able to penetrate the surface and migrate through the pores to the sorption sites present in the centre of the sponge.

4.4.4 Water absorption capacity

The WAC of the CTS/EVOH sponge was determined by calculating the specific absorption using the dried initial weight of the CTS/EVOH sponge minus the weight after absorption (final weight) as seen in Table 4.1 and then determining the percentage of water absorbed after saturation. The equation 4.1 was used to calculate the specific absorption, where W_m is the specific absorption (%), m_b is the mass when the material absorbs water to saturation(mg) and m_d is the mass when the material is dry (mg). Three measurements were taken and overall the swelling that occurred were approximately twice the weight of the initial dry mass.

$$W_m = (m_b - m_d \times 100 \tag{4.1}$$

Table 4.1: Water absorption capacity

Sample	Initial weight (mg)	Final weight (mg)	Percentage (%)
1	21	48	44
2	18	45	40
3	29	51	57

The swelling of the CTS/EVOH sponge, after 2 hours, to double the original weight indicates good water absorption capacity that can contribute to the overall adsorption capacity of the material.

4.4.5 Tensile Testing

The CTS/EVOH sponges were made in bulk by preparing it in a tube or syringe. This yielded long tubular sponge structures that could easily be used as tensile bars during tensile testing. During preparation of the CTS/EVOH sponges, it became apparent that a dry sponge sample behaves differently as soon as it is introduced into water. The CTS/EVOH sponges were therefore tested under two types of conditions, wet and dry, to see how the mechanical behaviour of the material changes under the different conditions. It has been observed during initial adsorption studies and preparation of the sponges that the mechanical qualities of the sponges changed as it changed from dry to wet (once placed in the aqueous solution). Table 4.2 shows Young's modulus, Tensile strength and extension and stress at breaking point. The Young's modulus (E) was calculated at a %strain of 22,43% for wet CTS/EVOH sponge and 1,609% for dry CTS/EVOH sponge. The % strain was divided by 100 to obtain a dimensionless value that was then used to calculated Young's modulus with the equation shown in Equation 4.2. Young's modulus is calculated according to the units of stress as MPa. According to Hooke's law, stress is force per unit area and strain is the deformation of a solid due to stress [118].

$$E = \frac{Stress}{Strain} \tag{4.2}$$

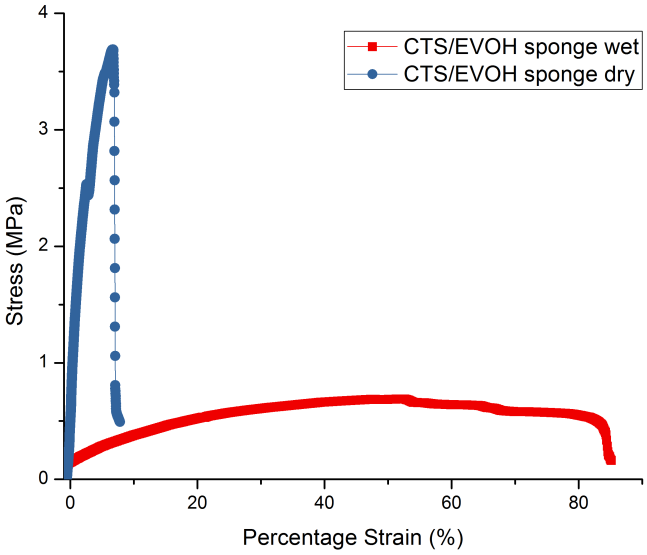

Figure 4.38: Stress-strain curve of a dry CTS/EVOH sponge vs wet CTS/EVOH sponge.

Table 4.2: Tensile properties of CTS/EVOH sponges

	CTS/EVOH (dry)	CTS/EVOH (wet)
Young's Modulus (MPa)	54,31	2,043
Tensile Strength (MPa)	3.600	0,6990
Extension at Break (%)	60.80	91.59

CTS/EVOH sponge has an interesting morphology that is represented through the tensile properties seen in the stress-strain plots in Figure 4.38. Dry CTS/EVOH sponges behaved like rigid and brittle material that have low elongation (extension) at the break and is not as pliable while dry. Dry CTS/EVOH sponges also show a higher Young's modulus compared to wet CTS/EVOH sponges. Dry CTS/EVOH show capability of withstanding applied force much more than wetted CTS/EVOH. Wet CTS/EVOH sponges showed greater ductile behaviour, becoming more pliable (flexible) in water. This behaviour allows for good elongation (extension) at the break which means that the material only breaks after a long duration of force is applied. The pores distributed throughout the CTS/EVOH sponge tube does affect the mechanical strength of the material. Crazing in irregular phases can be observed for the dry material. The tensile properties of this sponge are important to ensure that the sponge will maintain its structure during agitation and strain that it may be subjected to in real-world trials for wastewater removal in the future.

4.4.6 Thermo-gravimetric analysis

The degradation of the CTS/EVOH and the pristine components of the material progressed in two stages. The first stage was correlated with weight loss due to solvent evaporation and this was seen for each component and material except for EVOH. The second stage consists of the thermal degradation of the material which occurred in various gradients for each of the components or material. The peak for the TGA thermogram seen in Figure 4.39 shows the loss of moisture at 0 to 100 ℃ for CTS/EVOH sponge, which is considerably higher than that seen for CTS (before adsorption). The thermal degradation for pristine CTS occurred at 300 ℃ with a 50% weight loss up to 400 ℃ followed by a more gradual degradation slope up to a final 30% weight loss at 900 ℃. The CTS/EVOH sponge shows a combined thermal degradation behaviour between EVOH and CTS. The thermal degradation occurs at 400 ℃with a 80% weight loss and plateauing until 900 ℃ is reached. EVOH shows a more drastic thermal degradation with a total weight loss between 100 and 400 ℃. The overall thermal stability of the CTS/EVOH sponge is better than the pristine components showing the onset of degradation occurring at a higher temperature than seen for the pristine components. The large peak, correlated to the loss of moisture, seen for the CTS/EVOH sponge is not only indicative of good moisture absorption but also shows that the moisture is not as easily released which is one of the characteristics of a sponge.

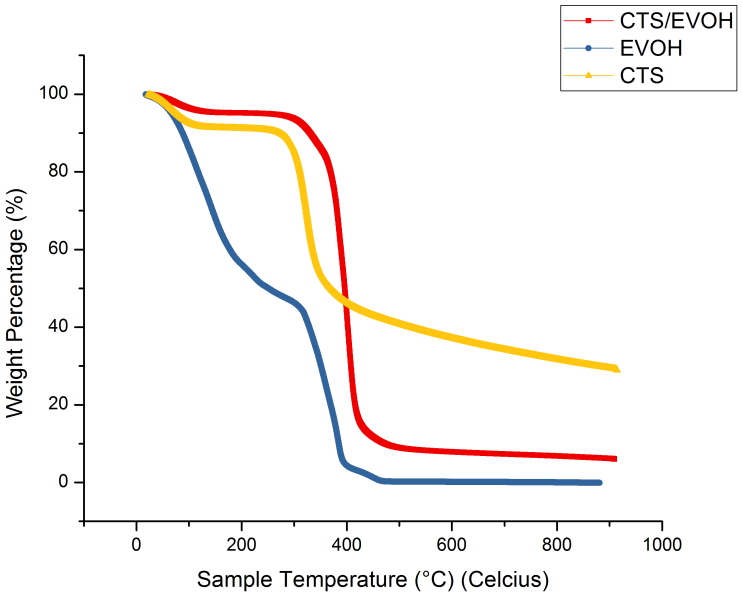

Figure 4.39: TGA thermogram of a CTS/EVOH sponge.

The loss of moisture indicates the presence of hydrophilic functional groups that make the material wettable in water. Amino-groups are hydrophilic and enhance the hydrophilicity

of the polymer, such as seen for CTS [87]. By blending EVOH with CTS and creating a porous structure, the modified surface morphology can contribute to moisture absorption. This could then lead to improved interaction with the sorbate present in the aqueous solution.

4.4.7 DSC

Figure 4.40 presents the CTS/EVOH sponge before and after adsorption of heavy metal ions. Shifts and changes in the melting and crystallization peak of the partially crystalline material are observed. These changes indicate that there is a decrease in the degree of crystallinity of this material after the adsorption of heavy metal ions occurred. A reduction in peak intensities, as well as a broadening of the peaks, can be seen, indicating a loss in the crystalline structure. The sponge showed the ability to retain heavy metal ions better compared to CTS powder during adsorption studies (Chapter 5), which could enhance the effects that these ions have on the DSC results for the CTS/EVOH sponge.

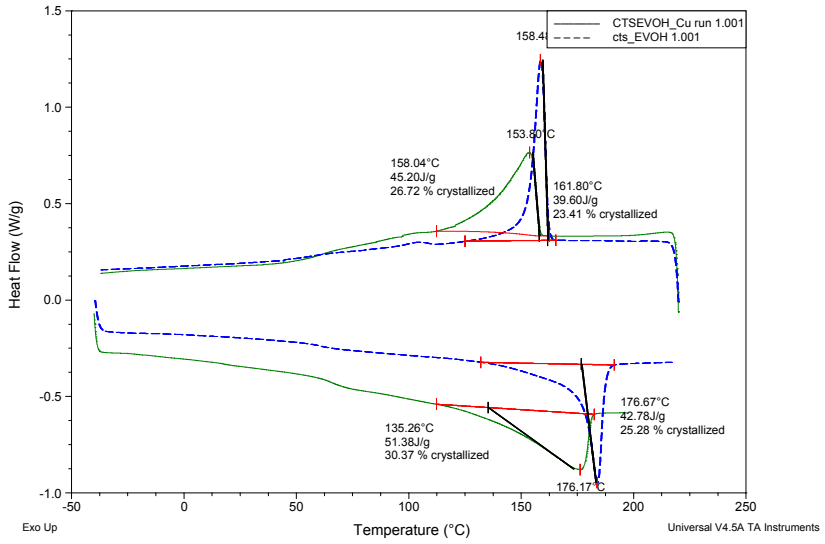

Figure 4.40: DSC thermogram of CTS/EVOH sponge before and after adsorption of heavy metal ions

4.5 CTS-NP/EVOH composite nanofibers

4.5.1 FTIR spectroscopy

The FTIR spectrum (Figure 4.41) of CTS-NP/EVOH composite nanofibers (NF) has bands belonging to the OH-and NH_2-groups located at 3400 to 3200 cm^{-1}, which are similar to those seen for CTS powder with N-H peaks located at 1570 cm^{-1} and 1374 cm^{-1}, approximately. CH_2-OH and CH-OH peaks can be seen at 1380 and 1422 cm^{-1}, while C=O peaks are located approximately at 1650 cm^{-1}. The compatibility of EVOH with CTS-NP are based on the hydroxyl groups present on both polymers. The spectrum presented for EVOH shows the absorption band of the hydroxyl group that overlaps with the band for CTS-NP. The peak corresponding to the CH-stretching vibration within the EVOH can be seen at 2900 cm^{-1}. The band overlapping with the CTS-NP amine groups at 1400 cm^{-1} can both be attributed to saturated CH-groups from the ethylene component. The bands found at 2928 and 2851 cm^{-1} are also allocated to the amine functional groups on the surface of the CTS-NP. Decreased peak intensities are seen for the peaks located at 3000 cm^{-1} and 2800 cm^{-1} of CTS-NP/EVOH composite nanofibers after adsorption with Pb(II), after normalization and baseline correction. All spectra concerning the influence of heavy metals on the CTS-NP/EVOH composite nanofibers will be shown in Appendix B.

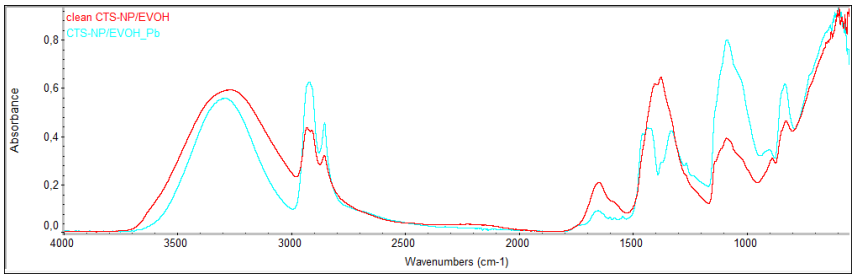

Figure 4.41: FITR of CTS-NP/EVOH composite nanofibers before and after adsorption with Cr(VI).

At closer inspection the reduction in the peak intensities of CTS-NP/EVOH after adsorption of Cr(VI) can be seen in Figure 4.42 specifically for the peaks located around 3000 cm^{-1}. These peaks belong to the amine and hydroxyl functional groups and are slightly diminished which indicate the possible interaction between the sorption site and the Pb(II). The shape of this peak is also slightly changed and show that the crystallinity is also affected by the presence of Pb(II) as is also seen in DSC later. The Pb(II) visibly appear to interact with CTS-NP/EVOH NF judging from the change in the shape and intensities of the peaks seen at 1400 - 1600 cm^{-1} seen in Figure 4.43. The larger peaks at 1100 and 900 cm^{-1} are actually similar in the area as seen in Figure 4.44 with matching

peak intensity due and comparable by using normalization.

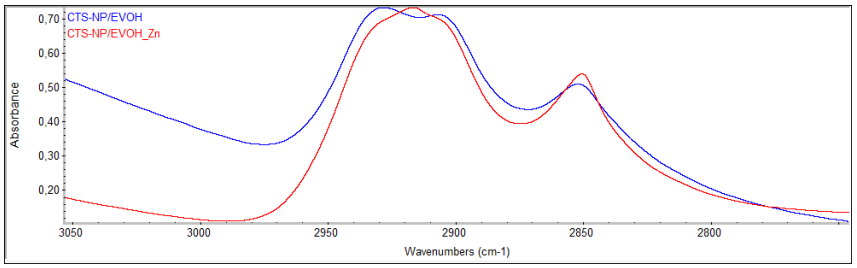

Figure 4.42: The influence of Pb(II) on the FTIR spectrum of CTS-NP/EVOH composite nanofibers.

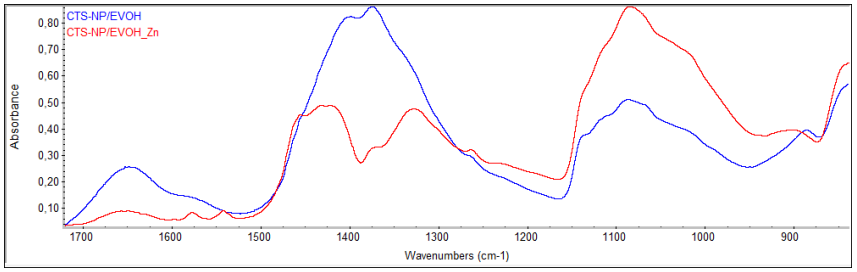

Figure 4.43: The influence of Pb(II) on the FTIR spectrum of CTS-NP/EVOH composite nanofibers.

Figure 4.45 shows the effect that initial sorbate concentration has on the spectra of CTS-NP/EVOH NF. The general trend, as seen in previous sections, indicate that the more interaction there was between the sorbent and heavy metal ions, the lower the peak intensities for the specific peaks at approximately 3000 cm^{-1} will be. The optimal initial Pb(II) concentration is indicated to be around 5 $mg.L^{-1}$.

4.5.2 SEM

Various CTS-NP loadings were tested to find the optimal ratio between EVOH and CTS-NP. As seen in Figure 4.46, the 2.5 wt% CTS-NP was too high in concentration and

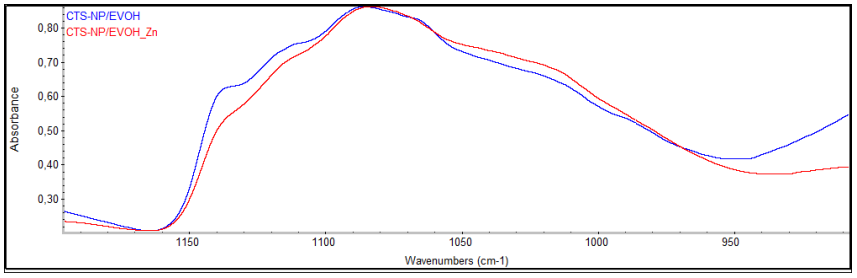

Figure 4.44: The influence of Pb(II) on the FTIR spectrum of CTS-NP/EVOH composite nanofibers.

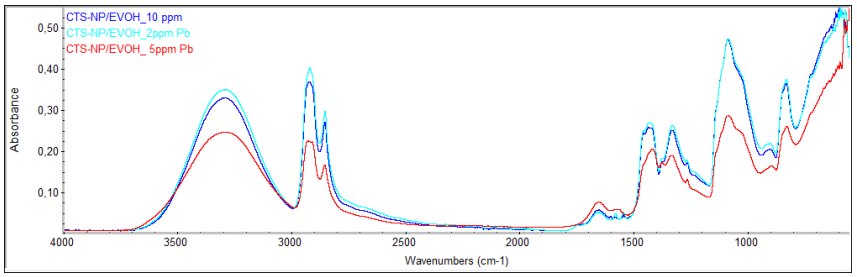

Figure 4.45: The effect of initial Pb(II) concentration on the spectrum of CTS-NP/EVOH composite nanofibers.

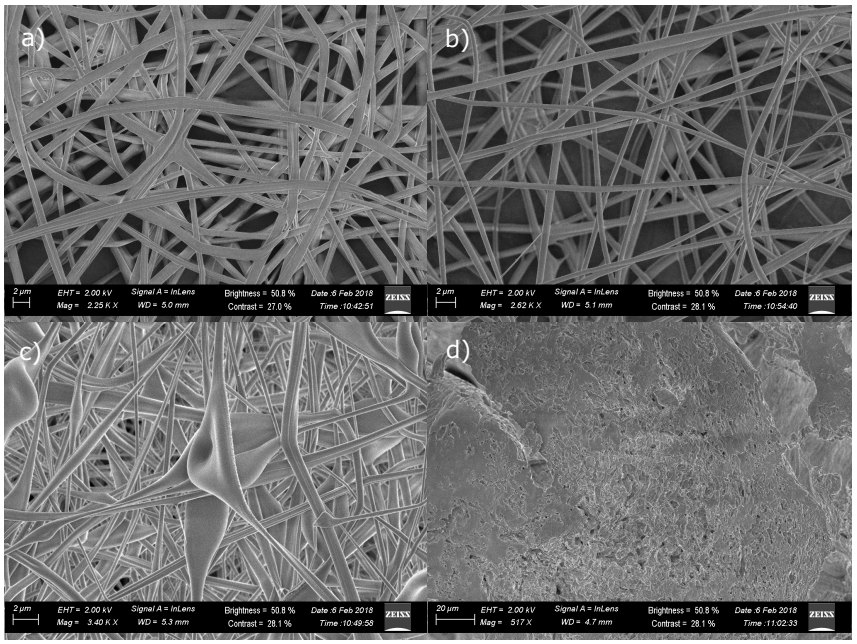

Figure 4.46: SEM images of CTS-NP/EVOH composite nanofibers with a) 2.5 wt%, b) 2 wt% and c) 1 wt% CTS-NP, and d) solvent casted CTS-NP/EVOH.

caused thick and large fibres that were non-uniform. A CTS-NP concentration of 2 wt% appeared to show better fibres with a smaller diameter of an average of 400 nm, while concentrations lower than this for CTS-NP caused beads to form. A sample was also prepared using solvent-casting. This sample, however, showed poor surface area and indicated the necessity to rather use fibres for better adsorption characteristics.

4.5.3 Confocal microscopy

In Figure 4.47 the fluorescence confocal images are shown for CTS-NP/EVOH composite nanofibers. The 3D section of the nanofibers indicated the presence of the CTS-NP throughout the fibre. The sections show that the CTS-NP are uniformly distributed on the surface and in the centre of the nanofiber. It is however expected that the adsorption process will occur predominantly on the surface of the nanofiber and in between the porous structure of the fibrous network.

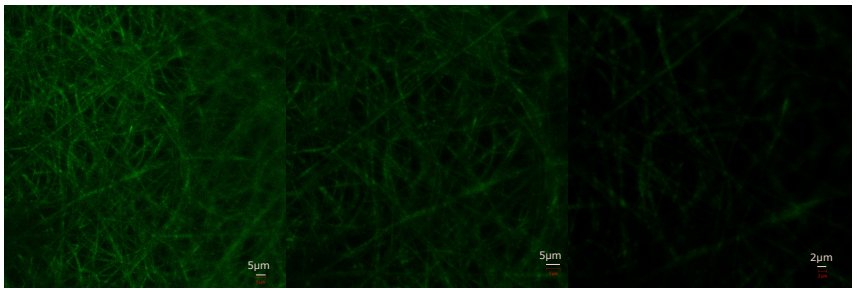

Figure 4.47: 3D stacked confocal fluorescence microscopy image of CTS-NP/EVOH composite nanofibers.

4.5.4 Thermo-gravimetric analysis

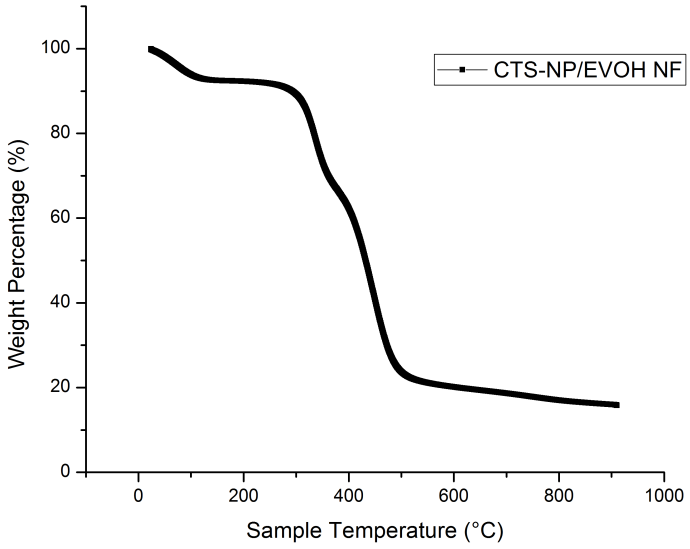

Figure 4.48: Thermogram of CTS-NP/EVOH composite nanofibers.

The TGA thermogram for CTS-NP/EVOH composite nanofibers is shown in Figure 4.48. The CTS-NP/EVOH composite nanofibers thermogram appears to be closer to the clean EVOH thermogram displayed in Section 4.4.6. This is due to the high EVOH content compared to the low CTS nanoparticles content within the nanofiber. The degradation of the CTS-NP/EVOH composite nanofibers occurs in two stages. The first stage is caused by loss of moisture and the second stage can be ascribed to the degradation of the fibre. The initial peak shows the loss of trapped solvent at 0 to 100 ℃ which is similar to that seen for the CTS/EVOH sponge. The onset of degradation occurs at 300 ℃which leads to a 70% weight loss after 500 ℃is reached. The thermal degradation appears to level out into a gradual slope that ends in a total weight loss of approximately 90% at 900

℃. The overall thermal stability of the CTS-NP/EVOH composite nanofibers appears to be suitable for water treatment applications. The initial moisture loss peak can indicate that CTS-NP/EVOH composite nanofibers retain moisture well and is wettable and good enough for application in water.

4.5.5 DSC

Figure 4.49 presents the DSC thermograms of CTS-NP/EVOH composite nanofibers before and after adsorption of heavy metal ions. Small shifts in the melting and crystallization peak of the partially crystalline material are observed. Similar small changes are seen overall for CTS or materials containing CTS.//

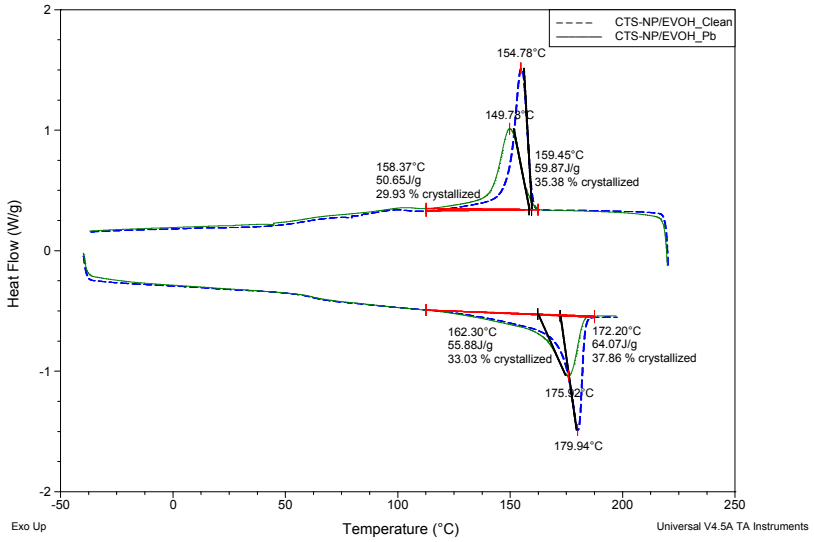

Figure 4.49: DSC thermogram of CTS-NP/EVOH composite nanofibers before and after adsorption of heavy metal ions.

4.6 Speciation of heavy metals

The study of adsorption in alkaline solutions is important since most heavy metals can be soluble in excess ammonia and easily transferable to the environment in this form. The batch solutions were made from a stock solution for each heavy metal salt with a concentration of 1000 ppm. The stock solution was diluted to final solutions where the volume required to pH adjustment was taken into consideration. The pH was adjusted to 2 using HCl. Excess ammonia was used for relevant heavy metals, discussed below, for the adjustment to a basic solution. The solution was checked for precipitation and

then the final solution was made and the pH was checked again. Slight adjustments were done in some cases to ensure that the pH is constant for each sample at pH 2, 5 or pH 11. ICP-AES was used to confirm the initial concentration of the heavy metal ions within each solution. After this, the adsorption procedure was followed with time and concentration and pH as the variables respectively for each type of biosorbent. The important step before each adsorption, however, was to check the pH and ensure no precipitation formed. The behaviour of each heavy metal salt in excess ammonia was investigated. Figure 4.50 and 4.51 shows the behaviour of Cu(II) and Ni(II) in excess ammonia.

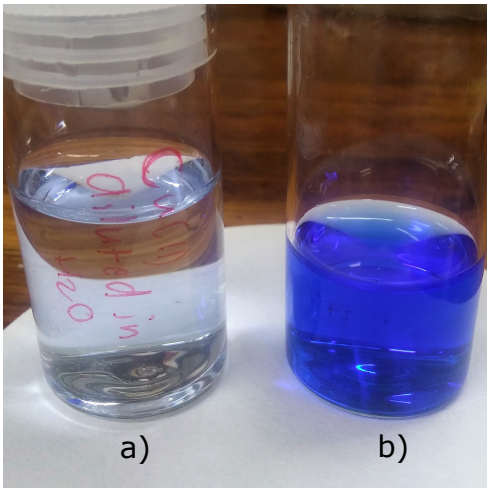

Figure 4.50: Cu(II) in a) pH 11 aqueous solution after dissolved in excess ammonia, b) in excess ammonia, pH 13.

Cu(II) from potassium dichromate salt forms a hydroxide, $Cu(OH)_2$, in basic solutions changing from a bright blue solution to blue precipitate. In excess ammonia the blue precipitate dissolves to form a dark blue solution, $[Cu(NH_3)_4]^{2+}{}_{(aq)}$. Ni(II) forms an apple green solid in pH $>$ 7. This hydroxide formation can, however, be reversed if the ammonia in the solution is present in excess. This solution can be adjusted to pH 11 thereafter without the formation of nickel hydroxide, this then allows for adsorption studies in alkaline solutions.

No precipitation was observed during adsorption at pH 11 for the Pb(II), Cr(VI) and Zn(II) indicating that the concentration of sorbate and aqueous ammonia was dilute enough for these metal ions to prevent the formation of basic salts or hydroxides as shown in Figure 4.52.

As mentioned before hexavalent chromium ions does not exist in the $[Cr(H_2O)_6]^{6+}$ form in an aqueous medium, but as the oxyanions $Cr_2O_7{}^{2-}$ or more often as $HCrO_4{}^-$ (in an acidic solution) and $CrO_4{}^{2-}$ (in a solution closer to neutral). The colour change of chromium, that indicate the different ionic forms, are visible in Figure 4.53. Analysis post-adsorption

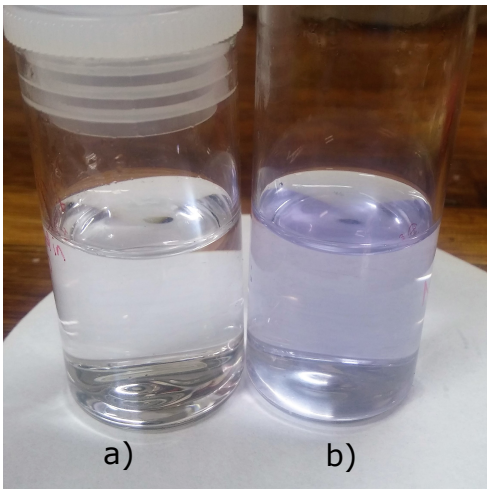

Figure 4.51: Ni(II) in a) pH 11 aquoeus solution after dissolved in excess ammonia and b) in excess ammonia, pH 13.

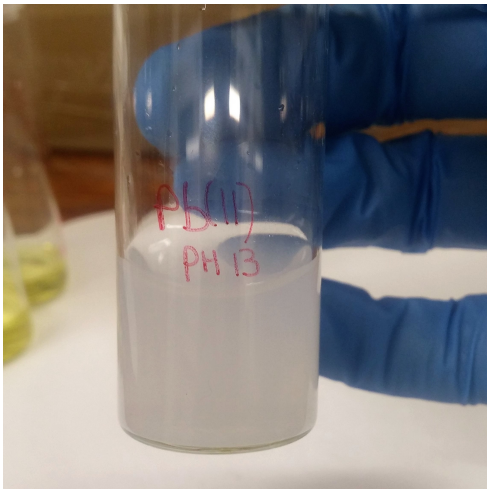

Figure 4.52: Formation of lead salt in excess ammonia of pH 13.

of the solution shows drastic changes in pH. This consumption of protons indicates that the presence of protons (H^+) play an important role during Cr(VI) removal during the adsorption process. No precipitation of zinc hydroxide was observed at very high pH in the presence of excess ammonia.

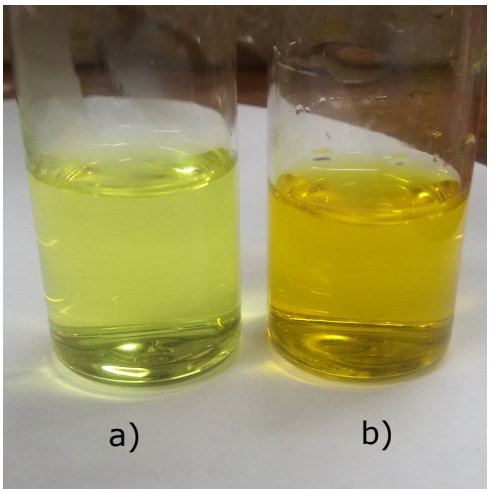

Figure 4.53: Change from a) yellow chromate, pH 11 to b) orange dichromate, pH 2

Chapter 5

Results and discussion: Adsorption of heavy metal ions

5.1 Evaluation of CTS powder sorbent

5.1.1 Effect of initial sorbate concentration

The effect of the initial sorbate concentration on the adsorption capacity of CTS powder was done using a solution with a pH of 5, at a varying initial sorbate concentration of 2, 5, 10, 20 and 100 mg.L^{-1}. A contact time of 30 minutes was used for CTS powder. The general trend shows that heavy metal removal percentage increases as the initial concentration of the sorbate increases, as shown in Figure 5.1. Further increase of the initial sorbate concentration lowers the heavy metal removal percentage, possibly due to the presence of more ions competing for the adsorption sites on the CTS powder surface. The increasing average adsorption percentage (heavy metal removal percentage) shows that an initial sorbate concentration of 2 mg.L^{-1} may not be high enough to occupy all of the sorption sites of CTS. As the initial sorbate concentration is increased the sorption sites becomes more occupied and the average sorption percentage increases. The optimum initial heavy metal (sorbate) concentration for CTS powder (0.002 g.mL^{-1}) appears to be in the region of 10 to 20 mg.L^{-1}, for the purpose of this study. These results concerning the effectiveness of the interaction, between the heavy metal ions and CTS powder, based on the initial sorbate concentration is supported by ATR-FTIR as seen in the previous chapter. CTS powder shows a general trend of increasing adsorption capacity with increasing initial sorbate concentration, as is seen in Figure 5.2.

5.1.2 Effect of pH

Each heavy metal ion used in this study has a different electron configuration, chemical properties and oxidation state that influence the mechanism of interaction for each heavy metal ion with the sorption sites as well as the affinity for specific sorption sites. Hard-

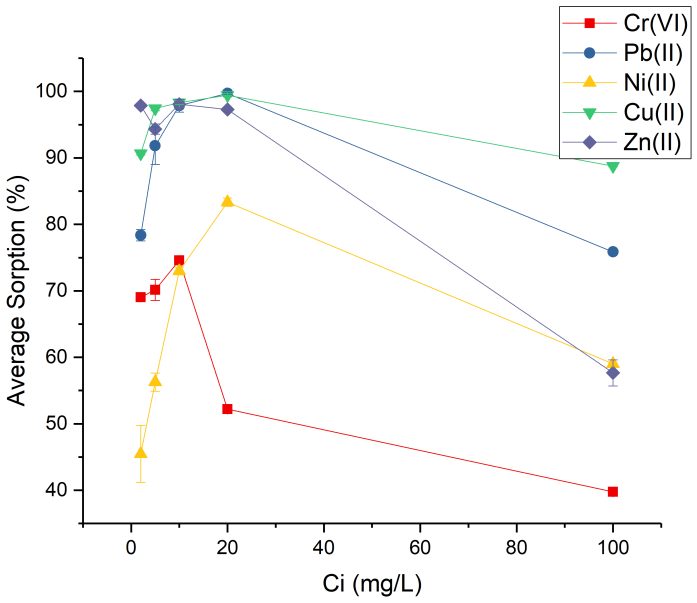

Figure 5.1: The effect of initial sorbate concentration on the adsorption capacity of CTS powder.

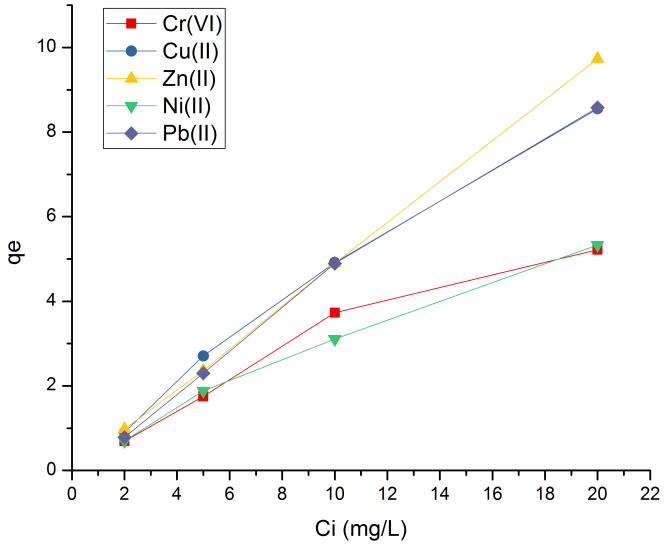

Figure 5.2: Initial sorbate concentration vs experimental adsorption capacity of CTS powder

soft-acid-base (HSAB) principle may be considered to establish a trend for the behaviour of each heavy metal during the adsorption process. The heavy metals may be classified into the hard or soft acid category as is seen in Table 5.1. Soft acids tend to be larger and more polarizable while hard acids are small and less polarizable. Hard acids also are known to have a high positive charge, high oxidative state and charge density. The polarizability of a heavy metal is the tendency of the electrons surrounding the nucleus

Table 5.1: HSAB classified compounds and elements.

	Hard	Borderline	Soft
Acids	Cr(III), Cr(IV)	Cu(II), Zn(II), Ni(II), Pb(II)	-
Bases	OH^-, NH_3, SO_4^{2-}	NO_2^-	-

to be distorted from its original shape [119]. The HSAB distinction is linked directly to the polarizability of the heavy metal ions. Borderline acids are in between hard and soft acids. Although Pb(II) is classified as a borderline acid, this metal is more polarizable and larger in ionic radius compared to the other heavy metals in this table. Pb(II) is, therefore, less of a hard acid and more closer to the soft acid category. Hard acids tend to bind to hard bases such as small ligands such as amine groups on the surface of CTS powder. Other hard acids such H^+, Li^+, Na^+ and K^+ can tend to present in trace amounts in aqueous solutions as contaminants, and may also compete for the available active sites to a certain extent.

The effect of pH was analyzed after a contact time of 120 minutes and the percentage adsorption for 10 $mg.L^{-1}$ heavy metal was used for analysis at varying pH of 2, 5 and 11. The acidic functional groups on the biosorbent changes under different pH conditions, becoming less protonated at higher pH and more protonated at lower pH. Changes in the degree of protonation of the functional groups change the charge of the surface on the polymer and this, in turn, affects the interaction between the heavy metal ions and the biosorbent. The electrostatic attraction between the heavy metal cations and the sorption sites on the CTS powder will increase as the functional groups on the biosorbent become more negatively charged in a more alkaline solution.

CTS powder easily dissolves in highly acidic media, and this was observed during the adsorption process at pH 2. Adsorption of the metal species did take place but only within the initial 30 minutes, whereafter the CTS powder began dissolving in the aqueous solution, at pH 2. The solution did not show any indication of color, and remained clear. The CTS could not be regenerated after dissolution occured and re-use of the sorbent was impossible. This lead to more CTS being required for the adsorption of the different heavy metal ions under acidic conditions, which can be less cost effective on a larger scale. CTS powder was not able to function as an effective adsorbent in highly acidic conditions, therefore no adsorption occurred after 120 minutes under these conditions.

CTS powder shows a general trend of increasing adsorption capacity at a pH of 2 and 5 and decreasing adsorption capacity as the pH is changed to 11. As seen in Figure 5.3, optimum adsorption took place at a pH of 5. A highly acidic solution, of pH 2, consists of

a higher concentration of protons that competes against the metal cations for the available negatively charged adsorption sites. The protonation of the adsorption sites causes a reduced negative charge on the surface of the CTS powder thus lowering the electrostatic forces between the surface of the adsorbent and the heavy metal cations, as discussed in Section 4.2.5. CTS powder shows high affinity for Cu(II) at optimal pH of 5 but shows the largest reduction in adsorption capacity of 59.1% as the pH changes from pH 5 to pH 11. This indicates that CTS powder is not as strongly bound to Cu(II) in alkaline solutions and has low retention for Cu(II) in a solution with a pH of 11. This desorption can also indicate alternative means to regenerate CTS powder rather than using an acidic media.

As the pH changed from 2 to 5, Cr(VI) was more easily adsorbed by CTS when comparing the first 30 minutes of the adsorption process, where total adsorption after 30 minutes was 8.357 and 62.990% for pH 2 and pH 5 respectively. This is similar to results found in literature by Salih et al. [40]. In acid solution chromium metal ions tend to exist in the form of H_2CrO_4 which is a neutral complex which leads to little interaction between the surface of the CTS and the heavy metal [40]. Cr(VI) also exist as $CrO_4{}^{-2}$ which will probably interact with the protons present in the solution at pH 2 more readily than with the protonated surface of the CTS and therefore the adsorption capacity is low in acidic solutions. When the pH is increased, the protonation decreases and allows the surface to become more negatively charged. This leads to less hindered interaction between the Cr(VI) and the CTS surface. As the pH is increased to 11, the $[OH]^-$ increases and the negative charge on the surface of the CTS increases even more. This can cause electrostatic repulsion of the $CrO_4{}^{-2}$ species that exist in the solution and also lowers the adsorption capacity.

The hydrated states of nickel and zinc in the form of the salts that were used for the preparation of the solutions can determine to a certain degree to which the heavy metal cations will be able to interact with the surface of the biosorbent. Bartczak et al. nickel adsorption specifically for Ni(II) that originated from nickel nitrate hexahydrate, due to low and that the hydration of the ion lowered the interaction with the adsorbent which was peat in this case [106]. As mentioned in Section 3.1, nickel sulfate heptahydrate is used for this study. This salt will dissolve in water and the nickel will dissociate from the sulfate to give a metal complex with water as the only ligand, $[Ni(H_2O)_6]^2+$. The high degree of hydration of the nickel ion as well as the low electron density of the ion complex, may lower the interaction with the surface of CTS. This may be the case, especially at low pH where the surface of the CTS powder is more protonated and therefore less negatively charged. As the pH is increased the amine sorption sites become less protonated and the charge on the surface of the surface of the CTS become more negative and therefore may attract the Ni(II) complex more readily, and thus increases the adsorption capacity.

Any further increase in pH, however appeared to lower the capacity of CTS for Ni(II) adsorption. Although Ni(II) adsorption is expected to increase, due to the theorised enhanced electrostatic attraction between the more negatively charged surface of CTS and the Ni(II) metal ions, it does appear that the heterogeneous nature of the CTS powder may influence the interaction between the metal ions and available sorption sites at pH 11. The presence of hyroxyl groups may have a larger effect than it may have on the more homogenous biosorbents in this study such as CTS-NF and CTS-NP/EVOH composite nanofibers. It is possible that in a basic solution the Ni(II) may form hydrated oxides that passifies the metal and hinders the interaction with the adsorption sites on the CTS [120, 121]. The irregular distribution of adsorption sites along with the low surface area of CTS also may have a greater effect on the adsorption capacity of Ni(II) adsorption at higher pH compared to other biosorbents discussed further in this study.

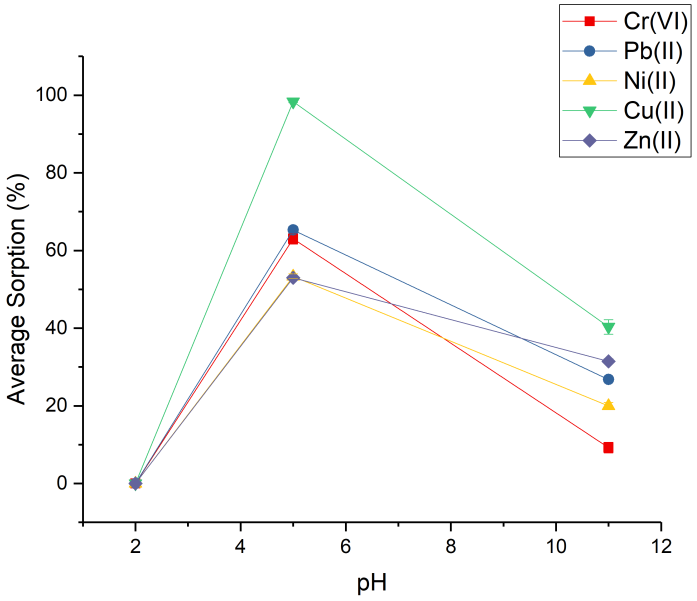

Figure 5.3: The effect of pH on the adsorption capacity of CTS powder.

5.1.3 Effect of contact time

The expected trend of increasing adsorption capacity with increasing contact time was not observed for CTS powder with the exception of Cu(II). The small amount of CTS powder (0.002 g.L^{-1}) that was used for the adsorption studies highlighted the poor metal ion retention ability of CTS powder more clearly. Optimal pH conditions (pH 5) and an initial sorbate concentration of 10 mg.L^{-1} was used for this study of the effect of contact time on the adsorption capacity. CTS powder appeared to retain adsorb metal ions up until 60 to 80 minutes as seen in Figure 5.4. CTS powder does show good affinity for

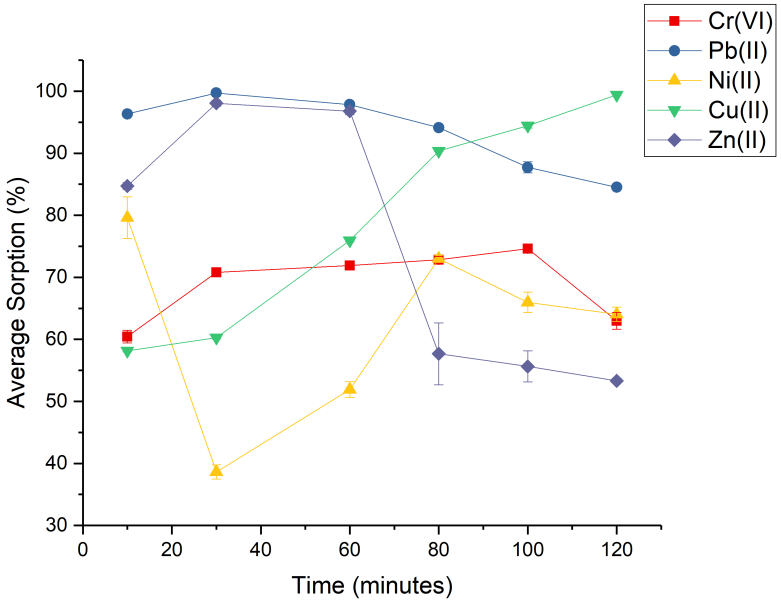

Figure 5.4: The effect of contact time on the adsorption capacity of CTS powder.

Cu(II) after 2 hours in a solution of pH 5. The fluctuations in adsorption capacity and retention that are observed for Ni(II) after 10 minutes and Zn(II) after 60 minutes could be ascribed to low electron density on these ions that are weakly bonded to the adsorption sites of CTS powder. It is also possible, especially with a more heterogeneous biosorbent like CTS powder that adsorption occur in a stepwise manner leading to the formation of different layers. The formation of the first adsorption layer is more favourable and as the contact time is increased the retention of the less favourable layer of metal ions will be lost [122]. Competing ions caused by the presence of contaminants can also have some effect on the initial adsorption process of the metal cations, but it has been found in the literature that contaminants such as sulfates, nitrates, and chlorides show insignificant effects on the overall adsorption capacity for heavy metal cations at a pH of 5 [69].

It has been found that larger ions such as Pb(II) are easily polarised leading to a lower degree of electron density on the nucleus, thus enhancing interaction with the surface of the biosorbent [6, 106]. This could be the reason why CTS powder shows a high affinity for Pb(II). The affinity of lead for amine groups may also influence the overall adsorption capacity and retainability of CTS powder for Pb(II) [77, 123].

CTS powder shows the highest affinity for Cu(II) followed closely by Pb(II), although some loss in retention for Pb(II) is observed after 2 hours [6, 124]. In general the trend seen for the affinity of CTS powder for the various heavy metal ions are well in agreement with available studies in literature, where Cu(II) has the highest affinity followed by Pb(II), Zn(II), Ni(II) and Cr(VI) [11, 77]. Copper has a higher electron density than chromium, zinc, and nickel. The good adsorption seen for Cu(II) can mainly be ascribed

to the mechanism of adsorption that is related to the hardness of the ligand donor sites when compared with the hardness of the metal ion. Cu(II) is harder than Pb(II), and thus prefers the harder oxygen donor sites of the hydroxyl groups. Cu(II) therefore forms bonds more readily with the available hydroxyl groups on the CTS surface which is an interaction that is not easy for Pb(II). The mechanism of adsorption of Cu(II) onto chitosan has been investigated by Terreux et al. and it has been found that the complex formation between a copper ion and the amine or hydroxyl adsorption sites on the chitosan can promote further adsorption, allowing for Cu(II) to bind readily to the surface of CTS [124]. Terreux et al. determined that the most stable interaction occurs between the nitrogen atom of the amine group and Cu(II) and that a stable complex forms between two amine groups that each belong to a different glucosamine monomer.

Zn(II) and Ni(II) has a lower electron density compared to Cu(II). These metal cations favour the more easily available adsorption sites that require the least amount of energy to reach. As soon as the more easily available adsorption sites are saturated the lower energy sites are the only remaining adsorption sites available for sorption on the heterogeneous surface of the CTS powder. These adsorption sites chelates poorly to the metal cations due to steric hindrances that has to do with the complexation of the Ni(II) and Zn(II) metal ions as well as the conformational interferences and the low surface area of the CTS powder. These obstacles can affect the retention ability of CTS powder after longer contact periods and can reduce the adsorption capacity. CTS powder shows better interaction with Cr(VI) with only slight loss in retention after 100 minutes. This could be due to the charge present on the hexavalent chromium specie in a solution of pH 5.

CTS powder adsorbed 99.4% of Cu(II) after 2 hours, while the removal of Pb(II) was slightly less at 84.5%. The adsorption for Ni(II), Zn(II) and Cr(VI) was 64.1%, 53.3%, and 62.9% respectively after 120 minutes at a pH of 5.

The overall optimal conditions for CTS powder was found to be at pH 5, for initial sorbate concentrations of 10 or 20 $mg.L^{-1}$, after a contact time of 30 minutes, with exception of Ni(II), where-after desorption tend to occur for some of the heavy metals that were studied. The experimental adsorption capacities for CTS powder, calculated using Equation 2.11 presented in Section 2.6.1, are shown in Table 5.2 including the standard deviation from the average of 3 measurements. This was done for each biosorbent.

Table 5.2: The experimental adsorption capacity for CTS powder for all initial heavy metal ion concentrations.

Heavy metal ions	$q_{e(exp)}$ (mg.g^{-1})			
	2 mg.L^{-1}	5 mg.L^{-1}	10 mg.L^{-1}	20 mg.L^{-1}
Cr	0.6905 ± 2.730 x 10^{-3}	1.753 ± 3.965 x 10^{-3}	3.730 ± 1.779 x 10^{-3}	5.220 ± 1.184 x 10^{-3}
Cu	0.9068 ± 3.000 x 10^{-3}	2.709 ± 1.220 x 10^{-2}	4.916 ± 1.730 x 10^{-2}	8.549 ± 4.900 x 10^{-3}
Zn	0.9788 ± 1.200 x 10^{-3}	2.359 ± 2.380 x 10^{-2}	4.903 ± 3.010 x 10^{-2}	9.730 ± 1.500 x 10^{-2}
Ni	0.7000 ± 1.490 x 10^{-2}	1.885 ± 4.120 x 10^{-2}	3.107 ± 6.750 x 10^{-2}	5.333 ± 7.850 x 10^{-2}
Pb	0.7837 ± 8.380 x 10^{-3}	2.296 ± 7.072 x 10^{-2}	4.893 ± 4.871 x 10^{-2}	8.579 ± 1.178 x 10^{-2}

5.2 Evaluation of CTS-NF sorbent

5.2.1 Effect of initial sorbate concentration

This study was carried out in an aqueous solution that was at a pH of 5, with varying initial sorbate concentrations of 2, 5, 10 and 20 and 100 mg.L^{-1}. The general trend seen in Figure 5.5 shows that as the initial concentration of heavy metal ion is increased, the adsorption percentage is reduced. As the concentration of the sorbate becomes higher, competition between the ions for the active sites increases and therefore interferes with the overall interaction with CTS-NF. The solubility of concentrated metal ion in a solution can be lower than for a solution with a lower sorbate concentration, specifically in more alkaline solutions. A general trend shows that a slight increase in percentage heavy metal removal is seen for an initial sorbate concentration increase of 0 to 10 mg.L^{-1}. The percentage of heavy metal removal (average sorption) then appears to decreases as the initial sorbate concentration is increased from 10 to 20 mg.L^{-1}. Ni(II) and Zn(II) show some deviation from this trend but show a further decrease in average percentage sorption as the initial sorbate concentration is increased further to 100 mg.L^{-1}. This is also visible for Pb(II) adsorption. Competition between the heavy metal ions for the adsorption sites of CTS-NF increases as the initial sorbate concentration reached 20 mg.L^{-1}. Not only can competition between the metal ions for the available sorption sites effect the adsorption rate and efficiency but other factors such as the qualities of the metals can also effect the adsorption at higher concentrations. The hydrated state of Ni(II) and Zn(II) within the aquaoues solution can lower the interaction with CTS-NF as the concentration and competition increases for adsorption sites. The association with water ligands in the solution for Ni(II) and Zn(II) affects the charge on the metal ions and reduces the affinity for adsorption sites on the surface of the CTS-NF. This hindered interaction becomes more prominent as the initial Ni(II) or Zn(II) concentration increase [120, 121]. CTS-NF shows good affinity for Cu(II) which is likely because Cu(II) forms more stable complexes with the N donor sites of the polymeric carrier. Cu(II) ions can form complexes with more than one amine at a time and also interact with hydroxyl groups. Cu(II) is able to be

involved in binding to the donor sites in a chelating fashion, involving both N,N and N,O chelates. Cr(VI) adsorption does not seem to become effected by the furhter increase of the initial Cr(VI) concentration. This means that the competition between the metal ions and the adsorption sites are too high at high Cr(VI) concentrations which may be aided by the good electrostatic attraction between the Cr(VI) specie and the amine groups on the CTS-NF.

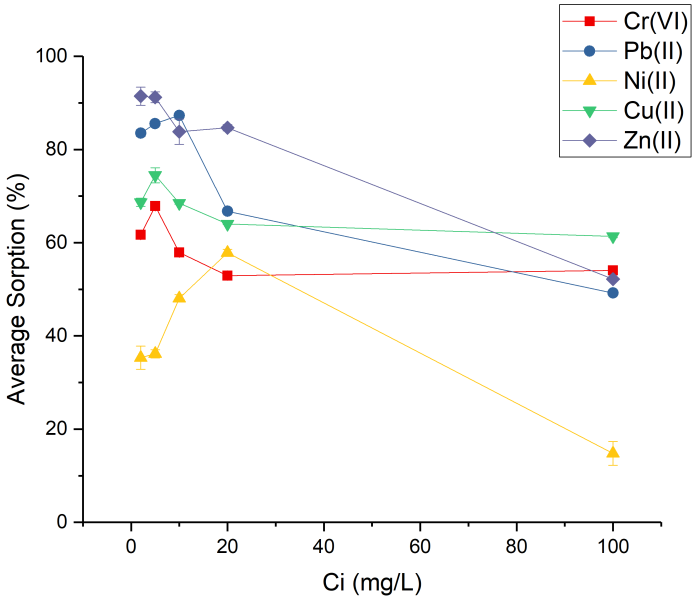

Figure 5.5: The effect of initial sorbate concentration on the adsorption capacity of CTS-NF.

Competition and the mechanism of adsorption, meaning the types of interaction that occur between the heavy metal ion and CTS-NF, are not the only factors that can affect the adsorption capacity of CTS-NF. The physical behaviour of these nanofibers in the aqueous solution also influences how well it behaves as a sorbent at higher sorbate concentrations. CTS-NF showed tendencies to recoil and fold during agitation. Although the nano-fibre mat does not adhere to itself it can remain folded for the duration of the agitation time thus lowering the number of metal ions that can enter into the fibre network. This can cause obstruction and lower interaction between the heavy metal and the available adsorption sites as well as effect the reproducibility of results. CTS-NF showed good adsorption capacity fora variety of heavy metal and in further studies it will may simply be necessary to focus on engineering a functional scaffold to hold the nanofiber mats in place, thus moving only the aqueous solution around the CTS-NF.

It appears that the optimal initial sorbate concentration, where the competition is minimal can be found at 10 and 20 mg.L^{-1}. Figure 5.6 shows the general trend of increasing

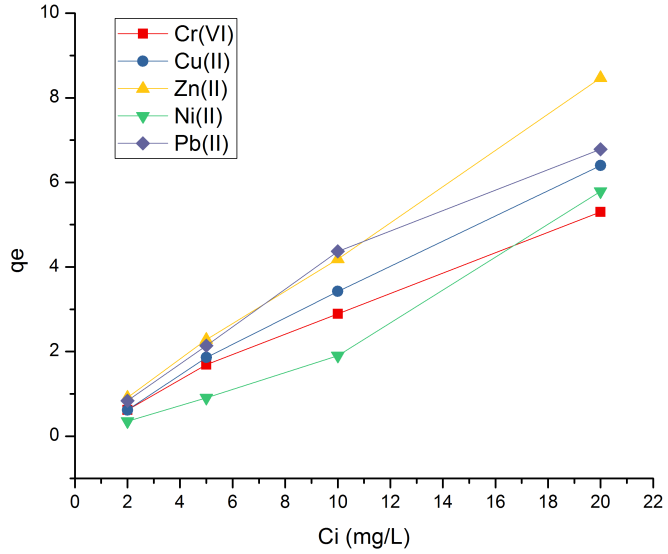

Figure 5.6: Initial sorbate concentration vs experimental adsorption capacity of CTS-NF

adsorption capacity of CTS-NF with increasing initial sorbate concentration.This trend was found for all the biosorbents in this study for the different metal ions.

5.2.2 Effect of pH

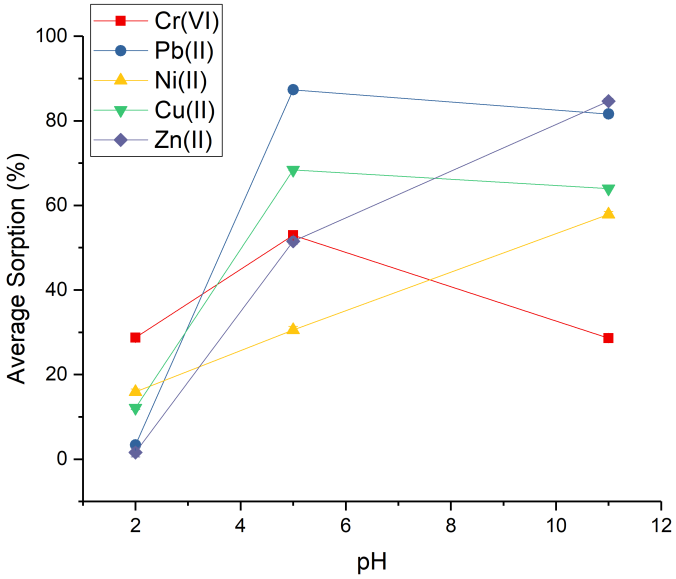

Figure 5.7: The effect of pH on the adsorption capacity of CTS-NF.

CTS-NF also showed instability in acidic solutions like the CTS powder but it was observed that the dissolution of the nanofibers is less rapid. About 50% of CTS-NF dissolve

after 120 minutes, however this percentage varies for each analyses and is therefore an approximation. Heavy metal adsorption is therefore still a possibility for CTS-NF in acidic solutions, but the nanofibers would need to be improved so that the stability of CTS-NF in acidic solutions can increase. CTS-NF appears to adsorb all heavy metals well in more basic solutions. Slightly better adsorption for Pb(II) and Cu(II) can be seen at pH 5 while Cr(VI) adsorption is better at pH 5 than in more basic solutions as is shown in Figure 5.7. It is known that the chromate anion exist in more alkaline solutions while the dichromate can be more predominant along with other forms of the metal ions in more acidic solutions. The increased charge of the surface of the CTS-NF due to the deprotonation of the amine groups causes a repulsive force against the chromate anions and thus lowers the adsorption capacity of CTS-NF for Cr(VI) at a pH of 11 [40,125,126]. The slight decrease in the Pb(II) and Cu(II) can also be due to interaction that exist between the OH^- and the metal ions in basic solutions.

Metal ions with higher electron densities are favoured for sorption due to the affinity for electrons that are provided by the sorption sites on the CTS-NF [127]. Cu(II) and Pb(II) shows a high affinity for the adsorption sites present on the surface of CTS-NF at pH 5 as well as pH 11. As the pH increases, the competition between the protons and heavy metal ions for the surface of the CTS-NF is lowered due to the decreased proton concentration. Many adsorption sites present on the CTS-NF are possibly less protonated, forming a negative charge on the surface of the nanofibers. The adsorption capacity increases for Zn(II) and Ni(II) more significantly than for Pb(II) and Cu(II) which could be ascribed to the increasing hardness of the metal ions as the pH increases. It has been noted by Arshadi et al. that Ni(II) showed an optimal adsorption at pH 11 on barley straw ash which corresponds well to the results found in this study for Ni(II) adsorption [120]. The lack of an inflection point seen in the plot for average sorption vs pH could also be explained by the increasing pH, that decreased the H_3O^+ concentration allowing the surface of the CTS-NF to be more negatively charged and therefore results in more biomass active sites available while electrostatic attraction was also more enhanced. Pb(II) is more polarisable and a softer acid than Cu(II) which may mean that the existing OH^- ions are more attracted to Pb(II) and therefore caused more interference the metal ions' interaction with the surface of the CTS-NF.

5.2.3 Effect of contact time

The results in Figure 5.8 shows the varying contact time for initial sorbate concentration of 10 $mg.L^{-1}$ at pH of 11, however, the results for Cr(VI) was investigated at the optimal pH of 5. The general trend indicated that an increasing contact time increases the average sorption percentage (heavy metal removal). The heavy metal removal after 2

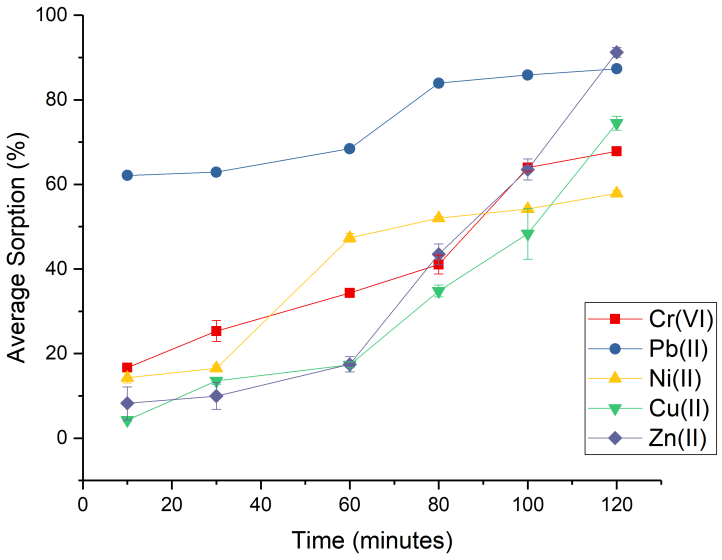

Figure 5.8: The effect of contact time on the adsorption capacity of CTS-NF.

hours indicated that CTS-NF had a good affinity for Pb(II), Cu(II) and Zn(II) followed by Cr(VI) and Ni(II). Ni(II) showed the lowest affinity for the adsorption sites of the CTS-NF after 120 minutes. As mentioned the hydration state of the nickel complex that exist in solution does effect interaction between the Ni(II) and the sorption sites to some degree. It has been suggested by Arshadi et al. that Ni(II) exclusively adsorbs via an ion exchange mechanism which can also be effected by the poor electron density of the nickel complex in solution.

Adsorption at optimal conditions for CTS-NF yielded excellent results for all of the heavy metal ions used in this study. The highest adsorption capacity of CTS-NF was seen for Zn(II), removing 91.21% from the aqueous solution, followed closely by the good adsorption of Pb(II) and Cu(II), removing 87.33% and 74.50% respectively. The removal of Cr(VI) and Ni(II) was 67.85% and 57.85% respectively.

The overall optimal conditions for CTS-NF was found to be at pH 11, for initial sorbate concentration of 10 mg.L^{-1}, after a contact time of 120 minutes. The experimental adsorption capacities for CTS-NF is shown in Table 5.3.

Table 5.3: The experimental adsorption capacity of CTS-NF for all initial heavy metal ion concentrations.

Heavy metal ions	$q_{e(exp)}$ (mg.g^{-1})			
	2 mg.L^{-1}	5 mg.L^{-1}	10 mg.L^{-1}	20 mg.L^{-1}
Cr(VI)	0.6170 ± 8.190 x 10^{-3}	1.696 ± 2.802 x 10^{-2}	2.895 ± 1.000 x 10^{-3}	5.294 ± 6.250 x 10^{-3}
Cu(II)	0.6868 ± 1.080 x 10^{-2}	1.862 ± 5.010 x 10^{-2}	3.424 ± 1.210 x 10^{-2}	6.352 ± 3.055 x 10^{-2}
Zn(II)	0.9145 ± 2.373 x 10^{-2}	2.280 ± 3.536 x 10^{-2}	4.192 ± 0.1675	8.466 ± 8.173 x 10^{-2}
Ni(II)	0.3533 ± 3.055 x 10^{-2}	0.9040 ± 0.8920	1.903 ± 0.0483	5.785 ± 8.789 x 10^{-2}
Pb(II)	0.8352 ± 7.200 x 10^{-3}	2.139 ± 4.000 x 10^{-3}	4.367 ± 2.460 x 10^{-2}	6.780 ± 8.600 x 10^{-2}

5.3 Evaluation of Chnw/EVOH composite nanofibers as sorbent

5.3.1 Effect of initial sorbate concentration

The initial sorbate concentration was investigated for chnw/EVOH composite nanofibers. The initial sorbate concentration for each heavy metal was increased stepwise from 2 to 20 mg.L^{-1}. The pH of the solution was kept constant at pH 5 and the results were taken after 2 hours (120 minutes).

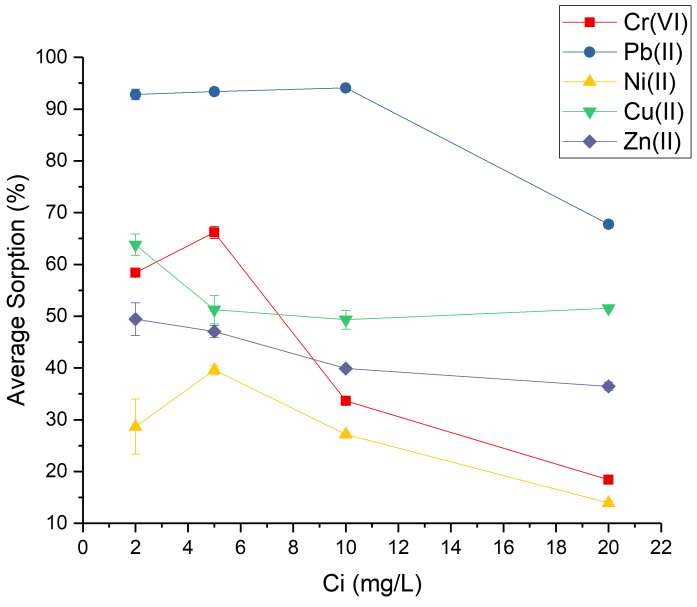

Figure 5.9: The effect of initial sorbate concentration on the adsorption capacity of chnw/EVOH composite nanofibers.

The concentration of available adsorption sites on the chnw/EVOH composite nanofibers appeared to be less compared to CTS-NF and CTS powder, causing a lower overall removal percentage of heavy metal ions. Poor sorption was seen for Zn(II) and Ni(II). As

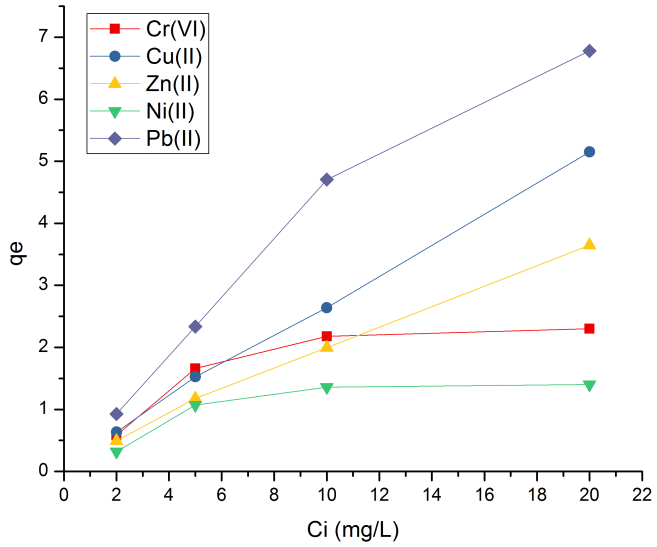

Figure 5.10: Initial sorbate concentration vs experimental adsorption capacity of chnw/EVOH composite nanofibers

the initial sorbate concentration was increased from 2 to 5 mg.L^{-1}, the adsorption capacity for Cr(VI) and Ni(II) increased while slight decrease in adsorption were seen for Zn(II) and Cu(II). The reduction in adsorption efficiency that were seen for Zn(II) and Cu(II), as the initial sorbate concentration increased, was possibly due to competition increasing between the metals for the limited adsorption sites. A good adsorption capacity was seen for Pb(II), however a significant drop in the adsorption capacity was seen for chnw/EVOH composite nanofibers as the initial Pb(II) concentration was increased from 10 to 20 mg.L^{-1} since the available sorption sites became more scarce. Cr(VI) showed a a similar decrease in sorption % as the initial Cr(VI) concentration was increased from 5 to 20 mg.L^{-1}. The same was seen for Ni(II), where the general adsorption efficiency was also much lower compared to the adsorption of the other heavy metals. This can be once again ascribed to the hydrated ion that exist in solution that formed by the nickel sulfate hepthydrate salt that the metal solutions are obtained from. The water ligands surrounding the Ni(II) can cause hindered interaction with the chnw/EVOH composite nanofibers, and since these nanofibers have less concentrated adsorption sites available on the surface it may have a greater effect on the adsorption.

As seen in Figure 5.10 the general trend shows an increasing adsorption capacity as the initial sorbate concentration increases which are the same trends seen for the other biosorbents in this study. Cr(VI) and Ni(II) shows a more gradual slope after 10 mg.L^{-1} that reaches a plateau. This may be related to a different mode of binding for these metals influenced by the speciation of Cr(VI) and the hydrated state of the Ni(II)-complex in solution. These factors for Cr(VI) and Ni(II) respectively can affect the mechanism of in-

teraction between the metal ions and the surface of the chnw/EVOH composite nanofiber [106].

5.3.2 Effect of pH

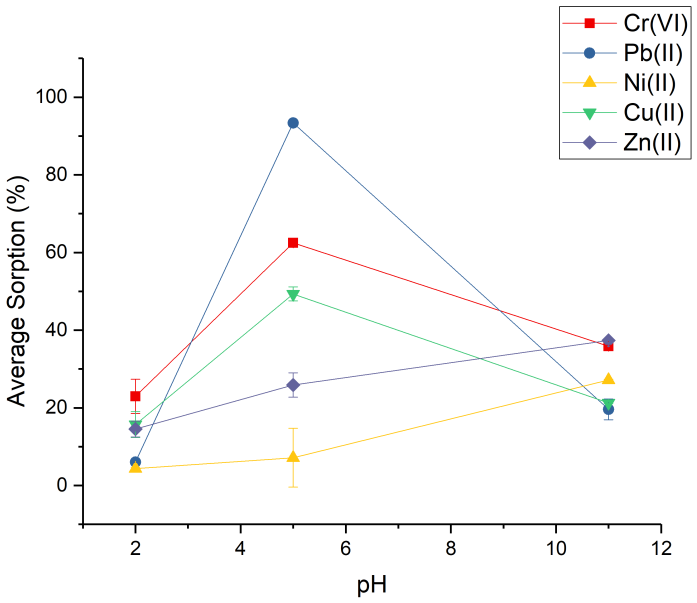

Figure 5.11: The effect of pH on the adsorption capacity of chnw/EVOH composite nanofibers.

The effect of pH on the adsorption effectiveness was investigated using a pH of 2, 5 and 11. An initial sorbate concentration of 5 mg.L^{-1} was used with a contact time of 120 minutes. The effect of pH yielded interesting results for chnw/EVOH composite nanofibers, showing similar behaviour than that seen for CTS-NF. Sorption of Ni(II) showed better removal at pH 11 than pH 5, similar to the work reported by Arshadie et al. and what was seen during the analyses of Ni(II) adsorption using CTS-NF [120]. This is a result that has also been seen by Bartczak et al. using peat in highly alkaline solutions [106]. This increase in sorption percentage can be due to a lower concentration of protons present in the solution, as discussed earlier. The same increase in sorption percentage can be seen for Zn(II) as the pH is changed for 5 to 11. This is also similar behaviour as seen for CTS-NF, although the adsorption results for chnw/EVOH composite nanofibers are slightly more diminished possibly due to the lower amount of available sorption sites on the surface of these composite nanofibers.

Chnw/EVOH composite nanofibers shows good stability in a highly acidic pH solution as seen in SEM images. Chnw/EVOH composite nanofibers does not seem to dissolve at a pH of 2 after 2 hours. The proton concentration at low pH are extremely high and causes

major competition for the available active sites on the biosorbent due to the protonation of sorption sites.

Good adsorption is seen for Pb(II), Cu(II) and Cr(VI) at pH 5 due to the good interaction in these conditions with the surface of the chnw/EVOH composite nanofibers. In a pH of 2, Cr(VI) metal ions mainly exist as neutral protonated metal species, H_2CrO_4, which limits the interaction with the surface of the sorbent. Remaining Cr(VI) ions in the form of $CrO_4{}^{-2}$ may experience competitions with H^+ in acidic solutions which also have a negative effect on the interaction between the metal ions and the sorption sites on the nanofibers at pH 2 which reduces the adsorption capacity. As the pH increases from 2 to 5 the negative charge on the surface of the chnw/EVOH composite nanofibers increases because of the reduced proton concentration. The higher pH solution causes the neutral species that exist in lower pH to become more negatively charged as deprotonation of these metal species takes place. The increased charge of these chromium sepcies allows for better electrostatic attraction with the sorption sites of the chnw [11]. However, as the pH is further increased to higher than pH 5, the protonation of the amine groups are reduced and the hydroxyl ion concentration is very high. The surface of the nanofibers are more negatively charged as the solution becomes more basic and this may lead to repulsive forces between the $CrO_4{}^{-2}$ species present at higher pH and the nanofiber surface, thus lowering the adsorption capacity of chnw/EVOH composite nanofibers for Cr(VI) in basic solutions [128]. A large reduction in adsorption capacity can be seen for Pb(II) at pH 11 probably caused by the interference of OH^- ions present in the highly alkaline medium. Another possible explanation could be that the deprotonation of the amine groups increases the hardness of these ligands and therefore the attraction between the softer Pb(II) metal ions and the amine groups can become weaker based on the HSAB principle where hard acids will attract hard bases. Relatively good adsorption is seen for Cu(II) as the pH increases from pH 2 to 5, which is also attributed to the lower proton concentration as the solution becomes less acidic. Adsorption of Cu(II) in a more basic solution also appears to become more challenging as hydroxyl ions may be interfering with the interaction of the metal ions and the sorption sites of the chnw/EVOH composite nanofibers.

Adsorption, at pH 5, yielded excellent results for Pb(II), removing 94% from the aqueous solution. Good adsorption was seen for Cr(VI), Cu(II), while Ni(II) and Zn(II) showed less effective removal that was improved as the pH increased to 11. Cr(VI) and Cu(II) removal resulted in 62.48% and 49.31% respectively at pH 5. The removal of Zn(II) and Ni(II) was 37.35% and 27.20% respectively, at pH 11.

5.3.3 Effect of contact time

Zn(II) and Ni(II) were analysed at an optimal pH of 11 while Cu(II), Pb(II) and Cr(VI) were analysed at a pH of 5. The optimal initial sorbate concentration of 5 mg.L^{-1} was used for each analysis.

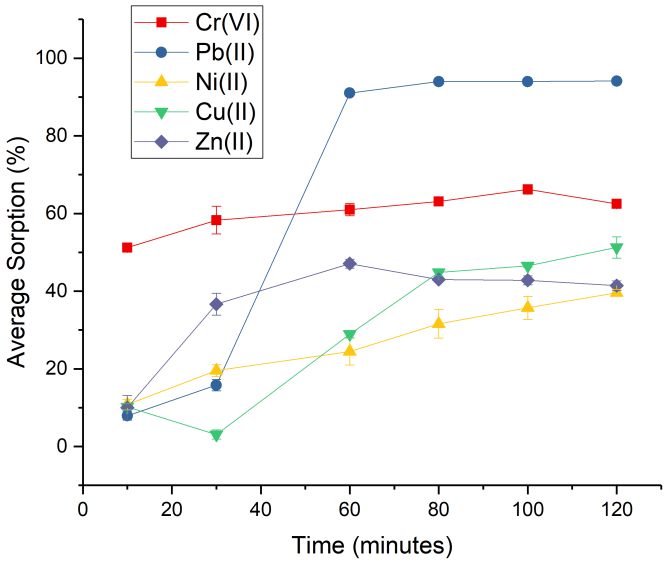

Figure 5.12: The effect of contact time on the adsorption capacity of chnw/EVOH composite nanofibers.

As the time of exposure increases between the metal ions and chnw/EVOH composite nanofibers, the adsorption percentage was increased. A plateau appears approximately after 30 to 60 minutes for most of the metals. Sorption after 120 minutes, shows a great affinity for Pb(II), followed by Cr(VI) and Cu(II) then Zn(II) and lastly Ni(II). Similar to that of CTS-NF, interaction with the surface of the chnw/EVOH composite nanofibers appears to be controlled mainly by electrostatic attraction and ion exchange as well as the number of available adsorption sites. Electron density and ion exchange may be two of the main factors that influence the interaction between the adsorption sites and the heavy metal ions. The interaction between the sorption sites and Cr(VI) seems to stabilise at 30 minutes indicating that the sorption sites may be more occupied which is also supported by the analysis of initial sorbate concentration. The adsorption capacity is listed for each initial sorbate concentration at optimal conditions for chnw/EVOH composite nanofibers in Table 5.4. Chnw/EVOH composite nanofibers shows similar adsorption rate for Cr(VI) as was seen for CTS powder, but the percentage Cr(VI) removed was higher using chnw/EVOH composite nanofibers compared to CTS powder. Chnw/EVOH composite nanofibers showed a high affinity for Pb(II) and plateaued after 60 minutes, removing 94% from the aqueous solution, which is similar to CTS-NF and 10% higher

than CTS powder. The high electron density of Pb(II) could allow for easy electrostatic interaction between the active site on the surface of the composite fibres and the lead metal ion [6].

Sorption for Ni(II) and Zn(II) are lower than for the rest of the heavy metal ions. The hydrated cations of Zn(II) and Ni(II), respectively, causes the atoms to cling to its surrounding electrons more strongly. The charge density of these cations are much lower, and therefore lowers the interaction between the adsorption sites which reduces the adsorption capacity. Chnw/EVOH composite nanofibers shows a slow sorption rate for Ni(II), which may indicate that the sorption sites are becoming more occupied. This increase in competition for available adsorption sites causes the process to slow down and have less of an incline or change over time. The adsorption capacity calculated with the experimental data is seen in Table 5.4 showing the effect of initial sorbate concentration ate the optimal pH and contact times for chnw/EVOH composite nanofibers and different heavy metal ions.

The largest amount of sorption of metal ions for chnw/EVOH composite nanofibers appeared to be after 120 minutes. It was challenging to establish an optimal pH for chnw/EVOH composite nanofibers since the behaviour of Zn(II) and Ni(II) was interesting, and showed better adsorption at higher pH. Using the general trend, an optimal pH of 11 for Zn(II) and Ni(II) was decided, and a pH of 5 for the Cu(II), Pb(II) and Cr(VI). The optimal initial sorbate concentration was 5 mg.L^{-1}. A plateau occurred after 30 - 60 minutes. Adsorption at optimal conditions for chnw/EVOH composite nanofibers yielded good results for all of the heavy metal ions used in this study with the exception of Zn(II) and Ni(II). The lower adsorption capacities for Zn(II) and Ni(II) could possibly be due to poor electrostatic attraction combined with limited adsorption sites on the surface of chnw/EVOH composite nanofibers. The highest adsorption capacity of chnw/EVOH composite nanofibers was seen for Pb(II), removing 94.09% from the aqueous solution, followed by good adsorption of Cr(VI) and Cu(II), removing 62.48% and 51.26% respectively. The removal of Zn(II) and Ni(II) was 41.40% and 39.59% respectively, at pH 11.

5.4 Evaluation of CTS/EVOH sponge as sorbent

5.4.1 Effect of initial sorbate concentration

The study of the effect of the initial sorbate concentration on the adsorption effectiveness was done in a solution with a pH of 5, at varying initial sorbate concentration of 2, 5, 10 and 20 mg.L^{-1}. The results at an optimal contact time of 120 minutes were used for the CTS/EVOH sponges. A general trend showed an increase in sorption from 2 to 5 mg.L^{-1}

Table 5.4: The experimental adsorption capacity of chnw/EVOH composite nanofibers for all initial heavy metal ion concentrations.

Heavy metal ions	$q_{e(exp)}$ (mg.g^{-1})			
	2 mg.L^{-1}	5 mg.L^{-1}	10 mg.L^{-1}	20 mg.L^{-1}
Cr(VI)	0.5838 ± 6.500 x 10^{-2}	1.655 ± 3.610 x 10^{-2}	2.180 ± 1.500 x 10^{-2}	2.300 ± 2.650 x 10^{-2}
Cu(II)	0.6350 ± 2.041 x 10^{-2}	1.525 ± 8.165 x 10^{-2}	2.638 ± 9.629 x 10^{-2}	5.150 ± 1.871 x 10^{-2}
Zn(II)	0.4943 ± 3.840 x 10^{-2}	1.177 ± 3.510 x 10^{-2}	1.995 ± 1.860 x 10^{-2}	3.647 ± 9.440 x 10^{-2}
Ni(II)	0.3183 ± 5.920 x 10^{-2}	1.065 ± 2.480 x 10^{-2}	1.358 ± 1.030 x 10^{-2}	1.393 ± 4.190 x 10^{-2}
Pb(II)	0.9282 ± 1.010 x 10^{-2}	2.334 ± 1.010 x 10^{-2}	4.705 ± 7.800 x 10^{-3}	6.777 ± 1.390 x 10^{-2}

but as the initial sorbate concentration increased to 10 mg.L^{-1}, the adsorption percentage of the CTS/EVOH sponge decreased, as shown in Figure 5.13. No effect is seen on the adsorption capacity as the initial sorbate concentration was increased further with the exception of Cu(II) and Ni(II). Interesting results are seen for the sponge in comparison to the other biosorbents in this study. CTS/EVOH sponges does show some similarities to CTS powder in terms of the heterogeneous nature of the sorbent material that influences the interaction with the metal ions. The sponge appears to have a better affinity for Ni(II) compared to CTS powder. The adsorption efficiency of the CTS/EVOH sponge decreased for Cu(II) and Ni(II) after the initial sorbate concentration was increased from 10 to 20 mg.L^{-1}. Adsorption efficiency clearly decreased as the initial sorbate concentration was increased therefore lowering the interaction between Ni(II) and CTS/EVOH sponge.

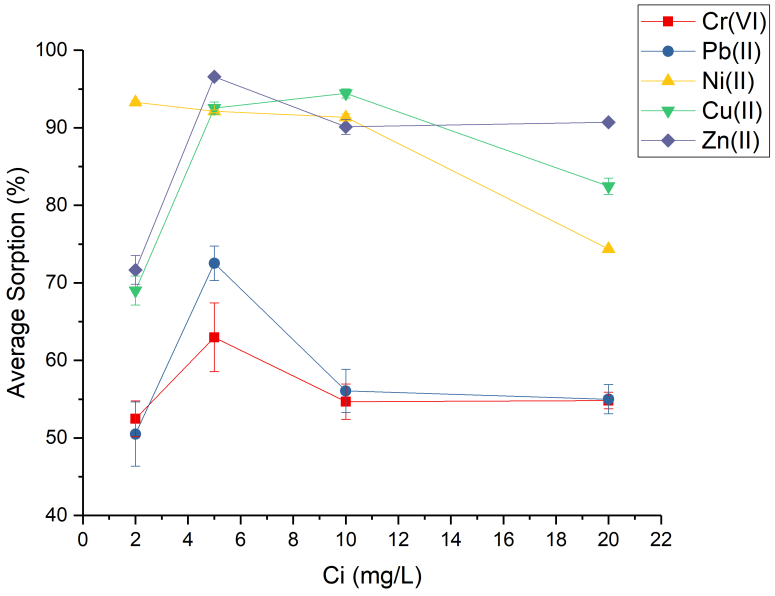

Figure 5.13: The effect of initial sorbate concentration on the adsorption capacity of CTS/EVOH sponge.

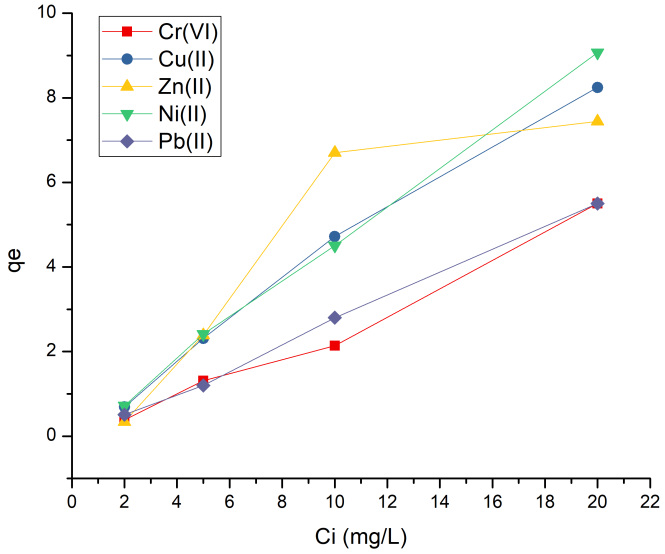

Figure 5.14: Initial sorbate concentration vs experimental adsorption capacity of CTS/EVOH sponge

The formation of a monolayer may create obstacles for the chromium metal ions to interact with the rest of the adsorption sites present inside the material. This may slow down the adsorption process and in turn affect the adsorption capacity of the CTS/EVOH sponge. The optimal initial sorbate concentration was 5 mg.L^{-1} for CTS/EVOH sponges.

Figure 5.14 shows the general trend where an increasing adsorption capacity is directly proportional to the initial sorbate concentration.

5.4.2 Effect of pH

The optimal pH conditions was in a solution with pH of 5 as seen in Figure 5.15. The CTS/EVOH sponges functioned very well in these conditions but also showed relatively good stability in more acidic conditions compared to the other chitosan materials. This could be due to the EVOH matrix that adds stability and protection to the CTS, which is also a attribute that could be observed for chnw/EVOH composite nanofibers. Sorption effectiveness increased at a pH of 5, with very good sorption seen for Cu(II), Ni(II) and Zn(II) especially. The adsorption capacities for all heavy metals were reduced significantly at a pH of 11. This may indicate the presence of competition and changes in the hydrophilicity of the EVOH matrix under these conditions. Interaction with the sorption sites that are inside the sponge centre can be affected by the change in wettability of the material which will have a major effect on the adsorption capacity. It is also interesting to note that for both heterogeneous type of sorbents, CTS powder and CTS/EVOH sponges, the metal ions do not adsorb well at pH of 11. This is not the case for the other types

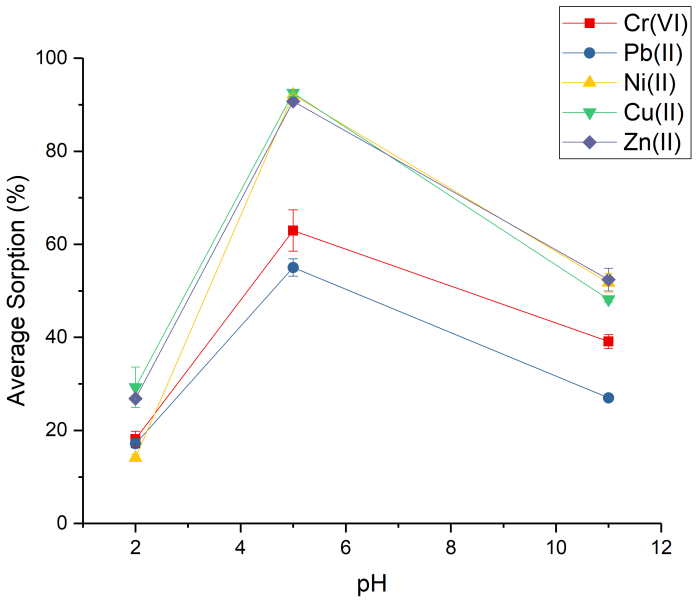

Figure 5.15: The effect of pH on the adsorption capacity of CTS/EVOH sponge.

of sorbent in this study which may lead to the assumption that the metal ions interact more readily with a homogeneous surface and tend to be less affected by hydroxylation that can cause interference with adsorption compared to a more irregular heterogeneous sorbent.

Adsorption at a pH of 5 was established to be the optimal pH for adsorption with CTS/EVOH sponges and yielded excellent results for Cu(II), Zn(II) and Ni(II) removing 92.5%, 90.7% and 92.1% from the aqueous solution. Relatively good adsorption was seen for Cr(VI), with 63.0% removal, followed by 55.0% removal for Pb(II).

5.4.3 Effect of contact time

Figure 5.16 shows the effect of contact time on the adsorption efficiency of CTS/EVOH sponge, with optimal conditions of pH 5 and initial sorbate concentration of 5 mg.L^{-1}. The general trend indicates that the increasing contact time increases the adsorption percentage.

Excellent adsorption was seen for Zn(II), Ni(II) and Cu(II) and the adsorption of Cr(VI) and Pb(II) were also relatively good at optimal conditions. Good retentivity was seen for each heavy metal even after long exposure time, especially at pH 5. It appears that the sorption sites for the CTS/EVOH sponge becomes saturated at an early stage and that the adsorption rate is very high in the initial 10 minutes of the process. The smaller the ionic radius, the greater the valence and the more closely and strongly the metal will

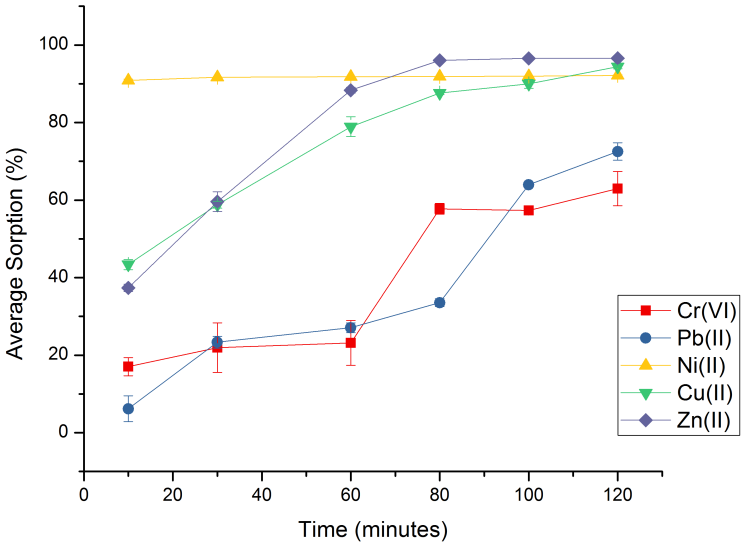

Figure 5.16: The effect of contact time on the adsorption capacity of CTS/EVOH sponge.

adsorb to the sorption sites of the sponge. It may be possible that the Ni(II) dissociates from the water ligands when migrating into the CTS/EVOH sponge where other electron donating ligands (amine groups) are abundant allowing for better adsorption. However, it may be more likely that CTS/EVOH sponges simply have more available sorption sites present on the surface as well as inside the sponge that enhances the chances for interaction and adsorption. CTS/EVOH sponges showed good affinity for Pb(II), likely due to the large electron density of this metal, but the adsorption rate was slow which could be explained by the HSAB principle for which a hard acid will prefer to interact with a hard base, whereas Pb(II) is a softer acid. Cr(VI) removal was similar to Pb(II) removal after 2 hours at optimal pH with similar adsorption rates visible in Figure 5.16. It is not quite clear why Cr(VI) adsorption is not as effective using CTS/EVOH sponges but similar low Cr(VI) adsorption was seen for CTS powder. The lower adsorption rate and capacity could be based on how quickly a monolayer formed on the surface of the sponge which might lower the rate of adsorption, since movement of chromium metal ions deeper into the sponge became more hindered. The sudden surge in the slope belonging to Cr(VI) curve for average sorption % vs time may indicate the successful migration of the ions into the sponge where adsorption was able to commence.

Sorption at optimal conditions (pH 5, 120 minutes, 5 $mg.L^{-1}$) for a CTS/EVOH sponge yielded excellent results for Zn(II), Cu(II) and Ni(II). Good adsorption was seen for Pb(VI) followed closely by Cr(VI). 96.60% of Zn(II) was removed from the aqueous solution, followed by Cu(II) and Ni(II) removal of 94.42% and 92.13% respectively. 72.53% Pb(II) and 62.80% Cr(VI) was removed. The experimental adsorption capacities obtained for CTS/EVOH sponges is shown in Table 5.5 The same trend was followed as seen for the

other biosorbents pertaining to initial sorbate concentration and the adsorption capacity of the sponge. The sorption sites on the CTS/EVOH sponge does appear to become heavily occupied with Ni(II) after 20 mg.L^{-1}. This can also be seen in the Figure 5.14 and Figure 5.16 where Ni(II) appears to plateau.

Table 5.5: The experimental adsorption capacity of the CTS/EVOH sponge for all initial heavy metal ion concentrations.

Heavy metal ions	$q_{e(exp)}$ (mg.g^{-1})			
	2 mg.L^{-1}	5 mg.L^{-1}	10 mg.L^{-1}	20 mg.L^{-1}
Cr(VI)	0.3850 ± 2.070 x 10^{-2}	1.307 ± 0.1124	2.143 ± 0.1087	5.482 ± 0.1314
Cu(II)	0.6900 ± 2.290 x 10^{-2}	2.313 ± 2.360x 10^{-2}	4.721 ± 3.590 x 10^{-2}	8.245 ± 0.1285
Zn(II)	0.7167 ± 1.841 x 10^{-3}	2.414 ± 2.460 x 10^{-3}	4.506 ± 4.857 x 10^{-2}	9.069 ± 7.170 x 10^{-3}
Ni(II)	0.3375 ± 1.200 x 10^{-3}	2.393 ± 4.800 x 10^{-3}	6.700 ± 3.340 x 10^{-2}	7.437 ± 1.030x 10^{-2}
Pb(II)	0.5050 ± 5.070 x 10^{-2}	1.197 ± 4.510 x 10^{-2}	2.803 ± 0.1710	5.500 ± 0.2291

5.5 Evaluation of CTS-NP/EVOH composite nanofibers as sorbent

5.5.1 Effect of initial sorbate concentration

The effect of the initial sorbate concentration on the sorption effectiveness was investigated for CTS-NP/EVOH composite nanofibers. The initial sorbate concentration was increased from 2 to 20 mg.L^{-1} as seen in Figure 5.17. At initial sorbate concentrations of 10 mg.L^{-1} and higher, Cr(VI) adsorption is lower than what was found for an initial Cr(VI) concentration of 5 mg.L^{-1}. The effect of the higher sorbate concentration of Cr(VI) on the adsorption efficiency is also observed for the curves belonging to the graphs fo the initial sorbate concentration effects on the sorption efficiency of chnw/EVOH composite nanofibers. The decrease in adsorption percentage can be ascribed to the occupation of the most of the adsorption sites at a higher sorbate concentration. Adsorption will therefore occur more slowly or become limited since the amount of available adsorption sites on the sorbent are less in higher sorbate concentrations. Cr(VI) adsorption does show a steep initial incline as the concentration of the metal ions are increased from 2 to 5 mg.L^{-1}, which may indicate that the optimal concentration for Cr(VI) is 5 mg.L^{-1}. At this initial metal ion concentration, Cr(VI) can interact with all available sorption sites on the CTS-NP/EVOH composite nanofibers, while monolayer formation may occur without influencing or hindering interaction between remaining metal ions in solution and sorption

sites on the surface of CTS-NP/EVOH composites nanofibers. CTS-NP/EVOH composite nanofibers shows a very good affinity for Pb(II). A decrease in sorption for Zn(II) and Pb(II) is also seen at an initial sorbate concentration of 10 mg.L^{-1} and higher similar to what is observed from the experimental data obtained for the other heavy metal ions, which supports the reasoning of the increasing competition for available sorption sites with increasing initial sorbate concentration[129].

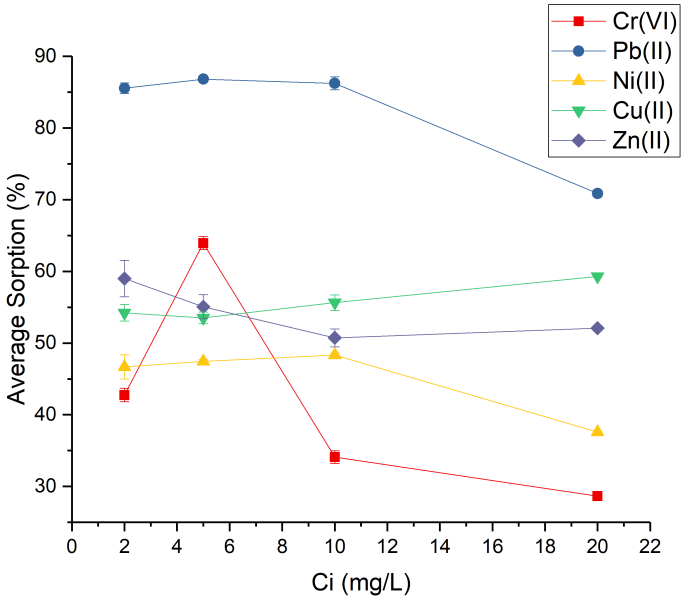

Figure 5.17: The effect of initial sorbate concentration on the adsorption capacity of CTS-NP/EVOH composite nanofibers.

Ni(II) showed a similar slope than what was seen for Pb(II) as the initial concentration was increased. Significantly lower sorption is seen for Ni(II). Ni(II) was found by Arshadi et al. to adsorb most commonly through an ion exchange mechanism [120]. If that is the case it may be the reason why Ni(II) adsorption is much lower compared to other heavy metals, with the exception of Cr(VI), since there are less adsorption sites available compared to that of CTS-NF and CTS/EVOH sponges. The CTS-NP are nanoscale and embedded in the EVOH matrix of the nanofibers which can effect the accessibility of the sorption sites especially. If the metal ion also has additional obstacles such as low electron density and a particular binding method, it can contribute even further to poor interaction with these active sites, which seemed to be the case for Ni(II). The surface of the CTS-NP/EVOH composite nanofibers are also expected to be less negatively charged due to the presence of the EVOH matrix compared to CTS-NF, which contained no additional polymer. Figure 5.18 shows the general trend for sorption capacity of CTS-NP/EVOH composite nanofibers. The heavy metal ions that are removed from the solutions does increase as the initial sorbate concentration is increased due the fact that more sorption

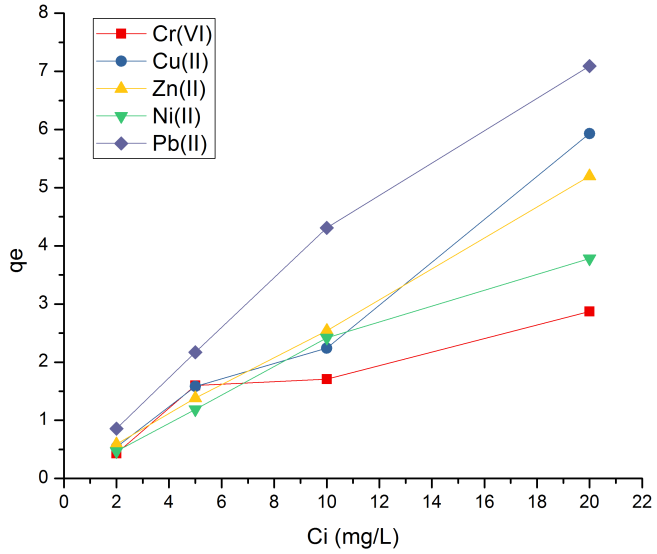

Figure 5.18: Initial sorbate concentration vs experimental adsorption capacity of CTS-NP/EVOH composite nanofibers

sites become used in the presence of more heavy metal ions even though the general trend for sorption efficiency indicated that the rate of adsorption may become effected due to competition between the sorbate and the free sorption sites on the sorbent.

5.5.2 Effect of pH

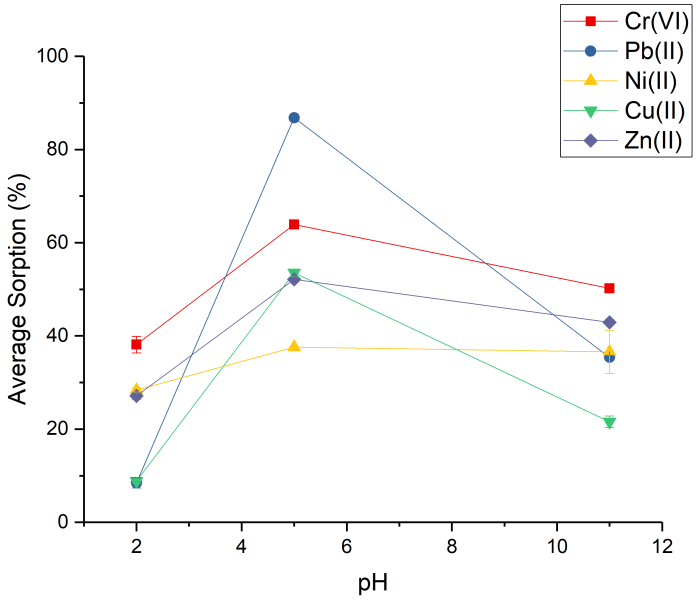

Figure 5.19: The effect of pH on the adsorption capacity of CTS-NP/EVOH composite nanofibers.

The effect of pH was investigated as seen in Figure 5.19, using a pH of 2, 5 and 11. The optimal pH was established as pH 5 for all of the heavy metals, after 120 minutes and with the optimal initial sorbate concentration of 5 mg.L^{-1}. Significant increases in adsorption were seen for Pb(II) and Cu(II), by focusing on the slope of the curves, as the pH changed from 2 to 5. A large decrease with a steep gradient was seen as the pH changed from 5 to 11 for Pb(II) and Cu(II). A less drastic increase and decrease were seen at the same point on the graph for Zn(II), Cr(VI) and Ni(II). The acidic conditions, at pH 2, has a negative effect on the adsorption capacity of CTS-NP/EVOH composites nanofibers because the CTS-NP within the fibres may have been affected. The poor sorption can also be caused by the high proton concentration present in the solution under these conditions that compete for the adsorption sites available on the surface of the nanofibers. At a pH of 5, the proton concentration is less and the surface of the nanofibers are more negatively charged, allowing for better interaction between the surface of the CTS-NP/EVOH composites nanofiber and the metal cations. At a pH of 11, hydroxide ions were present in the alkaline solution due to the excess ammonia. This hydroxide ion can compete against the sorbate for adsorption sites, thus lowering the interaction between the nanofibers and heavy metal ions. The large effect on Pb(II) and Cu(II) removal could be ascribed to the higher electron density compared to the other heavy metals, making them more susceptible to interference from other anions present in a more alkaline solution. The behaviour of Pb(II) and Cu(II) seems to be similar for chnw/EVOH composite nanofibers, CTS powder and CTS/EVOH sponge in a solution with a pH of 11. Although CTS-NF also showed a decrease in adsorption for Cu(II) and Pb(II) at a pH of 11, the affinity for these heavy metal ions caused the reduction of the sorption capacity to be relatively small.

5.5.3 Effect of contact time

Figure 5.20 shows the effect of contact time on the adsorption efficiency of CTS-NP/EVOH composite nanofibers with optimal pH of 5 and initial sorbate concentration chosen as 5 mg.L^{-1}. The general trend shows that an increase in contact time increases the sorption percentage of heavy metal ions. Apart from CTS powder, this trend seems to suit all other biosorbent in this study well. Longer exposure to the solution of heavy metal ions shows an increase in heavy metal removal for CTS-NP/EVOH composite nanofibers. The interaction between Cr(VI) and CTS-NP/EVOH composite nanofibers does not appear to increase after 30 minutes. This means that the available adsorption site had become too few and the competition too high for efficient interaction with the Cr(VI). Sorption appears to slow down for Ni(II) and Cu(II) after 30 minutes, and it is possible that the sorption sites on the CTS-NP/EVOH composite nanofibers might be starting to become hindered by a monolayer forming on the surface of the fibres after 2 hours. Sorption for Pb(II) is very good after 2 hours indicating a relatively high adsorption rate when compar-

ing the gradient to the slopes of the other heavy metal ions. CTS-NP/EVOH composite nanofibers shows good affinity for Pb(II) that may be ascribed to the electron density of Pb(II), which is a reoccurring trend seen for the more homogeneous biosorbents in this study. The surface of the CTS-NP/EVOH composite nanofibers are not porous, and the available adsorption sites are present only on the surface of the fibres, but a network of the fibres within the fibre mat creates a porous-like environment that allows the metal ions to migrate into the fibre mat to access adsorption sites. This was also seen for chnw/EVOH composite nanofibers and CTS-NF. The affinity of CTS-NP/EVOH composite nanofibers for the heavy metals are dependant on the mechanism in which the heavy metal ion reacts with the sorption sites and the chemical properties of the metal ions. The removal of Cr(VI) is higher than the final results seen for CTS powder and similar to the amount of Cr(VI) removed using CTS-NF, chnw/EVOH composite nanofibers and CTS/EVOH sponges.

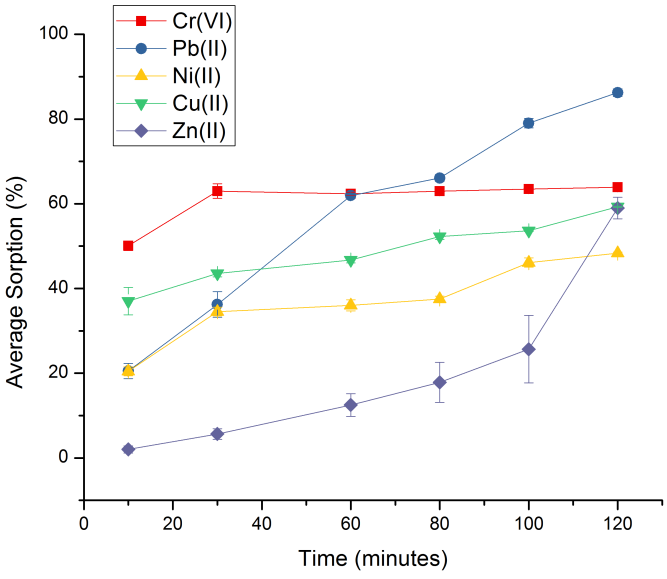

Figure 5.20: The effect of contact time on the adsorption capacity of CTS-NP/EVOH composite nanofibers.

The experimental adsorption capacities for CTS-NP/EVOH composite nanofibers is shown in Table 5.6. The same trend as for the previous biosorbents, show that the increasing contact time increases the adsorption percentage. Sorption at optimal conditions for CTS-NP/EVOH composite nanofibers yielded very good results for Pb(II), removing 86.20% after 120 minutes, at a pH of 5 and initial sorbate concentration of 5 mg.L^{-1}. Good adsorption was seen for the rest of the heavy metals showing a percentage removal of 63.93% Cr(VI), 59.31% Cu(II), 59.00% Zn(II) and 48.35% of Ni(II) after 120 minutes, in

a solution with pH of 5 and an initial sorbate concentration of 5 mg.L^{-1}.

Table 5.6: The experimental adsorption capacity of CTS-NP/EVOH composite nanofibers for all initial heavy metal ion concentrations.

Heavy metal ions	$q_{e(exp)}$ (mg.g^{-1})			
	2 mg.L^{-1}	5 mg.L^{-1}	10 mg.L^{-1}	20 mg.L^{-1}
Cr(VI)	0.4275 ± 1.146 x 10^{-2}	1.598 ± 2.754 x 10^{-2}	1.705 ± 5.408 x 10^{-2}	2.867 ± 3.014 x 10^{-2}
Cu(II)	0.5423 ± 1.420 x 10^{-2}	1.582 ± 2.930 x 10^{-2}	2.242 ± 0.2802	5.931 ± 1.700 x 10^{-2}
Zn(II)	0.5900 ± 2.550 x 10^{-2}	1.377 ± 4.190 x 10^{-2}	2.537 ± 6.249 x 10^{-2}	5.207 ± 8.500 x 10^{-3}
Ni(II)	0.4667 ± 1.700 x 10^{-2}	1.187 ± 6,000 x 10^{-3}	2.417 ± 1.320 x 10^{-2}	3.783 ± 3.010 x 10^{-2}
Pb(II)	0.8555 ± 9.100 x 10^{-3}	2.170 ± 9.000 x 10^{-3}	4.312 ± 5.480 x 10^{-2}	7.087 ± 5.510 x 10^{-2}

5.6 Desorption

The percentage sorption for each of the biosorbents are listed below in Table 5.7, 5.8, 5.11, 5.10 and 5.9. HCl, H_2SO_4, HNO_3 and EDTA, which is a multidentate chelating ligands, are all most commonly used in literature research for desorption studies. EDTA was chosen for the use in desorption studies since it did not appear to dissolve or effect the bisorbents in any visible way. EDTA is a strong chelating agent that can displace the sorbate from the biosorbent by forming a complex with the heavy metal ions. It was possible to use HCl for the desorption heavy metal ions from the biosorbents (CTS/EVOH sponges, CTS-NP/EVOH composite nanofibers, and chnw/EVOH composite nanofibers) without seeing any visible effect on the morphology. It appeared that HCl (0.01 M) displaces the heavy metals after 30 minutes from the CTS/EVOH sponge by protonating the sorption sites and reducing the charge on the surface of the sorbent and reversing the sorption process. Similar desorption results were obtained using EDTA (0.1 M) after 1 hour adn it was possible to use this more effectively on all sorbents.

Table 5.7: Percentage desorption (%) of all concentration of heavy metal ions for CTS powder.

Heavy metal ions	Percentage desorption (%)			
	2 mg.L^{-1}	5 mg.L^{-1}	10 mg.L^{-1}	20 mg.L^{-1}
Pb(II)	69.10	75.00	85.30	91.12
Cu(II)	65.2	69.07	78.00	82.30
Zn(II)	68.10	76.11	77.30	84.80
Ni(II)	71.80	75.80	80.70	89.23
Cr(VI)	68.70	74.15	81.90	84.71

The CTS/EVOH sponges, CTS-NP/EVOH-and chnw/EVOH composite nanofibers were reused 3 to 5 times before showing some deterioration. CTS-NF and CTS could be used in higher pH more than 2 times but in more acidic solutions it was limited to 1 use. In the table the percentage desorption was calculated after 1 hour,using 0.1 M EDTA, for biosorbents that adsorbed heavy metal ions in pH 5 solutions at different initial sorbate concentrations for 2 hours. The percentage desorption increased as the initial sorbate concentration increased since there were more heavy metal ions adsorbed to the sorbent. These studies were based on single measurements due to time and funding contraints

Table 5.8: Percentage desorption (%) of all concentration of heavy metal ions for CTS-NF.

Heavy metal ions	Percentage desorption (%)			
	2 mg.L^{-1}	5 mg.L^{-1}	10 mg.L^{-1}	20 mg.L^{-1}
Pb(II)	55.10	71.30	78.00	82.20
Cu(II)	61.2	74.81	82.60	88.13
Zn(II)	66.81	76.12	82.81	88.38
Ni(II)	75.10	81.27	87.43	92.05
Cr(VI)	70.87	76.70	80.48	87.10

The percentage desorption appears to correlate well to the affinity that the biosorbent have for each heavy metal ions and what was shown in the previous section. The desorption (%) of Pb(II) for CTS-NF is lower compared to the other heavy metal ions, especially Cr(VI) and Ni(II), that did not absorb as well onto CTS-NF as seen in Table 5.8.

Table 5.9: Percentage desorption (%) of all concentration of heavy metal ions for chnw/EVOH composite nanofibers.

Heavy metal ions	Percentage desorption (%)			
	2 mg.L^{-1}	5 mg.L^{-1}	10 mg.L^{-1}	20 mg.L^{-1}
Pb(II)	57.10	65.00	78.30	81.12
Cu(II)	65.20	69.73	81.00	89.30
Zn(II)	71.15	77.40	84.50	92.48
Ni(II)	72.00	79.42	85.07	93.10
Cr(VI)	64.80	71.51	80.38	87.20

The percentage desorption correlated well to the amount of sorption seen for chnw/EVOH composite nanofibers, showing an opposite behaviour. This indicates that metal ions with slightly less desorption percentage may have had more affinity for the adsorption sites on chnw/EVOH composite nanofibers. Chnw/EVOH composite nanofibers showed the best adsorption for Pb(II), similar to CTS-NF but had a lower desorption (%) for Pb(II) as seen in Table 5.9.

Table 5.10: Percentage desorption (%) of all concentration of heavy metal ions for CTS/EVOH sponges.

Heavy metal ions	Percentage desorption (%)			
	2 mg.L^{-1}	5 mg.L^{-1}	10 mg.L^{-1}	20 mg.L^{-1}
Pb(II)	65.10	75.00	88.30	91.12
Cu(II)	55.20	67.81	72.00	83.30
Zn(II)	57.80	66.24	73.69	89.74
Ni(II)	67.47	78.40	84.11	93.30
Cr(VI)	63.90	70.60	77.86	81.70

The percentage desorption correlated well to the amount of sorption seen for CTS/EVOH sponges. Copper and chromium showed a percentage of desorption that was slightly less than the other heavy metal ions, indicating a good affinity for this metal ions. Good adsorption was seen for Cu(II) as seen in Table 5.10.

Table 5.11: Percentage desorption (%) of all concentration of heavy metal ions for CTS-NP/EVOH composite nanofibers.

Heavy metal ions	Percentage desorption (%)			
	2 mg.L^{-1}	5 mg.L^{-1}	10 mg.L^{-1}	20 mg.L^{-1}
Pb(II)	66.10	72.00	81.31	90.10
Cu(II)	68.40	70.34	81.60	88.18
Zn(II)	65.80	76.20	82.91	89.20
Ni(II)	67.47	78.57	82.11	90.71
Cr(VI)	62.11	71.50	80.60	90.28

Good sorption was seen for Pb(II). CTS-NP/EVOH composite nanofibers showed good affinity for Pb(II) and Cr(VI). Chromium and lead showed a percentage of desorption that was slightly less than the other heavy metal ions, indicating a good affinity for this metal ions. Good sorption was seen for Cu(II) as seen in Table 5.11. It was possible to see this correlation between lower desorption % and good affinity for adsorption sites at lower initial sorbate concentrations.

Chapter 6

Results and discussion: Isotherms and Kinetic Models

The removal of the metal ions from the aqueous solution could be described using the parameters belonging to the two types of isotherm models, Freundlich and Langmuir. Each biosorbent were evaluated seperately for the best fit to each type of isotherm model, for the different types of heavy metals. The theoretical adsorption capacity at equilibrium will differ from that of the experimental values due to variations that occur in a real-world adsorption process that is excluded during calculations using the isotherms. The theoretical adsorption capacity was calculated for all initial sorbate concentrations of each biosorbent. The theoretical and experimental adsorption capacity for optimal pH conditions and contact time was compared which differed slightly for each biosorbent. In order to obtain consistency, the initial sorbate concentration was selected to be 5 $mg.L^{-1}$ for each biosorbent.

6.1 Langmuir and Freundlich Isotherms model

6.1.1 Evaluation of the isotherms for CTS powder

The adsorption sites are not all homogeneously distributed and equally available on the surface of the CTS powder, thus showing some correlation to Freundlich as well as Langmuir isotherm [129–131]. The isotherms for CTS powder and the different heavy metals are shown in Figure 6.1 and 6.2.

Poor linear fits were obtained with the Langmuir model for the adsorption of Cu(II) and Pb(II). Ni(II) and Cr(VI) showed very good linear fits to the Langmuir model. This indicate that adsorption occured via the formation of a monolayer for Ni(II) and Cr(VI). Ni(II) and Cr(IV) also fitted the Freundlich model very well showing the heterogeneous

nature of the CTS powder and leading to the assumption that these metal ions did not only adsorb via a monolayer formation but may have formed more than one layer while interacting with other adsorption site available on the sorbent as well as with other ions in the system [122]. This is a suitable assumption since it has been found in the previous chapter that CTS showed some loss in retention for heavy metals due to the possible formation of more than one adsorption layer as well as the low surface area and the presence of irregular dispersed sorption sites on some of the CTS powder. Pb(II) showed a better linear fit to the Freundlich model although the data still did not show a very good correlation and may therfore not well suited to describe the adsorption mechanism for Pb(II). Zn(II) adsorption showed a reasonably linear fit to Langmuir isotherm model, which was better compared to the linear fit for the Freundlich iostherm.

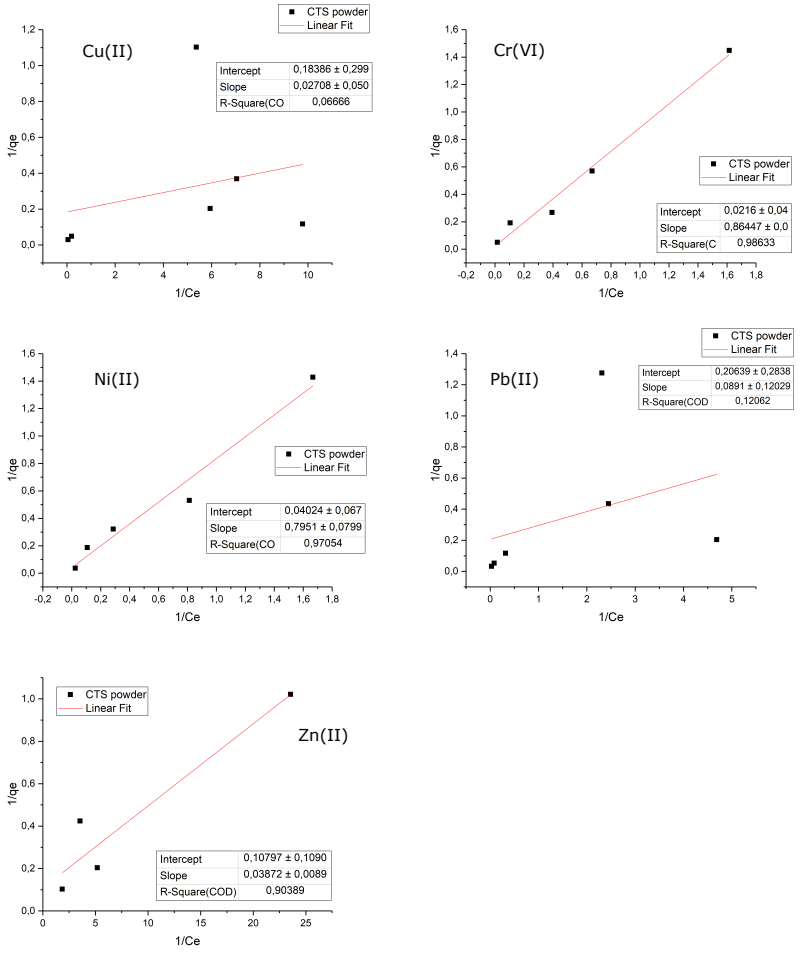

Figure 6.1: Langmuir isotherms of CTS powder for different heavy metals

The theoretical adsorption capacity ($q_{e(theo)}$) for Zn(II) adsorption using CTS powder was 4.083 mg.g^{-1} while the experimental adsorption capacity ($q_{e(exp)}$) was found to be almost half, 2.360 mg.g^{-1}. The irregular morphology of CTS powder can contribute to the poor correlation between the theoretically calculated and experimental adsorption

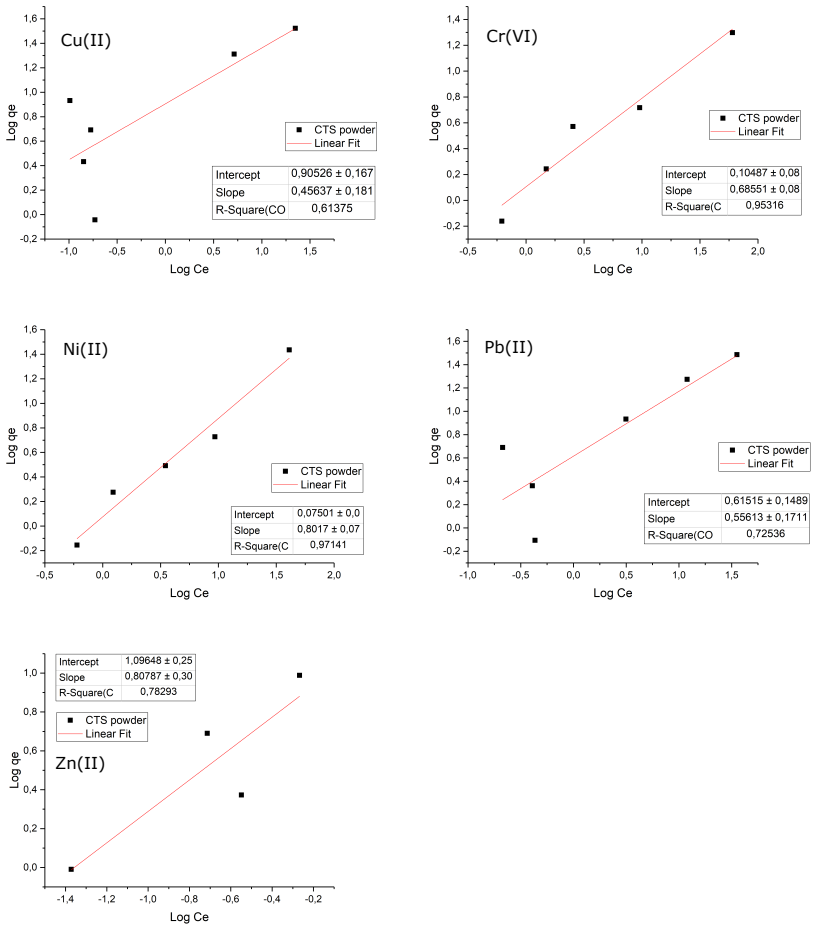

Figure 6.2: Freundlich isotherms of CTS powder for different heavy metals

capacity. The low surface area affected the availability of adsorption sites and hindered the absorbent's ability to form strong interactions with the Zn(II). The $q_{e(theo)}$ obtained from the Freundlich isotherm for Pb(II) adsorption using CTS powder was 0.8200 mg.g^{-1} while the $q_{e(exp)}$ was 2.296 mg.g^{-1}, which did not correlated well even though due to the poor linear fit obtained for each isotherm model. Adsorption occur in a stepwise manner that leads to the formation of different layers and in the case of CTS powder these additional layers are very weakly bound due to the low surface area of the sorbent and the unevenly distributed sorption sites on the surface of the CTS powder. The formation of the first layer is therefore more favourable at lower equilibrium concentrations and at higher equilibrium conditions the Langmuir plot may deviate from linearity due to the formation of more than one adsorption layer at a given equilibrium concentration [122]. The $q_{e(theo)}$ for Cr(VI) adsorption was 1.670 mg.g^{-1} which correlated well to the $q_{e(exp)}$ value of 1.750 mg.g^{-1}. The good correlation between the experimental and theoretical results corresponds to the good linear fit obtained from the Langmuir model for Cu(II) adsorption using CTS powder. It is interesting to see that the $q_{e(theo)}$ for Cu(II) adsorption was 2.669 mg.g^{-1} which correlated well to the $q_{e(exp)}$ of 2.709 mg.g^{-1} for CTS powder, considering that the linear fit was not suitable enough to show good correlation

for both isotherm models. Since Langmuir isotherm models are originally used to evaluate gas-solid adsorption, other parameters interfering during liquid-solid adsorption such as solute migration and speciation could effect the linearity of the model [132]. The $q_{e(theo)}$ for Ni(II) adsorption was 1.457 mg.g^{-1} compared to the experimental 1.880 mg.g^{-1}, which showed a good correlation between results and corresponds to the good linear fit obtained by the CTS powder for Ni(II) adsorption.

The maximum adsorption capacity (a_m) was calculated using the plot and equation described in Section 2.6.1, at optimal conditions for all biosorbents. The a_m of the CTS powder was 9.259 mg.g^{-1} for Zn(II), 5.440 mg.g^{-1} Cu(II), 46.30 mg.g^{-1} for Cr(VI), 4.850 mg.g^{-1} for Pb(II) and 24.88 mg.g^{-1} for Ni(II). This means that although Cu(II) could not be properly described by the isotherm models it did show the highest adsorption and the theoretical and experimental results correlated very well, with the closest fit obtained form Lanmguir indicating the favoured monolayer formation.

6.1.2 Evaluation of the isotherms for CTS-NF

The adsorption process for the different metal ions could all be adequately described using Langmuir as well as Freundlich isotherm models. This means that both models describes the same set of liquid-solid adsorption data at certain concentrations ranges. This is most often possible when the concentration of the sorbate is low and the adsorption capacity of the sorbent is high enough to make both isotherm equations approach a linear form [132]. Ni(II) adsorption was the only process that would not have been suitably described as a combination of Langmuir and Freundlich due to the bad linear fit for Freundlich. This means that Ni(II) favoured adsorption to the CTS-NF surface by forming a monolayer. The CTS-NF are much more homogeneous and therefore have better reproducibility. The isotherms for CTS-NF and the different heavy metals are shown in Figure 6.3 and 6.4.

The $q_{e(theo)}$ for Cu(II) adsorption using CTS-NF was 1.460 mg.g^{-1} while the $q_{e(exp)}$ was correlated well at 1.862 mg.g^{-1}. The $q_{e(theo)}$ for Pb(II) adsorption was 1.880 mg.g^{-1} which correlate slightly with $q_{e(exp)}$ at 2.140 mg.g^{-1}. The $q_{e(theo)}$ for Cr(VI) adsorption was 1.330 mg.g^{-1} while the $q_{e(exp)}$ was 1.690 mg.g^{-1}, showing a more acceptable fit. The $q_{e(theo)}$ for Ni(II) adsorption was 0.8900 mg.g^{-1} which was closely correlated to the experimental result of 0.9040 mg.g^{-1} confirming that the Langmuir model is a better fit for the evaluation of Ni(II) adsorption. The $q_{e(theo)}$ of Zn(II) adsorption was 2.110 mg.g^{-1} which compared well with 2.280 mg.g^{-1} that was obtained from the experimental results. In general, the correlation for all experimental and theoretical data correlated well enough. All the heavy metal adsorption processes could be described by both isotherms due to the good linear fit obtained for both models. The adsorption mechanism for these different

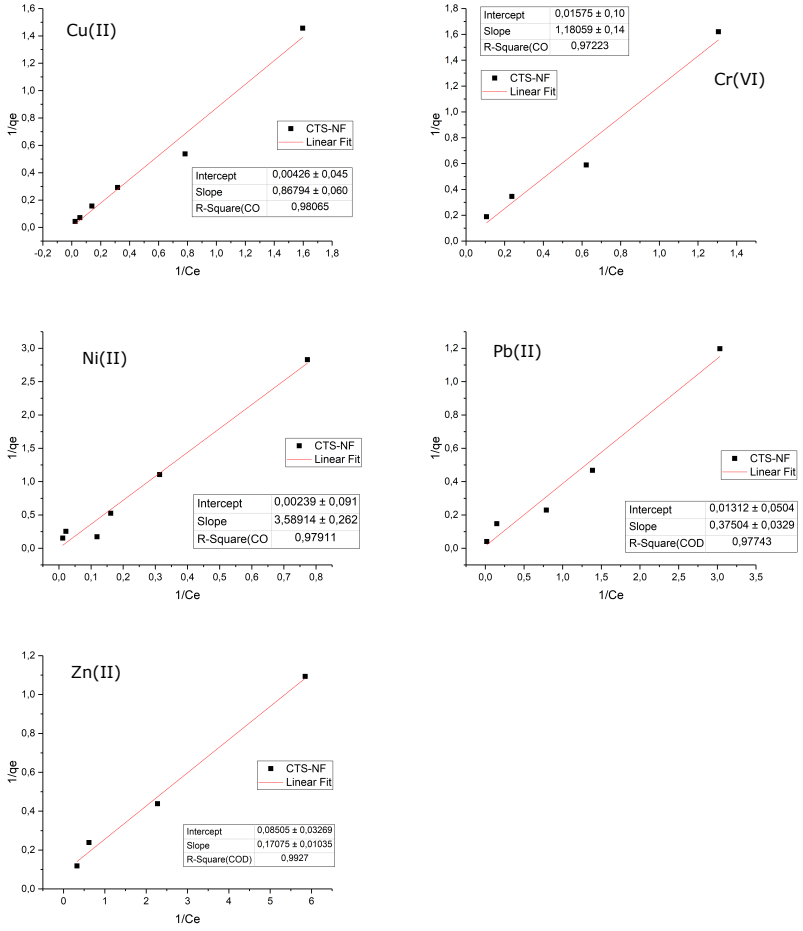

Figure 6.3: Langmuir isotherms of CTS-NF for different heavy metals.

types of metal ions can therefore be described as a combination of both models.

The a_m obtained for CTS-NF was 11.75 mg.g^{-1} Zn(II), 416.7 mg.g^{-1} Ni(II), 76.34 mg.g^{-1} Pb(II), 232.6 mg.g^{-1} Cu(II) and 63.69 mg.g^{-1} Cr(VI). CTS-NF showed significant adsorption capacity for Ni(II) and Cu(II). CTS-NF also had a higher maximum adsorption for all the heavy metals compared to CTS powder.

6.1.3 Evaluation of the isotherms for chnw/EVOH composite nanofibers

Although the linear fit of the chnw/EVOH composite nanofibers for the different metal ions appeared to suit the Langmuir model better, the linearity is not as great compared to what was seen for CTS-NF. If a variety of adsorption sites are present on the surface of the sorbent the linear fit to the Langmuir model will not be perfect. The Langmuir isotherm assumes monolayer coverage on a homogeneous surface with identical adsorption site participating with the metal ions during adsorption. The general adsorption mechanism that

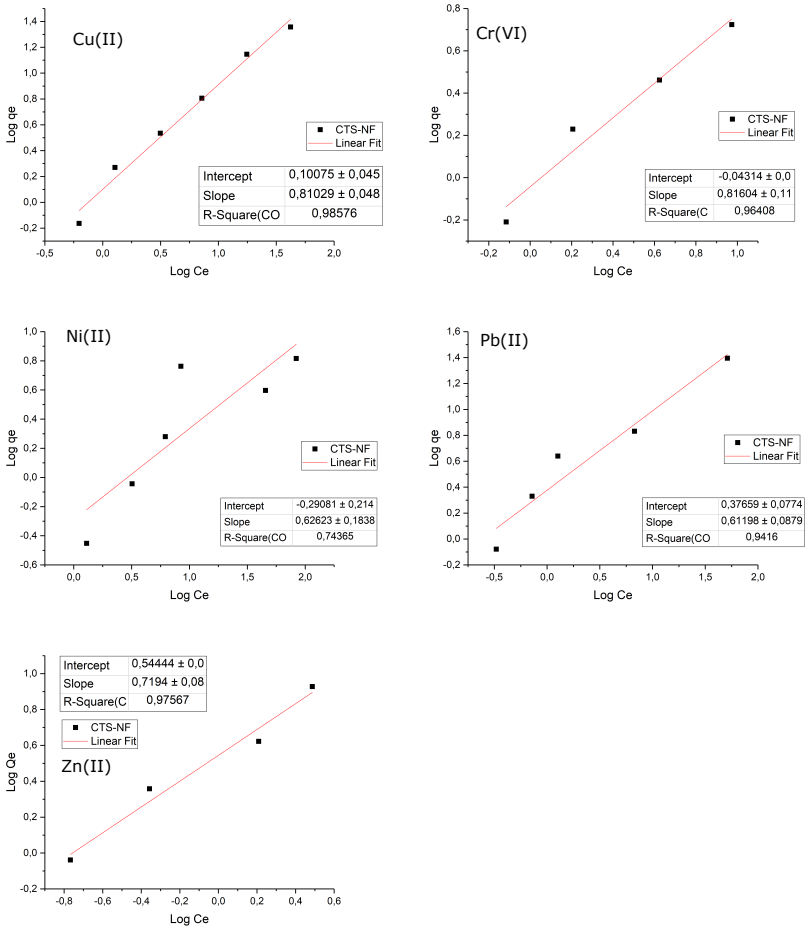

Figure 6.4: Freundlich isotherms of CTS-NF for different heavy metals

suitably described adsorption for all metals using chnw/EVOH composite nanpfibers is based on the Langmuir model. This means that metal adsorption occured predominantly via monolayer formation. The fluctuations in the data correlation does indicate that this was not the only mechanism that was used and that the surface of the chnw/EVOH composite nanofibers consisted of more than one adsorption site that may have influenced the adsorption process for some of the metal ions. The isotherms for CTS-NF and the different heavy metals are shown in Figure 6.5 and 6.6.

The $q_{e(theo)}$ of the chnw/EVOH composite nanofibers for Zn(II) adsorption was 1.157 mg.g^{-1} and the $q_{e(exp)}$ was 1.177 mg.g^{-1}. These two results correlated very well helping to confirm that the Langmuir model was more suitable for the description of the Zn(II) adsorption process using chnw/EVOH composite nanofibers even though the data also showed a good liner fit to the Freundlich isotherm. The $q_{e(theo)}$ for Ni(II) adsorption was 0.7460 mg.g^{-1} while the $q_{e(exp)}$ was 1.070 mg.g^{-1}. This was a slightly poorer correlation, that corresponds well enough to the slightly poorer linear fit on the Lanmguir plot compared to the other heavy metals. Ni(II) adsorption can still be better described using the Langmuir model rather than the Freundlich model. The $q_{e(theo)}$ for Cu(II) removal was

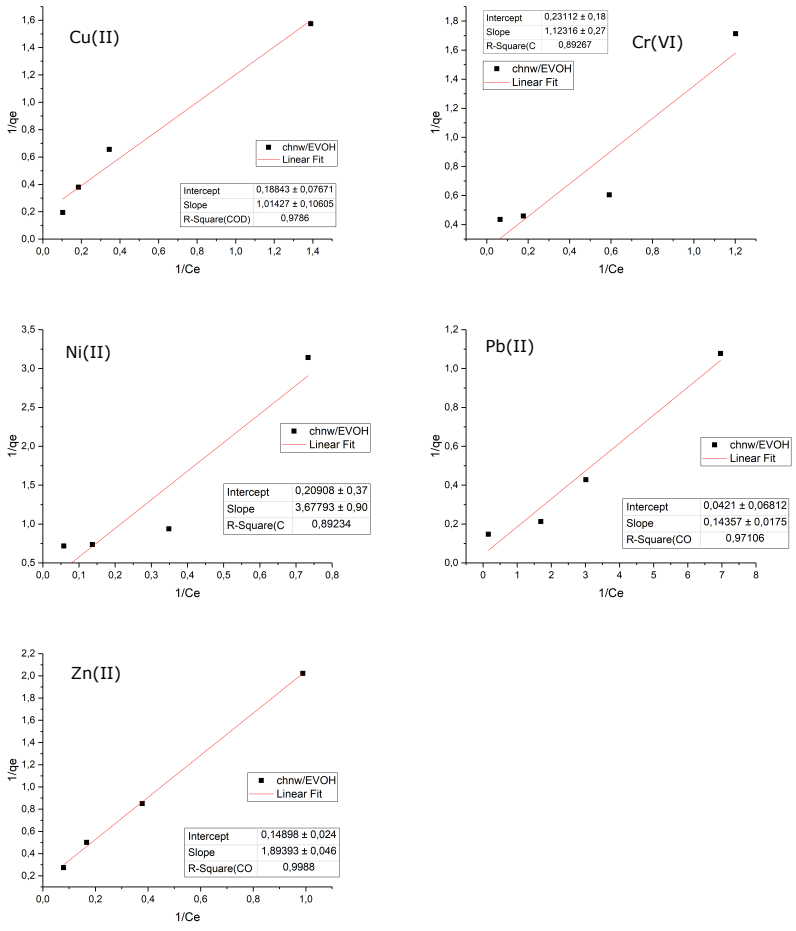

Figure 6.5: Langmuir isotherms of chnw/EVOH composite nanofibers for different heavy metals.

1.858 mg.g^{-1} and this correlated well enough to the $q_{e(exp)}$ of 1.525 mg.g^{-1}. The $q_{e(theo)}$ for Pb(II) adsorption was 2.110 mg.g^{-1} while the $q_{e(exp)}$ was 2.334 mg.g^{-1}, which agreed well. The good correlation between the experimental and theoretical data is supported by the good linearity of the Langmuir plots for Pb(II) and Cu(II). The $q_{e(theo)}$ for the adsorption of Cr(VI) was 1.117 mg.g^{-1} which agreed well with the experimental result of 1.660 mg.g^{-1}.

The a_m for the different metal ions were 6.711 mg.g^{-1} Zn(II), 4.782 mg.g^{-1} Ni(II), 5.308 mg.g^{-1} Cu(II), 23.75 mg.g^{-1} Pb(II) and 4.327 mg.g^{-1} Cr(VI), for the chnw/EVOH composite nanofibers. Chnw/EVOH composite nanofibers showed the largest maximum adsorption capacity for Pb(II) which exceeded the amount that was obtained by CTS powder for Pb(II) adsorption.

6.1.4 Evaluation of the isotherms for CTS/EVOH sponges

The first important thing to note when looking at the Figures 6.7 and 6.8 was that the linear fits for Zn(II) and Cu(II) were poor for both the Langmuir and Freundlich isotherm models. These results are similar to the results obtained for CTS powder. Although the

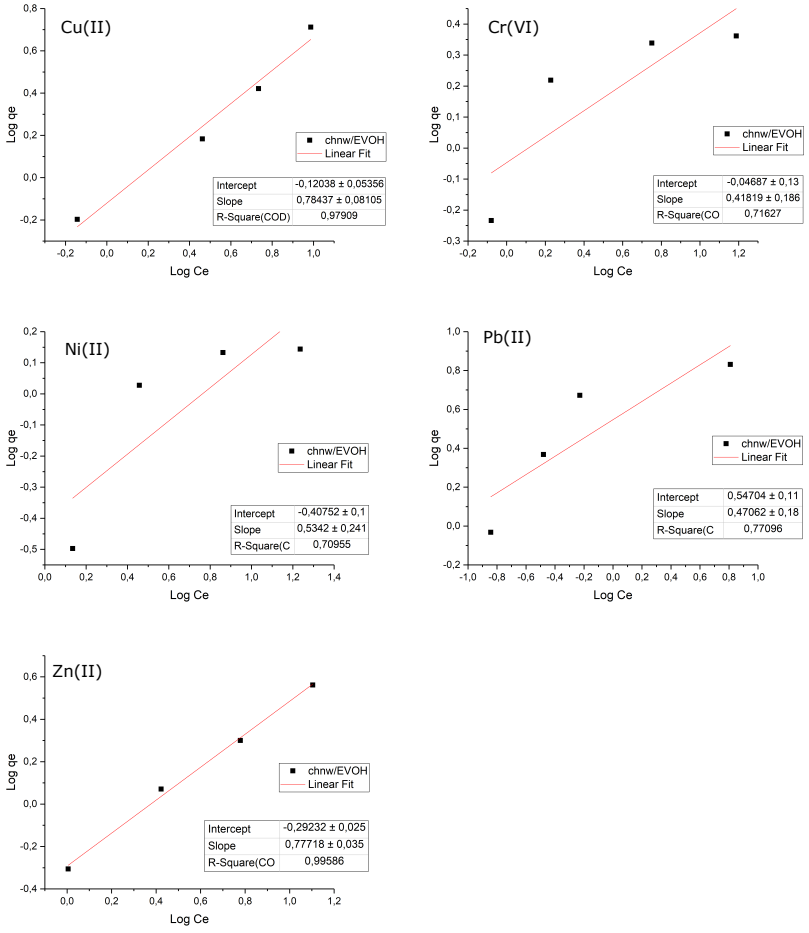

Figure 6.6: Freundlich isotherms of chnw/EVOH composite nanofibers for different heavy metals.

adsorption for Zn(II) and Cu(II) was high when using CTS/EVOH sponges, it is clear that the mechanism of adsorption was not straightforward possibly because of the heterogeneous nature of the CTS powder that is incorporated into the material and non-uniform dispersion of adsorption sites. CTS/EVOH sponges also have a variety of pores with different sizes and shapes that are distributed in a disarranged fashion across the surface of the sponge. The Freundlich isotherm describes the adsorption mechanism to occur on a heterogeneous surface as a multilayer adsorption with an energetic non-uniform distribution of active sites. Since this is only part of the description for the surface of the CTS/EVOH sponges, it may be expected that the linearity for the Freundlich isotherm will also be imperfect [133]. Good linearity was seen for Cr(VI), Ni(II) and Pb(II) for both the Langmuir and Freundlich model.

The $q_{e(theo)}$ of CTS/EVOH, obtained using Freundlich isotherm for Zn(II) adsorption was 3.377 mg.g^{-1} which was not so well correlated to the $q_{e(exp)}$ of 4.510 mg.g^{-1}. For Ni(II) adsorption, the $q_{e(theo)}$ was 2.330 mg.g^{-1} with the $q_{e(exp)}$ closely correlated at 2.390 mg.g^{-1}. The $q_{e(theo)}$ for Cu(II) removal was 1.437 mg.g^{-1} and the $q_{e(exp)}$ was 2.313 mg.g^{-1}

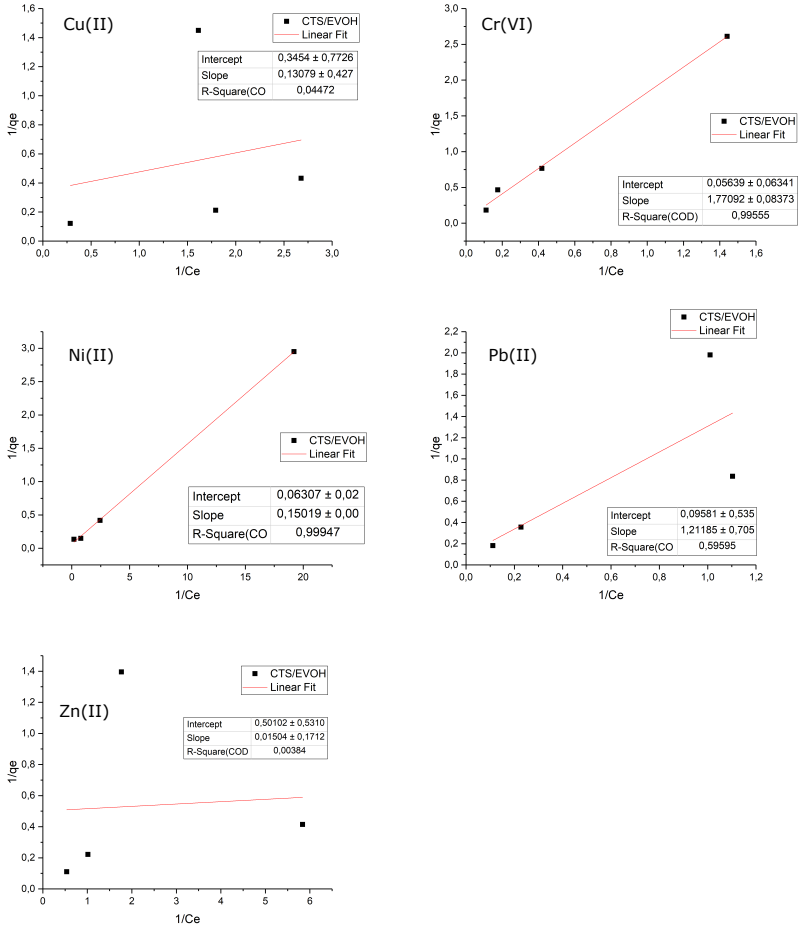

Figure 6.7: Langmuir isotherms of CTS/EVOH sponges for different heavy metals.

which was slightly higher and therefore not such a good fit to the experimental data as expected when comparing the results to the poor linear fit on both isotherm models. The $q_{e(theo)}$ for Pb(II) adsorption was 0.7290 mg.g^{-1} while the $q_{e(exp)}$ was at 1.197 mg.g^{-1}. This is not the best fit but still show some reasonably acceptable correlation. Cr(VI) adsorption showed a $q_{e(theo)}$ of 0.8290 mg.g^{-1} while the $q_{e(exp)}$ was at 1.310 mg.g^{-1} which is also not the most acceptable fit.

The a_m for CTS/EVOH sponges was 1.996 mg.g^{-1} Zn(II), 15.85 mg.g^{-1} Ni(II), 2.895 mg.g^{-1} Cu(II), 10.440 mg.g^{-1} Pb(II), 17.70 mg.g^{-1} Cr(VI). CTS/EVOH sponge showed the largest maximum adsorption for Cr(VI). The maximum adsorption capacity for Pb(II) obtained using CTS/EVOH sponges exceeded that of CTS powder by almost doubled the amount.

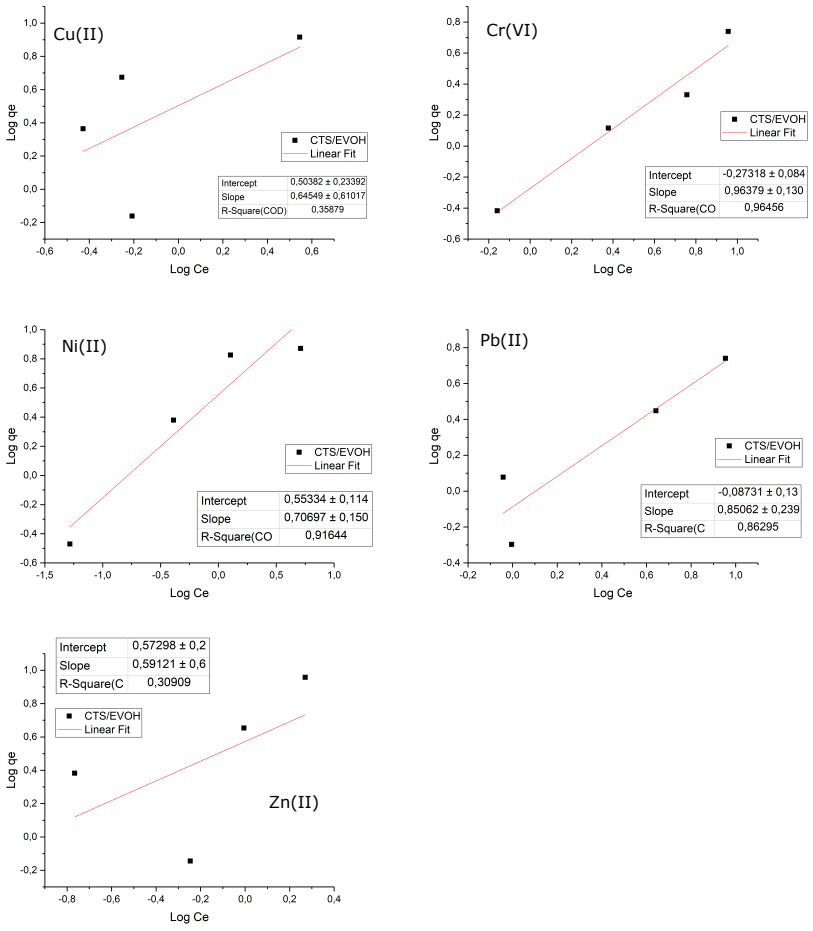

Figure 6.8: Freundlich isotherms of CTS/EVOH sponges for different heavy metals.

6.1.5 Evaluation of the isotherms for CTS-NP/EVOH composite nanofibers

Zn(II) and Cu(II) showed poor linear fits to the Langmuir isotherm model for CTS-NP/EVOH composite nanofibers which was similar to what was seen for CTS/EVOH sponges. The difference between the results seen for CTS/EVOH spones and the CTS-NP/EVOH composite nanofibers are that the Zn(II) and Cu(II) showed reasonable linear fits to the Freundlich isotherm model. Cr(VI), Ni(II) and Pb(II) showed good linear fits to the Langmuir isotherm whereas all metals showed a good linearity for the Freundlich plots. The Freundlich isotherm therefore described all the types of metal adsorption for the CTS-NP/EVOH composite nanofibers the best. This means that monolayer adsorption may have occured but not as predominantly and that some of the reaction that took place involved the interaction with other available sorption sites, as well as interaction between the metal ions. Cr(VI) shows a better linear fit to Langmuir and is therefore expected to behave more than what was seen for CTS-NF, therefore favouring monolayer formation as the dominant adsorption mechanism. The Figure 6.9 and 6.10 shows the isotherms for CTS-NP/EVOH composite nanofibers and the different heavy metals.

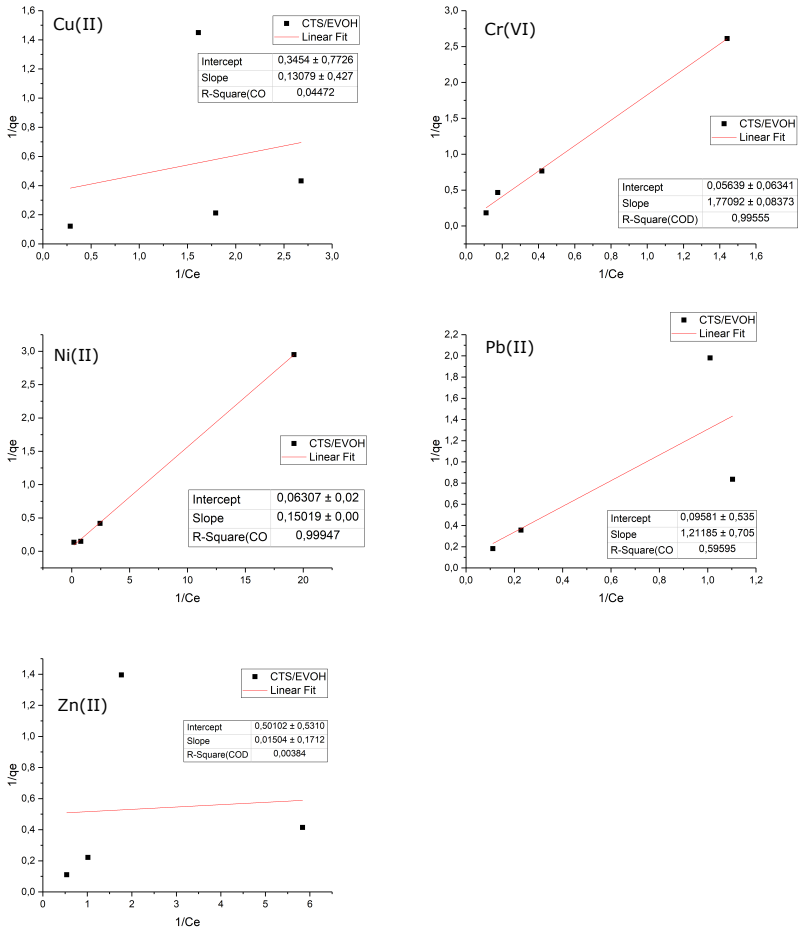

Figure 6.9: Langmuir isotherms of CTS-NP/EVOH sponges for different heavy metals.

The Zn(II) adsorption showed a $q_{e(theo)}$ for CTS-NP/EVOH composite nanofibers of 1.452 $mg.g^{-1}$ while the $q_{e(exp)}$ was closely correlated at 1.380 $mg.g^{-1}$.The $q_{e(theo)}$ for Ni(II) adsorption was 1.140 $mg.g^{-1}$, while the $q_{e(exp)}$ was closely correlated at 1.187 $mg.g^{-1}$. The $q_{e(theo)}$ for Cu(II) adsorption was 1.592 $mg.g^{-1}$ and the $q_{e(exp)}$ was closely correlated at 1.582 $mg.g^{-1}$. Pb(II) adsorption showed a $q_{e(theo)}$ of 1.940 $mg.g^{-1}$ which was closely correlated to the experimental result of 2.170 $mg.g^{-1}$. The $q_{e(theo)}$ for Cr(VI) removal was 0.7800 $mg.g^{-1}$, which was not very close to the experimental result of 1.600 $mg.g^{-1}$.

CTS-NP/EVOH composite nanofibers showed a a_m of 9.728 $mg.g^{-1}$ for Zn(II), 42.19 $mg.g^{-1}$ for Ni(II), 71.43 $mg.g^{-1}$ for Cu(II), 35.34 $mg.g^{-1}$ for Pb(II) and 10.89 $mg.g^{-1}$ Cr(VI). The a_m for Cr(VI) is lower than that for CTS/EVOH sponges, however CTS-NP/EVOH composite nanofibers showed a larger maximum adsorption capacity for lead compard to CTS powder and CTS/EVOH sponges, followed closely by chnw/EVOH composite nanofibers. CTS-NP/EVOH composite nanofibers also exceed CTS powder and

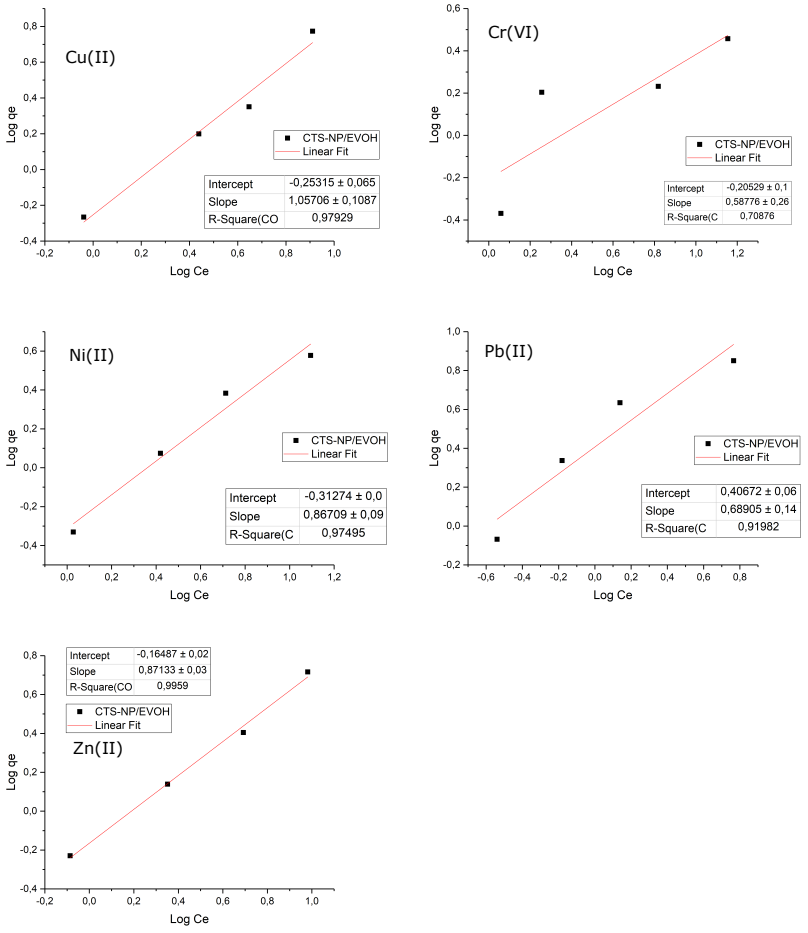

Figure 6.10: Freundlich isotherms of CTS-NP/EVOH sponges for different heavy metals.

CTS/EVOH sponges for the maximum adsorption of copper and nickel as well as zinc.

6.1.6 Evaluation of the Langmuir and Freundlich isotherms constants for each biosorbent

The separation factor of the Langmuir isotherm, R_L, for all biosorbents were between 0 and 1 and the adsorption processes were considered as favourable and normal. The mechanism of adsorption could be described either by ion exchange, electrostatic interaction or complexation. The b value of the Langmuir isotherm determines the affinity between the sorbent and the heavy metal. The larger the b value, the higher the affinity of the heavy metal ion for the adsorption sites of the biosorbents. K_F values for the Freundlich istoherms has similar meaning to the Langmuir value, b. High K_F values for the Freundlich isotherm model indicate greater affinity between the biosorbent and the heavy metal [77]. The highest K_F value for Zn(II) adsorption was obtained using CTS powder. This indicated that CTS powder showed the best affinity for zinc compared to the other biosorbents. It is interesting to note that based on the experimental results

in Table 6.1, the K_F or b values cannot be used to assume which sorbent will adsorb better.

Table 6.1: Langmuir and Freundlich isotherms constants and parameters of zinc removal for all biosorbents.

Adsorbent	Langmuir					
	$q_{e(theo)}$	R^2	a_m	b	R_L	Equation of q_e
CTS	4.08 ± 1.66	0.90	9.26	2.79	0.07	q_e=1/[(0,04)x(1/C_e)+(0,11)]
CTS-NF	2.11 ± 2.46	0.99	11.8	0.50	0.29	q_e = 1/[(0,17)x(1/C_e)+(0,09)]
chnw/EVOH	1.16 ± 1.08	0.10	6.71	0.08	0.72	q_e = 1/[(1,89)x(1/C_e)+(0,15)]
CTS-NP/EVOH	1.45 ± 1.35	1.00	9.73	0.08	0.72	q_e = 1/[(1,32)x(1/C_e)+(0,10)]
CTS/EVOH	1.94 ± 0.10	0.01	2.00	33.4	0.01	q_e = 1/[(0,02)x(1/C_e)+(0,50)]
	Freundlich					
	$q_{e(theo)}$	R^2	n	K_F		Equation of q_e
CTS	2.61 ± 2.06	0.78	1.24	12.5		q_e = 12,5 $C_e^{1,24}$
CTS-NF	1.12 ± 6.52	0.98	1.39	3.50		q_e = 3,50 $C_e^{1,39}$
chnw/EVOH	1.79 ± 5.035	1.00	1.29	0.51		q_e = 0,51 $C_e^{1,29}$
CTS-NP/EVOH	1.73 ± 3.31	1.00	1.15	0.68		q_e = 0,68 $C_e^{1,15}$
CTS/EVOH	3.38 ± 4.08	0.31	1.69	3.74		q_e = 3,74 $C_e^{1,69}$

The affinity for Ni(II) appeared to be low in general with the exception of the CTS/EVOH sponges followed by CTS powder when looking at the theoretical results for Freundlich and also how the theoretical adsorption capacities compared to the experimental results. CTS-NF shows good affinity ranking third, but it may be that the nanofibers prevents the Ni(II) from binding as closely to the sorption sites. It seems that the Ni(II) interacted better with CTS in less modified forms such as CTS powder or CTS powder in the EVOH matrix as a sponge. CTS powder and CTS/EVOH sponges also correlated well to both Langmuir and Freundlich isotherm models whereas CTS-NF correlated better to Langmuir isotherm model only supporting the idea that CTS-NF limits interaction for Ni(II) with adsorption only taking place through monolayer formation. The maximum adsorption capacity for Ni(II) can be obtained by using CTS-NF, however, followed by CTS-NP/EVOH composite nanofibers which means that these modifications are beneficial to contributing to the adsoption capacity.

Cu(II) show good affinity to CTS powder based on both the Langmuir and Freundlich values, b and K_F. It is interesting to see how the affinity between the metal ion and sorbent changes as the sorbent is physically modified. There is no general trend that can be concluded but there is a definite decrease in b and K_F as the sorbent is modified. CTS shows the highest affinity based on both Langmuir and Freundlich isotherm data for Pb(II) as well. CTS did, however, show poor correlation to the Freundlich and Langmuir models for both these metals, which was also the case for CTS/EVOH sponge. The other bisorbents showed better correlation to both models for Pb(II) and Cu(II) which

Table 6.2: Langmuir and Freundlich isotherms constants and parameters of nickel removal for all biosorbents.

Adsorbent	Langmuir					
	$q_{e(theo)}$	R^2	a_m	b	R_L	Equation of $q_{e(theo)}$
CTS	1.46 ± 1.06	0.97	24.9	0.05	0.80	$q_e = 1/[(0{,}80)x(1/C_e)+(0{,}04)]$
CTS-NF	0.89 ± 0.73	0.98	416.7	0.001	1.00	$q_e = 1/[(3{,}60)x(1/C_e)+(0{,}002)]$
chnw/EVOH	0.75 ± 0.75	0.89	4.80	0.06	0.78	$q_e = 1/[(3{,}68)x(1/C_e)+(0{,}21)]$
CTS-NP/EVOH	1.14 ± 1.69	1.00	42.2	0.011	0.95	$q_e = 1/[(2{,}24)x(1/C_e)+(0{,}02)]$
CTS/EVOH	2.33 ± 3.96	1.00	15.9	0.42	0.32	$q_e = 1/[(0{,}15)x(1/C_e)+(0{,}06)]$
	Freundlich					
	$q_{e(theo)}$	R^2	n	K_F		Equation of q_e
CTS	1.67 ± 2.42	0.97	1.43	1.24		$q_e = 0{,}512\ C_e^{1,60}$
CTS-NF	3.27 ± 5.54	0.74	1.60	0.52		$q_e = 3{,}50\ C_e^{1,39}$
chnw/EVOH	3.55 ± 32.4	0.71	1.87	0.39		$q_e = 0{,}39\ C_e^{1,87}$
CTS-NP/EVOH	1.48 ± 3.25	0.98	1.15	0.49		$q_e = 0{,}49\ C_e^{1,15}$
CTS/EVOH	1.01 ± 14.9	0.92	1.41	3.58		$q_e = 3{,}58\ C_e^{1,41}$

indicate that these b and K_F values are more reliable and accuarate compared to that for CTS/EVOH sponges and CTS powder.

Table 6.3: Langmuir and Freundlich isotherms constants and parameters of copper removal for all biosorbents.

Adsorbent	Langmuir					
	$q_{e(theo)}$	R^2	a_m	b	R_L	Equation of $q_{e(theo)}$
CTS	2.67 ± 0.31	0.07	5.44	6.79	0.03	$q_e = 1/[(0{,}03)x(1/C_e)+(0{,}18)]$
CTS-NF	1.46 ± 2.84	0.98	232	0.01	0.98	$q_e = 1/[(0{,}87)x(1/C_e)+(0{,}004)]$
chnw/EVOH	1.86 ± 1.03	0.98	5.31	0.19	0.52	$q_e = 1/[(1{,}02)x(1/C_e)+(0{,}19)]$
CTS-NP/EVOH	1.59 ± 1.47	1.00	71.4	0.008	0.96	$q_e = 1/[(1{,}69)x(1/C_e)+(0{,}01)]$
CTS/EVOH	1.44 ± 0.44	0.045	2.90	2.64	0.07	$q_e = 1/[(0{,}13)x(1/C_e)+(0{,}35)]$
	Freundlich					
	$q_{e(theo)}$	R^2	n	K_F		Equation of q_e
CTS	0.11 ± 0.056	0.61	2.19	8.04		$q_e = 8{,}04\ C_e^{2,19}$
CTS-NF	1.70 ± 5.41	0.99	1.23	1.26		$q_e = 1{,}26\ C_e^{1,23}$
chnw/EVOH	2.95 ± 4.99	0.98	1.28	0.76		$q_e = 0{,}76\ C_e^{1,28}$
CTS-NP/EVOH	1.46 ± 1.30	0.98	0.95	0.56		$q_e = 0{,}56\ C_e^{0,95}$
CTS/EVOH	0.69 ± 9.17	0.36	1.55	3.190		$q_e = 3{,}19007\ C_e^{1,550}$

CTS-NF showed good affinity for Cr(VI) based on the data from the Freundlich isotherm which was just below CTS powder. Good correlation and linearity was seen for all the biosorbents for Cr(VI) adsorption with the exception of CTS-NP/EVOH-and chnw/EVOH composite nanofibers that showed a slightly lower correlation coefficient for each isotherm model. CTS-NF did have the largest maximum adsorption capacity for Cr(VI) removal followed closely by CTS powder. Since chromium exists in different forms witing solutions

Table 6.4: Langmuir and Freundlich isotherms constants and parameters of lead removal for all biosorbents.

Adsorbent	Langmuir					
	$q_{e(theo)}$	R^2	a_m	b	R_L	Equation of $q_{e(theo)}$
CTS	0.08 ± 0.02	0.12	4.85	2.32	0.08	$q_e = 1/[(1{,}71)x(1/C_e)+(8{,}29)]$
CTS-NF	1.88 ± 5.50	0.98	76.3	0.04	0.85	$q_e = 1/[(0{,}36)x(1/C_e)+(0{,}013)]$
chnw/EVOH	2.11 ± 5.85	0.97	23.8	0.29	0.41	$q_e = 1/[(0{,}14)x(1/C_e)+(0{,}04)]$
CTS-NP/EVOH	1.94 ± 1.51	0.99	35.3	0.09	0.70	$q_e = 1/[(0{,}32)x(1/C_e)+(0{,}03)]$
CTS/EVOH	0.70 ± 4.36	0.60	10.44	0.08	0.72	$q_e = 1/[(1{,}21)x(1/C_e)+(0{,}10)]$
	Freundlich					
	$q_{e(theo)}$	R^2	n	K_F		Equation of q_e
CTS	0.82 ± 0.38	0.73	1.80	4.12		$q_e = 4{,}12\ C_e^{1,80}$
CTS-NF	1.40 ± 22.6	0.942	1.63	2.38		$q_e = 2{,}38\ C_e^{1,63}$
chnw/EVOH	0.34 ± 79.8	0.77	2.13	3.52		$q_e = 3{,}52\ C_e^{2,13}$
CTS-NP/EVOH	1.26 ± 13.5	0.92	1.45	2.55		$q_e = 2{,}55\ C_e^{1,45}$
CTS/EVOH	0.73 ± 4.12	0.86	1.18	0.82		$q_e = 1{,}39\ C_e^{0,99}$

that vary form pH 2 to pH 11, the mechanisms of Cr(VI) adsorption can vary as well. The various methods of interaction between chromium metal ions and the sorbent such as complexation, electrostatic attraction and ion exchange can be the reason for both isotherm models to suit the general adsorption behaviour of this metal.

Table 6.5: Langmuir and Freundlich isotherms constants and parameters of chromium removal for all biosorbents.

Adsorbent	Langmuir					
	$q_{e(theo)}$	R^2	a_m	b	R_L	Equation of $q_{e(theo)}$
CTS	1.67 ± 3.21	0.99	46.3	0.03	0.90	$q_e = 1/[(0{,}86)x(1/C_e)+(0{,}02)]$
CTS-NF	1.33 ± 2.51	0.97	63.7	0.01	0.94	$q_e = 1/[(1{,}18)x(1/C_e)+(0{,}016)]$
chnw/EVOH	1.12 ± 1.04	0.89	4.33	0.21	0.49	$q_e = 1/[(1{,}12)x(1/C_e)+(0{,}23)]$
CTS-NP/EVOH	0.78 ± 1.45	0.76	10.89	0.04	0.82	$q_e = 1/[(2{,}14)x(1/C_e)+(0{,}09)]$
CTS/EVOH	0.83 ± 1.38	1.00	17.7	0.03	0.86	$q_e = 1/[(1{,}77)x(1/C_e)+(0{,}06)]$
	Freundlich					
	$q_{e(theo)}$	R^2	n	K_F		Equation of q_e
CTS	2.29 ± 13.8	0.95	1.46	1.27		$q_e = 1{,}27\ C_e^{1,46}$
CTS-NF	1.62 ± 5.32	0.96	1.63	0.91		$q_e = 0{,}906\ C_e^{1,23}$
chnw/EVOH	3.15 ± 261	0.72	2.39	0.90		$q_e = 0{,}90\ C_e^{2,39}$
CTS-NP/EVOH	1.69 ± 23.0	0.71	1.70	0.62		$q_e = 0{,}62\ C_e^{1,70}$
CTS/EVOH	0.83 ± 1.89	0.97	1.04	0.53		$q_e = 1{,}95\ C_e^{1.00}$

6.2 Kinetic models

6.2.1 Pseudo-First-Order

All data for the Pseudo-First-Order kinetic model are noted with a subscript 1. The Pseudo-First-Order kinetic model was linearised using the plot of ln (q_e - q) vs time (minutes). This plot was used to determine the first-order constant, k_1 and the correlation coefficient, R^2. The adsorption capacity at equilibrium was calculated using the linearized equation of the Pseudo-First-Order kinetic model [104, 134, 135].

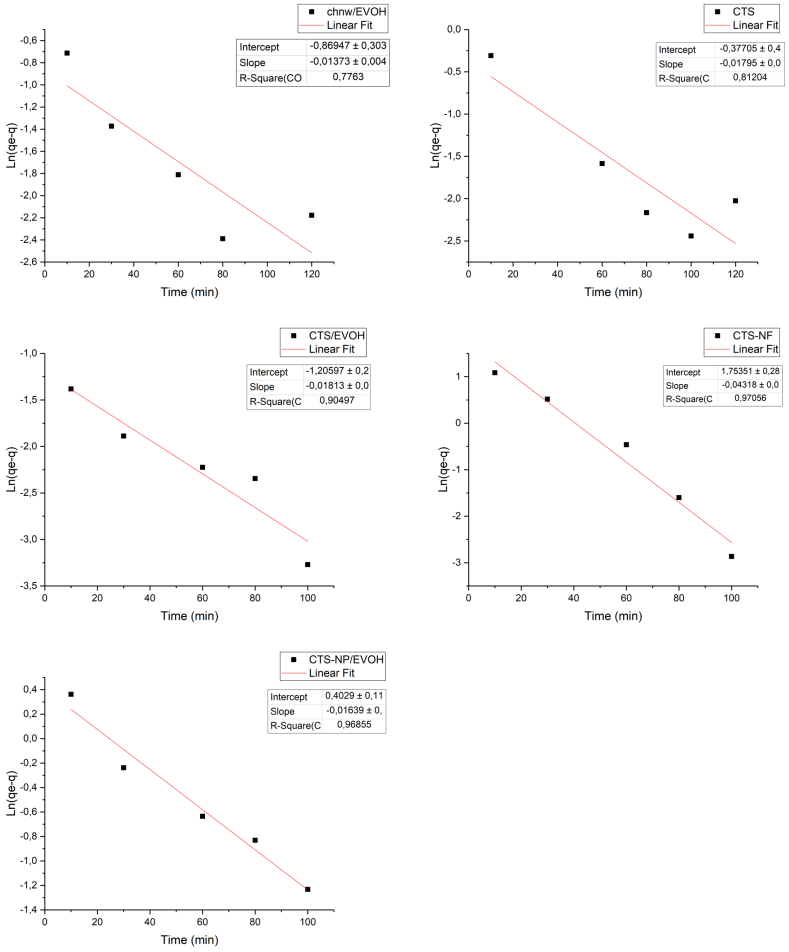

Figure 6.11: Pseudo-First-Order kinetic model of chromium removal for each biosorbent.

All calculated constants, correlation coefficients and adsorption capacities specifically for Cr(VI) removal for all biosorbents at each initial Cr(VI) concentration are listed in the Table 6.6 and Table 6.7. Poor correlation between the theoretical adsorption capacity ($q_{e(theo)1}$) calculated using the linear expression of Pseudo-First-Order and the experimental adsorption capacity ($q_{e(exp)}$) could be seen for the biosorbents if the correlation coefficient ($R^2{}_1$) were not close enough to 1. In Figure 6.11 the best linear fit found for each biosorbent is presented showing the intercept and slope that was used to calculate

Table 6.6: The k_1 and R^2 of Cr(VI) removal calculated from the Pseudo-First-Order kinetic model for initial sorbate concentration in $mg.L^{-1}$.

Biosorbents	k_1 min^{-1}				$R^2{}_1$			
	2	5	10	20	2	5	10	20
CTS	0.005	0.005	0.001	0.008	0.699	0.821	0.008	0.812
CTS-NF	0.005	0.010	0.007	0.019	0.710	0.686	0.611	0.971
chnw/EVOH	0.012	0.006	0.005	0.006	0.701	0.776	0.460	0.498
CTS-NP/EVOH	0.015	0.012	0.009	0.007	0.767	0.644	0.674	0.969
CTS/EVOH	0.008	0.012	0.009	0.009	0.905	0.751	0.831	0.847

Table 6.7: Theoretical adsorption capacities, $q_{e(theo)}$, of Cr(VI) removal calculated from the Pseudo-First-Order kinetic model for all biosorbents.

Biosorbents	$q_{e(theo)1}$ $mg.g^{-1}$			
	2 $mg.L^{-1}$	5 $mg.L^{-1}$	10 $mg.L^{-1}$	20 $mg.L^{-1}$
CTS powder	0.7810	1.510	0.2770	0.6860
CTS-NF	0.6170	2.240	2.750	5.780
chnw/EVOH	1.030	0.4190	2.904	3.310
CTS-NP/EVOH	0.6510	0.1940	0.6050	1.500
CTS/EVOH sponge	0.2990	1.720	2.540	2.660

k_1 and $q_{e(theo)1}$, as well as the $R^2{}_1$. The best correlation between the theoretical and the experimental adsorption capacity of CTS powder is found at the initial Cr(VI) concentration of 5 $mg.L^{-1}$, where the experimental q_e is 1.750 $mg.g^{-1}$ and the theoretical q_{e1} is 1.509 $mg.g^{-1}$. The same good correlation can be seen for chnw/EVOH composite nanofibers between the experimental and theoretical adsorption capacities where the best fit between the theoretical and the experimental adsorption capacity is found at the initial Cr(VI) concentration of 10 $mg.L^{-1}$, where the experimental q_e is 2.180 $mg.g^{-1}$ and the theoretical q_{e1} is 2.904 $mg.g^{-1}$. The best correlation for CTS-NF is found at a initial Cr(VI) concentration of 2 $mg.L^{-1}$, where the experimental q_e is 0.6200 $mg.g^{-1}$ and the theoretical q_{e1} is 0.6170 $mg.g^{-1}$. The best correlation for CTS/EVOH sponges is found at an initial Cr(VI) concentration of 10 $mg.L^{-1}$, where the experimental q_e is 2.140 $mg.g^{-1}$ and the theoretical q_{e1} is 2.539 $mg.g^{-1}$. The best correlation for CTS-NP/EVOH composite nanofibers is found at an initial Cr(VI) concentration of 2 $mg.L^{-1}$, where the experimental q_e is 0.4300 $mg.g^{-1}$ and the theoretical q_{e1} is 0.6510 $mg.g^{-1}$.

All calculated constants, correlation coefficients and adsorption capacities specifically for Cu(II) removal for all biosorbents at each initial Cu(II) concentration are listed in the Table 6.8 and Table 6.9. The best correlation between the theoretical and the experimental adsorption capacity of CTS powder is found at the initial Cu(II) concentration of 2 $mg.L^{-1}$, where the experimental q_e is 0.9070 $mg.g^{-1}$ and the theoretical q_{e1} is 0.9520 $mg.g^{-1}$. The same good correlation can be seen for chnw/EVOH composite nanofibers between the experimental and theoretical adsorption capacities where the best fit between

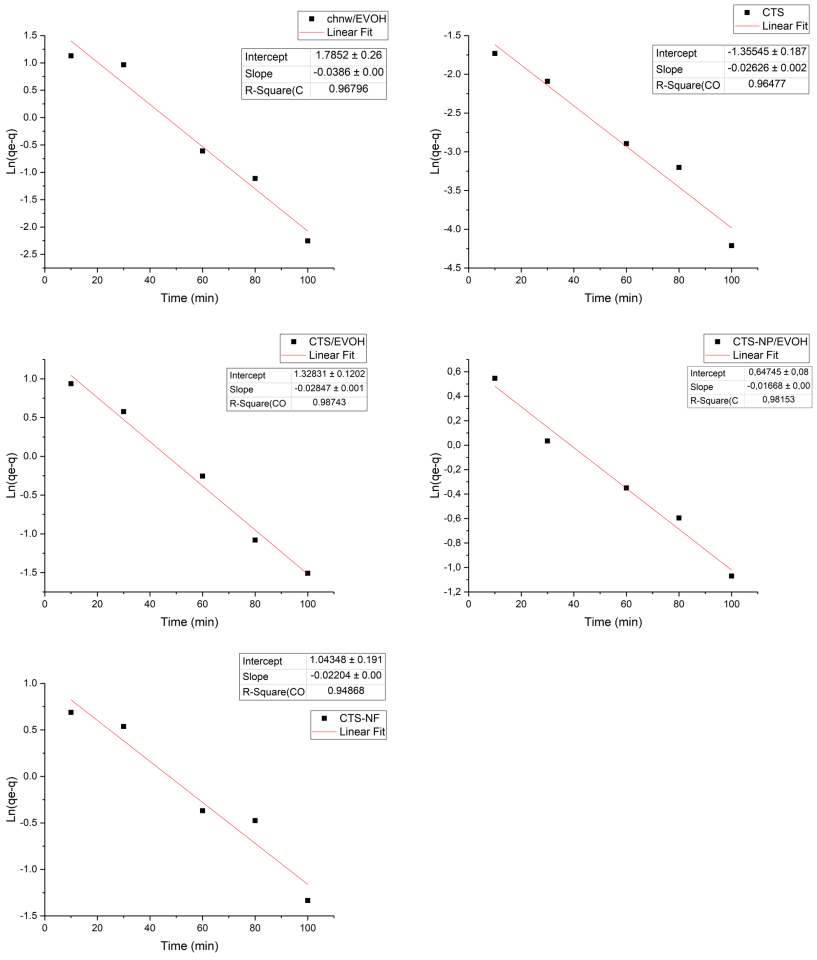

Figure 6.12: Pseudo-First-Order kinetic model of copper removal for each biosorbent.

Table 6.8: The k_1 and R^2 of Cu(II) removal calculated from the Pseudo-First-Order kinetic model for initial sorbate concentration in mg.L^{-1}.

Biosorbents	k_1 min^{-1}				R^2_1			
	2	5	10	20	2	5	10	20
CTS	0.003	0.011	0.011	0.011	0.677	0.965	0.935	0.916
CTS-NF	0.003	0.004	0.008	0.009	0.862	0.869	0.869	0.948
chnw/EVOH	0.018	0.012	0.007	0.017	0.952	0.889	0.759	0.968
CTS-NP/EVOH	0.004	0.012	0.007	0.007	0.829	0.566	0.982	0.966
CTS/EVOH	0.003	0.009	0.012	0.017	0.930	0.979	0.987	0.646

the theoretical and the experimental adsorption capacity is found at the initial Cu(II) concentration of 20 mg.L^{-1}, where the experimental q_e is 5.150 mg.g^{-1} and the theoretical q_{e1} is 5.961 mg.g^{-1}. The best correlation for CTS-NF is found at an initial Cu(II) concentration of 2 mg.L^{-1}, where the experimental q_e is 0.6870 mg.g^{-1} and the theoretical q_{e1} is 0.660 mg.g^{-1}. The best correlation for CTS/EVOH sponges is found at an initial Cu(II) concentration of 5 mg.L^{-1}, where the experimental q_e is 2.313 mg.g^{-1} and the theoretical q_{e1} is 1.889 mg.g^{-1}. The best correlation for CTS-NP/EVOH composite nanofibers is found at an initial Cu(II) concentration of 2 mg.L^{-1}, where the experimental q_e is 0.5420

Table 6.9: Theoretical adsorption capacities, $q_{e(theo)}$, of Cu(II) removal calculated from the Pseudo-First-Order kinetic model for all biosorbents.

Biosorbents	$q_{e(theo)1}$ mg.g^{-1}			
	2 mg.L^{-1}	5 mg.L^{-1}	10 mg.L^{-1}	20 mg.L^{-1}
CTS powder	0.9520	0.2580	0.5920	0.1670
CTS-NF	0.6600	2.122	3.899	2.839
chnw/EVOH	1.150	2.328	3.696	5.961
CTS-NP/EVOH	0.5770	2.225	1.911	2.635
CTS/EVOH sponge	0.5130	1.889	3.775	18.87

mg.g^{-1} and the theoretical q_{e1} is 0.5770 mg.g^{-1}. This excellent correlation between the theoretical data of the First-Order models and the experimental data is due to the good linear fit of the linearised plots with R^2 close to 1 as seen in Figure 6.12, where the best linear fit found for each biosorbent are presented.

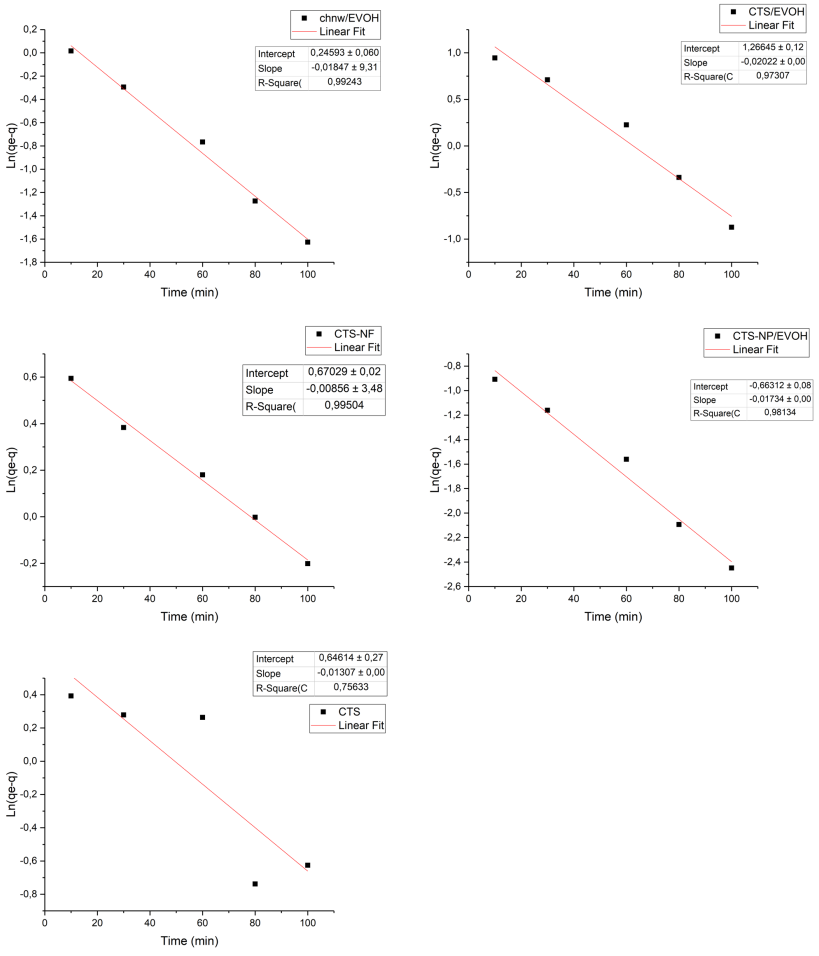

Figure 6.13: Pseudo-First-Order kinetic model of nickel removal for each biosorbent.

All calculated constants, correlation coefficients and adsorption capacities specifically for Ni(II) removal for all biosorbents at each initial Ni(II) concentration are listed in the

Table 6.10: The k_1 and R^2 of Ni(II) removal calculated from the Pseudo-First-Order kinetic model for initial sorbate concentration in $mg.L^{-1}$.

Biosorbents	k_1 min^{-1}				$R^2{}_1$			
	2	5	10	20	2	5	10	20
CTS	0.004	0.006	0.005	0.001	0.661	0.756	0.397	0.008
CTS-NF	0.001	0.004	0.004	0.010	0.814	0.904	0.995	0.941
chnw/EVOH	0.005	0.007	0.003	0.008	0.880	0.940	0.054	0.990
CTS-NP/EVOH	0.008	0.005	0.009	0.006	0.981	0.861	0.767	0.639
CTS/EVOH	- 0.010	0.010	0.010	- 0.004	0.290	0.790	0.973	0.661

Table 6.11: Theoretical adsorption capacities, $q_{e(theo)}$, of Ni(II) removal calculated from the Pseudo-First-Order kinetic model for all biosorbents.

Biosorbents	$q_{e(theo)1}$ $mg.g^{-1}$			
	2 $mg.L^{-1}$	5 $mg.L^{-1}$	10 $mg.L^{-1}$	20 $mg.L^{-1}$
CTS powder	0.8050	1.908	2.255	1.971
CTS-NF	0.3070	0.8210	1.955	0.9700
chnw/EVOH	0.2250	1.068	0.7490	1.279
CTS-NP/EVOH	0.5150	1.086	1.798	4.201
CTS/EVOH sponge	0.002000	0.02100	3.548	0.8970

Table 6.10 and Table 6.11. The best correlation between the theoretical and the experimental adsorption capacity of CTS powder is found at the initial Ni(II) concentration of 5 $mg.L^{-1}$, where the experimental q_e is 1.880 $mg.g^{-1}$ and the theoretical q_{e1} is 1.908 $mg.g^{-1}$. The same good correlation can be seen for chnw/EVOH composite nanofibers between the experimental and theoretical adsorption capacities where the best fit between the theoretical and the experimental adsorption capacity is found at the initial Ni(II) concentration of 5 $mg.L^{-1}$, where the experimental q_e is 1.070 $mg.g^{-1}$ and the theoretical q_{e1} is 1.067 $mg.g^{-1}$. The best correlation for CTS-NF is found at an initial Ni(II) concentration of 2 $mg.L^{-1}$, where the experimental q_e is 0.3610 $mg.g^{-1}$ and the theoretical q_{e1} is 0.3070 $mg.g^{-1}$. The best correlation for CTS/EVOH sponges is found at an initial Ni(II) concentration of 10 $mg.L^{-1}$, where the experimental q_e is 6.700 $mg.g^{-1}$ and the theoretical q_{e1} is 3.548 $mg.g^{-1}$, which is relatively good, but the worst correlation was seen in comparison with all other biosorbents. The best correlation for CTS-NP/EVOH composite nanofibers is found at an initial Ni(II) concentration of 2 $mg.L^{-1}$, where the experimental q_e is 0.4670 $mg.g^{-1}$ and the theoretical q_{e1} is 0.5150 $mg.g^{-1}$. The best linear fit found for each biosorbent are presented in Figure 6.13.

All calculated constants, correlation coefficients and adsorption capacities specifically for Pb(II) removal for all biosorbents at each initial Pb(II) concentration are listed in the Table 6.12 and Table 6.13 The best correlation between the theoretical and the experimental adsorption capacity of CTS powder is found at the intial Pb(II) concentration of

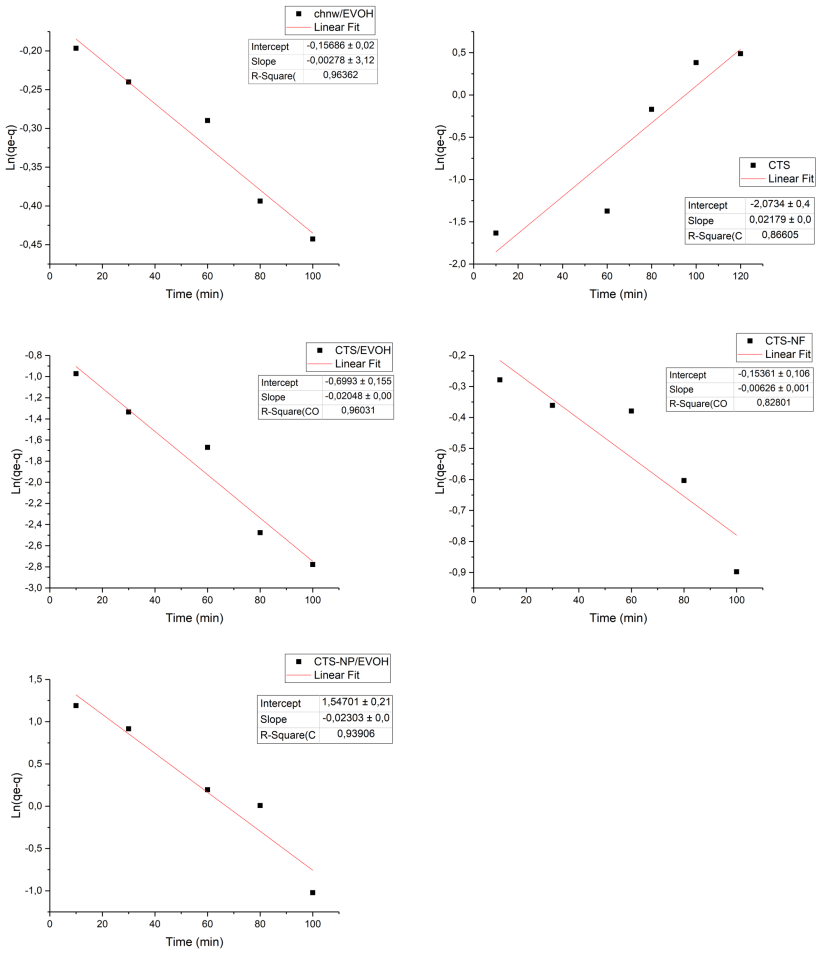

Figure 6.14: Pseudo-First-Order kinetic model of lead removal for each biosorbent.

Table 6.12: The k_1 and R^2 of Pb(II) removal calculated from the Pseudo-First-Order kinetic model for initial sorbate concentration in $mg.L^{-1}$.

Biosorbents	k_1 min^{-1}				R^2_1			
	2	5	10	20	2	5	10	20
CTS	-0.001	-0.006	-0.009	-0.007	0.057	0.314	0.866	0.596
CTS-NF	0.003	0.005	0.014	0.015	0.830	0.740	0.827	0.780
chnw/EVOH	0.001	0.024	0.012	0.011	0.964	0.942	0.865	0.791
CTS-NP/EVOH	0.002	0.007	0.009	0.012	0.921	0.883	0.939	0.915
CTS/EVOH	0.009	0.008	0.015	0.005	0.960	0.678	0.954	0.953

2 $mg.L^{-1}$, where the experimental q_e is 0.7840 $mg.g^{-1}$ and the theoretical q_{e1} is 0.3240 $mg.g^{-1}$. The same good correlation can be seen for chnw/EVOH composite nanofibers between the experimental and theoretical adsorption capacities where the best fit between the theoretical and the experimental adsorption capacity is found at the initial Pb(II) concentration of 2 $mg.L^{-1}$, where the experimental q_e is 0.9280 $mg.g^{-1}$ and the theoretical q_{e1} is 0.8550 $mg.g^{-1}$. The best correlation for CTS-NF is found at an initial Pb(II) concentration of 2 $mg.L^{-1}$, where the experimental q_e is 0.8350 $mg.g^{-1}$ and the

Table 6.13: Theoretical adsorption capacities, $q_{e(theo)}$, of Pb(II) removal calculated from the Pseudo-First-Order kinetic model for all biosorbents.

Biosorbents	$q_{e(theo)1}$ mg.g^{-1}			
	2 mg.L^{-1}	5 mg.L^{-1}	10 mg.L^{-1}	20 mg.L^{-1}
CTS powder	0.3240	0.09800	0.1260	0.1810
CTS-NF	0.8580	2.777	2.783	15.21
chnw/EVOH	0.8550	3.704	5.968	7.413
CTS-NP/EVOH	0.7750	2.384	4.697	2.980
CTS/EVOH sponge	0.4970	1.577	2.858	2.032

theoretical q_{e1} is 0.8580 mg.g^{-1}. The best correlation for CTS/EVOH sponges is found at an initial Pb(II) concentration is found at 10 mg.L^{-1}, where the experimental q_e is 2.800 mg.g^{-1} and the theoretical q_{e1} is 2.858 mg.g^{-1}. The best correlation for CTS-NP/EVOH composite nanofibers is found at an initial Pb(II) concentration of 5 mg.L^{-1}, where the experimental q_e is 2.170 mg.g^{-1} and the theoretical q_{e1} is 2.384 mg.g^{-1}. The best linear fit that was found for each biosorbent are presented in Figure 6.14.

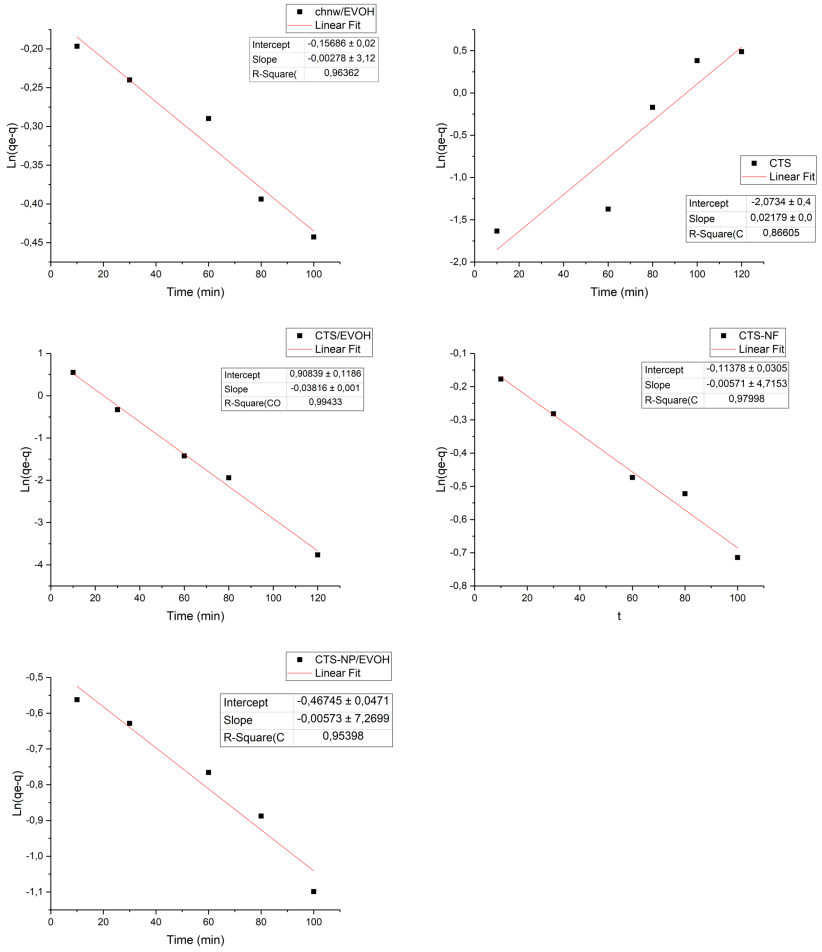

Figure 6.15: Pseudo-First-Order kinetic model of zinc removal for each biosorbent.

Table 6.14: The k_1 and R^2 of Zn(II) removal calculated from the Pseudo-First-Order kinetic model for initial sorbate concentration in $mg.L^{-1}$.

Biosorbents	k_1 min^{-1}				$R^2{}_1$			
	2	5	10	20	2	5	10	20
CTS	0.012	0.006	- 0.008	- 0.010	0.779	0.230	0.340	0.180
CTS-NF	0.003	0.005	0.007	0.006	0.980	0.804	0.828	0.831
chnw/EVOH	0.005	0.007	0.001	0.007	0.604	0.715	0.070	0.804
CTS-NP/EVOH	0.003	0.007	0.008	0.007	0.954	0.695	0.583	0.539
CTS/EVOH	0.003	0.032	0.017	0.022	0.981	0.936	0.994	0.473

Table 6.15: Theoretical adsorption capacities, $q_{e(theo)}$, of Zn(II) removal calculated from the Pseudo-First-Order kinetic model for all biosorbents.

Biosorbents	$q_{e(theo)1}$ $mg.g^{-1}$			
	2 $mg.L^{-1}$	5 $mg.L^{-1}$	10 $mg.L^{-1}$	20 $mg.L^{-1}$
CTS	0.03400	0.1600	0.2280	0.2220
CTS-NF	0.8920	2.770	5.876	11.13
chnw/EVOH	0.2930	0.6450	0.9320	0.5980
CTS-NP/EVOH	0.6270	0.8690	1.559	6.123
CTS/EVOH	0.2540	5.930	2.480	7.225

All calculated constants, correlation coefficients and adsorption capacities specifically for Zn(II) removal for all biosorbents at each initial Zn(II) concentration are listed in the Table 6.14 and 6.15. No correlation could be seen for CTS powder. Relatively good correlation can be seen for chnw/EVOH composite nanofibers between the experimental and theoretical adsorption capacities where the best fit between the theoretical and the experimental adsorption capacity is found at the initial Zn(II) concentration of 2 $mg.L^{-1}$, where the experimental q_e is 0.4940 $mg.g^{-1}$ and the theoretical q_{e1} is 0.2930 $mg.g^{-1}$. The best correlation for CTS-NF is found at an initial Zn(II) concentration of 5 $mg.L^{-1}$, where the experimental q_e is 2.280 $mg.g^{-1}$ and the theoretical q_{e1} is 2.770 $mg.g^{-1}$. The best correlation for CTS/EVOH sponges is found at an initial Zn(II) concentration of 10 $mg.L^{-1}$, where the experimental q_e is 4.506 $mg.g^{-1}$ and the theoretical q_{e1} is 2.480 $mg.g^{-1}$, fitting relatively well. The best correlation for CTS-NP/EVOH composite nanofibers is found at an initial Zn(II) concentration of 2 $mg.L^{-1}$, where the experimental q_e is 0.5900 $mg.g^{-1}$ and the theoretical q_{e1} is 0.5770 $mg.g^{-1}$. The best linear fit that was found for each biosorbent is presented in Figure 6.15. The poor linear fit seen for CTS powder could be the reason why there is no correlation between the theoretical and the experimental.

It was seen overall that good agreement between the theoretical and experimental data correlated well with a good linear fit on the plot of $\ln(q_e - q)$ vs t. The closer the R^2 was to 1 the closer the experimental adsorption capacity was to the one calculated using the First-Order kinetic model plots. It was found that CTS powder did not correlate

well over all the initial sorbate concentrations specifically for lead and zinc removal, and only correlated well with one initial concentration for each sorbate. CTS-NF, on the other hand, did correlate well overall concentrations for many of the heavy metal ions, with some exception seen for higher sorbate concentrations during lead and nickel removal. Chnw/EVOH composite nanofibers also showed similarly good correlation over a wider range of initial sorbate concentration with some exception seen for zinc removal. CTS/EVOH showed good correlation over a broad initial sorbate concentration, but less so as the concentration increased to 20 mg.L^{-1}. CTS/EVOH also showed poor correlation for nickel removal overall. CTS-NP/EVOH composite nanofibers showed good correlation, same as CTS/EVOH, where the correlation lowered as the concentration of the heavy metal ions were increased to 20 mg.L^{-1}. CTS-NP/EVOH composite nanofibers correlated the least with the theoretical data obtained for chromium removal.

6.2.2 Pseudo-Second-Order

All data for the Pseudo-Second-Order kinetic model are noted with a subscript 2. The Pseudo-Second-Order kinetic model have graphs of types 1 to 4 as mentioned in Section 2.7.2. The graph types that were best correlated to the biosorbents and described the adsorption process the best were selected for the discussion. The other results can be seen for A.

Table 6.16: The k_2 and R^2 of Cr(VI) removal calculated from the Pseudo-Second-Order kinetic model for initial sorbate concentration in mg.L^{-1}.

Biosorbents	k_2 g.mg^{-1}.min^{-1}				$R^2{}_2$			
	2	5	10	20	2	5	10	20
CTS	0.041	0.026	0.145	0.125	0.634	0.612	0.464	0.824
CTS-NF	0.052	0.019	0.024	0.014	0.738	0.894	0.583	0.989
chnw/EVOH	0.038	0.164	0.005	0.002	0.922	0.941	0.294	0.815
CTS-NP/EVOH	0.121	0.210	0.038	0.035	0.726	0.946	0.967	0.978
CTS/EVOH	0.134	0.029	0.0129	0.041	0.981	0.665	0.564	0.743

Table 6.17: Theoretical adsorption capacities, $q_{e(theo)}$, of Cr(VI) removal calculated from the Pseudo-Second-Order kinetic model for all biosorbents.

Biosorbents	$q_{e(theo)2}$ mg.g^{-1}			
	2 mg.L^{-1}	5 mg.L^{-1}	10 mg.L^{-1}	20 mg.L^{-1}
CTS	0.3870	1.227	3.610	5.313
CTS-NF	0.3950	1.488	2.070	5.888
chnw/EVOH	0.5300	2.167	0.3600	0.6550
CTS-NP/EVOH	0.3880	1.653	2.144	2.826
CTS/EVOH	0.3910	1.027	2.183	1.228

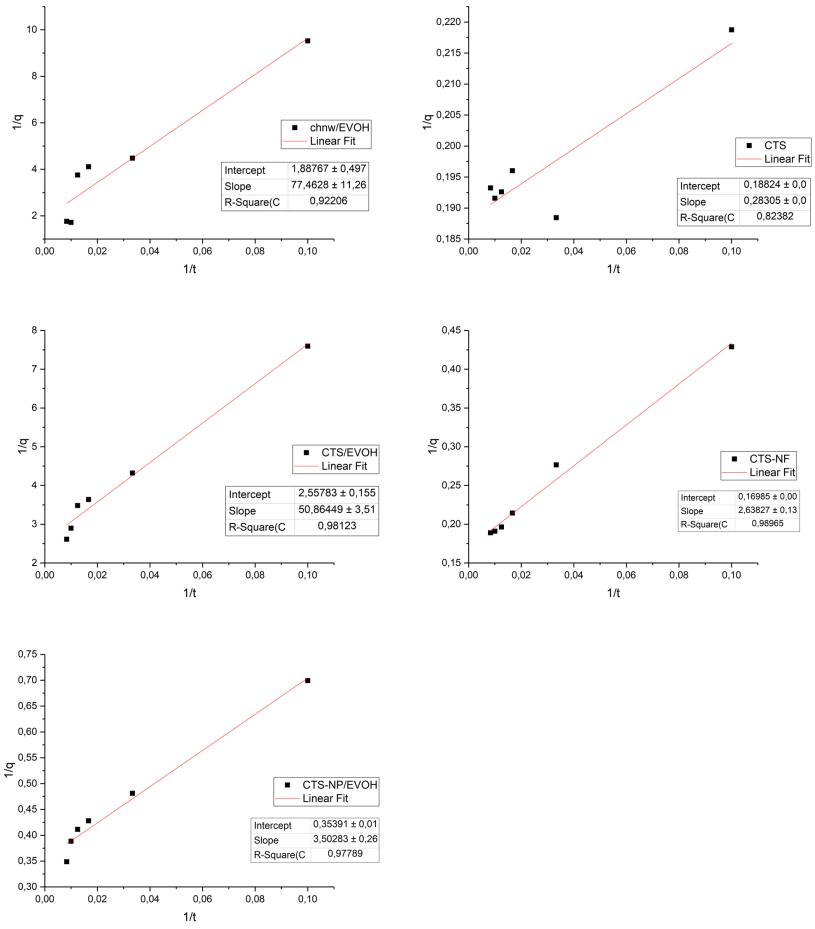

Figure 6.16: Pseudo-Second-Order kinetic model of chromium removal for each biosorbent.

All calculated constants, correlation coefficients and adsorption capacities specifically for Cr(VI) removal for all biosorbents at each initial Cr(VI) concentration are listed in the Table 6.16 and 6.17. Correlation for CTS powder was seen only at 20 mg.L^{-1} for Type 1 of the Pseudo-Second-Order kinetic model, where the experimental q_e is 5.220 mg.g^{-1} and the theoretical q_{e2} is 7.360 mg.g^{-1}. Although the linear fit for the plots was slightly less for Type 2 compared to Type 1, the correlation of the theoretical data was found to be closer and agreed well with the experimental adsorption capacities overall initial Cr(VI) concentrations. The best fit was found at 20 mg.L^{-1} where the experimental q_e is 5.220 mg.g^{-1} and the theoretical q_{e2} is 5.313 mg.g^{-1}. Good correlation can be seen for chnw/EVOH composite nanofibers, using Type 2, between the experimental and theoretical adsorption capacities where the best fit between the theoretical and the experimental adsorption capacity is found at the initial Cr(VI) concentration of 2 mg.L^{-1}, where the experimental q_e is 0.584 mg.g^{-1} and the theoretical q_{e2} is 0.5300 mg.g^{-1}. The best correlation for CTS-NF, using Type 2, is found at an initial Cr(VI) concentration of 20 mg.L^{-1}, where the experimental q_e is 5.300 mg.g^{-1} and the theoretical q_{e2} is 5.890 mg.g^{-1}. The best correlation for CTS/EVOH sponges, using Type 2, is found at an

initial Cr(VI)) concentration of 2 mg.L^{-1}, where the experimental q_e is 0.3850 mg.g^{-1} and the theoretical q_{e2} is 0.3910 mg.g^{-1}. CTS-NP/EVOH composite nanofibers showed good linear fit with Pseudo-Second-Order Type 1 but the theoretical data corresponded poorly with the experimental data overall initial chromium ion concentrations. A good linear fit was seen using Type 2 while the correlation between the experimental and theoretical data was highly improved. The best correlation for CTS-NP/EVOH for Type 1 was found at an initial Cr(VI) concentration of 5 mg.L^{-1}, where the experimental q_e is 1.600 mg.g^{-1} and the theoretical q_{e2} is 0.7230 mg.g^{-1}. However, a good fit between the data, using Type 2, was seen over the whole range of concentration with the best fit seen at 20 mg.g^{-1} where the experimental q_e is 2.870 mg.g^{-1} and the theoretical q_{e2} is 2.826 mg.g^{-1}. The best linear fit and correlation to the experimental adsorption capacity that was found for each biosorbent are presented in Figure 6.16. Good correlation was seen for CTS-NF, chnw/EVOH composite nanofibers, CTS/EVOH and CTS-NP/EVOH composite nanofibers with the Pseudo-Second-Order kinetic model indicating that Cr(VI) removal occurred via a chemisorption process, which can be via valence electrons, through sharing or exchanging between the Cr(VI) and the biosorbents. CTS also shows an R^2_2 close to 1 indicating that even though this biosorbent may not be effectively interacting with the chromium metal ion throughout the entirety of the adsorption process (over entire contact time) it does adhere to chemisorption at optimal conditions.

Table 6.18: The k_2 and R^2 of Cu(II) removal calculated from the Pseudo-Second-Order kinetic model for initial sorbate concentration in mg.L^{-1}.

Biosorbents	k_2 g.mg^{-1}.min^{-1}				R^2_2			
	2	5	10	20	2	5	10	20
CTS	0.018	0.528	0.244	0.016	0.631	0.840	0.789	0.662
CTS-NF	0.029	0.003	0.007	0.035	0.709	0.988	0.908	0.764
chnw/EVOH	0.022	0.013	0.005	0.012	0.574	0.084	0.085	0.839
CTS-NP/EVOH	0.029	0.039	0.022	0.030	0.897	0.635	0.985	0.843
CTS/EVOH	0.098	0.026	0.017	0.003	0.595	0.922	0.944	0.803

Table 6.19: Theoretical adsorption capacities, $q_{e(theo)}$, of Cu(II) removal calculated from the Pseudo-Second-Order kinetic model for all biosorbents.

Biosorbents	$q_{e(theo)2}$ mg.g^{-1}			
	2 mg.L^{-1}	5 mg.L^{-1}	10 mg.L^{-1}	20 mg.L^{-1}
CTS	0.3630	2.694	4.864	7.856
CTS-NF	0.3330	17.55	3.219	6.124
chnw/EVOH	0.5950	0.5210	0.6160	5.402
CTS-NP/EVOH	0.3910	1.186	2.809	5.509
CTS/EVOH	0.4610	2.299	4.866	6.725

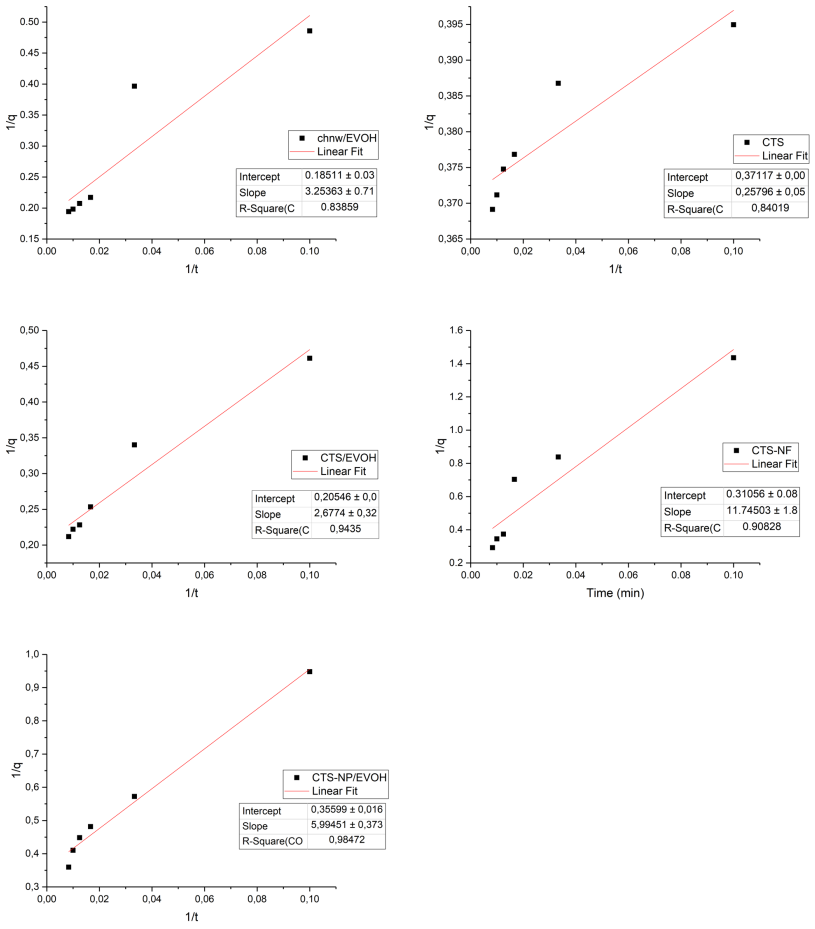

Figure 6.17: Pseudo-Second-Order kinetic model of copper removal for each biosorbent.

All calculated constants, correlation coefficients and adsorption capacities specifically for Cu(II) removal for all biosorbents at each initial Cu(II) concentration are listed in the Table 6.18 and 6.19. Correlation for CTS powder was seen only at 5 mg.L^{-1} for Type 1, where the experimental q_e is 2.709 mg.g^{-1} and the theoretical q_{e2} is 1.989 mg.g^{-1}. Although the linear fit for the plots was slightly less for Type 2 compared to Type 1, the correlation of the theoretical data was found to be closer and agreed well with the experimental adsorption capacities overall initial Cu(II) concentrations. The best fit was found at 5 mg.L^{-1} where the experimental q_e is 2.709 mg.g^{-1} and the theoretical q_{e2} is 2.694 mg.g^{-1}. Good correlation can be seen for chnw/EVOH composite nanofibers between the experimental and theoretical adsorption capacities, using Type 2, where the best fit between the theoretical and the experimental adsorption capacity is found at the initial Cu(II) concentration of 20 mg.L^{-1}, where the experimental q_e is 5.150 mg.g^{-1} and the theoretical q_{e2} is 5.402 mg.g^{-1}. The best correlation for CTS-NF is found, using Type 2, at an initial Cu(II) concentration of 10 mg.L^{-1}, where the experimental q_e is 3.424 mg.g^{-1} and the theoretical q_{e2} is 3.219 mg.g^{-1}. CTS EVOH showed good linear fit with Pseudo-Second-Order Type 1 but the theoretical data corresponded poorly with the experimental data overall initial copper ion concentrations. A slightly poorer linear fit was seen using

Type 2 but the correlation between the experimental and theoretical data was highly improved. The best correlation for CTS/EVOH was found at an initial Cu(II) concentration of 10 mg.L^{-1}, where the experimental q_e is 4.721 mg.g^{-1} and the theoretical q_{e2} is 4.866 mg.g^{-1}. The best correlation for CTS-NP/EVOH composite nanofibers is found, using Type 2, at an initial Cu(II) concentration of 10 mg.L^{-1}, where the experimental q_e is 2.242 mg.g^{-1} and the theoretical q_{e2} is 2.809 mg.g^{-1}. The best linear fit and correlation to the experimental adsorption capacity that was found for each biosorbent are presented in Figure 6.17. Good correlation, where $R^2{}_2$ is close to 1, was seen all the biosorbents with the Pseudo-Second-Order kinetic model indicating that Cu(II) removal occurred via a chemisorption process.

Table 6.20: The k_2 and R^2 of Ni(II) removal calculated from the Pseudo-Second-Order kinetic model for initial sorbate concentration in mg.L^{-1}.

Biosorbents	k_2 g.mg−1.min−1				$R^2{}_2$			
	2	5	10	20	2	5	10	20
CTS	0.010	0.015	0.109	-0.109	0.014	0.777	0.717	0.046
CTS-NF	0.083	0.026	0.014	0.005	0.531	0.946	0.923	0.759
chnw/EVOH	0.293	0.034	0.019	0.025	0.568	0.977	0.842	0.977
CTS-NP/EVOH	0.031	0.034	0.030	0.008	0.998	0.692	0.957	0.808
CTS/EVOH	-3.065	4.469	0.024	-0.038	0.075	0.939	0.819	0.438

Table 6.21: Theoretical adsorption capacities, $q_{e(theo)}$, of Ni(II) removal calculated from the Pseudo-Second-Order kinetic model for all biosorbents.

Biosorbents	$q_{e(theo)2}$ mg.g^{-1}			
	2 mg.L^{-1}	5 mg.L^{-1}	10 mg.L^{-1}	20 mg.L^{-1}
CTS	0.3760	1.310	2.706	7.622
CTS-NF	0.1370	0.7310	1.803	6.042
chnw/EVOH	0.2380	1.135	2.308	1.484
CTS-NP/EVOH	0.8190	0.7940	2.432	2.612
CTS/EVOH	0.3110	2.396	6.317	7.463

All calculated constants, correlation coefficients and adsorption capacities specifically for Ni(II) removal for all biosorbents at each initial Ni(II) concentration are listed in the Table 6.20 and 6.21. No correlation was visible between the experimental data and that obtained using Type 1 of the Pseudo-Second-Order kinetic model. Although the linear fit for the plots was slightly less for Type 2 compared to Type 1, the correlation of the theoretical data was found to be closer and agreed well with the experimental adsorption capacities overall initial Ni(II) concentrations. The best fit was found at 2 mg.L^{-1} where

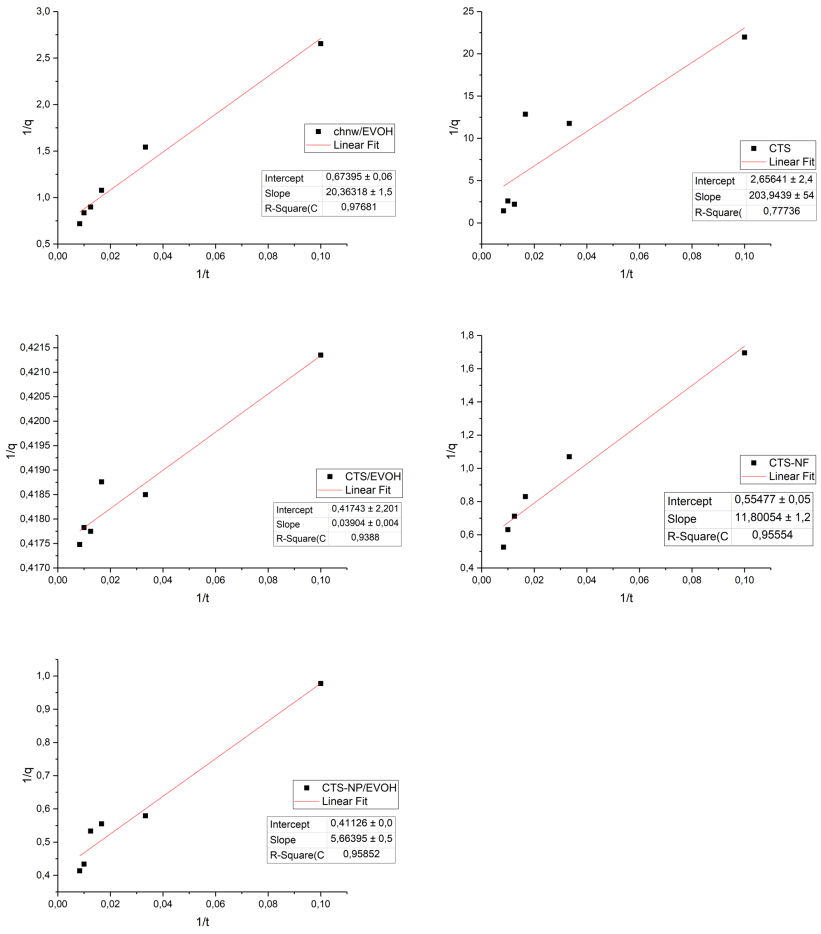

Figure 6.18: Pseudo-Second-Order kinetic model of nickel removal for each biosorbent.

the experimental q_e is 0.7000 mg.g^{-1} and the theoretical q_{e2} is 0.3760 mg.g^{-1}. Good correlation can be seen for chnw/EVOH composite nanofibers between the experimental and theoretical adsorption capacities, using Type 2, where the best fit between the theoretical and the experimental adsorption capacity is found at the initial Ni(II) concentration of 20 mg.L^{-1}, where the experimental q_e is 1.400 mg.g^{-1} and the theoretical q_{e2} is 1.484 mg.g^{-1}. The best correlation for CTS-NF is found, using Type 2, at an initial Ni(II) concentration of 10 mg.L^{-1}, where the experimental q_e is 3.424 mg.g^{-1} and the theoretical q_{e2} is 3.219 mg.g^{-1}. CTS EVOH showed good linear fit with Pseudo-Second-Order Type 1 but the theoretical data corresponded poorly with the experimental data overall initial nickel ion concentrations. Slightly lower R^2_2 values were obtained using Type 2 but the correlation between the experimental and theoretical data has highly improved. The best correlation for CTS/EVOH was found at an initial Ni(II) concentration of 5 mg.L^{-1}, where the experimental q_e is 2.390 mg.g^{-1} and the theoretical q_{e2} is 2.396 mg.g^{-1}. The best correlation for CTS-NP/EVOH composite nanofibers is found, using Type 2, at an initial Ni(II) concentration of 10 mg.L^{-1}, where the experimental q_e is 2.417 mg.g^{-1} and the theoretical q_{e2} is 2.432 mg.g^{-1}. The best linear fit and correlation to the experimental adsorption capacity that was found for each biosorbent are presented in Figure 6.18.

Good correlation, where R^2_2 is close to 1, was seen all the biosorbents with the Pseudo-Second-Order kinetic model indicating that Ni(II) removal occurred via a chemisorption process. CTS/EVOH sponge showed the lowest R^2_2 value for the Type 2 plots but the adsorption capacities agreed very well.

Table 6.22: The k_2 and R^2 of Pb(II) removal calculated from the Pseudo-Second-Order kinetic model for initial sorbate concentration in $mg.L^{-1}$.

Biosorbents	k_2 $g.mg^{-1}.min^{-1}$				R^2_2			
	2	5	10	20	2	5	10	20
CTS	1.550	- 0.189	- 0.061	- 0.112	0.003	0.167	0.310	0.193
CTS-NF	0.013	0.003	0.058	0.001	0.851	0.818	0.541	0.984
chnw/EVOH	0.017	0.006	0.002	0.008	0.730	0.987	0.952	0.785
CTS-NP/EVOH	0.011	0.010	0.007	0.024	0.966	0.927	0.976	0.987
CTS/EVOH	0.063	0.007	0.021	0.049	0.986	0.982	0.968	0.618

Table 6.23: Theoretical adsorption capacities, $q_{e(theo)}$, of Pb(II) removal calculated from the Pseudo-Second-Order kinetic model for all biosorbents.

Biosorbents	$q_{e(theo)2}$ $mg.g^{-1}$			
	2 $mg.L^{-1}$	5 $mg.L^{-1}$	10 $mg.L^{-1}$	20 $mg.L^{-1}$
CTS	0.4280	1.804	3.747	9.217
CTS-NF	0.4390	1.241	4.086	-3.946
chnw/EVOH	0.3360	124.7	-32.28	6.093
CTS-NP/EVOH	0.6120	2.015	5.024	7.243
CTS/EVOH	0.5720	5.685	3.055	4.880

All calculated constants, correlation coefficients and adsorption capacities specifically for Pb(II) removal for all biosorbents at each initial Pb(II) concentration are listed in the Table 6.22 and 6.23. No correlation was visible between the experimental data and that obtained using Type 1 of the Pseudo-Second-Order kinetic model. Although the linear fit for the plots was slightly less for Type 2 compared to Type 1, the correlation of the theoretical data was found to agree well with the experimental adsorption capacities overall initial Pb(II) concentrations. The best fit was found at 10 $mg.L^{-1}$ where the experimental q_e is 4.893 $mg.g^{-1}$ and the theoretical q_{e2} is 3.747 $mg.g^{-1}$. Good correlation can be seen for chnw/EVOH composite nanofibers between the experimental and theoretical adsorption capacities, using Type 2, where the best fit between the theoretical and the experimental adsorption capacity is found at the initial Pb(II) concentration of 20 $mg.L^{-1}$, where the experimental q_e is 6.780 $mg.g^{-1}$ and the theoretical q_{e2} is 6.093 $mg.g^{-1}$. The best correlation for CTS-NF is found, using Type 2, at an initial Pb(II)

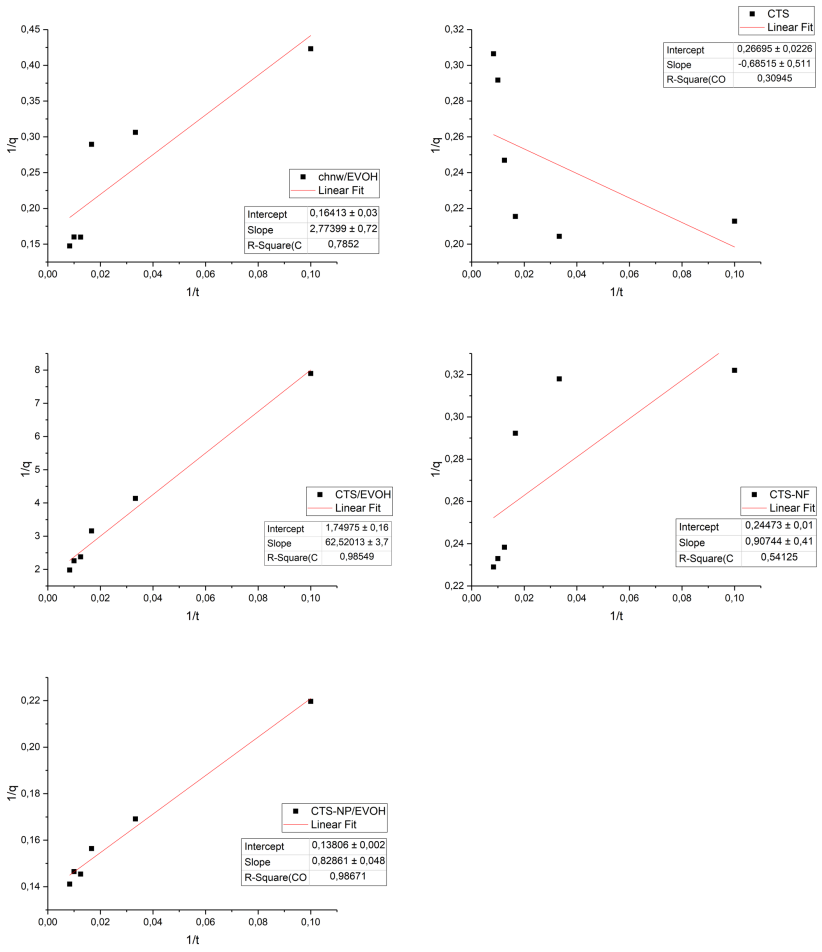

Figure 6.19: Pseudo-Second-Order kinetic model of lead removal for each biosorbent.

concentration of 10 mg.L^{-1}, where the experimental q_e is 4.370 mg.g^{-1} and the theoretical q_{e2} is 4.086 mg.g^{-1}. CTS/EVOH showed good linear fit with Pseudo-Second-Order Type 1 but there was no correlation between the theoretical data and the experimental data, overall initial lead ion concentration. Slightly lower R^2_2 values were obtained using Type 2 but the correlation between the experimental and theoretical data far better. The best correlation for CTS/EVOH was found at an initial Pb(II) concentration of 2 mg.L^{-1}, where the experimental q_e is 0.5100 mg.g^{-1} and the theoretical q_{e2} is 0.5720 mg.g^{-1}. The best correlation for CTS-NP/EVOH composite nanofibers is found, using Type 2, at an initial Pb(II) concentration of 20 mg.L^{-1}, where the experimental q_e is 7.090 mg.g^{-1} and the theoretical q_{e2} is 7.243 mg.g^{-1}. The best linear fit and correlation to the experimental adsorption capacity that was found for each biosorbent are presented in Figure 6.19. Good correlation, where R^2_2 is close to 1, was seen for CTS-NP/EVOH composite nanofibers, chnw/EVOH composite nanofibers and CTS/EVOH with the Pseudo-Second-Order kinetic model indicating that Pb(II) removal occurred via a chemisorption process. Although the adsorption capacities (theoretical and experimental) correlated extremely well, the linear fit was not as good for CTS and CTS-NF, showing the low R^2_2 value for the Type 2 plots. This can indicate that the behavior of these two biosorbents was

effected during the time it was exposed to the metal ions by other factors that may have caused some experimental errors to occur and influence the adsorption process of the lead metal cation.

Table 6.24: The k_2 and R^2 of Zn(II) removal calculated from the Pseudo-Second-Order kinetic model for initial sorbate concentration in $mg.L^{-1}$.

Biosorbents	k_2 $g.mg^{-1}.min^{-1}$				$R^2{}_2$			
	2	5	10	20	2	5	10	20
CTS	3.951	0.404	-0.036	-0.018	0.804	0.657	0.253	0.259
CTS-NF	0.010	0.004	0.001	0.001	0.973	0.727	0.272	0.943
chnw/EVOH	0.025	0.021	0.018	0.016	0.941	0.952	0.833	0.961
CTS-NP/EVOH	0.029	0.039	0.022	0.030	0.897	0.635	0.985	0.843
CTS/EVOH	0.378	0.025	0.033	0.030	0.573	0.981	0.998	0.331

Table 6.25: Theoretical adsorption capacities of Zn(II) removal calculated from the Pseudo-Second-Order kinetic model for all biosorbents.

Biosorbents	$q_{e(theo)2}$ $mg.g^{-1}$			
	2 $mg.L^{-1}$	5 $mg.L^{-1}$	10 $mg.L^{-1}$	20 $mg.L^{-1}$
CTS	0.9790	2.346	3.101	6.234
CTS-NF	0.8140	1.204	1.095	15.75
chnw/EVOH	80.321	2.344	1.965	4.391
CTS-NP/EVOH	-0.9490	1.859	2.229	2.987
CTS/EVOH	0.6090	2.814	4.787	8.361

All calculated constants, correlation coefficients and adsorption capacities specifically for Zn(II) removal for all biosorbents at each initial Zn(II) concentration are listed in the Table 6.24 and 6.25. The data for the theoretical adsorption capacities calculated with Type 2 plot correlated extremely well with the experimental adsorption capacities of CTS powder. The linear fit for the plot belonging to Type 1, however, was closer to 1 than that seen for Type 2. The best fit for CTS powder was found at 2 $mg.L^{-1}$, using Type 2, where the experimental q_e is 0.9800 $mg.g^{-1}$ and the theoretical q_{e2} is 0.9790 $mg.g^{-1}$. Good correlation can be seen for chnw/EVOH composite nanofibers between the experimental and theoretical adsorption capacities, using Type 2, where the best fit between the theoretical and the experimental adsorption capacity is found at the initial Zn(II) concentration of 10 $mg.L^{-1}$, where the experimental q_e is 1.995 $mg.g^{-1}$ and the theoretical q_{e2} is 1.965 $mg.g^{-1}$. The best correlation for CTS-NF is found, using Type 2, at an initial Zn(II) concentration of 2 $mg.L^{-1}$, where the experimental q_e is 0.9140 $mg.g^{-1}$ and the theoretical q_{e2} is 0.8140 $mg.g^{-1}$. CTS/EVOH showed good linear fit with Pseudo-Second-Order Type 1 but there was no correlation between the theoretical data and the

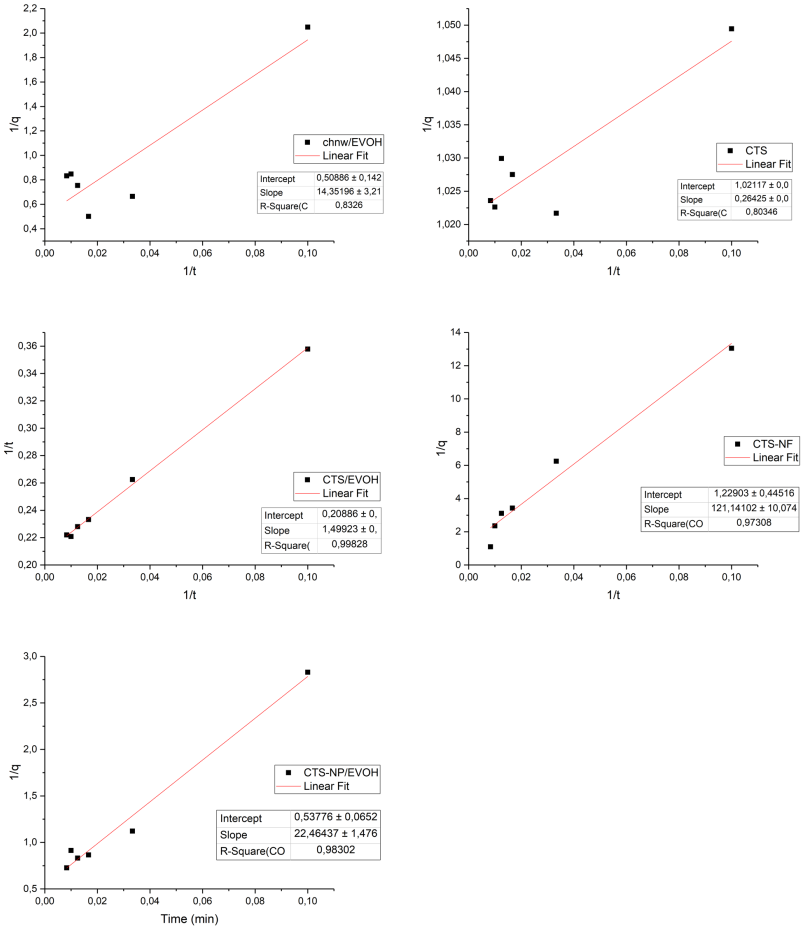

Figure 6.20: Pseudo-Second-Order kinetic model of zinc removal for each biosorbent.

experimental data, overall initial zinc ion concentration. Slightly lower R^2_2 values were obtained using Type 2 but the correlation between the experimental and theoretical data was improved. The best correlation for CTS/EVOH was found at an initial Zn(II) concentration of 10 mg.L^{-1}, where the experimental q_e is 4.506 mg.g^{-1} and the theoretical q_{e2} is 4.787 mg.g^{-1}. The best correlation for CTS-NP/EVOH composite nanofibers is found, using Type 2, at an initial Zn(II) concentration of 5 mg.L^{-1}, where the experimental q_e is 1.380 mg.g^{-1} and the theoretical q_{e2} is 1.859 mg.g^{-1}. The best linear fit and correlation to the experimental adsorption capacity that was found for each biosorbent are presented in Figure 6.20. Good correlation, where R^2_2 is close to 1, was seen for all biosorbents with the Pseudo-Second-Order kinetic model indicating that Zn(II) removal occurred via a chemisorption process.

The linear fit did not seem to correspond to how well the agreement between the theoretical and experimental adsorption capacities are. The best correlation between the experimental and theoretical adsorption capacities was obtained using the Pseudo-Second-Order kinetic model Type 2, for all biosorbents. CTS/EVOH and CTS powder favored Type 1, with good linear fit to the data and R^2_2 close to 1. The overall linear fit us-

ing Type 2 was acceptable for CTS/EVOH and CTS powder and excellent for CTS-NF, chnw/EVOH-and CTS-NP/EVOH composite nanofibers. Some negative values for the Pseudo-Second-Order of type 2 can be seen indicating that the kinetic model does not describe the behavior of the sorption process as effectively for that specific initial sorbate concentration. This could be caused by other influencing factors that could be playing a role in hindering sorption, such as contaminants, poor dispersion or poor retention of the heavy metal ions. The linearised plots for Type 1 and 2 where applicable are shown in full for each biosorbent in Appendix A.

Overall, the theoretical and experimental data correlated well for the Pseudo-first-order kinetic models, as the correlation coefficient (R^2) approached 1. CTS powder did not seem to correlate well with the data obtained using Pseudo-first-order. The accuracy of the correlation between the theoretical and experimental data also seemed to be affected by the initial sorbate concentration. For the Pseudo-second-order kinetic models, the R^2 value did not appear to have an affect on how well the theoretical and experimental data correlate. Type 2 of the Pseudo-second-order kinetic models appeared to fit the best with all the data of belonging to each biosorbent. CTS/EVOH sponges and CTS powder appeared to fit better with on the linearised plots of Type 1 of the Pseudo-second-order kinetic models. However, as mentioned, Type 2 fitted the experimental adsorption capacity the best between all types of Pseudo-second-order and first-order kinetic models.

Chapter 7

General conclusions and recommendations

7.1 Summary

The biosorbents from this study were compared with several other low-cost polymers and materials that were previously investigated in literature studies, and that were also tested for the removal of the same heavy metals investigated during this research. The results for each of the materials with corresponding adsorption capacity for a specific heavy metal ion are listed in Table 7.1. It is important to note that this is just a general comparison and that for complete accuracy in direct comparison, the experimental procedures and parameters, as well as variables, should be similar. Unfortunately, many of these studies use different initial sorbate concentrations, slightly different pH-conditions, different temperatures, different time intervals and different analysis and preparation instrumentation. The amount of adsorbent can also influence the adsorption process and results that could affect the overall theoretical values that are used for comparison. Different types and amounts of contaminants in the systems can also cause variations in the results of different lab environments and affect the adsorption capacities. It is therefore just as important to note that this comparison is simply to show the effectiveness of each adsorbent in general and to give some idea how the newly developed biosorbents, from this study, can compete with existing low cost adsorbents.

During this study the effect of initial sorbate concentration, pH and contact times were investigated for each biosorbent (CTS powder, CTS-NF, chnw/EVOH composite nanofibers, CTS-NP/EVOH composite nanofibers and CTS/EVOH sponges) with various types of heavy metal ions (copper, chromium, nickel, zinc and lead). Other studies have neglected to report the drastic desorption that was generally observed for CTS powder after a longer contact time (seen for small dosages of CTS powder), in this study. Effective retention of heavy metal ions is an important aspect that needs to be taken into consideration when

Table 7.1: Adsorption capacities of other available low cost adsorbents.

Biosorbents	Maximum adsorption capacity ($mg.g^{-1}$)					Ref
	Zn(II)	Cu(II)	Pb(II)	Ni(II)	Cr(VI)	This research
CTS powder	9.26	5.44	4.84	24.88	46.29	This research
CTS-NF	11.75	232.56	76.34	416.67	63.69	This research
chnw/EVOH composites nanofibers	6.71	5.31	23.75	4.78	4.33	This research
CTS-NP/EVOH composites nanofibers	9.73	71.43	35.34	42.19	10.89	This research
CTS/EVOH sponge	1.99	2.89	10.44	15.85	17.73	This research
Peat			82.31	61.27		[106]
Wheat straw				41.84	47.16	[42, 131]
Barley straw				35.80		[136]
Tea factory waste				18.42		[137]
Peat (Brazil)	12.00			14.00	37.90	[138]
Peat (Ireland)				11.42		[77]
Jute Fibers	3.55	4.33		3.37		[29]
Peat (Indonesia)	23.00		79.68			[139]
Coconut shell			24.24			[140]
Rice straw			24.17			[140]
Hyacinth Roots			24.94			[140]
Orange peel				9.80		[96]
Peat (Bruneian)			14.97			[130]
Commercial activated carbon	10.50		12.30	10.50	12.80	[138]
Rice Husk carbon	8.21		7.96	9.62	37.20	[138]
Modified Jute fibers (dye loaded)	8.02	7.73		5.57		[29]
Natural Zeolite	1.32	1.12				[105]
Peanut husk charcoal	0.37	0.35				[105]
Natural Chitosan					65.70	[87]

selecting a suitable biosorbent. Another aspect of selecting an acceptable sorbent is the ease of removal without leaving behind residue or requiring additional steps of filtration. CTS powder along with other low-cost adsorbents mentioned in the Table above are only removed using filtration (filter paper or filtration syringes). This leads to unnecessary waste and increased the duration of the removal process as well as larger chances for contaminants to be introduced into the analyte.

The increase in initial sorbate concentration (C_i) showed an increase in adsorption capacity for all biosorbents. The general trend for an increase in contact time was an increase in adsorption capacity, with the exception seen for CTS powder due to low retention possibly caused by a low surface area. CTS-NF showed the highest maximum adsorption capacity for all heavy metals followed by CTS-NP/EVOH composite nanofibers and CTS powder. CTS/EVOH sponges also showed a high adsorption capacity for the heavy metal ions. Chnw/EVOH composite nanofibers had a higher maximum adsorption capacity for lead compared to CTS/EVOH sponges, while CTS powder presented the lowest maximum adsorption capacity for lead. All biosorbents showed favourable adsorption with the R_L and

K_F values adhering to the optimal parameters. At optimal conditions, the biosorbents showed good correlation to the Langmuir isotherm model and the Psuedo-second-order kinetic model. The theoretical and experimental data ($q_{e(theo)}$ and $q_{e(exp)}$) correlated well for all biosorbents using the Langmuir isotherm model Type 1 and Pseudo-second-order type 2. Desorption studies established the reusability of the biosorbents and showed that the CTS powder and the CTS-NF were more vulnerable to the changing conditions (acidic solutions) in the environment, while chnw/EVOH composite nanofibers proved to be the most stable. The CTS-NP/EVOH composite nanofibers and CTS/EVOH sponges also showed relatively good stability compared to CTS-NF and CTS powder, but some dissolution occurred for the CTS and CTS-NP. CTS/EVOH sponges and CTS-NP/EVOH composite nanofibers were slightly more challenging for the heavy metal ions to desorb from the material, indicating good retention for heavy metal ions. Each biosorbent had different optimal parameters for the most effective removal of heavy metal ions. Similar to literature studies, CTS powder had an optimal adsorption in a solution with a pH of 5. CTS-NP/EVOH composite nanofibers and CTS/EVOH sponges showed the best adsorption under the same pH conditions as CTS powder while CTS-NF and chnw/EVOH composite nanofibers, interestingly, showed good adsorption in a solution with a pH of 5 and 11 specifically for Ni(II) and Zn(II). The optimal initial sorbate concentration varied slightly for each biosorbent was establish to be within the range of 5 to 10 $mg.L^{-1}$. The adsorption capacity increased as the initial adsorption capcity increased but the general adsorption rate decreased due to higher competition between the metal ions for available sorption sites. CTS powder showed good adsorption for initial sorbate concentration of 10 $mg.L^{-1}$ after 30 minutes. CTS-NF, chnw/EVOH composite nanofibers, CTS/EVOH sponges and CTS-NP/EVOH composite nanofibers had high percentage removal of heavy metal ions after 120 minutes at initial sorbate concentrations varying between 5 to 10 $mg.L^{-1}$. The chnw/EVOH and CTS-NP/EVOH composite nanofibers showed some limited sorption sites available for interaction with heavy metals and therefore exhibited signs of increased competition at higher initial sorbate concentration. The heavy metal ions showed preference to oxygenated and nitrogen-rich sorption sites. Parameters that played a role with the affinity of each heavy metal for a specific sorption site appeared to be the chemical properties such electronegativity, charge density, polarizability (based on ionic radii) and the HSAB principle where hard acids are more likely to interact with hard bases, such as the amine ligand found on the biosorbents.

CTS-NF shows excellent sorption capabilities over a wide range of heavy metals. The only drawback for CTS-NF is that the nanofibers does not seem to hold well after regeneration and can become unstable during re-use. CTS-NP/EVOH composite nanofibers shows similarly good adsorption capacity for a wide range of heavy metals and proved to be more stable under changing conditions and after regeneration. Chnw/EVOH composite nanofibers showed high selectivity for softer metal ions such as Pb(II). This biosorbent

behaved excellently in extreme pH conditions and remained stable after regeneration. CTS/EVOH sponges showed a high affinity and selectivity for harder metal ions such as Ni(II) and Zn(II).

All the materials used in the synthesis of the biosorbents of this study are abundant, locally available and low cost. Each biosorbent showed good adsorption capacity for either specific or all heavy metal ions. These biosorbents are considered viable for the removal of heavy metal ions from aqueous solutions and can compete with other low-cost adsorbents currently available.

7.2 Future work and Recommendations

In future studies, an additional modification to the surface of chnw/EVOH composite nanofibers should be made to enhance the sorption efficiency of the sorption sites. The surface can be coated with an oxidizer such as nitric acid to enhance the charge on the surface of the material. More types of heavy metals can be investigated in future studies, such as iron and cadmium. The effect of temperature variation can also be investigated in future research for these specific biosorbents. Contact angle studies should be done to obtain the contact between the solute and sorbent (fibres) as well as the wettability of the sorbent. Selectivity of the biosorbents can be investigated in more detail using mixed samples from mining facilities and industrial wastewater. Investigation and collaboration with engineering scientists is suggested to manufacture an environmentally friendly scaffold that can hold the nanofiber sorbents in place thus allowing maximum exposure during the adsorption process.

Appendix A

Kinetic models

A.1 Pseudo-First-Order

A.2 Pseudo-Second-Order

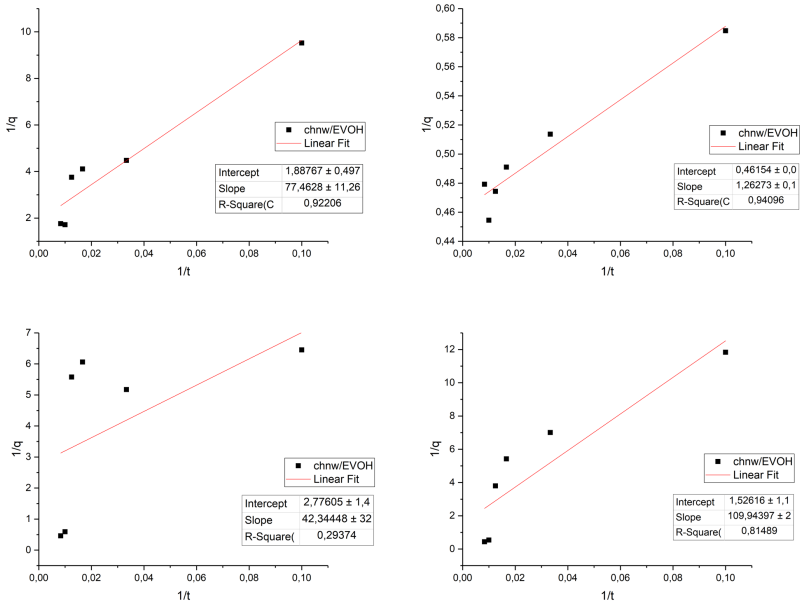

Figure A.1: Kinetic second order Type 2 of Cr(VI) removal for chnw/EVOH NF for all initial sorbate concentration.

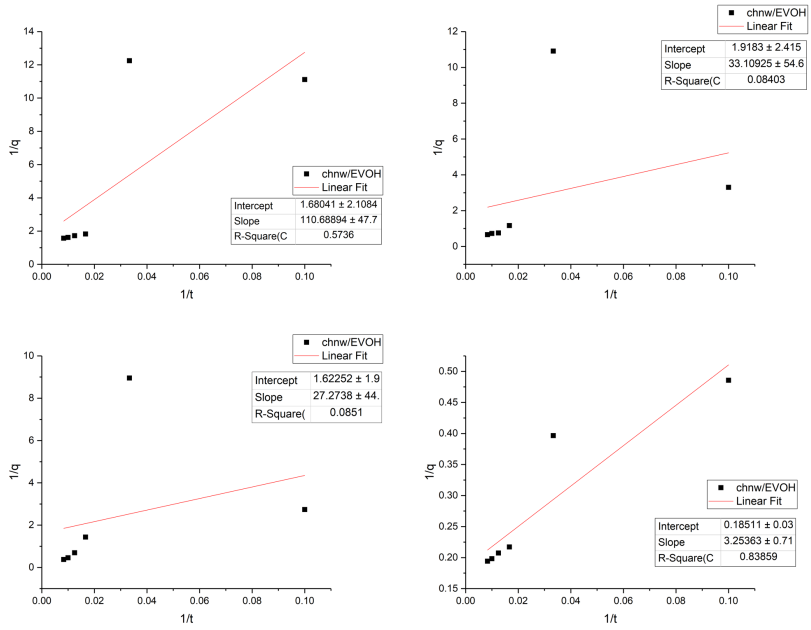

Figure A.2: Kinetic second order Type 2 of Cu(II) removal for chnw/EVOH NF for all initial sorbate concentration.

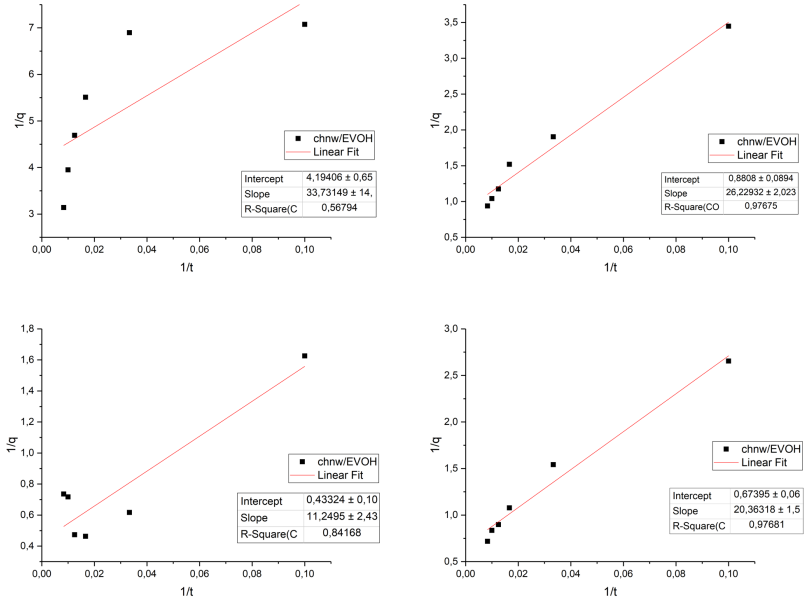

Figure A.3: Kinetic second order Type 2 of Ni(II) removal for chnw/EVOH NF for all initial sorbate concentration.

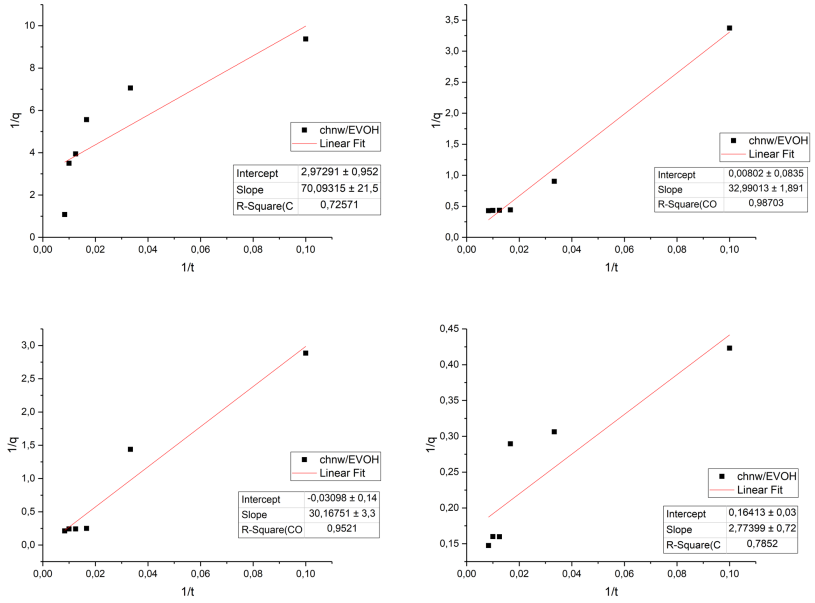

Figure A.4: Kinetic second order Type 2 of Pb(II) removal for chnw/EVOH NF for all initial sorbate concentration.

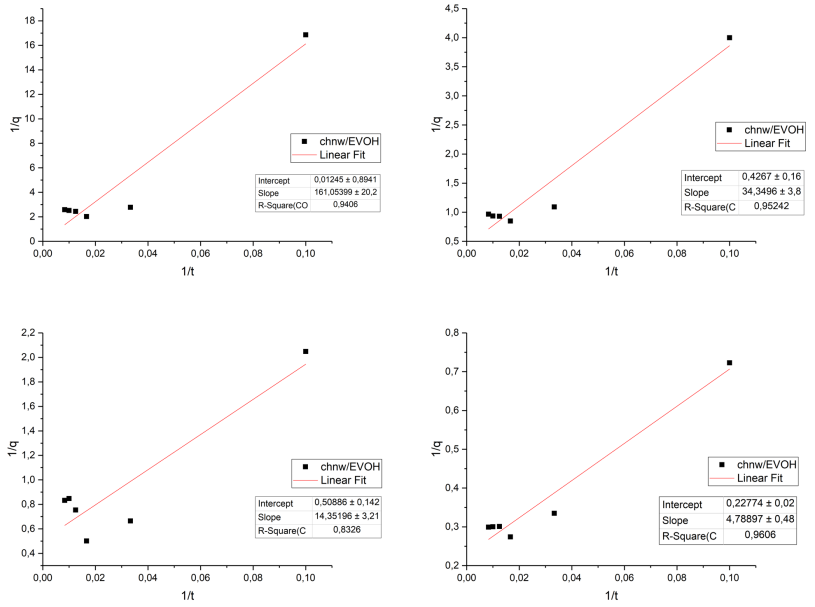

Figure A.5: Kinetic second order Type 2 of Zn(II) removal for chnw/EVOH NF for all initial sorbate concentration.

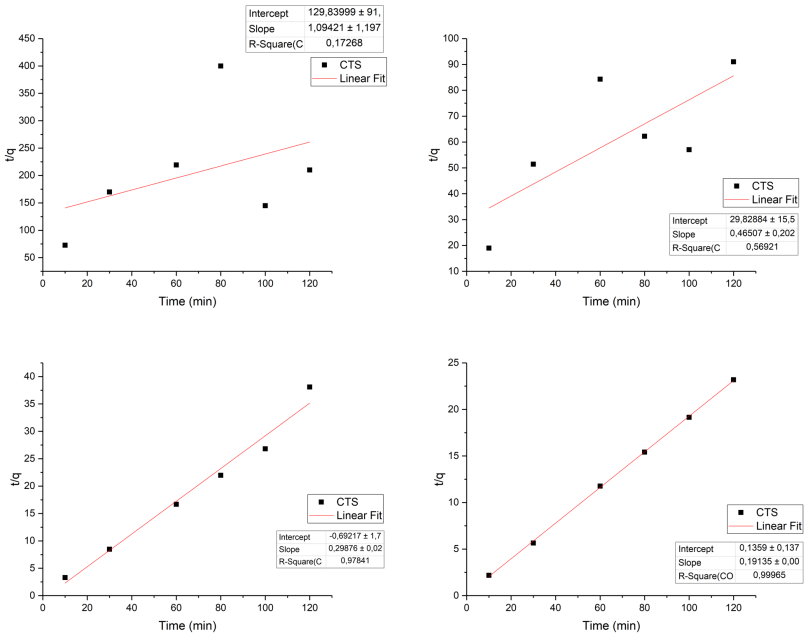

Figure A.6: Kinetic second order Type 1 of Cr(VI) removal for CTS powder for all initial sorbate concentration.

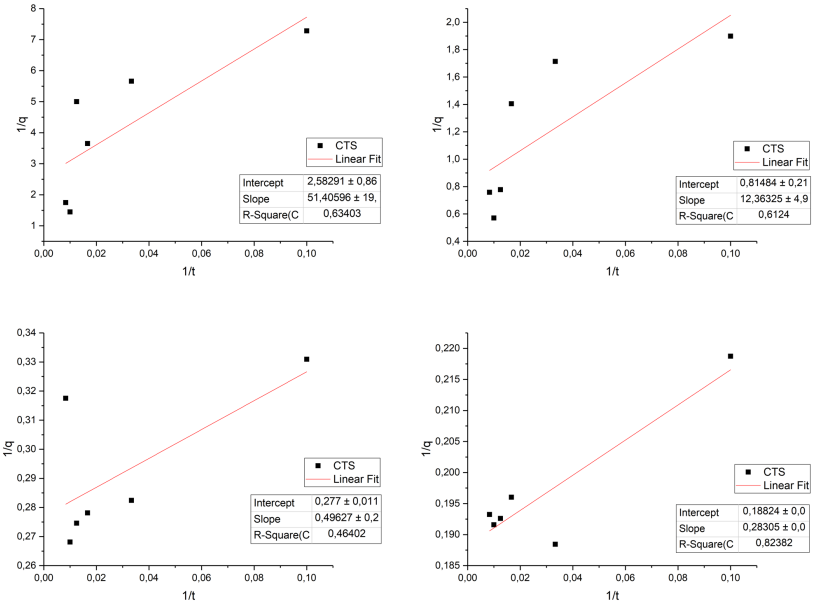

Figure A.7: Kinetic second order Type 2 of Cr(VI) removal for CTS powder for all initial sorbate concentration.

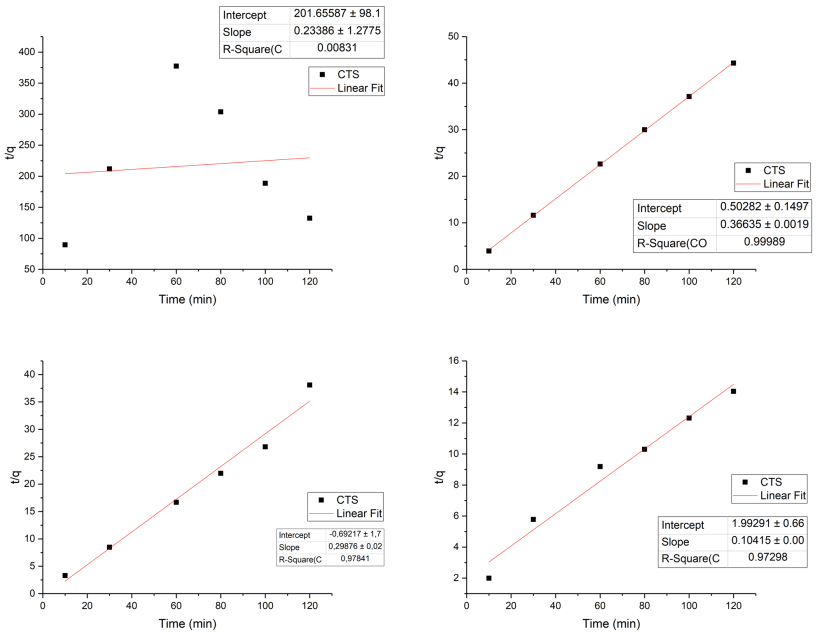

Figure A.8: Kinetic second order Type 1 of Cu(II) removal for CTS powder for all initial sorbate concentration.

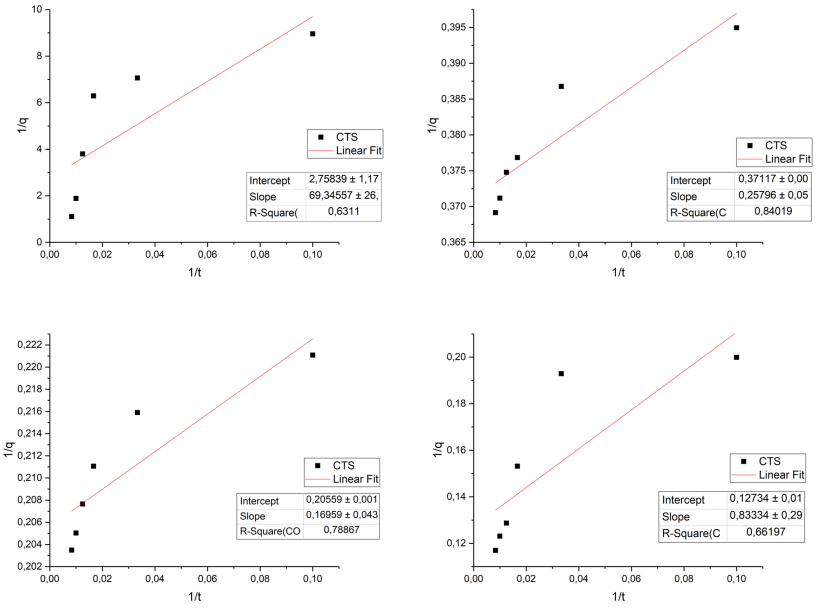

Figure A.9: Kinetic second order Type 2 of Cu(II) removal for CTS powder for all initial sorbate concentration.

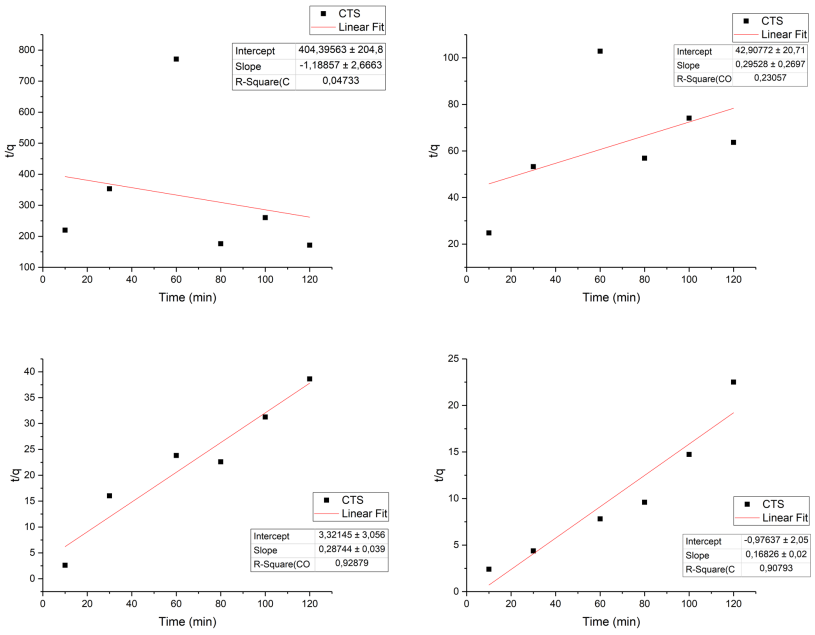

Figure A.10: Kinetic second order Type 1 of Ni(II) removal for CTS powder for all initial sorbate concentration.

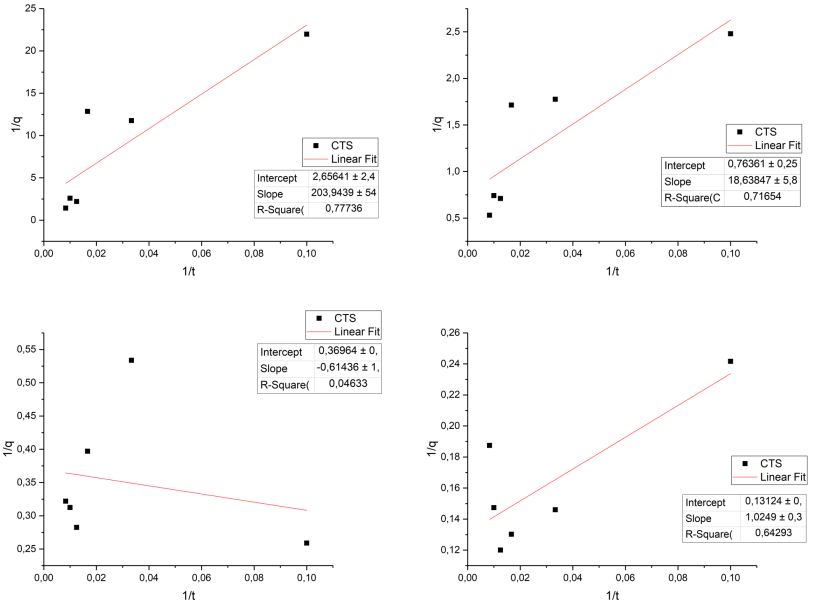

Figure A.11: Kinetic second order Type 2 of Ni(II) removal for CTS powder for all initial sorbate concentration.

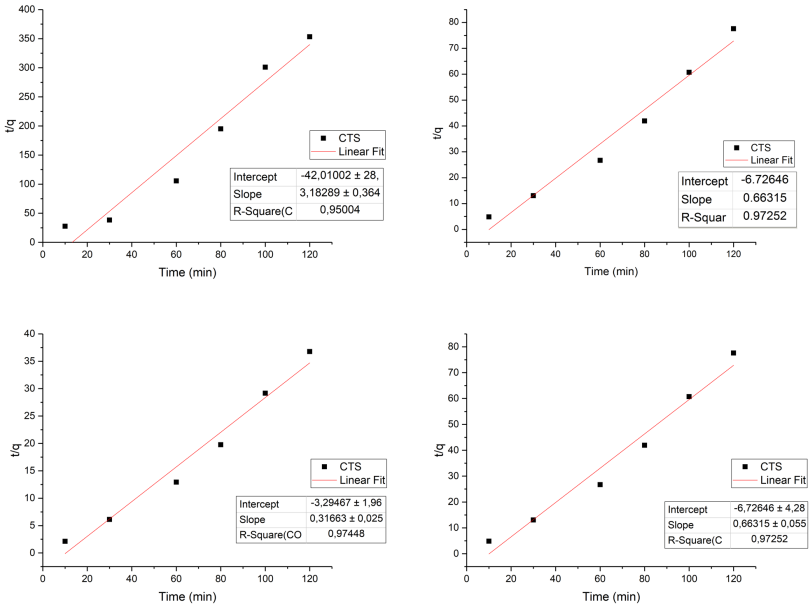

Figure A.12: Kinetic second order Type 1 of Pb(II) removal for CTS powder for all initial sorbate concentration.

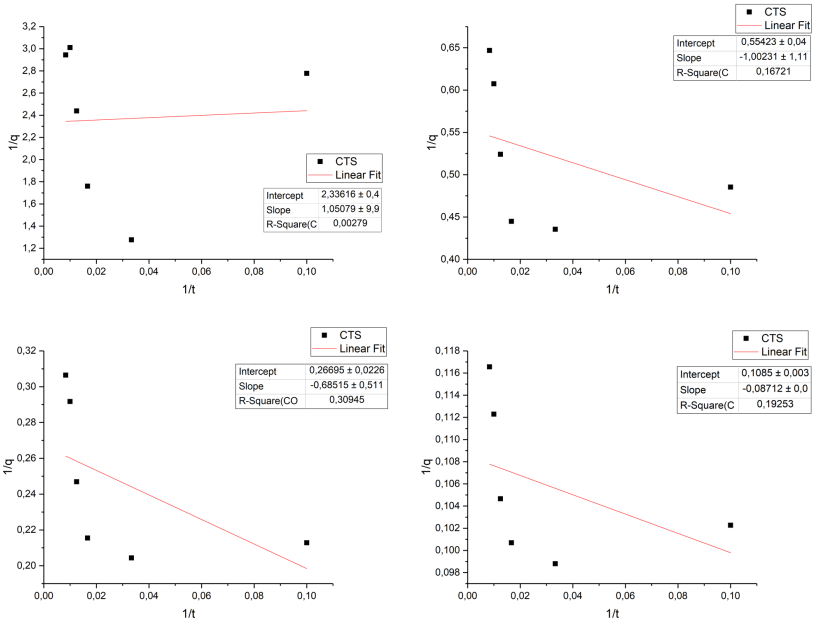

Figure A.13: Kinetic second order Type 2 of Pb(II) removal for CTS powder for all initial sorbate concentration.

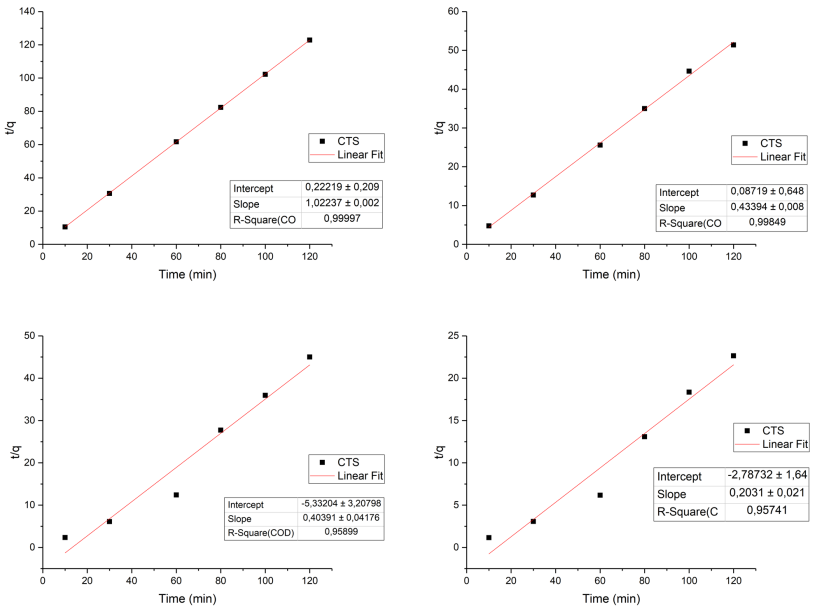

Figure A.14: Kinetic second order Type 1 of Zn(II) removal for CTS powder for all initial sorbate concentration.

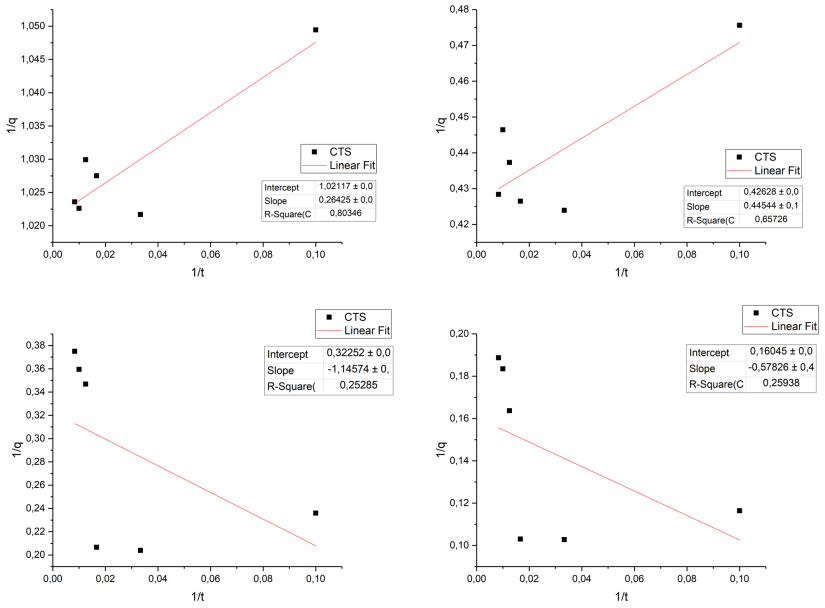

Figure A.15: Kinetic second order Type 2 of Zn(II) removal for CTS powder for all initial sorbate concentration.

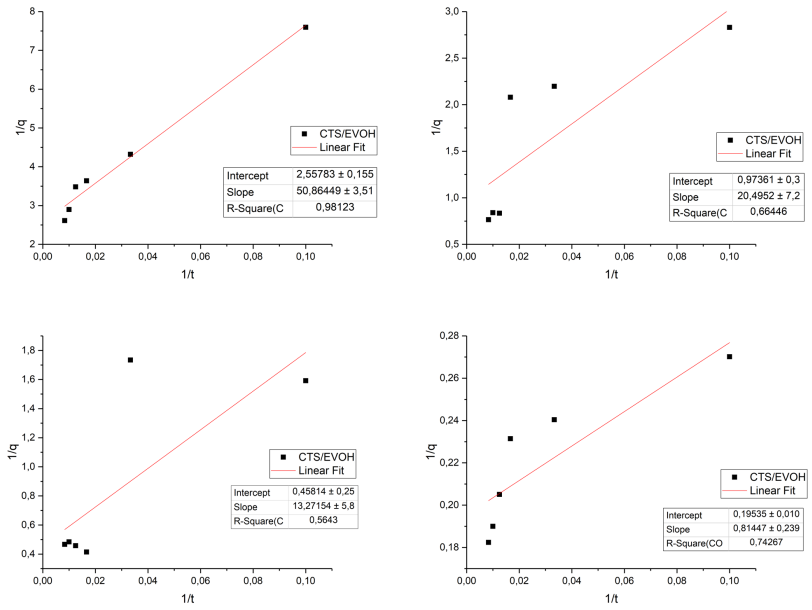

Figure A.16: Kinetic second order Type 2 of Cr(VI) removal for CTS/EVOH sponge for all initial sorbate concentration.

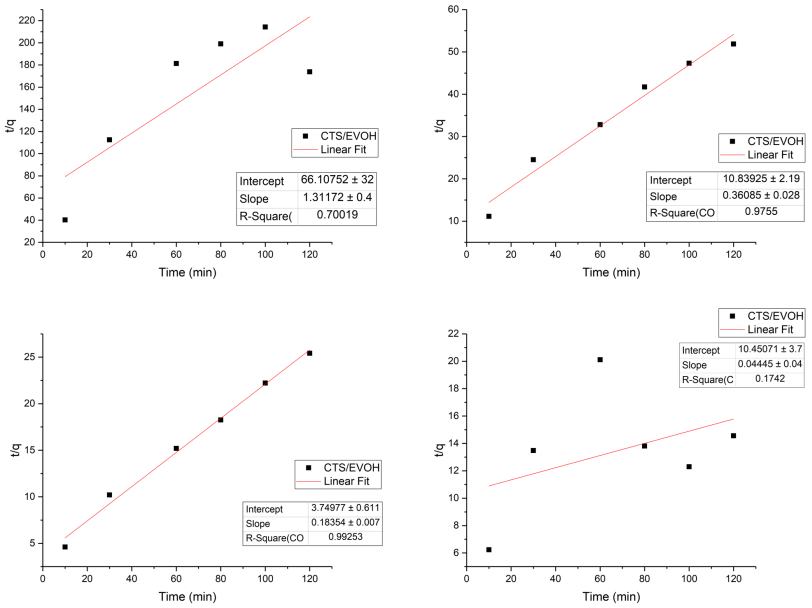

Figure A.17: Kinetic second order Type 1 of Cu(II) removal for CTS/EVOH sponge for all initial sorbate concentration.

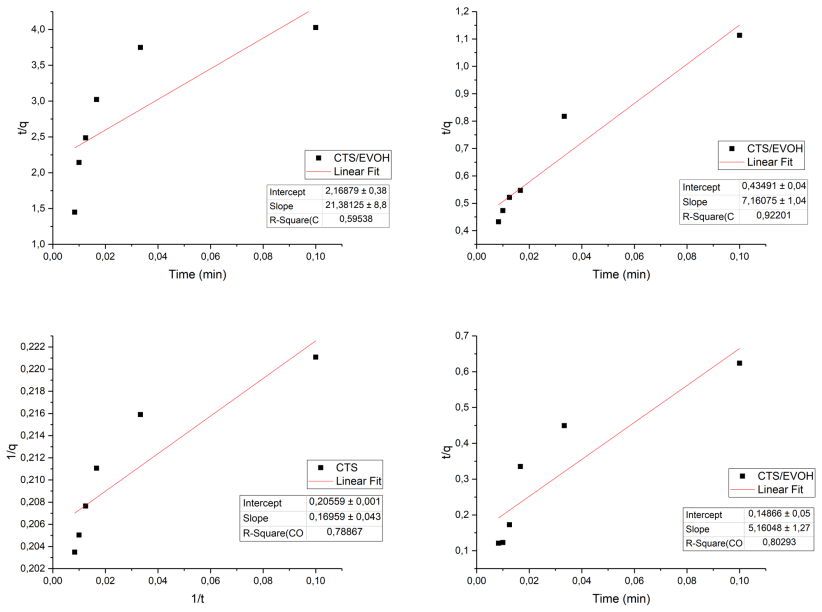

Figure A.18: Kinetic second order Type 2 of Cu(II) removal for CTS/EVOH sponge for all initial sorbate concentration.

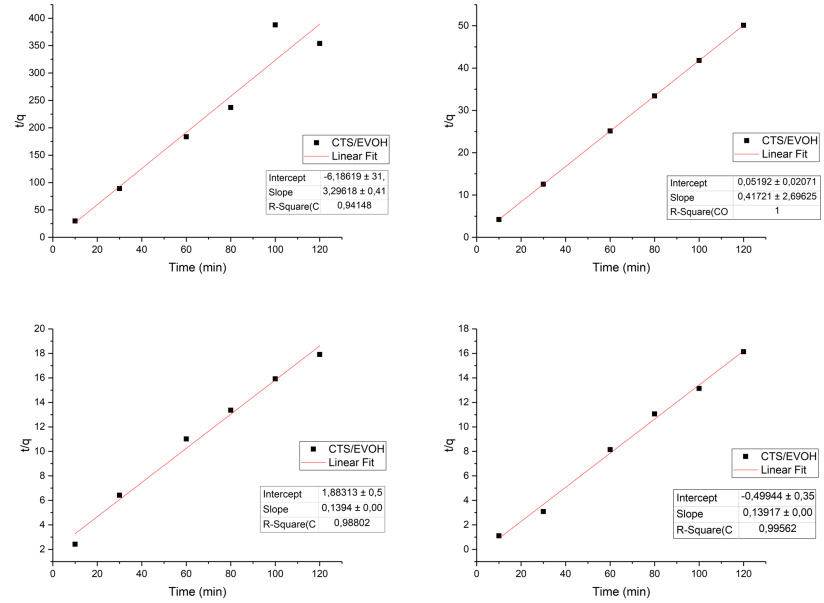

Figure A.19: Kinetic second order Type 1 of Ni(II) removal for CTS/EVOH sponge for all initial sorbate concentration.

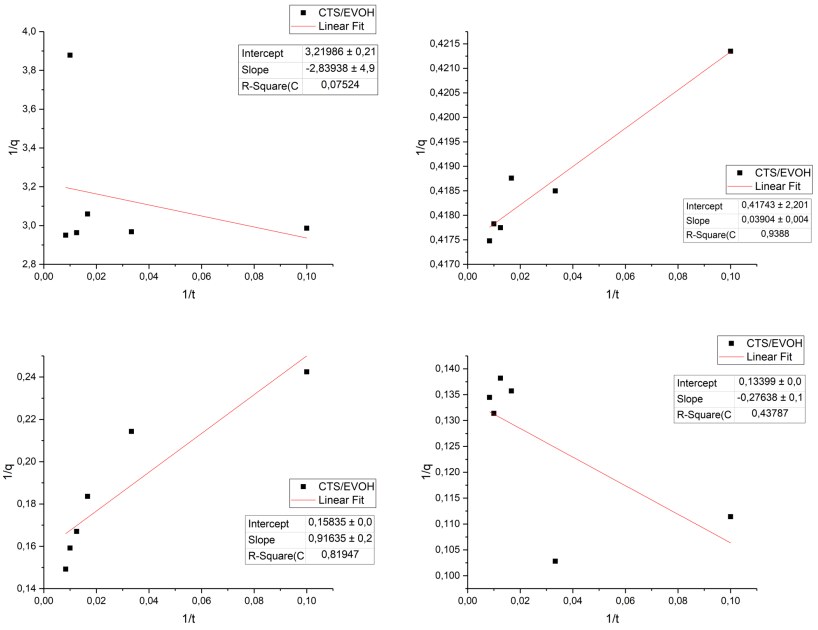

Figure A.20: Kinetic second order Type 2 of Ni(II) removal for CTS/EVOH sponge for all initial sorbate concentration.

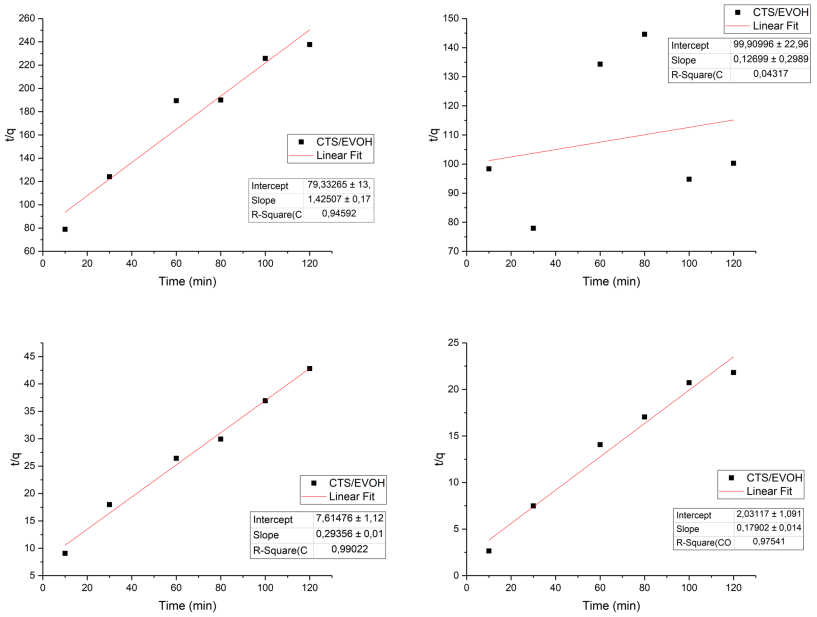

Figure A.21: Kinetic second order Type 1 of Pb(II) removal for CTS/EVOH sponge for all initial sorbate concentration.

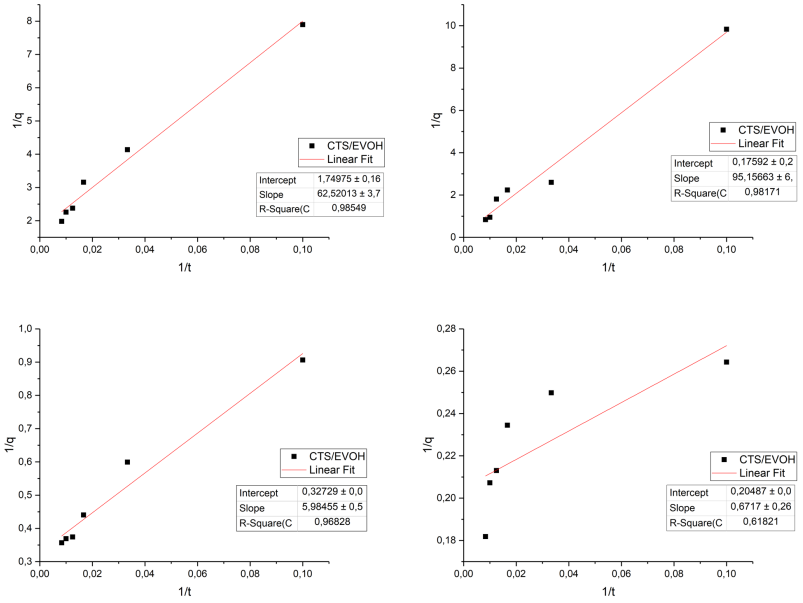

Figure A.22: Kinetic second order Type 2 of Pb(II) removal for CTS/EVOH sponge for all initial sorbate concentration.

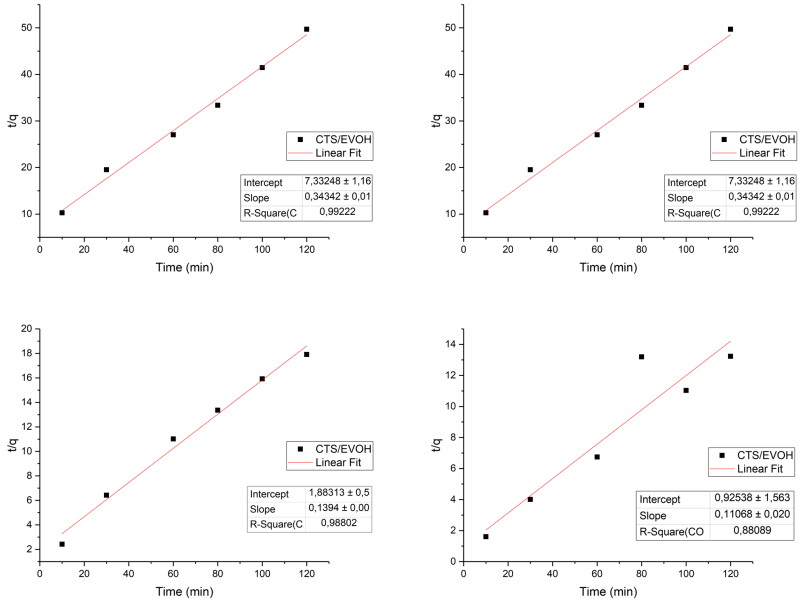

Figure A.23: Kinetic second order Type 1 of Zn(II) removal for CTS/EVOH sponge for all initial sorbate concentration.

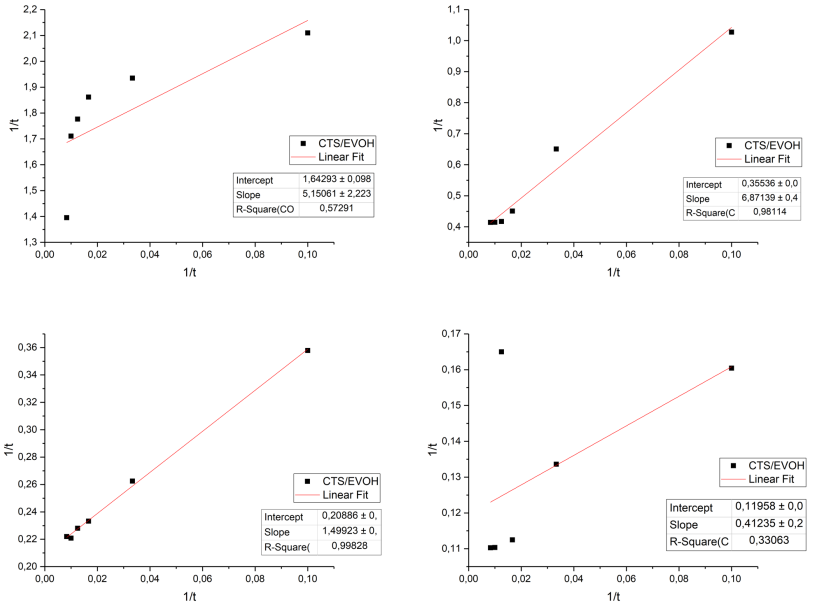

Figure A.24: Kinetic second order Type 2 of Zn(II) removal for CTS/EVOH sponge for all initial sorbate concentration.

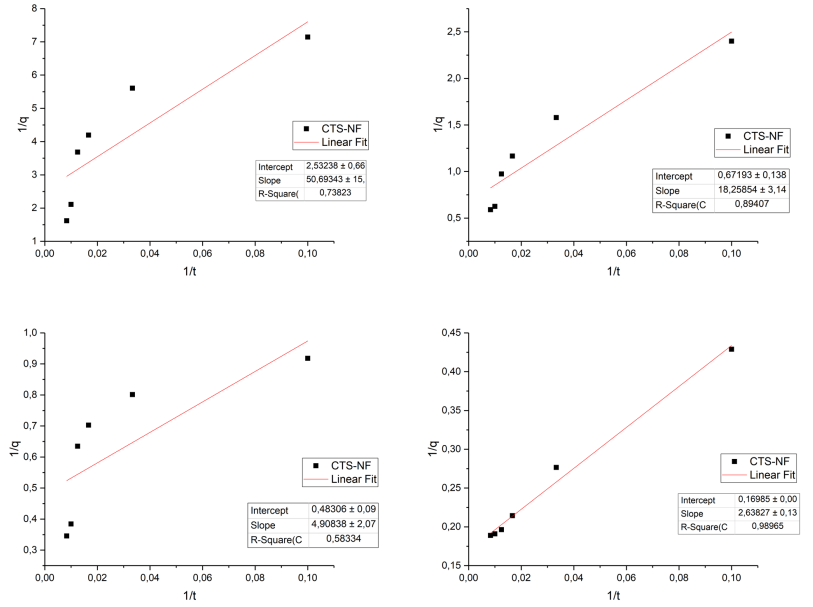

Figure A.25: Kinetic second order Type 2 of Cr(VI) removal for CTS-NF for all initial sorbate concentration.

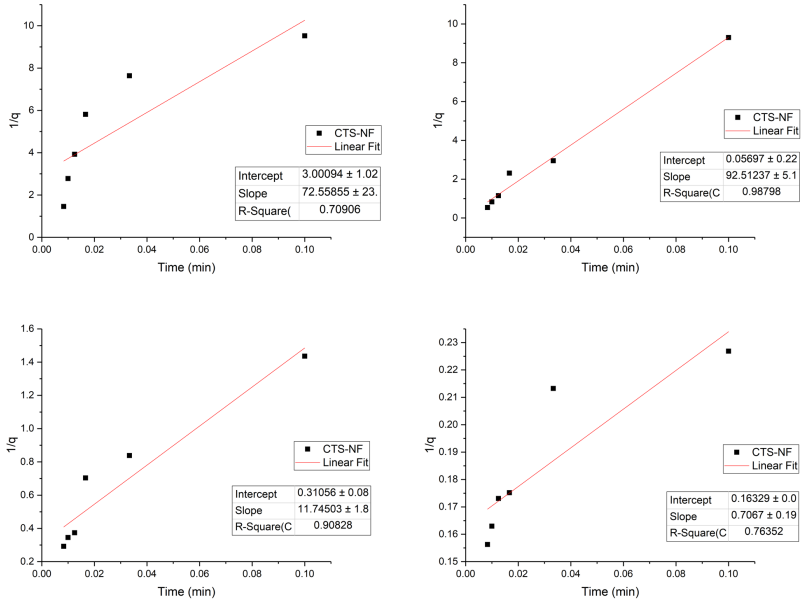

Figure A.26: Kinetic second order Type 2 of Cu(II) removal for CTS-NF for all initial sorbate concentration.

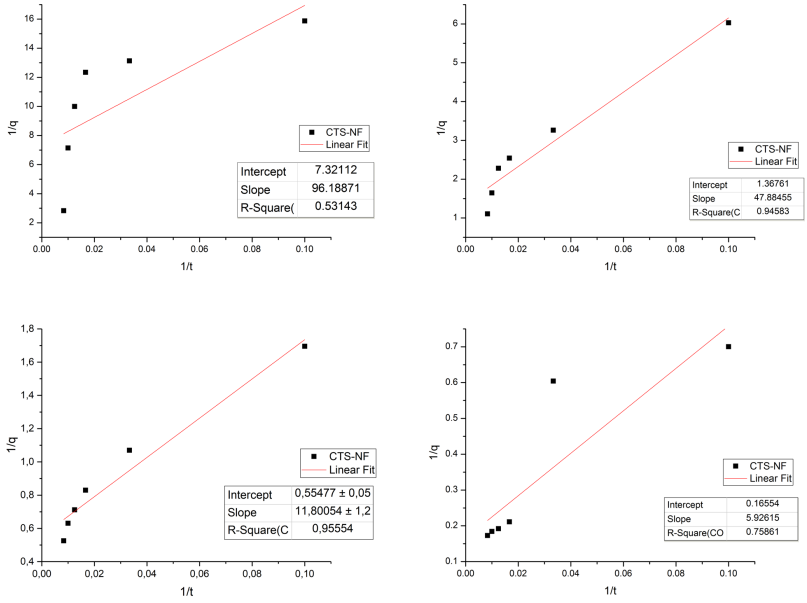

Figure A.27: Kinetic second order Type 2 of Ni(II) removal for CTS-NF for all initial sorbate concentration.

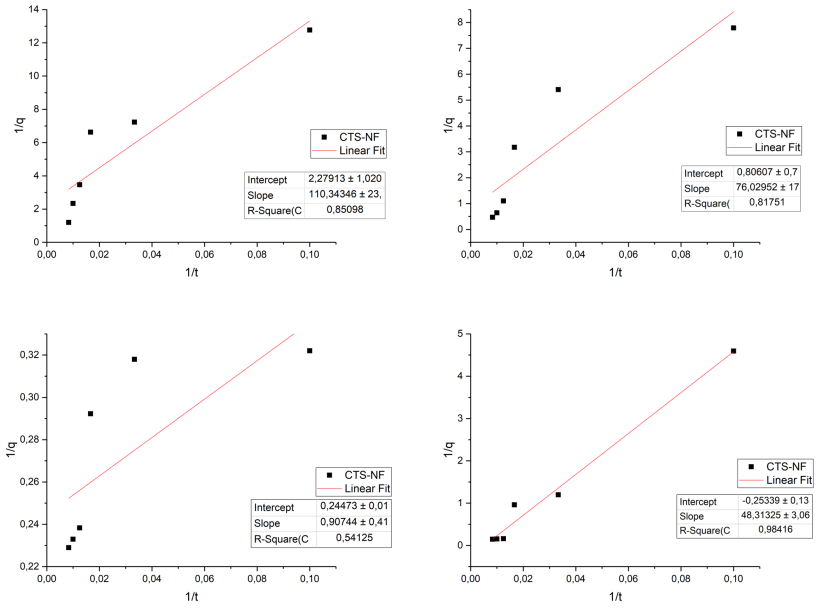

Figure A.28: Kinetic second order Type 2 of Pb(II) removal for CTS-NF for all initial sorbate concentration.

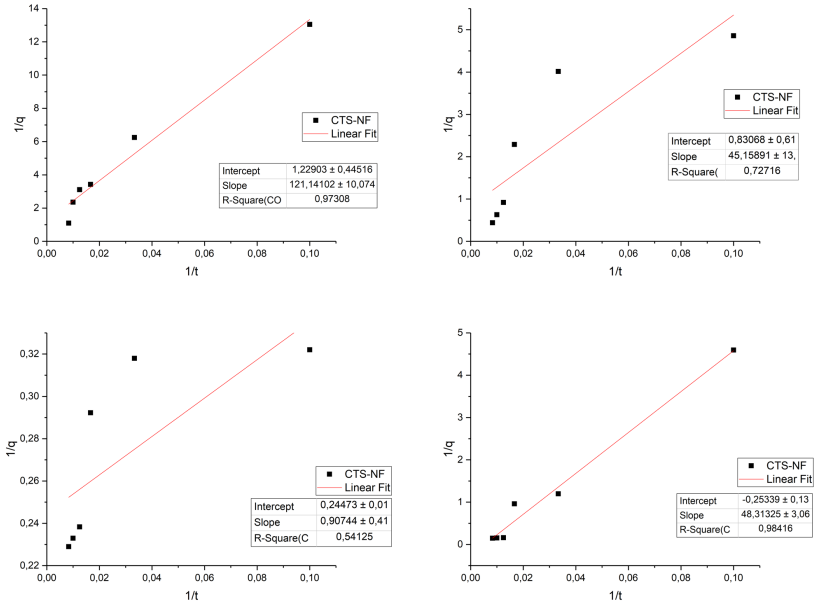

Figure A.29: Kinetic second order Type 2 of Zn(II) removal for CTS-NF for all initial sorbate concentration.

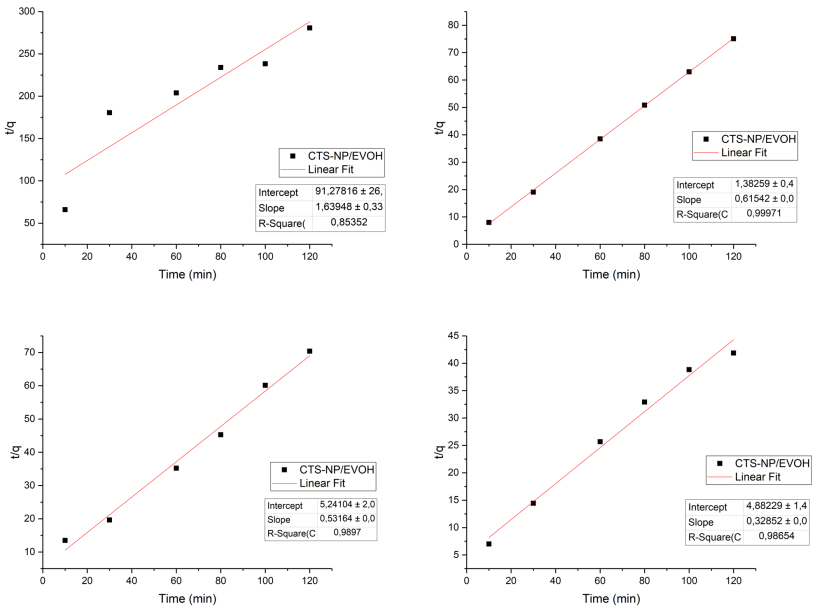

Figure A.30: Kinetic second order Type 1 of Cr(VI) removal for CTS-NP/EVOH NF for all initial sorbate concentration.

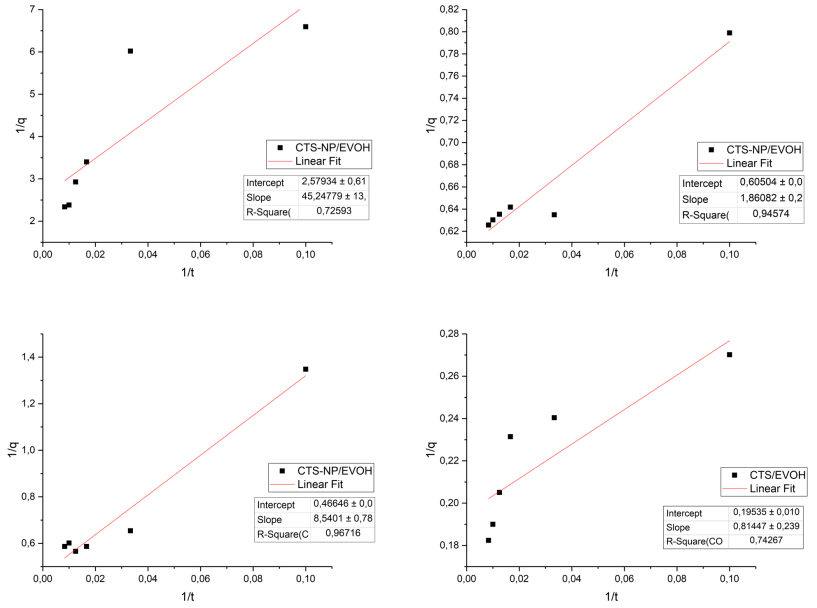

Figure A.31: Kinetic second order Type 2 of Cr(VI) removal for CTS-NP/EVOH NF for all initial sorbate concentration.

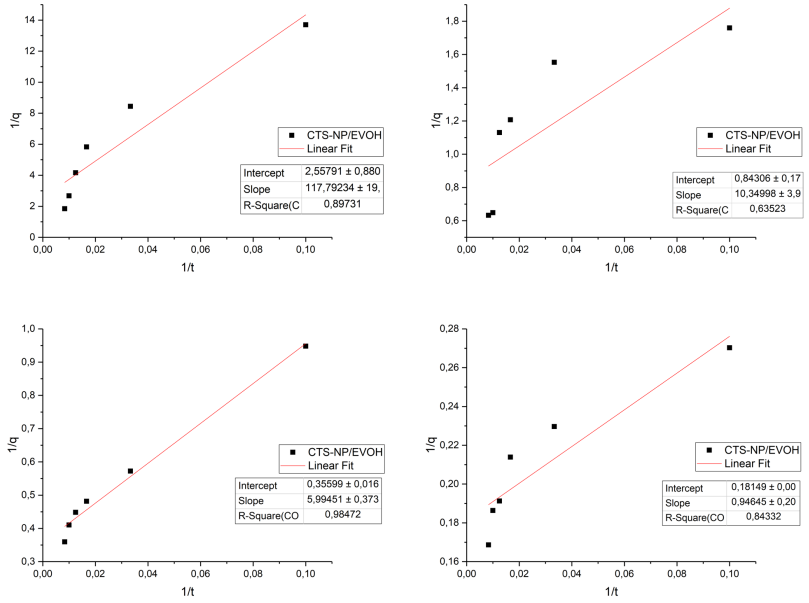

Figure A.32: Kinetic second order Type 2 of Cu(II) removal for CTS-NP/EVOH NF for all initial sorbate concentration.

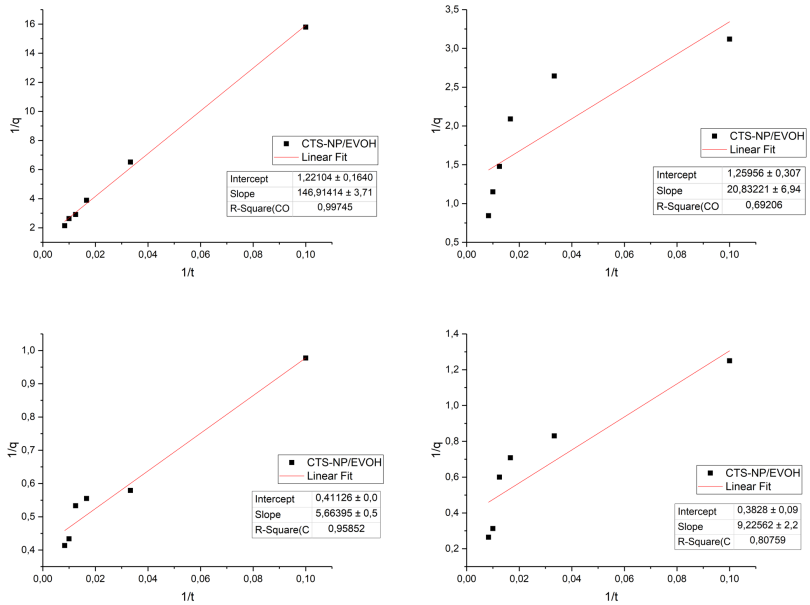

Figure A.33: Kinetic second order Type 2 of Ni(II) removal for CTS-NP/EVOH NF for all initial sorbate concentration.

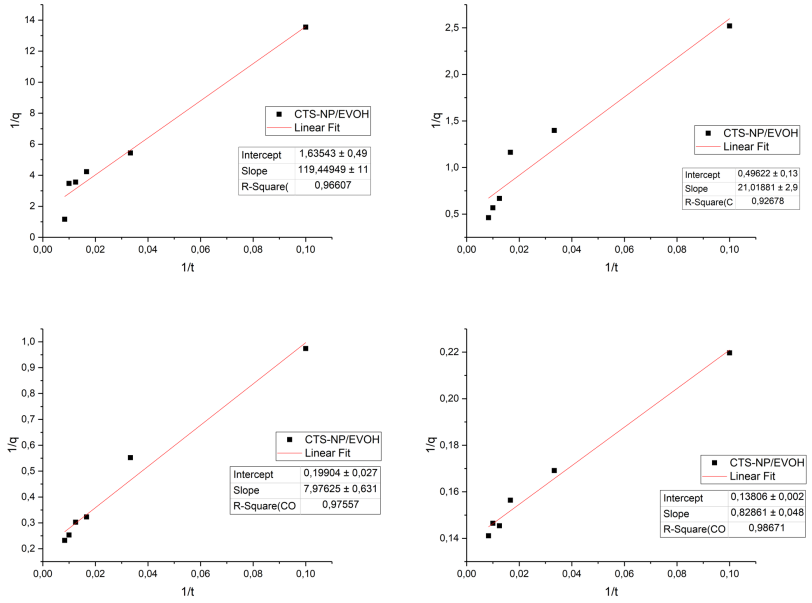

Figure A.34: Kinetic second order Type 2 of Pb(II) removal for CTS-NP/EVOH NF for all initial sorbate concentration.

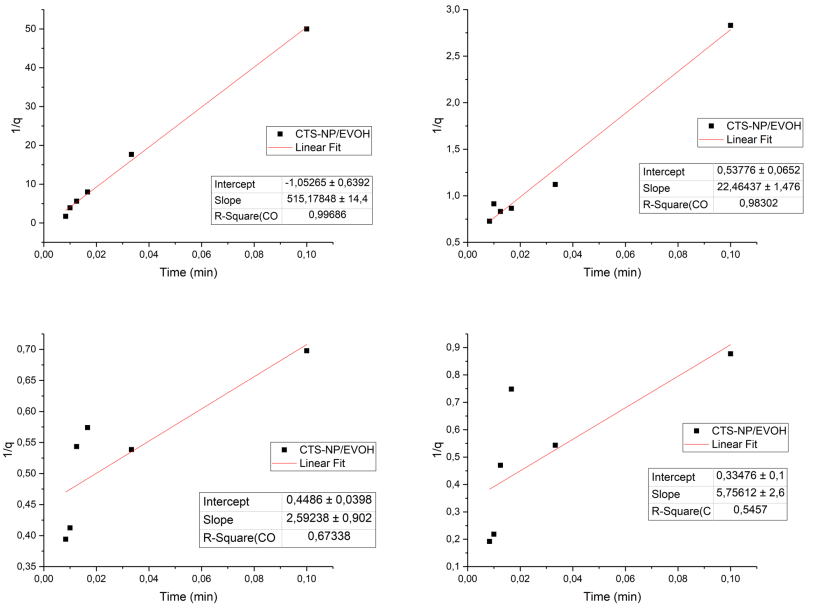

Figure A.35: Kinetic second order Type 2 of Zn(II) removal for CTS-NP/EVOH NF for all initial sorbate concentration.

Appendix B

Additional characterisation and adsorption data

B.1 Adsorption data for prisitine EVOH

Additional crude adsorption studies were conducted on EVOH in pristine form, in order to verify that the main adsorption occurs on the chitosan and chitin nanowhisker components. In Figure B.1 the results are summarised for pristine EVOH for the adsorption of Zn(II).

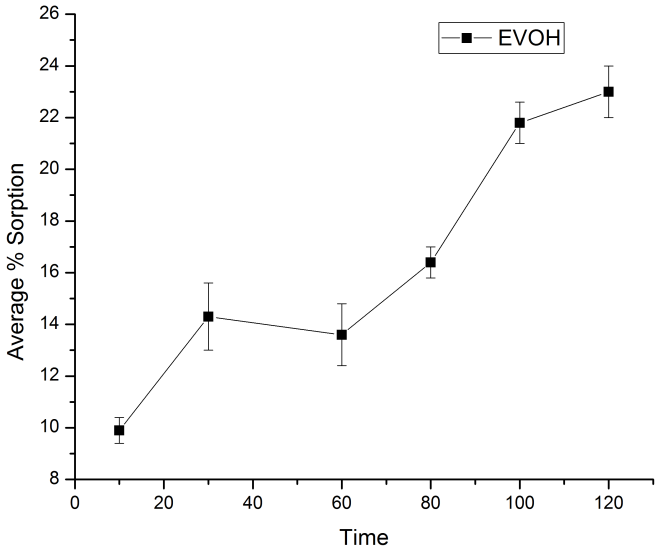

Figure B.1: Adsorption of Zn using pristine EVOH

The insignificant change in concentration gives the impression that EVOH does not adsorb efficiently even when in pristine condition where the hydroxyl groups are not interacting

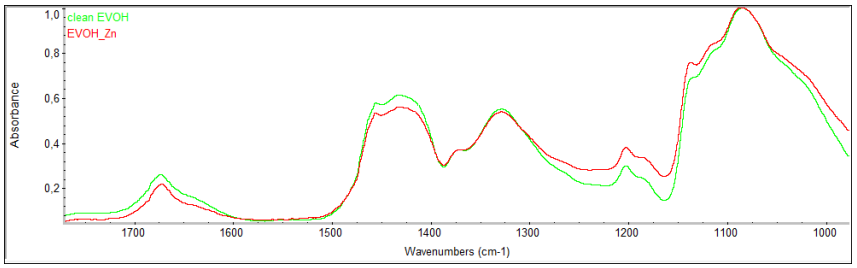

Figure B.2: FTIR of Pristine EVOH before and after Zn(II) adsorption

with chnw. The adsorption capacity of EVOH remains low even after 2 hours in ambient pH conditions of pH 5.

B.2 Additional FTIR data

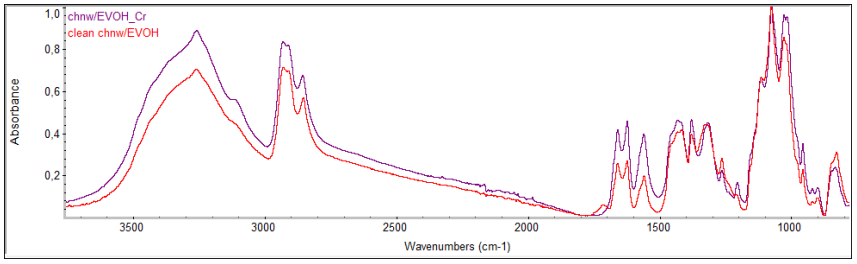

Figure B.3: The influence of Cr(VI) on the FTIR spectrum of chnw/EVOH nanofiber.

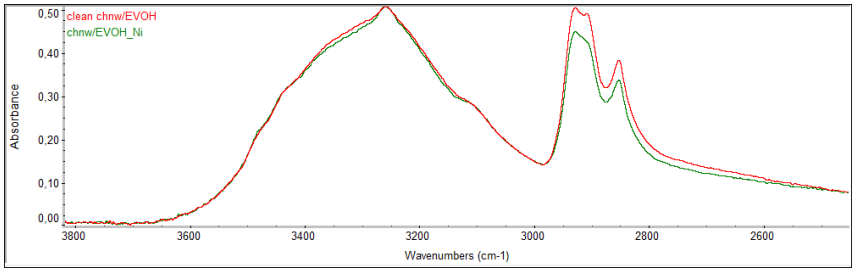

Figure B.4: Influence of Ni(II) on the peaks of chnw/EVOH nanofibers.

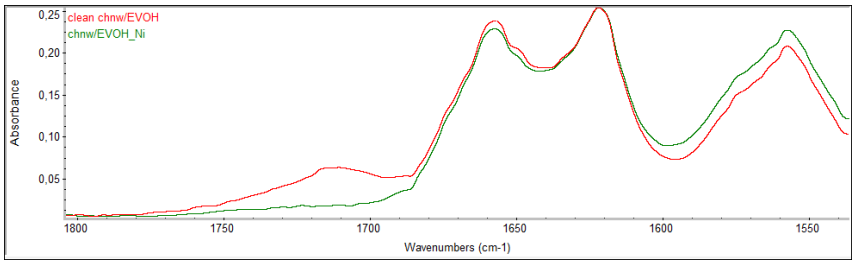

Figure B.5: Influence of Ni(II) on the peak intensities of chnw/EVOH nanofibers.

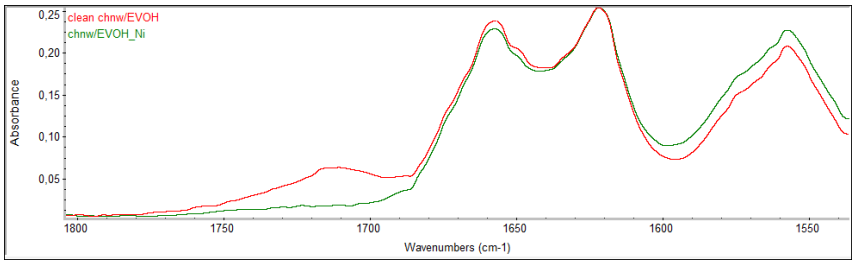

Figure B.6: Influence of Ni(II) on the peak intensities of chnw/EVOH nanofibers.

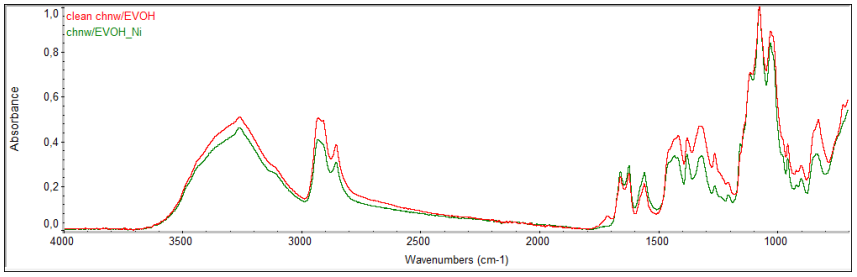

Figure B.7: Influence of Ni(II) on the peak intensities of chnw/EVOH nanofibers.

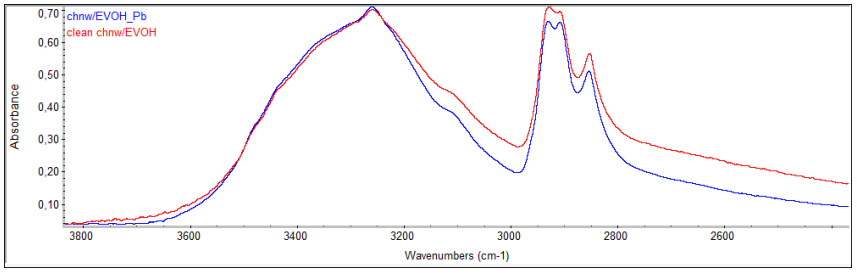

Figure B.8: FTIR of chnw/EVOH NF before and after Pb(II) adsorption

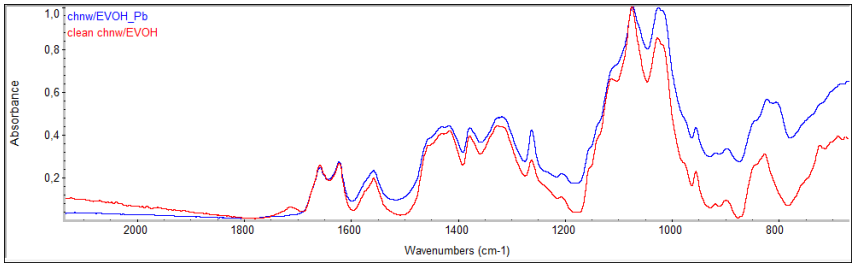

Figure B.9: FTIR of chnw/EVOH NF before and after Pb(II) adsorption

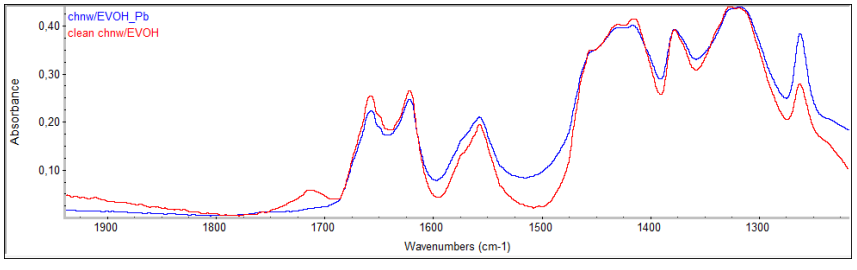

Figure B.10: FTIR of chnw/EVOH NF before and after Pb(II) adsorption

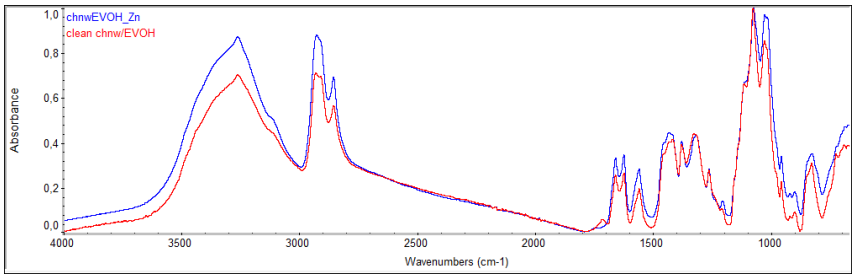

Figure B.11: FTIR of chnw/EVOH NF before and after Zn(II) adsorption

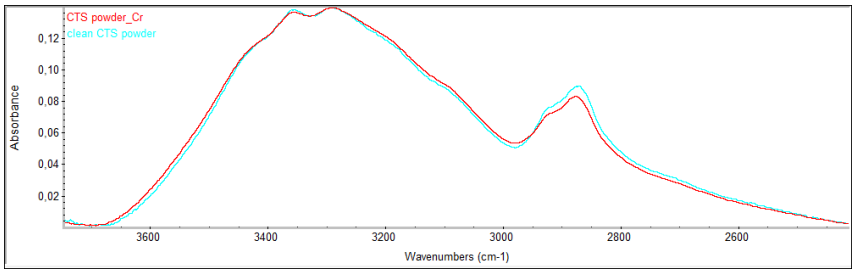

Figure B.12: FTIR of CTS powder before and after Cr(VI) adsorption

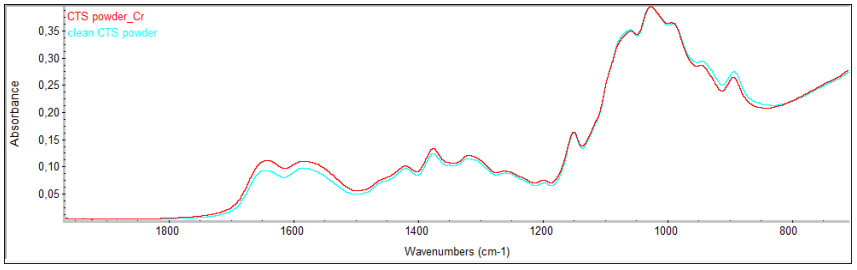

Figure B.13: FTIR of CTS powder before and after Cr(VI) adsorption

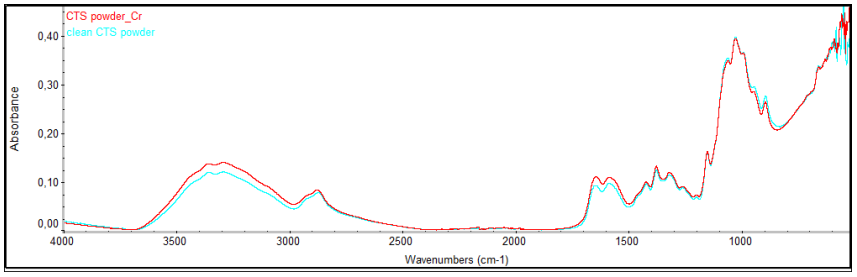

Figure B.14: FTIR of CTS powder before and after Cr(VI) adsorption

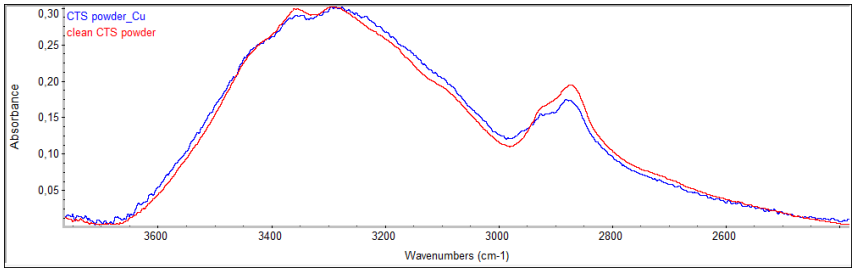

Figure B.15: FTIR of CTS powder before and after Cu(II) adsorption

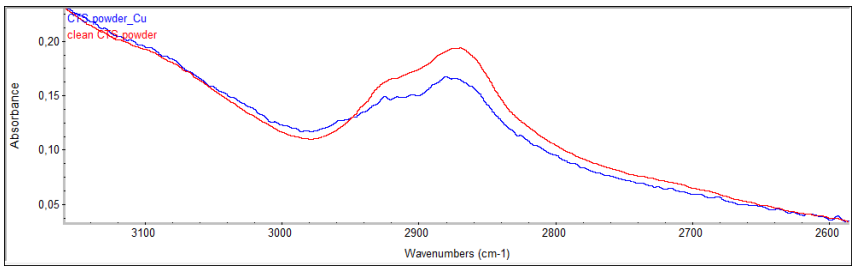

Figure B.16: FTIR of CTS powder before and after Cu(II) adsorption

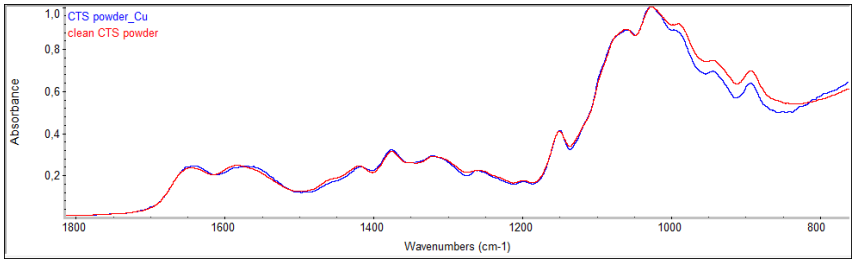

Figure B.17: FTIR of CTS powder before and after Cu(II) adsorption

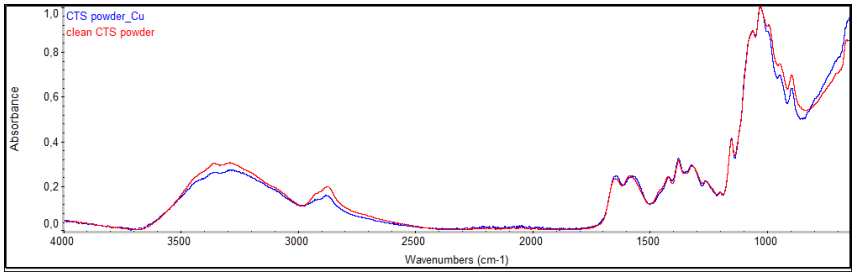

Figure B.18: FTIR of CTS powder before and after Cu(II) adsorption

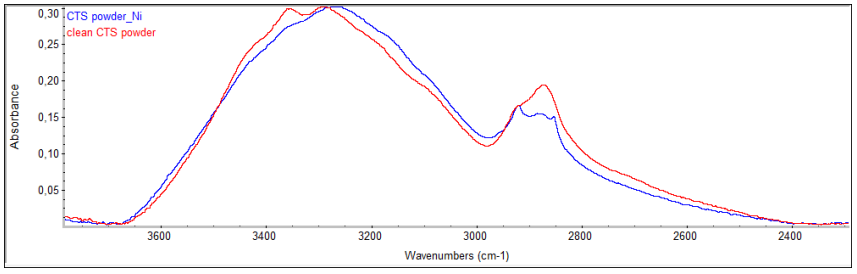

Figure B.19: FTIR of CTS powder before and after Ni(II) adsorption

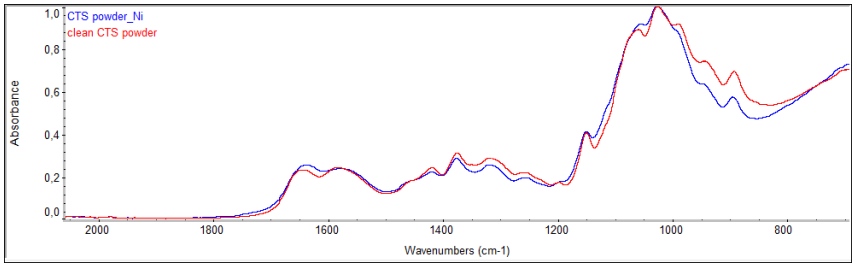

Figure B.20: FTIR of CTS powder before and after Ni(II) adsorption

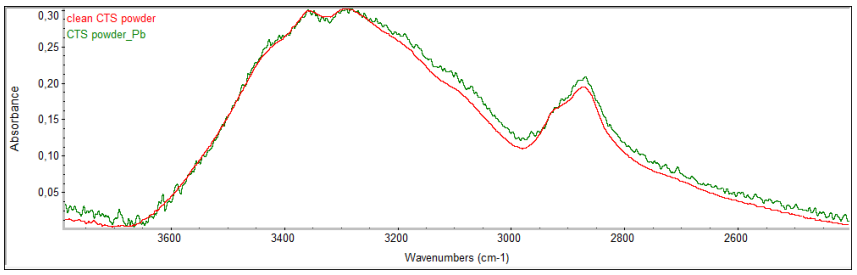

Figure B.21: FTIR of CTS powder before and after Pb(II) adsorption

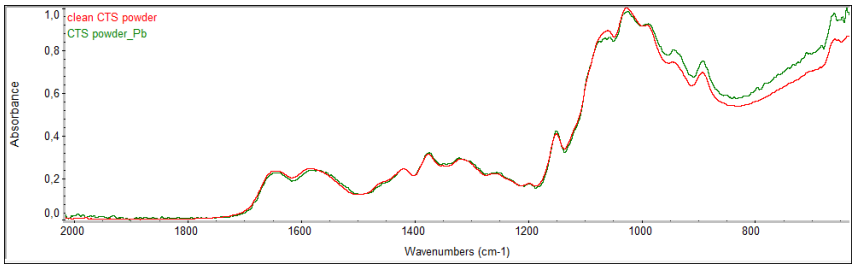

Figure B.22: FTIR of CTS powder before and after Pb(II) adsorption

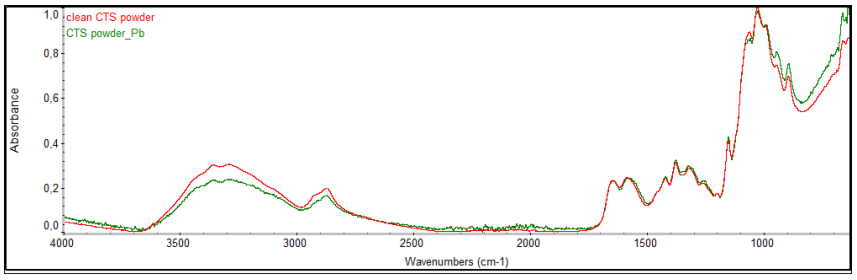

Figure B.23: FTIR of CTS powder before and after Pb(II) adsorption

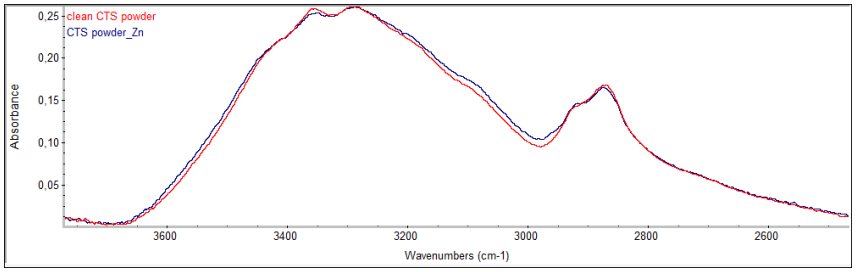

Figure B.24: FTIR of CTS powder before and after Zn(II) adsorption

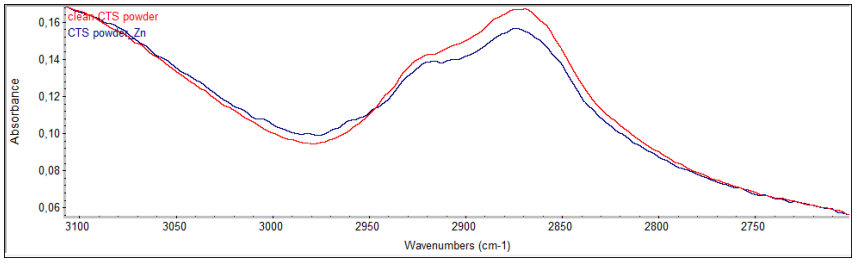

Figure B.25: FTIR of CTS powder before and after Zn(II) adsorption

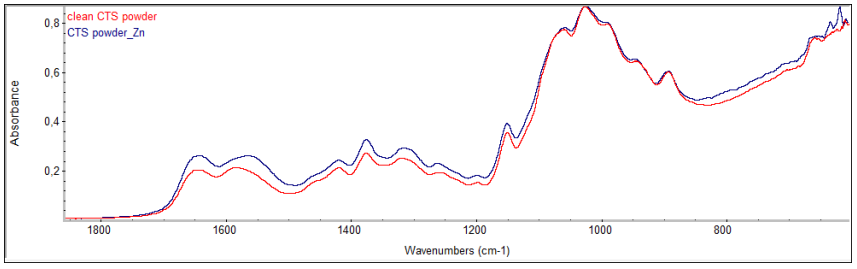

Figure B.26: FTIR of CTS powder before and after Zn(II) adsorption

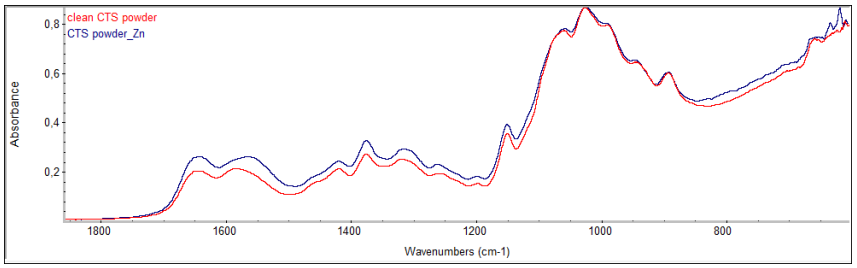

Figure B.27: FTIR of CTS powder before and after Zn(II) adsorption

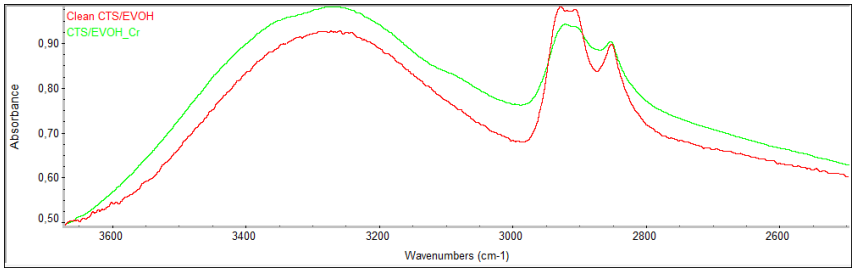

Figure B.28: FTIR of CTS/EVOH sponge before and after Cr(VI) adsorption

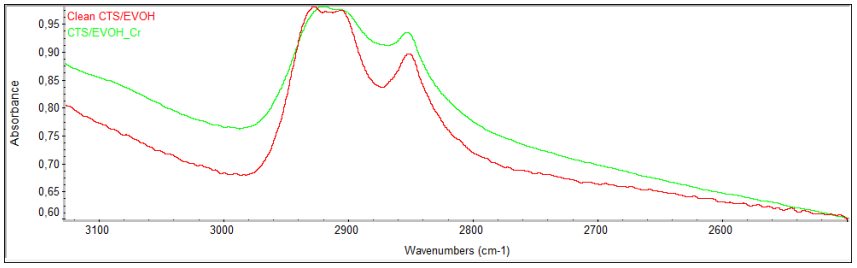

Figure B.29: FTIR of CTS/EVOH sponge before and after Cr(VI) adsorption

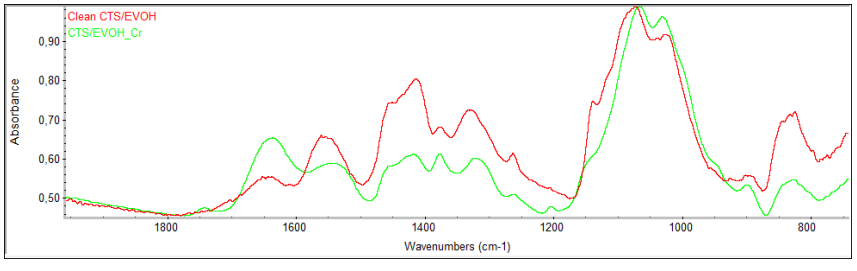

Figure B.30: FTIR of CTS/EVOH sponge before and after Cr(VI) adsorption

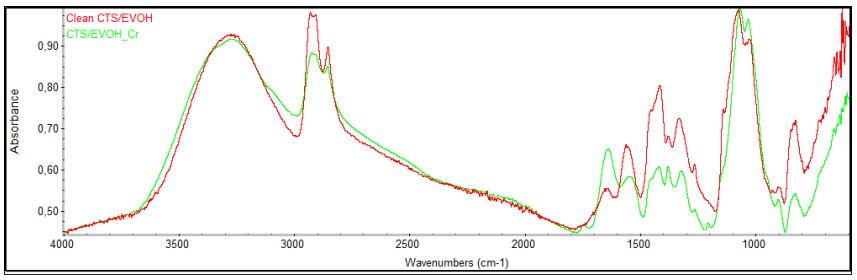

Figure B.31: FTIR of CTS/EVOH sponge before and after Cr(VI) adsorption

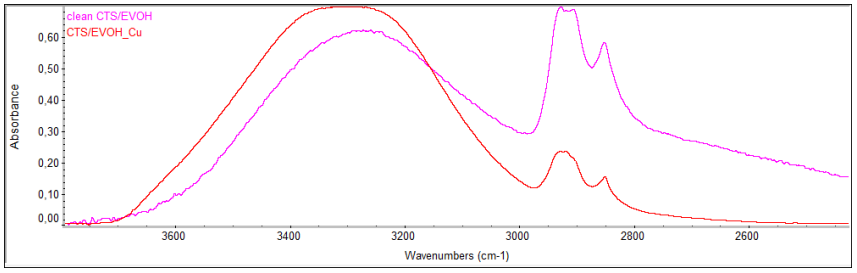

Figure B.32: FTIR of CTS/EVOH sponge before and after Cu(II) adsorption

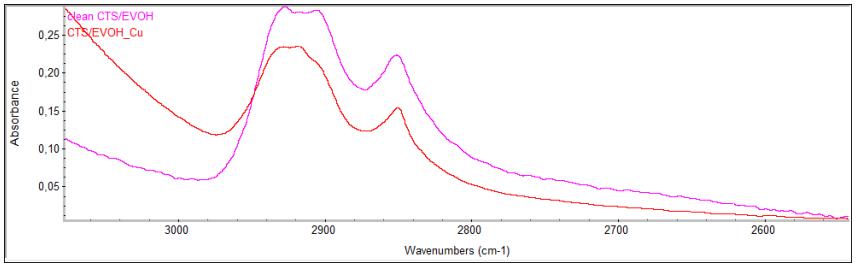

Figure B.33: FTIR of CTS/EVOH sponge before and after Cu(II) adsorption

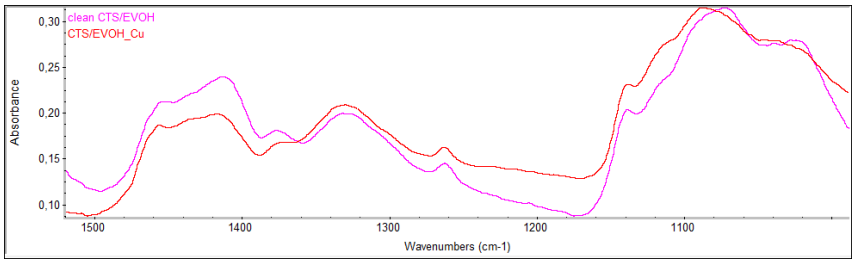

Figure B.34: FTIR of CTS/EVOH sponge before and after Cu(II) adsorption

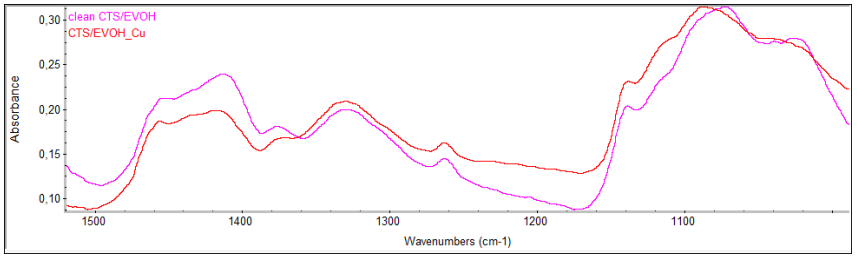

Figure B.35: FTIR of CTS/EVOH sponge before and after Cu(II) adsorption

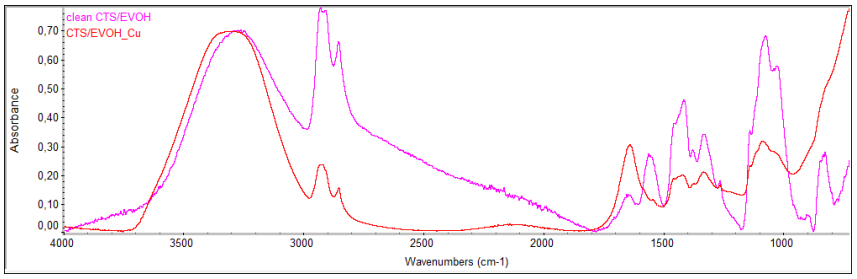

Figure B.36: FTIR of CTS/EVOH sponge before and after Cu(II) adsorption

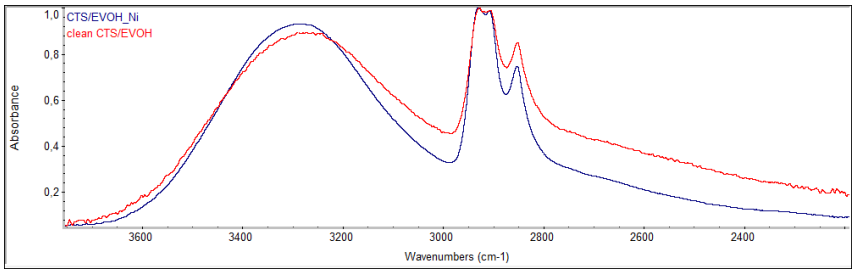

Figure B.37: FTIR of CTS/EVOH sponge before and after Ni(II) adsorption

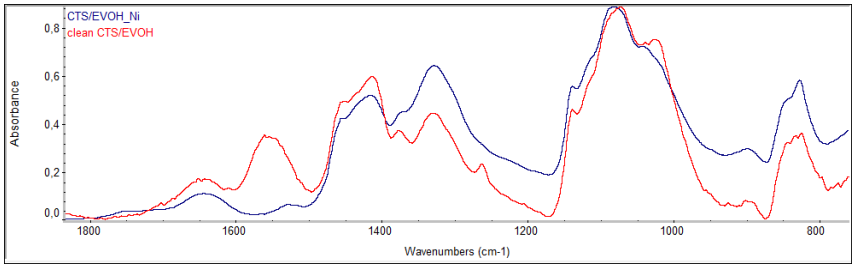

Figure B.38: FTIR of CTS/EVOH sponge before and after Ni(II) adsorption

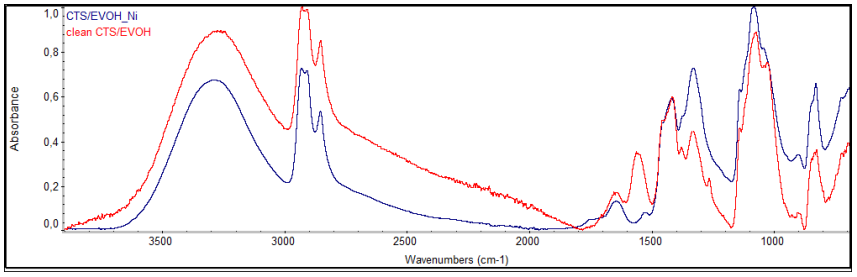

Figure B.39: FTIR of CTS/EVOH sponge before and after Ni(II) adsorption

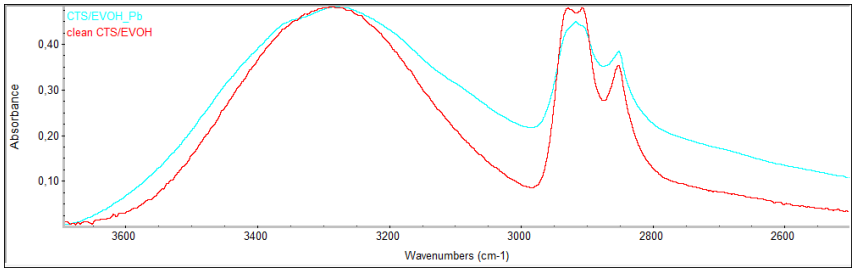

Figure B.40: FTIR of CTS/EVOH sponge before and after Pb(II) adsorption

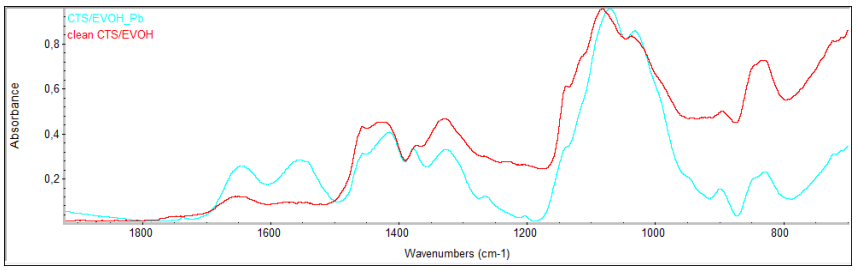

Figure B.41: FTIR of CTS/EVOH sponge before and after Pb(II) adsorption

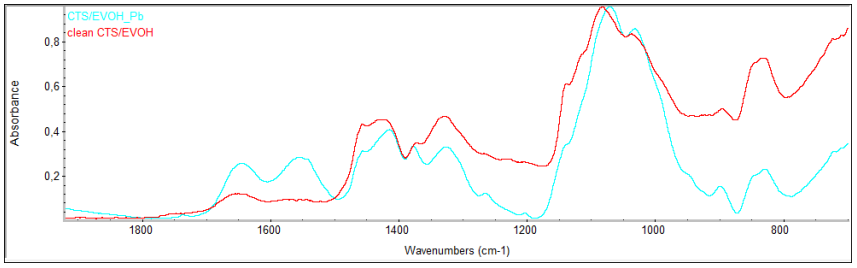

Figure B.42: FTIR of CTS/EVOH sponge before and after Pb(II) adsorption

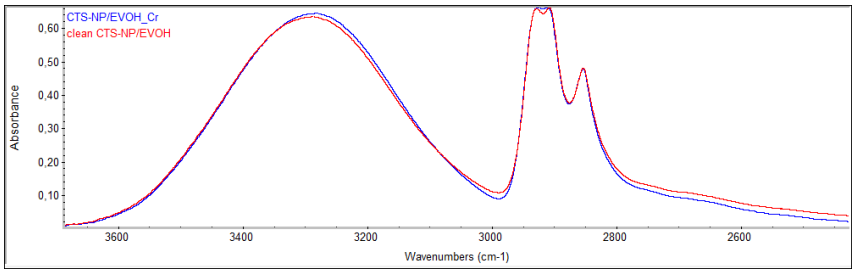

Figure B.43: FTIR of CTS-NP/EVOH sponge before and after Cr(VI) adsorption

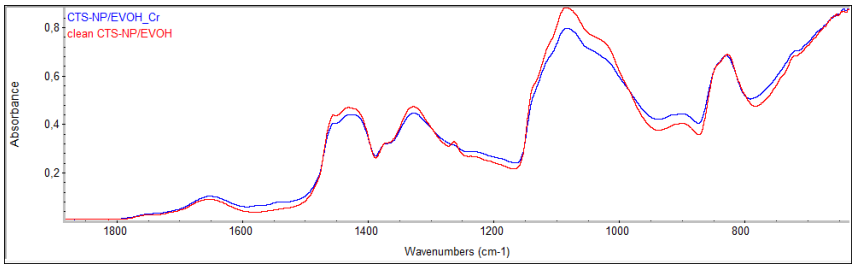

Figure B.44: FTIR of CTS-NP/EVOH sponge before and after Cr(VI) adsorption

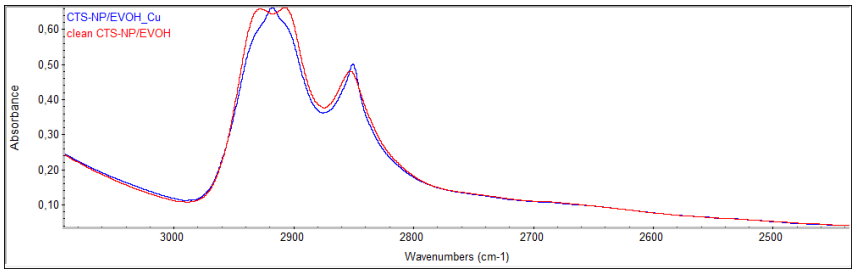

Figure B.45: FTIR of CTS-NP/EVOH before and after Cu(II) adsorption

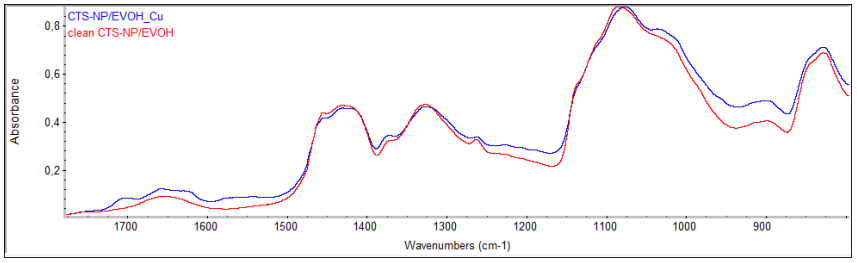

Figure B.46: FTIR of CTS-NP/EVOH before and after Cu(II) adsorption

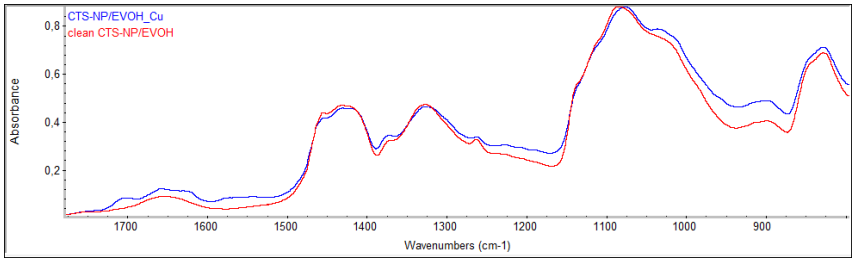

Figure B.47: FTIR of CTS-NP/EVOH before and after Cu(II) adsorption

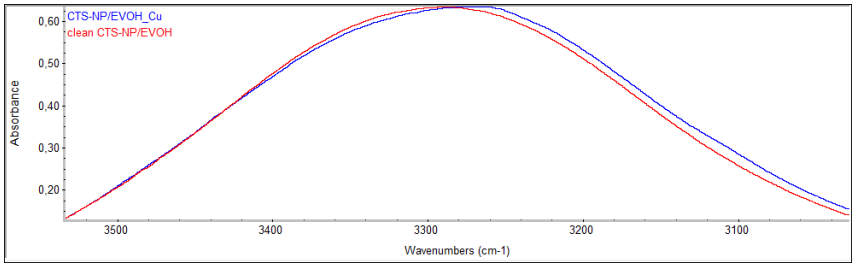

Figure B.48: FTIR of CTS-NP/EVOH before and after Cu(II) adsorption

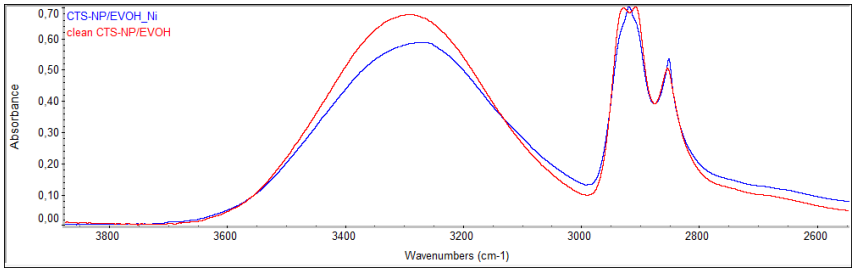

Figure B.49: FTIR of CTS-NP/EVOH before and after Ni(II) adsorption

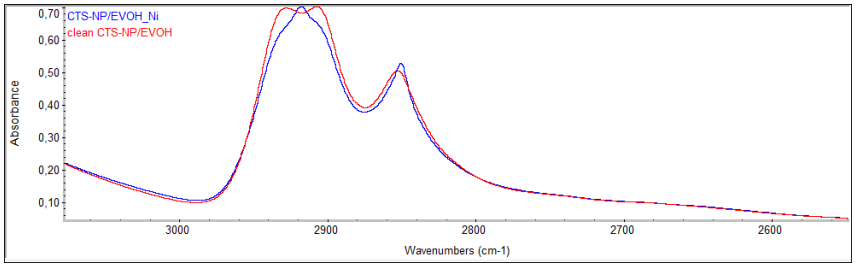

Figure B.50: FTIR of CTS-NP/EVOH before and after Ni(II) adsorption

It has been speculated that the shifts could be caused by a change in mass that is altered after adsorption took place onto the materials. The increase in mass after the bonding of heavy metal can cause a decrease in the vibration frequency of the molecules thus shifting the peaks to a lower wavenumber. Bond length can also affect the shifting. Bond length changes due to the changes in electronegativity of the neighbouring atom on the material due to association with the heavy metal ions. As the bond length increases, the wavenumber decreases [141]. These shifts and changes, seen for CTS/EVOH sponge, also indicate that not only are the NH-groups behaving as an active site but so is the OH-groups located on the CTS within the nanofibers.

Appendix C

Characterization techniques and instruments

This section discusses the various instrumentation and techniques that were used for the characterisation of the materials that were developed and used for adsorption studies.

C.0.1 Transmission electron microscopy (TEM)

Electrons are sent through the prepared sample that then allows the viewer to see detailed images on a very small scale (to the order of a few angstroms). Negative staining with urinal acetate is most often used to increase the contrast between the different phases present in the sample. TEM allows us to observe the morphological structure of chitin nanowhiskers and observe how these nanocrystals interact with each other in dilute and concentrated solutions. The sizes (length and diameter) and shapes of these nanocrystals can be established by using TEM.

C.0.2 Scanning electron microscopy (SEM)

Topographic information is acquired via the use of electrons that scan over the surface of prepared (gold-or-carbon-coated) sample. The homogeneity of the composite or blend as well as presence and size of voids and pores can be studied on the surface of a polymer sample using this technique. Diameter and lengths can also be determined for fibre-mats. SEM can analyse the presence of heavy metals on the surface of a polymer in normal SEM mode if the concentration and conductivity of the heavy metals are high. SEM-EDX (energy-dispersive x-ray) mode is also an important method for analysing the presence of heavy metals particles on the surface of a sample. It is important to use aluminium-tape instead of carbon-tape during the preparation of the sample to prevent background interference during SEM-EDX analysis [113, 142–146].

C.0.3 Confocal fluorescence microscopy

TEM and SEM lack to provide decent imagery of the behaviour of a nanoparticle or nanocrystal within a blend or nanofiber, especially on such a small scale and when layers are present. Confocal fluorescence microscopy can give an enhanced image with improved resolution and show the dispersion of the nanoparticle/crystal in the polymer matrix, on a 3D level. This is done by using thin optical sections which can be obtained when combined with a laser scanning microscope (LSM). These sections can be stacked and form the 3D picture that can show particle dispersion within the matrix on various levels and depths. If the sample has natural fluorescence it might not be necessary to use a stain or dye or label it with a fluoresce sing agent. However, it may be required to use attach a fluorescing agent such as FITC (fluorescein isothiocyanate) that have fluorescence in the wavelength for green light.

C.0.4 Tensile testing

The mechanical strength of the blended components can be determined using this relatively inexpensive and easy technique. The material will react to the force that is applied to it and behave in a certain way. The material can either break immediately or elongate before it fractures. The amount of tension and the rate at which it is applied can be controlled during the experiment by choosing the correct cell loading to apply the required force on the sample. If the sample is not expected to resist high loadings, then it would be more accurate to use smaller loadings for the analysis. The diameter and thickness of the area that is being tested for tensile strength is important to provide accurate and reproducible results.

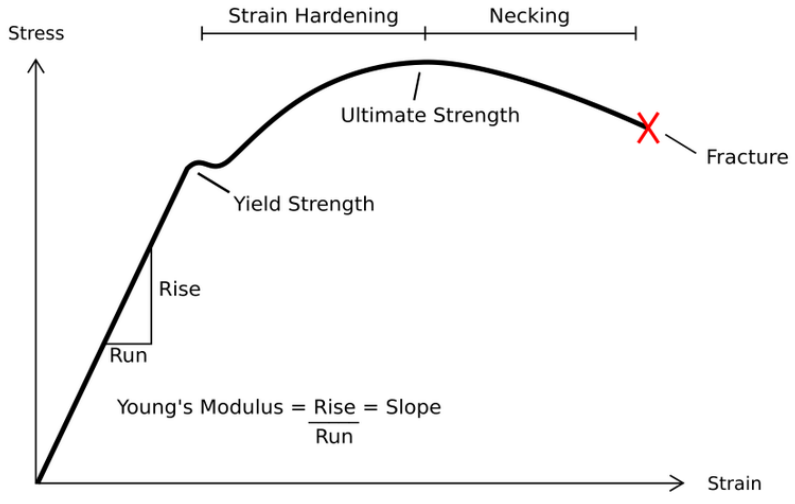

Figure C.1: An example of a stress-strain cruve.

Tensile strength, determined at room temperature, are analysed during the yield for a ductile material and at break for a brittle material. The Young's modulus can be determined from the slope of the elastic region using the stress-strain curve obtained via tensile testing. An example of the important aspects concerning a stress-strain curve is presented in Figure C.1. Elongation at break is determined as the strain that causes a material to break at a controlled temperature. Strain at yield occurs where the degree of strain on the material has become too high. An indication of good tensile properties for the analysis of strain at yield would be a where a ductile material does not show a yield point but only high elongation to break. In general, brittle material is expected to have a poor elongation at break with either a yield point or none. Stiffness and toughness are difficult to measure since these results tend to vary with time and temperature. Oxidative ageing and other environmental factors such as thermal and ultraviolet exposure can influence the toughness and stiffness of a polymer [147].

The physical properties of the polymers also influence the mechanical properties. Rigidity has an inverse effect on the impact strength of a polymer. Macro-particles usually cause negative effects on the mechanical properties of a blend that is caused by the presence of defects, agglomeration and low surface area. The presence of pores is also expected to cause some weakness within in a blend, where crazing may occur prematurely.

C.0.5 Water absorption capacity

Water absorption occurs via the pore of a sponge and the interaction between the water molecules and the charged components of the material. If a material is introduced to water or and aqueous solution, swelling can indicate the presence of pores and that the material is wettable and able to attract to water molecules. The retention of water also indicates that the material has behaviour indicative of a sponge. If the water does not seep out of the material without force being applied it indicates that the sponge can trap water effectively.

It is therefore important to measure the water adsorption capacity (WAC) of a sponge material in order to establish whether it truly has sponge-like behaviour. The WAC is measured using the difference between the initial weight of the sponge material subtracting from the weight after the material was left in a aqueous solution to absorb moisture (water).

C.0.6 Thermogravimetric analysis (TGA)

This technique allows the study of the thermal stability of composites and their individual components. This technique is used to measure any sort of loss in the weight of a sample with regards to temperature. This is done in a controlled environment where conditions, except for the temperature, are held constant. Samples will lose weight when it undergoes decomposition, oxidation or dehydration at certain temperature intervals. This analysis can contribute to the way we understand the behaviour of the polymer and blends, especially in terms of moisture adsorption and thermal stability.

C.0.7 Attenuated total reflectance-Fourier transform infrared (ATR-FTIR)

Fourier transform infrared (FTIR) analysis is based on the vibration of atoms. The spectrum is obtained most commonly by allowing a infrared electromagnetic radiation to pass through a sample [148]. If this sample has a permanent of induced dipole then the incident radiation that is absorbed in particular energy can be determined. Identification of certain bond type within the sample is then possible using the frequency of the vibration belonging to a molecule which will appear as a peak in the absorption spectrum [149]. Functional groups on a polymer can absorb infrared radiation at various wavelengths. When analysing a blend, it is possible to observe the compatibility of the polymers that were added to each other and confirm the presence of each polymer. It is even possible, to a certain degree, to observe the concentration or wt% of each polymer present in the blend, fibre or composite. Specific functional groups within blend etc are easily determined by the individual functional groups that specifically belong to the polymer in question. Problems that may occur, is the possibility of two polymers containing the same functional groups, causing an overlap in the spectra. These issues can be overcome by evaluating the intensity of the peaks compared to the peaks found in the FTIR-ATR spectra of the pristine polymers before blending.

Attenuated total reflectance-Fourier transform infrared is a very effective and simple instrument to use. Information about the chemical composition of the material, as well as evidence proving the presence of specific particles within the material (blend, composites etc.), can be acquired.

C.0.8 Differential scanning calorimetry (DSC)

This technique can help to determine the physical composition of the sample. The thermal transition of a sample can be measured while the conditions are completely controlled with a heating profile preprogrammed before the sample can run. Information such as the crystallinity, melting point, polydispersity of crystals as well as the glass transition

temperature can be ascertained. DSC can also be used to detect changes in crystallinity and thermal stability of the material caused by the adsorption of heavy metals onto the surface of the biosorbent.

C.0.9 Zeta potential

Zeta potential is measured using a Zetasizer. This analyses the electro-kinetic potential of a colloidal suspension for a specific sample. It is important that samples that are used for this type of analysis are small particles that do not cause sedimentation and remain well dispersed during measurements. The charge on the particles in a solution can be measured and the change in the surface charge can be observed as the solution pH is changed. This can give an excellent idea of the behaviour of a polymer material in an aqueous solution under varying conditions. High zeta potential can be obtained for molecules or particles that are stable in solutions and does not flocculate or coagulate[111].

Figure C.2: An example of a zetasizer instrument.

References

[1] L. Mouni, D. Merabet, D. Robert, and A. Bouzaza, "Batch studies for the investigation of the sorption of the heavy metals Pb^{2+} and Zn^{2+} onto Amizour soil (Algeria)," *Geoderma*, vol. 154, no. 1-2, pp. 30–35, 2009.

[2] M. Lewis, J. Worobey, D. S. Ramsay, and M. K. McCormack, "Prenatal exposure to heavy metals: effect on childhood cognitive skills and health status," *Pediatrics*, vol. 89, no. 6 Pt. 1, pp. 1010–1015, 1992.

[3] F. Islam, T. Yasmeen, M. Riaz, M. S. Arif, S. Ali, and S. H. Raza, "Proteus mirabilis alleviates zinc toxicity by preventing oxidative stress in maize (Zea mays) plants," *Ecotoxicology and Environmental Safety*, vol. 110, pp. 143–152, 2014.

[4] M. Muchuweti, J. W. Birkett, E. Chinyanga, and R. Zvauya, "Heavy metal content of vegetables irrigated with mixtures of wastewater and sewage sludge in Zimbabwe : Implications for human health," *Agriculture, Ecosystems and Environment*, vol. 112, no. 1, pp. 41–48, 2006.

[5] O. B. Akpor and M. Muchie, "Remediation of heavy metals in drinking water and wastewater treatment systems : Processes and applications," *International Journal of the Physical Sciences*, vol. 5, no. 12, pp. 1807–1817, Oct 2010.

[6] M.-W. Wan, C.-C. Kan, B. D. Rogel, and M. L. P. Dalida, "Adsorption of copper (II) and lead (II) ions from aqueous solution on chitosan-coated sand," *Carbohydrate Polymers*, vol. 80, no. 3, pp. 891–899, 2010.

[7] F. Edition, I. The, and F. Addendum, *WHO limits to drinking water*, 2006.

[8] M. A. Barakat, "New trends in removing heavy metals from industrial wastewater," 2011.

[9] K. Anoop Krishnan, K. Sreejalekshmi, and R. Baiju, "Nickel(II) adsorption onto biomass based activated carbon obtained from sugarcane bagasse pith," *Bioresource Technology*, vol. 102, no. 22, pp. 10 239–10 247, Nov 2011.

[10] N. M. Salem and A. M. Awwad, "Biosorption of Ni(II) from electroplating wastewater by modified (Eriobotrya japonica) loquat bark," *Journal of Saudi Chemical Society*, vol. 18, no. 5, pp. 379–386, Nov 2014.

[11] S. Babel and T. A. Kurniawan, "Cr(VI) removal from synthetic wastewater using coconut shell charcoal and commercial activated carbon modified with oxidizing agents and/or chitosan," *Chemosphere*, vol. 54, pp. 951–967, Feb 2004.

[12] US Department of Labor, "Health Effects of Hexavalent Chromium," *OSHA Fact Sheet*, vol. 2014, no. 1st October, pp. 1–2, 2006.

[13] A. P. Das and S. Mishra, "Hexavalent chromium (VI) : Environment pollution and health hazard," *Journal of Environmental Research And Development*, vol. 2, no. 3, pp. 386–392, 2008.

[14] V. Iyer and N. Mastorakis, "Unsafe chromium and its environmental health effects of Orissa chromite mines," *Proceedings of the International Conference on Energy and Environment Technologies and EquipmProceedings of the International Conference on Energy and Environment Technologies and Equipment, EEETE '10*, no. September 2017, pp. 111–122, 2010.

[15] C. Pellerin, S. M. Booker, and L. Claudio, "Reflections on hexavalent chromium: health hazards of an industrial heavyweight\rNTP Studies: Focusing on the Future," *Environ Health Perspect*, vol. 108, no. 9, pp. A402–7, 2000.

[16] H. A. Hegazi, "Removal of heavy metals from wastewater using agricultural and industrial wastes as adsorbents," *HBRC Journal*, 2013.

[17] J.-P. Simonin, "On the comparison of pseudo-first order and pseudo-second order rate laws in the modeling of adsorption kinetics," *Chemical Engineering Journal*, vol. 300, pp. 254–263, Sep 2016.

[18] D. Le Maitre, "TOWARDS A WATER-SAFE FUTURE – EXPERTS MEET ABOUT SOUTH AFRICA ' S STRATEGIC SURFACE AND GROUNDWATER SOURCE AREAS," 2018.

[19] G. Crini, "Recent developments in polysaccharide-based materials used as adsorbents in wastewater treatment," *Progress in Polymer Science*, vol. 30, no. 1, pp. 38–70, Jan 2005.

[20] X.-j. Hu, J.-s. Wang, Y.-g. Liu, X. Li, G.-m. Zeng, Z.-l. Bao, X.-x. Zeng, A.-w. Chen, and F. Long, "Adsorption of chromium (VI) by ethylenediamine-modified cross-linked magnetic chitosan resin: Isotherms, kinetics and thermodynamics," *Journal of Hazardous Materials*, vol. 185, no. 1, pp. 306–314, Jan 2011.

[21] W. W. Ngah and S. Fatinathan, "Adsorption characterization of Pb(II) and Cu(II) ions onto chitosan-tripolyphosphate beads: Kinetic, equilibrium and thermodynamic studies," *Journal of Environmental Management*, vol. 91, no. 4, pp. 958–969, Mar 2010.

[22] A. J. Varma, S. V. Deshpande, and J. F. Kennedy, "Metal complexation by chitosan and its derivatives: A review," *Carbohydrate Polymers*, vol. 55, no. 1, pp. 77–93, 2004.

[23] Y. O. Kang, I. S. Yoon, S. Y. Lee, D. D. Kim, S. J. Lee, W. H. Park, and S. M. Hudson, "Chitosan-coated poly(vinyl alcohol) nanofibers for wound dressings," *Journal of Biomedical Materials Research - Part B Applied Biomaterials*, vol. 92, no. 2, pp. 568–576, 2010.

[24] G. Wang, Y. Xin, and H. Uyama, "Facile fabrication of mesoporous poly(ethylene-co-vinyl alcohol)/chitosan blend monoliths," *Carbohydrate Polymers*, 2015.

[25] V. Muriel-Galet, G. López-Carballo, R. Gavara, and P. Hernández-Muñoz, "Antimicrobial food packaging film based on the release of LAE from EVOH," *International Journal of Food Microbiology*, 2012.

[26] P. Ding, K. L. Huang, G. Y. Li, and W. W. Zeng, "Mechanisms and kinetics of chelating reaction between novel chitosan derivatives and Zn(II)," *Journal of Hazardous Materials*, vol. 146, no. 1-2, pp. 58–64, 2007.

[27] P. Singh and R. Nagendran, "A comparative study of sorption of chromium (III) onto chitin and chitosan," *Applied Water Science*, no. Iii, pp. 1–6, 2014.

[28] M. Toor and B. Jin, "Adsorption characteristics, isotherm, kinetics, and diffusion of modified natural bentonite for removing diazo dye," *Chemical Engineering Journal*, vol. 187, pp. 79–88, 2012.

[29] S. Shukla and R. S. Pai, "Adsorption of Cu(II), Ni(II) and Zn(II) on modified jute fibres," *Bioresource Technology*, vol. 96, no. 13, pp. 1430–1438, Sep 2005.

[30] L. Li, Y. Li, and C. Yang, "Chemical filtration of Cr (VI) with electrospun chitosan nanofiber membranes," *Carbohydrate Polymers*, vol. 140, pp. 299–307, Apr 2016.

[31] J. Iqbal, F. Hamid Wattoo, M. Hamid Sarwar Wattoo, R. Malik, S. Ahmad Tirmizi, M. Imran, and A. Bux Ghangro, "Adsorption of acid yellow dye on flakes of chitosan prepared from fishery wastes," *Arabian Journal of Chemistry*, vol. 4, pp. 389–395, 2011.

[32] H. Celebi, M. Gurbuz, S. Koparal, and A. Dogan, "Development of antibacterial electrospun chitosan/poly(vinyl alcohol) nanofibers containing silver ion-incorporated HAP nanoparticles," *Composite Interfaces*, vol. 20, no. 9, pp. 799–812, 2013.

[33] N. Horzum, E. Boyaci, A. E. Erolu, T. Shahwan, and M. M. Demir, "Sorption efficiency of chitosan nanofibers toward metal ions at low concentrations," *Biomacromolecules*, vol. 11, no. 12, pp. 3301–3308, 2010.

[34] R. N. Wijesena, N. Tissera, Y. Y. Kannangara, Y. Lin, G. A. J. Amaratunga, and K. M. N. De Silva, "A method for top down preparation of chitosan nanoparticles and nanofibers," *Carbohydrate Polymers*, vol. 117, pp. 731–738, 2015.

[35] S. Haider and S.-Y. Park, "Preparation of the electrospun chitosan nanofibers and their applications to the adsorption of Cu(II) and Pb(II) ions from an aqueous solution," *Journal of Membrane Science*, vol. 328, no. 1-2, pp. 90–96, Feb 2009.

[36] M. Mincea, A. Negrulescu, and V. Ostafe, "Preparation , Modification , and Applications of Chitin Nanowhiskers : a Review," *Adv. Mater. Sci.*, vol. 30, pp. 225–242, 2012.

[37] N. E. Mushi, N. Butchosa, M. Salajkova, Q. Zhou, and L. A. Berglund, "Nanostructured membranes based on native chitin nanofibers prepared by mild process," *Carbohydrate Polymers*, vol. 112, pp. 255–263, 2014.

[38] A. G. Pereira, E. C. Muniz, and Y.-L. Hsieh, "Chitosan-sheath and chitin-core nanowhiskers," *Carbohydrate Polymers*, vol. 107, pp. 158–166, Jul 2014.

[39] V. Mohanasrinivasan, M. Mishra, J. S. Paliwal, S. K. Singh, E. Selvarajan, V. Suganthi, and C. Subathra Devi, "Studies on heavy metal removal efficiency and antibacterial activity of chitosan prepared from shrimp shell waste," *3 Biotech*, 2014.

[40] S. S. Salih and T. K. Ghosh, "Preparation and characterization of bioadsorbent beads for chromium and zinc ions adsorption," *Cogent Environmental Science*, vol. 3, no. 1, pp. 1–14, 2017.

[41] K. G. Nair and A. Dufresne, "Crab Shell Chitin Whisker Reinforced Natural Rubber Nanocomposites. 1. Processing and Swelling Behavior," *Biomacromolecules*, vol. 4, no. 3, pp. 657–665.

[42] K. V. Kumar, "Optimum sorption isotherm by linear and non-linear methods for malachite green onto lemon peel," *Dyes and Pigments*, vol. 74, no. 3, pp. 595–597, 2007.

[43] K. Kurita, H. Yoshino, K. Yokota, M. Ando, S. Inoue, S. Ishii, and S. Nishimura, "Preparation of tosylchitins as precursors for facile chemical modifications of chitin," *Macromolecules*, vol. 25, no. 14, pp. 3786–3790, Jul 1992.

[44] K. Kurita, S. Inoue, and S.-I. Nishimura, "Preparation of soluble chitin derivatives as reactive precursors for controlled modifications: Tosyl- and iodo-chitins," *Journal of Polymer Science Part A: Polymer Chemistry*, vol. 29, no. 6, pp. 937–939, May 1991.

[45] A. Dufresne, S. Thomas, and L. A. Pothan, *Biopolymer nanocomposites : processing, properties, and applications*. Wilwy, 2013.

[46] P. Wongpanit, N. Sanchavanakit, P. Pavasant, T. Bunaprasert, Y. Tabata, and R. Rujiravanit, "Preparation and characterization of chitin whisker-reinforced silk fibroin nanocomposite sponges," *European Polymer Journal*, vol. 43, no. 10, pp. 4123–4135, Oct 2007.

[47] L. Yu, J. Gong, C. Zeng, and L. Zhang, "Preparation of zeolite-A/chitosan hybrid composites and their bioactivities and antimicrobial activities," *Materials Science and Engineering: C*, vol. 33, no. 7, pp. 3652–3660, Oct 2013.

[48] P. Agrawal and K. Pramanik, "Chitosan-poly(vinyl alcohol) nanofibers by free surface electrospinning for tissue engineering applications," *Tissue Engineering and Regenerative Medicine*, vol. 13, no. 5, pp. 485–497, 2016.

[49] A. Mera, J. Araki, T. Ohtsuki, M. Shimosaka, and N. Yoshida, "Chitin Nanowhiskers Mediate Transformation of Escherichia coli by Exogenous Plasmid DNA," *Journal of Biotechnology & Biomaterials*, vol. 01, no. 06, Sep 2011.

[50] J.-F. Revol and R. Marchessault, "In vitro chiral nematic ordering of chitin crystallites," *International Journal of Biological Macromolecules*, vol. 15, no. 6, pp. 329–335, Dec 1993.

[51] M. Paillet and A. Dufresne, "Chitin whisker reinforced thermoplastic nanocomposites," 2001.

[52] A. Morin and A. Dufresne, "Nanocomposites of Chitin Whiskers from Riftia Tubes and Poly(caprolactone)," *Macromolecules*, vol. 35, no. 6, pp. 2190–2199, Mar 2002.

[53] A. Watthanaphanit, P. Supaphol, H. Tamura, S. Tokura, and R. Rujiravanit, "Fabrication, structure, and properties of chitin whisker-reinforced alginate nanocomposite fibers," *Journal of Applied Polymer Science*, vol. 110, no. 2, pp. 890–899, Oct 2008.

[54] Yongshang Lu, , Lihui Weng, and L. Zhang*, "Morphology and Properties of Soy Protein Isolate Thermoplastics Reinforced with Chitin Whiskers," *Biomacromolecules*, vol. 5, no. 3, pp. 1046–1051, 2004.

[55] Y. Fan, T. Saito, and A. Isogai, "Chitin Nanocrystals Prepared by TEMPO-Mediated Oxidation of α-Chitin," *Biomacromolecules*, vol. 9, no. 1, pp. 192–198, Jan 2008.

[56] Y. Fan, T. Saito, and A. Isogai, "Preparation of Chitin Nanofibers from Squid Pen β-Chitin by Simple Mechanical Treatment under Acid Conditions," *Biomacromolecules*, vol. 9, no. 7, pp. 1919–1923, Jul 2008.

[57] Y. Fan, T. Saito, and A. Isogai, "Individual chitin nano-whiskers prepared from partially deacetylated α-chitin by fibril surface cationization," *Carbohydrate Polymers*, vol. 79, no. 4, pp. 1046–1051, Mar 2010.

[58] L. M. Zhao, L. E. Shi, Z. L. Zhang, J. M. Chen, D. D. Shi, J. Yang, and Z. X. Tang, "Preparation and application of chitosan nanoparticles and nanofibers," *Brazilian Journal of Chemical Engineering*, vol. 28, no. 3, pp. 353–362, 2011.

[59] S. Ifuku, M. Nogi, K. Abe, M. Yoshioka, M. Morimoto, H. Saimoto, and H. Yano, "Preparation of Chitin Nanofibers with a Uniform Width as α-Chitin from Crab Shells," *Biomacromolecules*, vol. 10, no. 6, pp. 1584–1588, Jun 2009.

[60] S. Ifuku, M. Nogi, M. Yoshioka, M. Morimoto, H. Yano, and H. Saimoto, "Fibrillation of dried chitin into 10–20 nm nanofibers by a simple grinding method under acidic conditions," *Carbohydrate Polymers*, vol. 81, no. 1, pp. 134–139, May 2010.

[61] K. Ryota and Tetsuo Konde, "Favorable 3D-network Formation of Chitin Nanofibers Dispersed in Water Prepared Using Aqueous Counter Collision," *SEN'I GAKKAISHI*, vol. 67, no. 4, pp. 91–95, 2011.

[62] J.-i. Kadokawa, A. Takegawa, S. Mine, and K. Prasad, "Preparation of chitin nanowhiskers using an ionic liquid and their composite materials with poly(vinyl alcohol)," *Carbohydrate Polymers*, vol. 84, no. 4, pp. 1408–1412, Apr 2011.

[63] J.-B. Zeng, Y.-S. He, S.-L. Li, and Y.-Z. Wang, "Chitin Whiskers: An Overview," *Biomacromolecules*, vol. 13, no. 1, pp. 1–11, Jan 2012.

[64] L. Feng, Z. Zhou, A. Dufresne, J. Huang, M. Wei, and L. An, "Structure and properties of new thermoforming bionanocomposites based on chitin whisker-graft-polycaprolactone," *Journal of Applied Polymer Science*, vol. 112, no. 5, pp. 2830–2837, Jun 2009.

[65] T. Sabu, N. Neethu, M. Sneha, and F. Elizabeth, *Natural Polymers, Biopolymers, Biomaterials, and Their Composites, Blends, and IPNs*. Apple Academic Press, 2012, vol. 2.

[66] Y. Yamamoto, T. Nishimura, T. Saito, and T. Kato, "CaCO3/chitin-whisker hybrids: formation of CaCO3 crystals in chitin-based liquid-crystalline suspension," *Polymer Journal*, vol. 42, no. 7, pp. 583–586, Jul 2010.

[67] P. Hariraksapitak and P. Supaphol, "Preparation and properties of α-chitin-whisker-reinforced hyaluronan-gelatin nanocomposite scaffolds," *Journal of Applied Polymer Science*, vol. 117, no. 6, pp. n/a–n/a, Sep 2010.

[68] J. Junkasem, R. Rujiravanit, and P. Supaphol, "Fabrication of α-chitin whisker-reinforced poly(vinyl alcohol) nanocomposite nanofibres by electrospinning," *Nanotechnology*, vol. 17, no. 17, pp. 4519–4528, Sep 2006.

[69] S. S. Salih and T. K. Ghosh, "Adsorption of Zn(II) ions by chitosan coated diatomaceous earth," *International Journal of Biological Macromolecules*, vol. 106, pp. 602–610, 2018.

[70] S. Azizian, "Kinetic models of sorption: a theoretical analysis," *Journal of Colloid and Interface Science*, vol. 276, pp. 47–52, 2004.

[71] Y. T. Jia, J. Gong, X. H. Gu, H. Y. Kim, J. Dong, and X. Y. Shen, "Fabrication and characterization of poly (vinyl alcohol)/chitosan blend nanofibers produced by electrospinning method," *Carbohydrate Polymers*, vol. 67, no. 3, pp. 403–409, 2007.

[72] S. J. Lee, D. N. Heo, J. H. Moon, W. K. Ko, J. B. Lee, M. S. Bae, S. W. Park, J. E. Kim, D. H. Lee, E. C. Kim, C. H. Lee, and I. K. Kwon, "Electrospun chitosan nanofibers with controlled levels of silver nanoparticles. Preparation, characterization and antibacterial activity," *Carbohydrate Polymers*, vol. 111, pp. 530–537, 2014.

[73] H. K. Boparai, M. Joseph, and D. M. O'Carroll, "Kinetics and thermodynamics of cadmium ion removal by adsorption onto nano zerovalent iron particles," *Journal of Hazardous Materials*, vol. 186, no. 1, pp. 458–465, 2011.

[74] L. Qi, Z. Xu, X. Jiang, C. Hu, and X. Zou, "Preparation and antibacterial activity of chitosan nanoparticles," *Carbohydrate Research*, vol. 339, no. 16, pp. 2693–2700, 2004.

[75] P. Miretzky and A. F. Cirelli, "Hg (II) removal from water by chitosan and chitosan derivatives : A review," *Journal of Hazardous Materials*, vol. 167, pp. 10–23, 2009.

[76] K. Desai, K. Kit, J. Li, and S. Zivanovic, "Morphological and Surface Properties of Electrospun Chitosan Nanofibers," *Biomacromolecules*, vol. 9, no. 3, pp. 1000–1006, Mar 2008.

[77] D. Liu, Z. Li, Y. Zhu, Z. Li, and R. Kumar, "Recycled chitosan nanofibril as an effective Cu(II), Pb(II) and Cd(II) ionic chelating agent: Adsorption and desorption performance," *Carbohydrate Polymers*, vol. 111, pp. 469–476, 2014.

[78] J. Synowiecki and N. A. Al-Khateeb, "Production, Properties, and Some New Applications of Chitin and Its Derivatives," *Critical Reviews in Food Science and Nutrition*, vol. 43, no. 2, pp. 145–171, 2003.

[79] K. Devarayan, H. Hanaoka, M. Hachisu, J. Araki, M. Ohguchi, B. K. Behera, and K. Ohkawa, "Direct electrospinning of cellulose-chitosan composite nanofiber," *Macromolecular Materials and Engineering*, vol. 298, no. 10, pp. 1059–1064, 2013.

[80] Y. Fan, H. Fukuzumi, T. Saito, and A. Isogai, "Comparative characterization of aqueous dispersions and cast films of different chitin nanowhiskers/nanofibers," *International Journal of Biological Macromolecules*, vol. 50, no. 1, pp. 69–76, Jan 2012.

[81] A. L. de Pinho Neves, C. C. Milioli, L. Müller, H. G. Riella, N. C. Kuhnen, and H. K. Stulzer, "Factorial design as tool in chitosan nanoparticles development by ionic gelation technique," *Colloids and Surfaces A: Physicochemical and Engineering Aspects*, vol. 445, pp. 34–39, 2014.

[82] P. Fernandez-Saiz, M. J. Ocio, and J. M. Lagaron, "Antibacterial chitosan-based blends with ethylene-vinyl alcohol copolymer," *Carbohydrate Polymers*, vol. 80, no. 3, pp. 874–884, 2010.

[83] E.-R. Kenawy, J. M. Layman, J. R. Watkins, G. L. Bowlin, J. A. Matthews, D. G. Simpson, and G. E. Wnek, "Electrospinning of poly(ethylene-co-vinyl alcohol) fibers," *Biomaterials*, vol. 24, no. 6, pp. 907–913, Mar 2003.

[84] C. Zhang, Y. Shangguan, R. Chen, and Q. Zheng, "Study on thermal behavior of impact polypropylene copolymer and its fractions," *Journal of Applied Polymer Science*, vol. 119, no. 3, pp. 1560–1566, Feb 2011.

[85] C. Arboleda E., A. I. Mejía G., and B. L. López, "Poly (vinylalcohol-co-ethylene) biodegradation on semi solid fermentation by phanerochaete chrysosporium," *Acta Farm. Bonaerense*, vol. 23, pp. 123–128, 2004.

[86] H. F. H. F. Mark and J. I. Kroschwitz, *Encyclopedia of polymer science and engineering*. Wiley, 1985.

[87] P. Baroni, R. Vieira, E. Meneghetti, M. da Silva, and M. Beppu, "Evaluation of batch adsorption of chromium ions on natural and crosslinked chitosan membranes," *Journal of Hazardous Materials*, vol. 152, no. 3, pp. 1155–1163, Apr 2008.

[88] C. Rosales-Landeros, C. E. Barrera-Díaz, B. Bilyeu, V. V. Guerrero, and F. U. Núñez, "A Review on Cr(VI) Adsorption Using Inorganic Materials," *American Journal of Analytical Chemistry*, vol. 04, no. 07, pp. 8–16, 2013.

[89] E. Lakay, "Novel ion-exchange materials derived from poly (styrene- co -maleimide) and a study of the extraction and recovery of gold (III) chloride from acidic solutions By Eugene Marlin Lakay," *PhD thesis*, no. March, 2013.

[90] P. B. Hamilton, "Analytical Ion-Exchange Procedures in Chemistry and Biology—Theory, Equipment, Techniques. J. X. Khym. Prentice-Hall Inc., Englewood Cliffs, N. J., 1974, xii + 257 pp. Paperback. $14.50," *Clinical Chemistry*, vol. 21, no. 2, 1975.

[91] R. W. Grimshaw and C. E. C. E. Harland, *Ion-exchange : introduction to theory and practice.* Chemical Society, 1975.

[92] D. M. D. M. Ruthven, *Principles of adsorption and adsorption processes.* Wiley, 1984.

[93] Y. Ho and G. McKay, "The sorption of lead(II) ions on peat," *Water Research*, vol. 33, no. 2, pp. 578–584, Feb 1999.

[94] K. Foo and B. Hameed, "Insights into the modeling of adsorption isotherm systems," *Chemical Engineering Journal*, vol. 156, no. 1, pp. 2–10, Jan 2010.

[95] D. A.O, "Langmuir, Freundlich, Temkin and Dubinin–Radushkevich Isotherms Studies of Equilibrium Sorption of Zn 2+ Unto Phosphoric Acid Modified Rice Husk," *IOSR Journal of Applied Chemistry*, vol. 3, no. 1, pp. 38–45, 2012.

[96] N. Feng, X. Guo, S. Liang, Y. Zhu, and J. Liu, "Biosorption of heavy metals from aqueous solutions by chemically modified orange peel," *Journal of Hazardous Materials*, vol. 185, no. 1, pp. 49–54, Jan 2011.

[97] Z. Reddad, C. Gerente, Y. Andres, and P. Le Cloirec, "Adsorption of Several Metal Ions onto a Low-Cost Biosorbent: Kinetic and Equilibrium Studies," *Environmental Science & Technology*, vol. 36, no. 9, pp. 2067–2073, May 2002.

[98] A. Suna Erses, M. A. Fazal, T. T. Onay, and W. H. Craig, "Determination of solid waste sorption capacity for selected heavy metals in landfills." *Journal of hazardous materials*, vol. 121, no. 1-3, pp. 223–32, May 2005.

[99] F. Veglio' and F. Beolchini, "Removal of metals by biosorption: a review," *Hydrometallurgy*, vol. 44, no. 3, pp. 301–316, Mar 1997.

[100] R. Sime, "The Langmuir Adsorption Isotherm," *Infohost.Nmt.Edu*, p. 7, 2000.

[101] C. Gerente, V. K. C. Lee, P. L. Cloirec, and G. McKay, "Application of Chitosan for the Removal of Metals From Wastewaters by Adsorption—Mechanisms and Models Review," *Critical Reviews in Environmental Science and Technology*, vol. 37, no. 1, pp. 41–127, Jan 2007.

[102] T. W. Weber and R. K. Chakravorti, "Pore and Solid Diffusion Models for fixed-bed adsorbers," *AIChE Journal*, vol. 20, no. 2, Mar 1974.

[103] K. Kadirvelu, K. Thamaraiselvi, and C. Namasivayam, "Adsorption of nickel(II) from aqueous solution onto activated carbon prepared from coirpith," *Separation and Purification Technology*, vol. 24, no. 3, pp. 497–505, Sep 2001.

[104] D. D. Do, *Adsorption Analysis: Equilibria and Kinetics*, ser. Series on Chemical Engineering. PUBLISHED BY IMPERIAL COLLEGE PRESS AND DISTRIBUTED BY WORLD SCIENTIFIC PUBLISHING CO., Sep 1998, vol. 2.

[105] O. E. Abdel Salam, N. A. Reiad, and M. M. ElShafei, "A study of the removal characteristics of heavy metals from wastewater by low-cost adsorbents," *Journal of Advanced Research*, 2011.

[106] P. Bartczak, M. Norman, Ł. Klapiszewski, N. Karwańska, M. Kawalec, M. Baczyńska, M. Wysokowski, J. Zdarta, F. Ciesielczyk, and T. Jesionowski, "Manuscript title : Removal of nickel (II) and lead (II) ions from aqueous solution using peat as a low-cost adsorbent : A kinetic and equilibrium study Short title : Removal of nickel (II) and lead (II)," *Arabian Journal of Chemistry*, no. Ii, 2015.

[107] M. L. du Toit, "Incorporation of polysaccharide nanowhiskers into a poly (ethylene-co-vinyl alcohol) matrix," no. March, 2013.

[108] H. Pan, L. Li, L. Hu, and X. Cui, "Continuous aligned polymer fibers produced by a modified electrospinning method," *Polymer*, vol. 47, no. 14, pp. 4901–4904, Jun 2006.

[109] D. Li and Y. Xia, "Electrospinning of Nanofibers: Reinventing the Wheel?" *Advanced Materials*, vol. 16, no. 14, pp. 1151–1170, Jul 2004.

[110] V. Jacobs, R. D. Anandjiwala, and M. Maaza, "The influence of electrospinning parameters on the structural morphology and diameter of electrospun nanofibers," *Journal of Applied Polymer Science*, 2010.

[111] P. Yousefpour, F. Atyabi, R. Dinarvand, and E. Vasheghani-Farahani, "Preparation and comparison of chitosan nanoparticles with different degrees of glutathione thiolation." *Daru : journal of Faculty of Pharmacy, Tehran University of Medical Sciences*, vol. 19, no. 5, pp. 367–75, 2011.

[112] C. C. Sipoli, N. Santana, A. A. M. Shimojo, A. Azzoni, and L. G. de la Torre, "Scalable production of highly concentrated chitosan/TPP nanoparticles in different pHs and evaluation of the in vitro transfection efficiency," *Biochemical Engineering Journal*, vol. 94, pp. 65–73, 2015.

[113] P. Lu and Y.-L. Hsieh, "Preparation and properties of cellulose nanocrystals: Rods, spheres, and network," *Carbohydrate Polymers*, vol. 82, no. 2, pp. 329–336, Sep 2010.

[114] C. Kriegel, K. M. Kit, D. J. McClements, and J. Weiss, "Influence of surfactant type and concentration on electrospinning of chitosan-poly(ethylene oxide) blend nanofibers," *Food Biophysics*, vol. 4, no. 3, pp. 213–228, 2009.

[115] M. El-Sadaawy and O. Abdelwahab, "Adsorptive removal of nickel from aqueous solutions by activated carbons from doum seed (Hyphaenethebaica) coat," *Alexandria Engineering Journal*, vol. 53, no. 2, pp. 399–408, Jun 2014.

[116] A. K. Bhattacharya, S. N. Mandal, and S. K. Das, "Adsorption of Zn(II) from aqueous solution by using different adsorbents," *Chemical Engineering Journal*, vol. 123, no. 1-2, pp. 43–51, 2006.

[117] V. A. Alvarez, R. A. Ruseckaite, and A. Va, "Kinetic Analysis of Thermal Degradation in Poly (ethylene - vinyl alcohol) Copolymers."

[118] J. Williams and C. Gamonpilas, "Using the simple compression test to determine Young's modulus, Poisson's ratio and the Coulomb friction coefficient," *International Journal of Solids and Structures*, vol. 45, no. 16, pp. 4448–4459, Aug 2008.

[119] J. L. Gazquez, "The Hard and Soft Acids and Bases Principle," 1997.

[120] M. Arshadi, M. Amiri, and S. Mousavi, "Kinetic, equilibrium and thermodynamic investigations of Ni(II), Cd(II), Cu(II) and Co(II) adsorption on barley straw ash," *Water Resources and Industry*, vol. 6, pp. 1–17, Aug 2014. [Online]. Available: https://linkinghub.elsevier.com/retrieve/pii/S2212371714000158

[121] International Agency for Research on Cancer (IARC), "Arsenic, Metals, Fibres and Dusts: Nickel and Nickel Compounds," *IARC Monographs on the Evaluation of Carcinogenic Risks to Humans*, vol. 100C, pp. 169–218, 2012. [Online]. Available: https://monographs.iarc.fr/wp-content/uploads/2018/06/mono100C-10.pdf

[122] M. R. Samarghandy, E. Hoseinzade, M. Taghavi, and S. Hoseinzadeh, "Biosorption of reactive black 5 from aqueous solution using acid-treated biomass from potato peel waste," *BioResources*, vol. 6, no. 4, pp. 4840–4855, 2011. [Online]. Available: https://bioresources.cnr.ncsu.edu/BioRes{_}06/BioRes{_}06{_}4{_}4840{_}Samarghandy{_}HTR{_}Biosorp{_}RxK5{_}Aq{_}Soln{_}pdf

[123] P. Bartczak, M. Norman, Ł. Klapiszewski, N. Karwańska, M. Kawalec, M. Baczyńska, M. Wysokowski, J. Zdarta, F. Ciesielczyk, and T. Jesionowski, "Removal of nickel(II) and lead(II) ions from aqueous solution using peat as a low-cost

adsorbent: A kinetic and equilibrium study," *Arabian Journal of Chemistry*, Aug 2015.

[124] R. Terreux, M. Domard, C. Viton, and A. Domard, "Interactions study between the copper II ion and constitutive elements of chitosan structure by DFT calculation," *Biomacromolecules*, vol. 7, no. 1, pp. 31–37, 2006.

[125] A. D. Apte, V. Tare, and P. Bose, "Extent of oxidation of Cr(III) to Cr(VI) under various conditions pertaining to natural environment," *Journal of Hazardous Materials*, vol. 128, no. 2-3, pp. 164–174, 2006.

[126] T. Zhou, C. Li, H. Jin, Y. Lian, and W. Han, "Effective Adsorption/Reduction of Cr(VI) Oxyanion by Halloysite@Polyaniline Hybrid Nanotubes," *ACS Applied Materials & Interfaces*, vol. 9, no. 7, pp. 6030–6043, Feb 2017. [Online]. Available: http://pubs.acs.org/doi/10.1021/acsami.6b14079

[127] C. M. Futalan, C.-C. Kan, M. L. Dalida, K.-J. Hsien, C. Pascua, and M.-W. Wan, "Comparative and competitive adsorption of copper, lead, and nickel using chitosan immobilized on bentonite," *Carbohydrate Polymers*, vol. 83, no. 2, pp. 528–536, Jan 2011.

[128] L. J. Yu, S. S. Shukla, K. L. Dorris, A. Shukla, and J. Margrave, "Adsorption of chromium from aqueous solutions by maple sawdust," *Journal of Hazardous Materials*, vol. 100, no. 1-3, pp. 53–63, Jun 2003. [Online]. Available: https://linkinghub.elsevier.com/retrieve/pii/S0304389403000086

[129] M. B. Desta, "Batch sorption experiments: Langmuir and freundlich isotherm studies for the adsorption of textile metal ions onto teff straw (eragrostis tef) agricultural waste," *Journal of Thermodynamics*, vol. 1, no. 1, 2013.

[130] T. Zehra, L. B. L. Lim, and N. Priyantha, "Removal behavior of peat collected from Brunei Darussalam for Pb(II) ions from aqueous solution: equilibrium isotherm, thermodynamics, kinetics and regeneration studies," *Environmental Earth Sciences*, vol. 74, no. 3, pp. 2541–2551, Aug 2015.

[131] B. Dhir and R. Kumar, "Adsorption of Heavy Metals by Salvinia Biomass and Agricultural Residues," *Int. J. Environ. Res*, vol. 4, no. 3, pp. 427–432, 2010.

[132] B.-M. Min, S. W. Lee, J. N. Lim, Y. You, T. S. Lee, P. H. Kang, and W. H. Park, "Chitin and chitosan nanofibers: electrospinning of chitin and deacetylation of chitin nanofibers," *Polymer*, vol. 45, no. 21, pp. 7137–7142, Sep 2004.

[133] W.-Z. Wang, M. L. Brusseau, and J. F. Artiola, "Nonequilibrium and Nonlinear Sorption during Transport of Cadmium, Nickel, and Strontium through Subsurface

Soils," *Adsorption of Metals by Geomedia*, pp. 427–443, Jan 1998. [Online]. Available: https://www.sciencedirect.com/science/article/pii/B9780123842459500219

[134] S. K. R. Yadanaparthi, D. Graybill, and R. von Wandruszka, "Adsorbents for the removal of arsenic, cadmium, and lead from contaminated waters," *Journal of Hazardous Materials*, vol. 171, no. 1-3, pp. 1–15, 2009.

[135] H. A. Hegazi, "Removal of heavy metals from wastewater using agricultural and industrial wastes as adsorbents," *HBRC Journal*, vol. 9, no. 3, pp. 276–282, 2013.

[136] A. Thevannan, R. Mungroo, and C. H. Niu, "Biosorption of nickel with barley straw," *Bioresource Technology*, vol. 101, no. 6, pp. 1776–1780, Mar 2010.

[137] E. Malkoc and Y. Nuhoglu, "Investigations of nickel(II) removal from aqueous solutions using tea factory waste," *Journal of Hazardous Materials*, vol. 127, no. 1-3, pp. 120–128, Dec 2005.

[138] R. M. Lattuada, M. C. R. Peralba, J. H. Z. D. Santos, and A. G. Fisch, "Peat, Rice Husk and Rice Husk Carbon as Low-Cost Adsorbents for Metals from Acidic Aqueous Solutions," *Seperation Science and Technology*, pp. 101–111, 2014.

[139] R. Balasubramanian, S. V. Perumal, and K. Vijayaraghavan, "Equilibrium Isotherm Studies for the Multicomponent Adsorption of Lead, Zinc, and Cadmium onto Indonesian Peat," *Ind. Eng. Chem. Res.*, no. 4, pp. 2093–2099, 2009.

[140] B. Singha, S. K. Das, V. Kumar, G. B. Singha, and S. K. Das, "Removal of Pb(II) ions from aqueous solution and industrial effluent using natural biosorbents," *Environ Sci Pollut Res*, vol. 19, pp. 2212–2226, 2012.

[141] B. S. Hopkins, "Textbook of Inorganic Chemistry. Fifth edition (Partington, J. R.)," *Journal of Chemical Education*, vol. 14, no. 12, p. 600, Dec 1937.

[142] M. S. Peresin, Y. Habibi, J. O. Zoppe, J. J. Pawlak, and O. J. Rojas, "Nanofiber Composites of Polyvinyl Alcohol and Cellulose Nanocrystals: Manufacture and Characterization," *Biomacromolecules*, vol. 11, no. 3, pp. 674–681, Mar 2010.

[143] R. T. Olsson, R. Kraemer, A. López-Rubio, S. Torres-Giner, M. J. Ocio, and J. M. Lagarón, "Extraction of Microfibrils from Bacterial Cellulose Networks for Electrospinning of Anisotropic Biohybrid Fiber Yarns," *Macromolecules*, vol. 43, no. 9, pp. 4201–4209, May 2010.

[144] Ingvild Kvien, , Bjørn S. Tanem, and K. Oksman*, "Characterization of Cellulose Whiskers and Their Nanocomposites by Atomic Force and Electron Microscopy," *Biomacromolecules*, vol. 6, no. 6, pp. 3160–3165, Oct 2005.

[145] P. Visakh, S. Thomas, K. Oksman, and A. P. Mathew, "Crosslinked natural rubber nanocomposites reinforced with cellulose whiskers isolated from bamboo waste: Processing and mechanical/thermal properties," *Composites Part A: Applied Science and Manufacturing*, vol. 43, no. 4, pp. 735–741, Apr 2012.

[146] My Ahmed Saïd Azizi Samir, Fannie Alloin, Jean-Yves Sanchez, Nadia El Kissi, and Alain Dufresne, "Preparation of Cellulose Whiskers Reinforced Nanocomposites from an Organic Medium Suspension," *Macromolecules*, vol. 37, no. 4, pp. 1386–1393, Jan 2004.

[147] T. R. Crompton, "Chapter 1: Mechanical Properties of Polymers," *Physical Testing of Plastics*, pp. 1–148, 2012.

[148] K. Prabu and E. Natarajan, "Isolation and FTIR spectroscopy characterization of chitin from local sources," *Pelagia Research Library Advances in Applied Science Research*, vol. 2012, no. 2, pp. 1870–1875.

[149] J. Kumirska, M. Czerwicka, Z. Kaczynski, A. Bychowska, K. Brzozowski, J. Thoming, and P. Stepnowski, "Application of spectroscopic methods for structural analysis of chitin and chitosan." *Marine drugs*, vol. 8, no. 5, pp. 1567–636, Apr 2010.